

# Enhancing the usability of atmospheric oxygen measurements through emission source characterization and airborne measurements

## Dissertation

zur Erlangung des akademischen Grades doctor rerum naturalium  
(Dr. rer. nat.)

durchgeführt am Max-Planck-Institut für Biogeochemie Jena

vorgelegt dem Rat der Chemisch-Geowissenschaftlichen Fakultät  
der  
Friedrich-Schiller-Universität Jena



von Dipl. Phys. Julia Steinbach  
geboren am 7.4.1980 in Mainz

Gutachter:

1. Dr. Christoph Gerbig, Max-Planck-Institut für Biogeochemie Jena
2. Prof. Lothar Viereck-Götte, Friedrich-Schiller-Universität Jena

Datum der öffentlichen Verteidigung: 17.9.2010

# Abstract

Understanding of the global carbon cycle and its feedbacks on the climate system is an urgent scientific challenge, especially with the background of the ongoing climate change. High-precision measurements of atmospheric oxygen play an increasingly important role to improve our knowledge on carbon cycle processes. In combination with CO<sub>2</sub> measurements, they allow partitioning of global oceanic and terrestrial sinks of anthropogenic CO<sub>2</sub>. In addition, influences from biospheric processes and anthropogenic emissions on observed CO<sub>2</sub> variations can be distinguished using simultaneously measured O<sub>2</sub> mixing ratios, since these processes have different oxidative ratios (defined as  $OR = -\Delta O_2 / \Delta CO_2$ ).

The growing number of atmospheric monitoring stations in recent decades, especially on continents, has increased the scientific knowledge on carbon cycle processes. However, the proximity of continental stations to anthropogenic sources requires the characterization of these emission sources, their spatial and temporal variability and their influence on the atmospheric composition. This aspect is addressed in Chapter 2 of this thesis, investigating the possibility to use atmospheric simultaneous O<sub>2</sub> and CO<sub>2</sub> measurements for identifying emission sources. This is possible as different combustion processes have different oxidative ratios, depending on fuel composition. For the purpose of this chapter, the COFFEE (CO<sub>2</sub> release and Oxygen uptake from Fossil Fuel Emissions Estimate) dataset, a high-resolution inventory of anthropogenic CO<sub>2</sub> emissions and the corresponding O<sub>2</sub> uptake is created from emission inventories and fuel consumption data. Using model simulations with input from this dataset, it is investigated whether the influence of the local fuel mix can be detected in measured signals of atmospheric oxygen. Model simulations are compared to observational results from two monitoring stations, the Ochsenkopf tall tower in Germany and Hateruma Island in Japan. In addition, the influence of variable oxidative ratios on the partitioning of the land and ocean carbons sinks as derived from inverse transport modeling of CO<sub>2</sub> and O<sub>2</sub> combined (known as atmospheric potential oxygen (APO) inversions) is investigated by assessing which part of the fossil fuel signal is misinterpreted as oceanic signal when employing a constant oxidative ratio for fossil fuel burning. Results from synthetic data experiments with

different sets of monitoring stations show that systematic offsets in APO fluxes arise from this simplification as soon as observational input from more polluted stations is used.

Another challenge for interpreting results from continental monitoring stations is the characterization of the spatial heterogeneity of atmospheric mixing ratios in between monitoring stations. Airborne measurements are best suited for this task, as they provide access to different temporal and spatial scales, but are also perfectly qualified for measuring three-dimensional distributions of atmospheric tracers or to follow air masses. Thus Chapter 3 and 4 focus on interpretation and improvement of airborne measurements for atmospheric oxygen.

In Chapter 3,  $O_2/CO_2$  ratios from flask samples taken during the BARCA (Balanço Atmosférico Regional de Carbono na Amazônia) aircraft campaign in the Brazilian Amazon basin are studied and the feasibility to use such ratios to separate different processes is investigated. The results show clear differences between background signals at higher altitudes and local influences (mainly biospheric processes) within the planetary boundary layer. Apart from biospheric processes, surface influences include contributions from biomass and fossil fuel combustion that could be identified with the help of the additional tracer CO. However, as robust detection of different signatures is limited by the low sampling density of flask samples, continuous measurement of  $CO_2$  and  $O_2$  are required to resolve more details.

The need for in-situ measurements is addressed in Chapter 4 by presenting the development of a new instrument, based on vacuum ultraviolet (VUV) absorption technique. The design of the instruments targets the use aboard small research aircrafts, therefore being small, lightweight, robust, insensitive to vibrations and able to perform measurements fully automated. This is achieved by a two-cell design that allows simultaneous measurement of the sample and a reference gas and is based on creating equal pressure and temperature conditions in the two cells rather than controlling them. A prototype version of this instrument has been built and tested in the laboratory in the course of this thesis.



# Zusammenfassung

Die Erforschung des globalen Kohlenstoffkreislaufes und seiner Wechselwirkungen mit dem Klima ist eine der herausragenden wissenschaftliche Herausforderungen, besonders in Anbetracht des aktuellen Klimawandels. Hochpräzise Messungen des atmosphärischen Sauerstoffgehalts tragen wesentlich zum Verständnis des globalen Kohlenstoffkreislaufes bei. Da der biogeochemische Sauerstoffzyklus eng an den Kohlenstoffzyklus gekoppelt ist, können verschiedene Prozesse durch charakteristische stöchiometrische Faktoren charakterisiert werden. Diese Faktoren, die sich aus dem molaren Verhältnis von Sauerstoff ( $O_2$ ) zu Kohlendioxid ( $CO_2$ ) ergeben, werden als Oxidationsverhältnisse (*oxidative ratios*) bezeichnet und sind folgendermaßen definiert:

$$OR = -\Delta O_2 [mol] / \Delta CO_2 [mol] \quad (1)$$

Messungen der atmosphärischen Sauerstoffkonzentration können daher gemeinsam mit  $CO_2$ -Messungen zur Bestimmung der ozeanischen und terrestrischen Komponente der globalen Kohlenstoffsinken verwendet werden, sowie zur Identifizierung verschiedener Prozesse, welche die atmosphärische  $CO_2$ -Konzentration beeinflussen.

Die Herausforderung bei atmosphärischen Sauerstoffmessungen liegt darin, dass die relevanten Signale in der Größenordnung von einigen ppm (*parts per million*) liegen, die gegenüber dem atmosphärischen Hintergrund von 21% Sauerstoff aufgelöst werden müssen. Daher wird die gemessene Sauerstoffkonzentration auch durch Änderungen in der Konzentration anderer Luftkomponenten, zum Beispiel Kohlendioxid oder Wasserdampf beeinflusst, weswegen Änderungen des atmosphärischen Sauerstoffgehalts meist als Änderungen des Sauerstoff- zu Stickstoffverhältnissen ( $\delta O_2/N_2$ ) angegeben werden, da Änderungen dieses Verhältnisses hauptsächlich durch Sauerstoffänderungen hervorgerufen werden. Bei der geringen Größe der Messsignale werden zudem Artefakte durch sogenannte Fraktionierungseffekte signifikant. Als Fraktionierung bezeichnet man die diffusive Separation verschiedener Moleküle aufgrund von Temperatur-, Druck- und Feuchtegradienten, Adsorption an Oberflächen oder Permeation durch Membrane.

Innerhalb der letzten 20 Jahre hat sich der wissenschaftliche Horizont im Bezug auf das Verständnis atmosphärischer Prozesse durch Weiterentwicklung von Messtechniken und

die Verdichtung des Netzwerks für atmosphärische Messungen wesentlich erweitert. Die steigende Anzahl von kontinentalen Beobachtungsstation erlaubt eine genauere Charakterisierung von Flüssen atmosphärischer Spurengase auf regionalen bis kontinentalen Skalen. Allerdings erschwert die Nähe der Kontinentalstationen zu lokalen (anthropogenen) Quellen und Senken die Interpretation der Messdaten.

Diese Arbeit beschäftigt sich mit verschiedenen Aspekten, die zu einer verbesserten Interpretation dieser Daten beitragen können. Der erste Aspekt ist die Charakterisierung anthropogener Emissionsquellen, ihrer räumlichen und zeitlichen Variabilität sowie ihr Einfluss auf die Zusammensetzung der Atmosphäre. Dieser Gesichtspunkt wird in Kapitel 2 dieser Arbeit behandelt. Hierbei wird untersucht, ob gleichzeitige Messungen von Kohlendioxid und Sauerstoff zur Identifizierung verschiedener Emissionsquellen verwendet werden können. Dies ist prinzipiell möglich, da sich verschiedene Verbrennungsvorgänge durch verschiedene Oxidationsverhältnisse auszeichnen, die durch die jeweilige Zusammensetzung des Brennstoffes bestimmt sind. Der Bereich der Oxidationsverhältnisse reicht dabei von 1 bis 1.95, der globale Mittelwert (gewichtet mit dem unterschiedlichen Verbrauch verschiedener Brennstoffe) liegt bei 1.4.

Zu diesem Zweck wurde unter Verwendung von Emissionsdatenbanken und verschiedener Informationen zum Brennstoffverbrauch ein hochaufgelöster Datensatz kreiert. Der *COFFEE*-Datensatz (*COFFEE* steht hier für *CO<sub>2</sub> release and Oxygen uptake from Fossil Fuel Emissions Estimate*) enthält anthropogene CO<sub>2</sub>-Emissionen und die entsprechende Sauerstoffaufnahme für die Jahre von 1995 bis 2008 mit einer zeitlichen Auflösung von 1h und einer räumlichen Auflösung von 1° x 1°. Dieser Datensatz wurde in Kombination mit Simulationen von atmosphärischen Transportmodellen verwendet, um zu untersuchen, inwieweit der lokale Brennstoffmix messbare Signaturen in der Atmosphäre hinterlässt. Modellsimulation unter Verwendung eines globalen (TM3) und eines regionalen Modells (REMO) zeigen, dass die Einflüsse auf die atmosphärischen Signale, wie sie an den Beobachtungsstationen detektiert werden, in der Größenordnung von einigen ppm liegen. Damit sind die Effekte nur unwesentlich größer als die Messgenauigkeit für atmosphärische Sauerstoffmessungen. Ob sie daher tatsächlich messbar sind, wurde für zwei verschiedene Messstationen untersucht: Den Ochsenkopf-Turm in Deutschland, der vom Max-Planck-Institut für Biogeochemie in Jena (MPI-BGC)

betrieben wird, und die Station Hateruma Island auf der japanischen Insel Hateruma, betrieben vom japanischen NIES-Institut (National Institute of Environmental Studies). Die Auflösung verschiedener fossiler Signale ist im Fall der Ochsenkopf-Station nicht möglich, da die atmosphärische Zusammensetzung dort hauptsächlich von biosphärischen Einflüssen (mit einem Oxidationsverhältnis von etwa 1.1) bestimmt wird. Die fossile Komponente der atmosphärischen O<sub>2</sub>- und CO<sub>2</sub>-Signale ist zu klein und zu wenig variabel, um signifikante Einflüsse gegenüber dem starken Signal der Biosphäre zu hinterlassen. Für Hateruma Island sehen die Ergebnisse jedoch anders aus, da das atmosphärische Signal dort hauptsächlich durch fossile Einflüsse vom asiatischen Festland bestimmt wird und der Brennstoffmix der verschiedenen asiatischen Länder (China, Korea und Japan) sehr unterschiedlich ist. Somit können verschiedene „pollution events“ aufgrund ihres O<sub>2</sub>/CO<sub>2</sub>-Verhältnisses den verschiedenen Ländern zugeordnet werden und damit zur Analyse der Herkunft der Luftmassen herangezogen werden.

Schlussendlich wird in Kapitel 2 noch der globale Aspekt variabler Oxidationsverhältnisse betrachtet. Dabei wird untersucht, inwieweit sich die Variationen des fossilen Oxidationsverhältnisses auf die Bestimmung der ozeanischen und terrestrischen CO<sub>2</sub>-Senken auswirkt. Eine Methode, die Austauschflüsse zwischen der Atmosphäre und dem Ozean bzw. der Biosphäre zu berechnen, sind sogenannte atmosphärische Inversionen. Für die Bestimmung der ozeanischer Prozesse wird üblicherweise die Messgröße APO (*Atmospheric Potential Oxygen*) verwendet. APO stellt eine gewichtete Summe der Änderungen in den atmosphärischen O<sub>2</sub> und CO<sub>2</sub>-Verhältnissen dar und ist folgendermaßen definiert:

$$\Delta APO = \Delta O_2 + 1.1 \Delta CO_2 \quad (2)$$

Der Gewichtungsfaktor 1.1 ist dabei so gewählt, dass APO unabhängig von Änderungen durch biosphärische Prozesse ist. Allerdings hängt das Signal immer noch leicht von Einflüssen durch fossile Verbrennung ab, die üblicherweise unter Verwendung von Emissionsdatenbank korrigiert werden. Dies geschieht allerdings unter Annahme eines konstanten Oxidationsverhältnisses von 1.4 für fossile Verbrennung. Diese Annahme ist gerechtfertigt, solange die atmosphärischen Signale nicht stark durch lokale Verbrennungseffekt mit  $OR \neq 1.4$  beeinflusst sind. Die Inversionsmethode berechnet Austauschflüsse zwischen der Atmosphäre und dem Ozean bzw. der Biosphäre, in dem

die Diskrepanz zwischen der an den Stationen gemessenen Zusammensetzung der Luft und den Ergebnissen der Modellierung mit einem atmosphärischen Transportmodell minimiert wird. Bei der Verwendung von Stationen, deren atmosphärische Konzentration signifikant durch fossile Signale mit  $OR \neq 1.4$  beeinflusst wird, wird ein Teil dieser fossilen Signale als Ozeansignale fehlinterpretiert. Inversionsszenarien unter Verwendung verschiedener Stationen zeigen, dass diese Fehlinterpretation in einigen Gegenden signifikante Änderungen des Langzeitmittelwerts der APO-Flüsse hervorruft, sobald Messdaten von Stationen wie Hateruma Island verwendet werden, deren Signale stärker durch fossile Verbrennung beeinflusst sind. Zukünftige Inversionen werden auch Daten neuerer Messstationen verwenden, die sich hauptsächlich in Europa und Nordamerika befinden. Ergebnisse der Inversionsszenarien zeigen, dass die Verwendung dieser Stationen zu einer signifikanten Verschiebung der Signale im Nordatlantik führt. Der hier entwickelte Datensatz zur Charakterisierung anthropogener Kohlendioxid-Emissionen und der entsprechenden Sauerstoffaufnahme ist daher äußerst nützlich, um solche Fehlinterpretationen zu vermeiden.

Die Kapitel 3 und 4 dieser Arbeit befassen sich mit einem weiteren Aspekt, der wichtig für die Interpretation von Messdaten kontinentaler Stationen ist: Die Charakterisierung der räumlichen Variabilität zwischen den Messstationen. Dazu können flugzeuggestützte Messungen verwendet werden, die eine bessere räumliche und zeitliche Auflösung ermöglichen und bestens dazu geeignet sind, die horizontale und vertikale Verteilung von atmosphärischen Messgrößen zu charakterisieren. Außerdem können Flugzeuge für sogenannte *Lagrange-Experimente* verwendet werden, bei denen das Flugzeug einer bestimmten Luftmasse folgt, um ein besseres Verständnis atmosphärischer Transportprozesse zu erlangen. Trotz der technischen Fortschritte im Bezug auf atmosphärische Sauerstoffmessungen in den letzten 20 Jahren, sind flugzeuggestützte  $O_2$ -Messungen noch selten und meist auf Luftprobennahmen in sogenannten *Flasks* beschränkt. Hierbei handelt es sich um Glasbehälter, die während des Fluges mit Luft gefüllt und später im Labor analysiert werden. Diese Methode ist zwar sehr zuverlässig, erlaubt aber nur geringe räumliche und zeitliche Auflösung.

In Kapitel 3 dieser Arbeit wurden  $O_2/CO_2$ -Verhältnisse in solchen Luftproben analysiert, die während der im Rahmen dieser Arbeit durchgeführten *BARCA* (*Balanço Atmosférico*

*Regional de Carbono na Amazônia*) Flugkampagne im brasilianischen Amazonasbecken gesammelt wurden. Diese Flugkampagne hatte das Ziel, die CO<sub>2</sub>-Bilanz des Amazonasbecken zu charakterisieren, das unter klimatischen Aspekten eine der interessantesten Gegenden der Welt ist, da es mehr als die Hälfte des globalen Regenwaldes enthält. Dieser stellt eine enorme CO<sub>2</sub>-Senke dar, die einen Großteil der anthropogenen CO<sub>2</sub>-Emissionen neutralisiert. In den letzten Jahrzehnten haben jedoch Brandrodung der Regenwälder sowie die Nutzung ehemaliger Waldflächen für Ackerbau zu einer negativen CO<sub>2</sub>-Balance beigetragen. Erkenntnisse zur Gesamtbilanz für CO<sub>2</sub> sind mit starken Unsicherheiten behaftet, es ist bisher noch nicht einmal eindeutig geklärt, ob das Amazonasbecken insgesamt eine Quelle oder eine Senke von CO<sub>2</sub> darstellt.

Im Rahmen dieser Doktorarbeit wurde untersucht, inwieweit Oxidationsverhältnisse in den gesammelten Luftproben zur Identifikation verschiedener Prozesse und damit zur besseren Interpretation der gemessenen CO<sub>2</sub>-Daten verwendet werden können. Die Oxidationsverhältnisse der Luftproben wurden durch lineare Regression der Sauerstoff- gegen die Kohlendioxidkonzentration bestimmt. Hierbei zeigen Luftproben aus höheren atmosphärischen Schichten (insbesondere der freien Troposphäre) signifikant höhere Werte als Luftproben, die innerhalb der planetaren Grenzschicht genommen worden. Dies ist auch zu erwarten, da die atmosphärische Zusammensetzung in größerer Höhe mehr ein Hintergrundsignal darstellt, dass durch einen größeren Einflussbereich charakterisiert ist, in dem auch Austauschprozesse zwischen Atmosphäre und Ozean (mit höherem Oxidationsverhältnis) eine Rolle spielen. In Bodennähe dagegen bestimmen eher lokale Einflüsse die gemessenen Signale. Das Oxidationsverhältnis für die Luftproben innerhalb der planetaren Grenzschicht entspricht mit  $1.10 \pm 0.03$  dem Verhältnis für biosphärische Aktivität, was erwartungsgemäß der dominierende Prozess im Amazonasgebiet ist. Zusätzlich konnten allerdings auch lokale Einflüsse von fossiler und Biomassenverbrennung in einigen Proben detektiert werden. Dies geschah sowohl unter Verwendung des Oxidationsverhältnisses als auch der ebenfalls gemessenen Konzentration von Kohlenmonoxid (CO) in den Luftproben, da hohe CO-Werte ein Indikator für Verbrennungsprozesse sind. Die robuste Identifizierung dieser Prozesse wurde durch zwei Faktoren erschwert: zum Einen durch die Tatsache, dass die atmosphärische Zusammensetzung durch eine Mischung verschiedener Prozesse bestimmt ist (und damit auch die Luft in den verbrennungsbeeinflussten Proben eine starke biosphärische

Komponente enthält) und zum Anderen durch die begrenzte Probenmenge und -dichte. Die begrenzte Menge von Luftproben, die unter bestimmten Bedingungen genommen wurden, begrenzt die statistische Signifikanz der  $O_2/CO_2$ -Regressionen, während die geringe räumliche und zeitliche Auflösung der Messwerte die genaue Charakterisierung und die Analyse des zeitlichen Verlaufs verschiedener Prozesse erschwert. Für eine robuste Identifikation verschiedener Einflussfaktoren und die genauere Charakterisierung von Prozessen sind also kontinuierliche Messungen – sowohl von  $CO_2$  als auch von  $O_2$  – unbedingt erforderlich.

Kontinuierliche Messungen des atmosphärischen Sauerstoffgehalts an Bord von Flugzeugen sind zurzeit hauptsächlich durch den Mangel an geeigneten Messgeräten begrenzt. Die meisten Techniken, die Sauerstoff mit der erforderlichen Präzision messen können, erfordern schwere und unhandliche Geräte (zum Beispiel Massenspektrometer) oder sind durch ihre Bewegungsempfindlichkeit ungeeignet für die flugzeuggestützte Nutzung. Im Rahmen dieser Arbeit wurde daher ein Messgerät für kontinuierliche flugzeuggestützte Sauerstoffmessungen entwickelt, das in Kapitel 4 beschrieben wird. Das *ICON*-Gerät (*ICON* steht für *In-situ Capability for  $O_2/N_2$* ) wurde insbesondere für die Nutzung an Bord kleinerer Forschungsflugzeuge entwickelt. Dies erfordert neben Robustheit, niedrigem Gewicht und kompaktem Design auch eine komplette Automatisierung und eine schnelle Reaktionszeit des Geräts. Das zugrunde liegende Messprinzip ist UV-Absorption im sogenannten Vakuum-Ultraviolett-Bereich (VUV), da Licht in diesem Wellenlängenbereich besonders stark vom Luftsauerstoff absorbiert wird. Die VUV-Methode erlaubt eine schnelle Reaktionszeit und ist relativ unempfindlich gegenüber Vibrationen und anderen Bewegungen, die an Bord eines Flugzeuges auftreten. Zudem wurde sie bereits erfolgreich für flugzeuggestützte  $O_2$ -Messungen verwendet. Da für diese Methode keine kommerziellen Geräte verfügbar sind, mussten die benötigten Komponenten einzeln ausgesucht bzw. entwickelt und individuell angefertigt werden.

Zum kompakten Design des Geräts trägt die Tatsache bei, dass es über zwei Probenzellen verfügt, was die simultane Messung von Probenluft und einem Referenzgas ermöglicht. Zudem kann dadurch die Regelung des Probendrucks differentiell erfolgen, d.h. es wird nur der Druckunterschied zwischen den beiden Messzellen geregelt, anstatt den Absolutdruck aufwendig auf ppm-Level konstant zu halten. Damit wird ein platz- und

gewichtsintensives Druckregelungssystem vermieden. Zusätzlich erfordern die niedrige Flussraten, die das Gerät benötigt, nur einen geringen Bedarf an Referenzgas, wodurch für die Kalibrierung während des Fluges kleine 1L-Aluminium-Druckdosen statt schwerer Gaszylinder verwendet werden können. Für das zwei Zellen-Design wird das Licht einer 147nm-UV-Lampe durch einen Strahlteiler so aufgeteilt, dass beide Zellen den gleichen Ausschnitt der Lampe sehen und die optischen Wege gleich lang sind. Das Herzstück des Geräts, welches Lampe, Strahlteiler, Probenzellen, Detektoren zur Erfassung des Signal und die zugehörige Verstärkerelektronik beherbergt, wurde so konstruiert, dass sowohl hohes Gewicht als auch lange optische Wege vermieden werden, und in der Werkstatt des MPI-BGC angefertigt. Das individuell angefertigte 23Bit-System zur Signalerfassung und -aufzeichnung des Geräts ist in der Lage, Variationen im ppm-Bereich zu detektieren und äußerst rauscharm aufzuzeichnen. Nach ausführlicher Untersuchung der Einzelkomponenten wurde der gesamte Aufbau in ein 19-Zoll-Standardgehäuse integriert. Mit einer Größe von 44 cm x 36 cm x 23 cm und einem Gewicht von 12kg, kann das ICON-Gerät ohne Probleme an Bord kleinerer Forschungsflugzeuge untergebracht werden.

Im Rahmen dieser Doktorarbeit konnte gezeigt werden, dass die angestrebte Messgenauigkeit des Geräts im Bezug auf die Leistungsfähigkeit der einzelnen Komponenten erreicht werden kann. Vor dem endgültigen Einsatz des Geräts an Bord von Forschungsflugzeugen sind allerdings noch weitere Laboruntersuchungen des zusammengebauten Messsystems erforderlich. Schlussendlich muss der Einsatz bei Testflügen zeigen, wie sich die einzelnen Komponenten unter echten Flugbedingungen verhalten.

Vor dem Hintergrund der Entwicklung des ICON-Geräts wurden zudem Laborexperimente zur Charakterisierung möglicher Fraktionierung am Ansaugrohr des Flugzeugs (Inlet) durchgeführt. Für flugzeuggestützte Messungen können diese Effekte problematisch sein, da sich die Umgebungsbedingungen (Druck, Temperatur und Flugzeuggeschwindigkeit) mit der Flughöhe ändern. Die entstehenden Gradienten und die Änderung des Strömungsverhaltens können die Zusammensetzung der Probenluft beeinflussen und damit die Messungen verfälschen. Bei Flaskmessungen können diese Effekte durch gleichzeitige Messung des Argon-Stickstoff-Verhältnisses ( $\text{Ar}/\text{N}_2$ ) in den gesammelten Luftproben entdeckt und korrigiert werden. Dies ist möglich, da die meisten Fraktionierungseffekte für  $\text{O}_2/\text{N}_2$  auch für  $\text{Ar}/\text{N}_2$  auftreten, hier jedoch größer und damit

leichter zu entdecken sind. Diese Kontrollmöglichkeit gibt es jedoch nicht bei in-situ Messungen, wie sie mit dem *ICON*-Gerät gemacht werden. Zudem *ICON* vermutlich besonders anfällig für Fraktionierungseffekte, da die niedrigen Flussraten des Geräts zu hohen Unterschieden zwischen Flugzeug- und Einlaßgeschwindigkeit führen.

In Laborexperimenten zur Charakterisierung dieses Effekts wurde Luft in ein miniaturisiertes Inlet (eine Kapillare mit 0.5 mm Durchmesser) gesaugt, dass sich einem verkleinerten Windkanal mit laminarer Strömung befand. Diese Experimente zeigen einen signifikanten Fraktionierungseffekt, der mit zunehmender „Flugzeuggeschwindigkeit“, d.h. höheren Strömungsgeschwindigkeiten im Windkanal zunimmt. Mithilfe von CFD (*Computational Fluid Dynamics*) Simulationen konnten die Zentrifugalkräfte, die die Luftmoleküle auf dem Weg ins Inlet erfahren, als Ursache der Fraktionierung identifiziert werden. Derselbe Fraktionierungsmechanismus kann auch verwendet werden, um höhenabhängige Variation in Ar/N<sub>2</sub> zu erklären, die während der Flugzeugkampagnen BARCA (siehe oben) und COBRA (CO<sub>2</sub> Budget and Rectification Airborne study) beobachtet wurden. Weitere CFD-Simulationen sind nötig, um den Fraktionierungseffekt als allgemeine Funktion der Inletgeometrie, der Flugzeuggeschwindigkeit und der Umgebungsbedingungen (Druck und Temperatur) zu beschreiben.

Insgesamt trägt diese Arbeit einige nützliche Erkenntnisse zum aktuellen Wissensstand im Bezug auf atmosphärische Sauerstoffmessungen bei, besonders unter dem Aspekt der Interpretation von Messdaten kontinentaler Beobachtungsstationen, die durch die Nähe zu variablen Quellen und Senken beeinflusst sind. In Kapitel 2 und 3 wurden zwei Beispiele gezeigt, wie die Kombination von atmosphärischen CO<sub>2</sub> und O<sub>2</sub>-Messungen zur Identifikation verschiedener Prozesse genutzt werden kann. Dabei wurde diskutiert, unter welchen Bedingungen die Trennung verschiedener Prozesse aufgrund gemessener Oxidationsverhältnisse möglich ist, und was die limitierenden Faktoren bei dieser Methode sind. Zudem wurden im Verlauf dieser Arbeit zwei nützliche Werkzeuge entwickelt: Der *COFFEE*-Datensatz als Hilfsmittel für die Interpretation atmosphärischer O<sub>2</sub> und CO<sub>2</sub>-Messungen und das *ICON*-Messgerät als experimentelles Werkzeug, um die Messungen selbst zu verbessern.



# Table of contents

ABSTRACT .....	I
ZUSAMMENFASSUNG .....	III
TABLE OF CONTENTS .....	XI
LIST OF FIGURES .....	XIV
LIST OF ACRONYMS .....	XVI
CHAPTER 1 INTRODUCTION .....	1
1.1 The global carbon cycle .....	2
1.2 The airborne fraction of CO <sub>2</sub> .....	3
1.3 Atmospheric O <sub>2</sub> as tracer for carbon cycle processes .....	5
1.3.1 The global budgets of atmospheric CO <sub>2</sub> and O <sub>2</sub> .....	8
1.3.2 Atmospheric Potential Oxygen .....	10
1.4 Oxygen measurements .....	10
1.4.1 Measurement techniques .....	11
1.4.2 The O <sub>2</sub> /N <sub>2</sub> ratio .....	11
1.4.3 Gas handling issues and fractionation effects .....	13
1.5 Platforms for CO <sub>2</sub> and O <sub>2</sub> measurements .....	17
1.5.1 Ground-based measurements .....	17
1.5.2 Airborne measurements .....	19
1.6 Thesis objectives .....	20
1.7 References .....	22
CHAPTER 2 O <sub>2</sub> /CO <sub>2</sub> RATIOS FROM FOSSIL FUEL COMBUSTION .....	31
2.1 Oxidative ratios for fossil fuel combustion .....	31
2.2 The COFFEE dataset .....	32
2.2.1 Data and Methodology .....	32
2.2.2 Spatial distribution of fossil fuel related oxidative ratios .....	35
2.2.3 Temporal variations in fossil fuel related oxidative ratios .....	38
2.3 Influence of fuel mix on atmospheric O <sub>2</sub> concentration .....	40
2.4 Comparison with observations .....	46
2.4.1 Ochsenkopf .....	46
2.4.2 Hateruma Island .....	51
2.5 Impact on separation of ocean and land carbon sinks .....	54
2.6 Conclusion .....	63
2.7 References .....	65

CHAPTER 3 O <sub>2</sub> /CO <sub>2</sub> RATIOS DERIVED FROM AIRBORNE FLASK SAMPLING IN AMAZONIA.....	67
3.1 The BARCA mission .....	67
3.1.1 Motivation .....	67
3.1.2 Aircraft campaigns.....	68
3.1.3 Measurements during BARCA .....	70
3.2 O <sub>2</sub> /N <sub>2</sub> ratios from flask samples.....	70
3.2.1 Flask sampling and analysis.....	70
3.2.2 Merging flask and in-situ data .....	71
3.2.3 Fractionation correction for O <sub>2</sub> /N <sub>2</sub> .....	73
3.3 O <sub>2</sub> /CO <sub>2</sub> results .....	77
3.3.1 Background signals versus local influences .....	78
3.3.2 Fossil fuel .....	83
3.3.3 Biomass burning .....	86
3.4 Conclusion .....	90
3.5 References .....	92
CHAPTER 4 DEVELOPMENT OF AN INSTRUMENT FOR AIRBORNE IN-SITU MEASUREMENTS OF ATMOSPHERIC O <sub>2</sub> /N <sub>2</sub> .....	95
4.1 Motivation.....	95
4.2 Measurement principle.....	96
4.3 Instrument design .....	100
4.3.1 Optical system .....	100
4.3.2 Signal detection and amplification .....	101
4.3.3 Data acquisition.....	101
4.3.4 Gas handling .....	102
4.3.5 Packaging.....	103
4.4 Instrument performance .....	105
4.4.1 Signal resolution and short-term noise .....	105
4.4.2 In-flight calibration .....	107
4.4.3 Current instrument status .....	111
4.5 Investigation of possible inlet fractionation effects .....	112
4.5.1 Experimental setup.....	113
4.5.2 Experimental results.....	116
4.5.3 Theoretical considerations .....	118
4.5.4 Scaling to aircraft measurements.....	122
4.6 Conclusion and Outlook.....	123
4.7 References .....	126
CHAPTER 5 SUMMARY AND CONCLUSIONS.....	128

APPENDIX 1 DERIVATION OF FLASK WEIGHTING FUNCTION.....	134
APPENDIX 2 DERIVATION OF OPTIMAL OPTICAL DENSITY .....	135
SELBSTSTÄNDIGKEITSERKLÄRUNG.....	138
CURRICULUM VITAE .....	139
ACKNOWLEDGEMENTS .....	140

# List of figures

Figure 1.1	Global carbon cycle .....	3
Figure 1.2	Airborne fraction of CO <sub>2</sub> .....	4
Figure 1.3	Partitioning of fossil fuel CO <sub>2</sub> uptake using O <sub>2</sub> measurements .....	9
Figure 1.4	Locations of ground-based stations measuring O <sub>2</sub> /N <sub>2</sub> . ....	18
Figure 2.1	Fossil fuel related CO <sub>2</sub> emissions and O <sub>2</sub> from COFFEE dataset. ....	36
Figure 2.2	Fossil fuel related oxidative ratio from COFFEE dataset. ....	37
Figure 2.3	Change in the fossil fuel related oxidative ratio from 1996 to 2006. ....	37
Figure 2.4	Global average OR <sub>ff</sub> , derived from different fossil fuel inventories.....	38
Figure 2.5	Location of model output from TM3 and REMO.....	41
Figure 2.6	Comparison of results from TM3 REMO for Ochsenkopf station .....	42
Figure 2.7	Model output for selected stations (ALT, OXK, LUT, HAT).....	43
Figure 2.8	Boxplot of modeled OR <sub>ff</sub> for all monitoring stations .....	46
Figure 2.9	Comparison of observed and modeled OR at Ochsenkopf station .....	48
Figure 2.10	Biospheric and fossil fuel contributions from STILT for OXK station...	49
Figure 2.11	Comparison of OR from observations and STILT model at OXK.....	50
Figure 2.12	Comparison of OR from STILT for constant and variable fuel mix .....	51
Figure 2.13	Comparison of observed and modeled OR at Hateruma station.....	53
Figure 2.14	Hemispherically integrated fossil fuel and oceanic APO fluxes .....	55
Figure 2.15	Temporal variation of $\Delta F_{APOff}$ and $F_{APO}$ on gridcell level.....	59
Figure 2.16	Long-term mean of $\Delta F_{APOff}$ and $F_{APO}$ on gridcell level.....	60
Figure 2.17	Results for $\Delta F_{APOff}$ from inversion without Hateruma station. ....	61
Figure 2.18	Results for $\Delta F_{APOff}$ from inversion with all monitoring stations .....	62
Figure 3.1	Flighttracks of BARCA-A campaign .....	69
Figure 3.2	Typical cross section of flights during BARCA-A.....	69
Figure 3.3	Flow diagram of the flask sampler used during the BARCA campaign.	70
Figure 3.4	Flask weighting function and timeseries of flask pressure .....	72
Figure 3.5	Spatial variations in measured Ar/N <sub>2</sub> ratios of flask samples.....	74
Figure 3.6	Altitude variation of Ar/N <sub>2</sub> . ....	74
Figure 3.7	Variation of Ar/N <sub>2</sub> ambient pressure and temperature .....	75
Figure 3.8	Fractionation correction of O <sub>2</sub> /N <sub>2</sub> profiles using measured Ar/N <sub>2</sub> . ....	76
Figure 3.9	Orthogonal distance regression of O <sub>2</sub> versus CO <sub>2</sub> . ....	77
Figure 3.10	Altitude distribution of CO <sub>2</sub> and O <sub>2</sub> mole fractions.....	78
Figure 3.11	Diurnal variation in PBL height.....	79
Figure 3.12	Altitude dependence of O <sub>2</sub> /CO <sub>2</sub> ratio.....	80
Figure 3.13	Determination of PBL height from potential temperature.....	81
Figure 3.14	Variability of CO <sub>2</sub> and O <sub>2</sub> within and above PBL .....	82
Figure 3.15	Oxidative ratios for samples within and above PBL .....	83
Figure 3.16	CO <sub>2</sub> emissions and oxidative ratios from fossil burning for Brazil .....	84
Figure 3.17	O <sub>2</sub> vs CO <sub>2</sub> regression for flasks taken in the Manaus area. ....	84
Figure 3.18	Fossil fuel part of CO <sub>2</sub> concentrations in the Manaus flasks.....	85
Figure 3.19	Flight areas influenced by biomass burning. ....	87

Figure 3.20 CO distribution of flasks influenced by biomass burning.....	87
Figure 3.21 O <sub>2</sub> versus CO <sub>2</sub> regression of flasks influenced by biomass burning.....	88
Figure 3.22 CO/CO <sub>2</sub> ratios of flasks influenced by biomass burning.....	89
Figure 4.1 Xenon emission lines and O <sub>2</sub> absorption cross section .....	97
Figure 4.2 Effective optical density and signal to noise ratio .....	98
Figure 4.3 Absorption coefficients of CO <sub>2</sub> and H <sub>2</sub> O .....	99
Figure 4.4 Optical design of the ICON instrument .....	100
Figure 4.5 Gas handling scheme of the ICON .....	102
Figure 4.6 Core part of ICON.....	104
Figure 4.7 Final ICON instrument.....	105
Figure 4.8 Short-term noise levels of the signals from ICON.....	107
Figure 4.9 Setup for stability tests for small reference tanks. ....	108
Figure 4.10 O <sub>2</sub> /N <sub>2</sub> ratios from small cylinders .....	109
Figure 4.11 Linear drift of O <sub>2</sub> /N <sub>2</sub> ratios from small cylinders .....	110
Figure 4.12 Typical signal of the ICON instrument after repackaging. ....	111
Figure 4.13 Inlet and wind tunnel for inlet fractionation experiments.....	113
Figure 4.14 Experimental setup for on inlet fractionation experiments. ....	114
Figure 4.15 Example of the differential O <sub>2</sub> signal from Oxzilla .....	116
Figure 4.16 Measured inlet fractionation effect. ....	117
Figure 4.17 CFD simulations of particle trajectories entering the inlet .....	120
Figure 4.18 Separation nozzle effect for particle trajectories.....	121

# List of acronyms

## Atmospheric components and tracers

APO	– atmospheric potential oxygen ( $O_2 + 1.1 CO_2$ )
Ar	– Argon
CFC	– Chlorofluorocarbon
CH <sub>4</sub>	– Methane
CO	– Carbon monoxide
CO <sub>2</sub>	– Carbon dioxide
H <sub>2</sub> O	– Water (vapor)
N <sub>2</sub>	– Nitrogen
N <sub>2</sub> O	– Nitrous oxide
O <sub>2</sub>	– Oxygen
O <sub>3</sub>	– Ozone

## Units and measurement conventions

PgC	– Petagrams of Carbon = $10^{15}$ g of Carbon
ppm	– parts per million (here used as $\mu\text{mole/mole} = 10^{-6}$ mole/mole)
ppb	– parts per billion (here used as $10^{-9}$ mole/mole)
per meg	– measurement convention for changes in atmospheric $O_2/N_2$ ratios

$$\text{with } \delta(O_2 / N_2) [\text{per meg}] = \left( \frac{(O_2 / N_2)_{\text{sample}} - (O_2 / N_2)_{\text{reference}}}{(O_2 / N_2)_{\text{reference}}} \right) \times 10^6$$

sccm	– standard cubic ccm (used as sccm/min for flow rates, referring to flow at standard pressure and temperature conditions)
Tmol	– Teramoles = $10^{12}$ moles

## Scientific Institutions and Departments

CDIAC	– Carbon Dioxide Information Analysis Center (Oak Ridge, USA)
INPE	– Instituto Nacional de Pesquisas Espaciais (São Paulo, Brazil)
IPCC	– Intergovernmental Panel of Climate Change
MPI-BGC	– Max Planck Institute for Biogeochemistry (Jena, Germany)
NIES	– National Institute of Environmental Studies (Japan)
NOAA	– National Oceanic and Atmospheric Administration (Boulder, USA) – CMDL – Climate Monitoring and Diagnostics Laboratory – GMD – Global Monitoring Division – ESRL – Earth System Research Laboratory
SIO	– Scripps Institute of Oceanography (San Diego, USA)

# Chapter 1

## Introduction

The Earth's climate is determined by several complex physical, biological, and chemical processes that involve interactions among the atmosphere, the ocean, and the land. Understanding these – often non-linear – processes and their feedbacks on the climate system is an urgent scientific challenge, especially since it has become increasingly apparent that recent human activities are causing unprecedented changes to this system that might even be irreversible.

Direct observations of atmospheric and oceanic temperature show that the global mean temperature has increased  $0.74^{\circ}\text{C} \pm 0.18^{\circ}\text{C}$  over the last century (estimate for the period 1906–2005, CRU/Hadley Centre Dataset CRUTEM3, (Brohan et al. 2006)) with an increasing growth rate over the recent decades. Besides, there is evidence for changes in other climate aspects: changing patterns in precipitation, rise of sea level, decreasing extent of ice and snow cover and glacier retreat as well as a growing frequency of extreme weather events (Trenberth et al. 2007). In the last decades it has become increasingly evident that the observed climate changes are mostly anthropogenic, as a result of the enhanced atmospheric greenhouse gas concentrations caused by fossil fuel burning (e.g. Barnett et al. 2001; Levitus et al. 2001; Stott et al. 2001; Stone et al. 2007).

Major greenhouse gases include natural abundant species such as water vapor ( $\text{H}_2\text{O}$ ), carbon dioxide ( $\text{CO}_2$ ), methane ( $\text{CH}_4$ ), tropospheric ozone ( $\text{O}_3$ ) and nitrous oxide ( $\text{N}_2\text{O}$ ) and predominantly man-made compounds such as chlorofluorocarbons (CFCs). Contained in the atmosphere, these greenhouse gases are transparent to the incoming short-wave solar radiation, but absorb long-wave (infrared) radiation, emitted by the Earth's surface, thus trapping heat within the atmosphere. This 'greenhouse effect' was discovered in 1824 by Joseph Fourier (1824) and quantified in 1896 by Svante Arrhenius, who also identified  $\text{CO}_2$  as a major source of this effect (Arrhenius 1896). Natural abundances of greenhouse gases are responsible for a warming of the Earth surface on the order of  $33^{\circ}\text{C}$ .

Arrhenius already predicted that anthropogenic emissions of CO<sub>2</sub> would be strong enough to lead to additional global warming, since the amount of heating depends on the concentration of greenhouse gases in the atmosphere. He estimated that the Earth temperature would increase by 5 to 6 degrees in case of doubling CO<sub>2</sub> concentration, not that different from recent estimates that range from 2 to 4.5 °C (Hegerl 2007).

To characterize how anthropogenic and natural forces influence the global climate, changes are expressed in terms of ‘radiative forcing’, i.e the radiative imbalance (in W/m<sup>2</sup>) in the climate system caused by these influences. The largest individual contribution (about 63 %, (Hofmann et al. 2006)) to the anthropogenic increase in radiative forcing comes from CO<sub>2</sub>. The atmospheric CO<sub>2</sub> concentration has risen from 275-285 ppm (parts per million, 1ppm = 1μmole/mole) in pre-industrial times (years 1000-1750, (Etheridge et al., 1996)) to 379 ppm in 2005 (IPCC 2007) with growth rates progressively higher each decade (Tans 2010). That increase is mainly due to anthropogenic CO<sub>2</sub> emissions from fossil fuel combustion (including minor contributions from cement production and gas flaring), but also due to land use changes such as deforestation (Houghton 2003) and biomass burning (Andreae and Merlet 2001). Present fossil fuel emissions amount to 8.5 Pg C/yr, while emissions due to land use change are about 1.5 Pg C/yr (Canadell et al. 2007; Le Quéré et al. 2009)

## 1.1 The global carbon cycle

The atmospheric CO<sub>2</sub> concentration is regulated by the biogeochemical carbon cycle (Figure 1.1). CO<sub>2</sub> in the atmosphere constitutes only a small fraction of the carbon stored in other reservoirs: About 80% of the total carbon is contained in sedimentary rocks in the form of organic compounds and carbonate. Dissolved inorganic carbon (DIC) in the ocean is the largest near-surface pool, containing 56 times more carbon than the atmosphere. On land, most of the carbon is contained in soils. The carbon cycle involves the continuous exchange of carbon among the different carbon pools, i.e. the interaction of the carbon in the atmosphere with the terrestrial biosphere, the ocean and the marine biosphere, as well as on longer time scales interactions with



sediments and the lithosphere. For example, CO<sub>2</sub> is removed from the atmosphere and converted into organic matter by plants via photosynthesis, while carbon returns to the atmosphere via decomposition. The CO<sub>2</sub> fluxes between the land biosphere, the atmosphere, and the ocean have maintained an approximately constant level of atmospheric CO<sub>2</sub> for the past 10000 years until the onset of the Industrial Revolution.

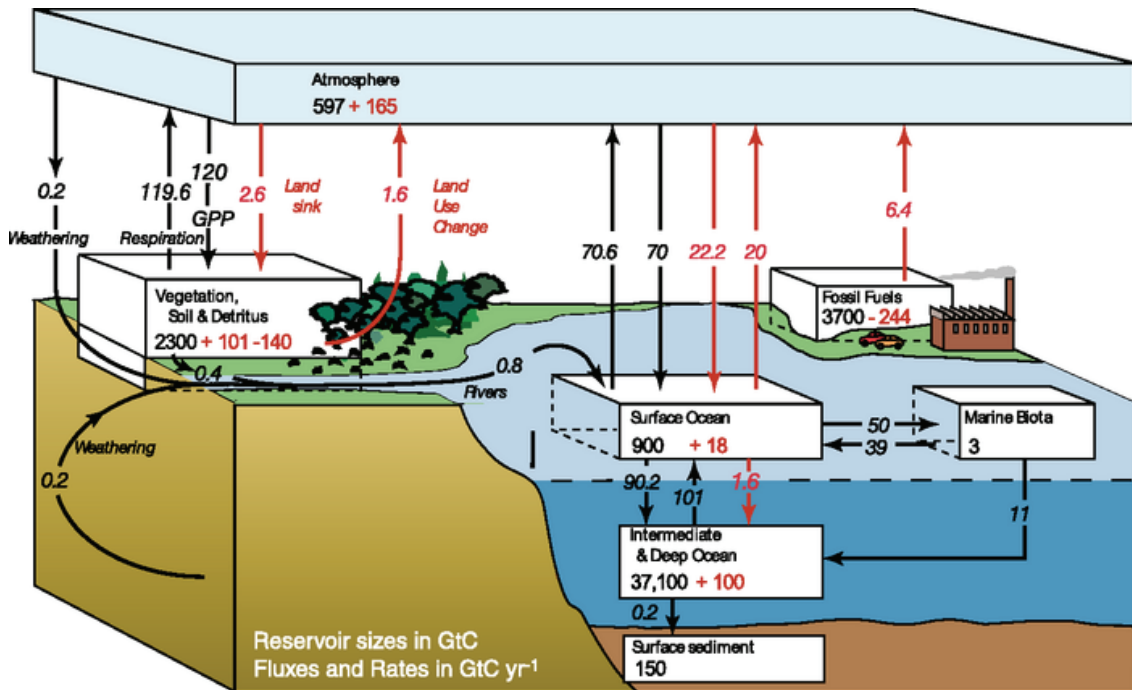


Figure 1.1 Global carbon cycle, taken from (IPCC 2007). Carbon fluxes are given in GtC/yr with natural fluxes depicted as black arrows and anthropogenic fluxes as red arrows.

Although anthropogenic CO<sub>2</sub> emissions (represented by red arrows in Figure 1.1) are small compared to the natural fluxes, they are still strong enough to cause significant perturbation of the equilibrium in the carbon cycle, leading to an accumulation of CO<sub>2</sub> in the atmosphere and the above-mentioned enhancement of the natural greenhouse effect.

## 1.2 The airborne fraction of CO<sub>2</sub>

Comparison of the atmospheric CO<sub>2</sub> growth rate with the estimated emissions from fossil fuel burning and land use (Marland et al. 2007) shows that only about 45% of

the total anthropogenic  $\text{CO}_2$  emitted stays in the in the atmosphere (the ‘airborne fraction’, see figure 1.2); the remainder is taken up by dissolution in the ocean and increased photosynthesis in terrestrial ecosystems. Estimates using different methods show that over the last decades the anthropogenic  $\text{CO}_2$  has been taken up by the land biosphere and ocean in comparable proportions (Rayner et al. 1999; Battle et al. 2000; Manning and Keeling 2006; Canadell et al. 2007). There is some evidence indicating that the airborne fraction might be increasing over the recent decades due to saturation of sinks (Le Quéré et al. 2007; Le Quéré et al. 2009), however analysis of longer time periods seems to show otherwise (Knorr 2009)

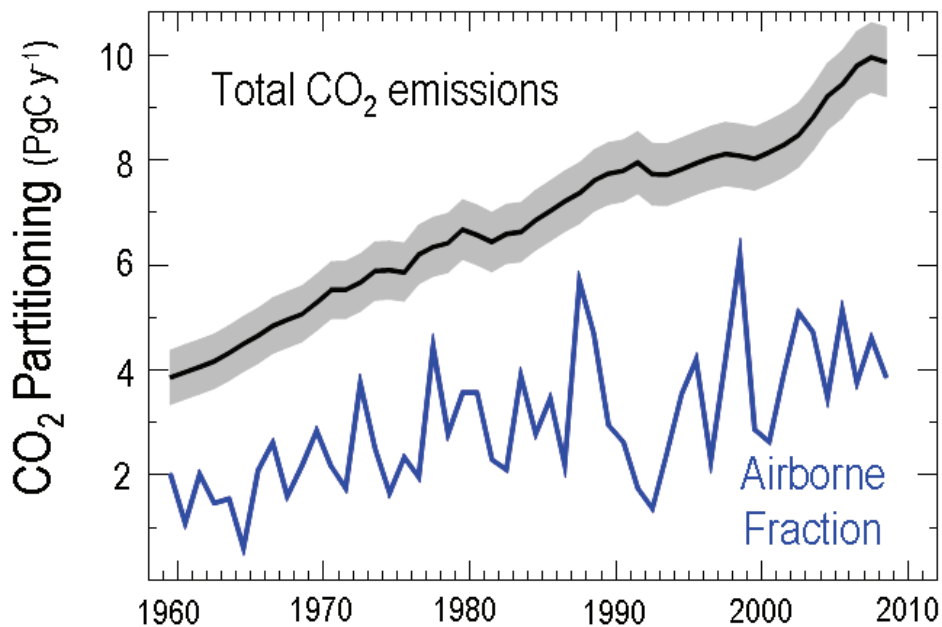


Figure 1.2: Airborne fraction of  $\text{CO}_2$ , taken from the Global Carbon Project homepage (<http://www.globalcarbonproject.org/>), data from NOAA/CDIAC, (Le Quéré et al. 2009)

The partitioning of the ocean and the terrestrial biosphere  $\text{CO}_2$  uptake is important because the fate of carbon stored in these two reservoirs is substantially different. Carbon stored in the land biosphere is sensitive to climate and human intervention and can therefore rapidly return to the atmosphere as  $\text{CO}_2$ , for example by biomass burning or deforestation. In contrast, for  $\text{CO}_2$  taken up by the oceans, most of the

carbon is not likely to re-enter the atmosphere quickly due to the slow mixing time of the oceans. Thus on longer time scales the ocean uptake may be more important for counteracting the effect of anthropogenic emissions. Therefore, in order to predict future atmospheric CO<sub>2</sub> concentrations it is crucial to determine the relative contributions of the two carbon sinks and to identify the underlying processes (Friedlingstein et al. 2006).

### 1.3 Atmospheric O<sub>2</sub> as tracer for carbon cycle processes

Direct measurements of carbon inventory changes in the ocean and the terrestrial biosphere are difficult. Furthermore, spatial and temporal inhomogeneities in the biosphere and the ocean complicate estimates of the strength of carbon sources and sinks. Therefore, we have to rely on indirect methods for determining the partitioning of anthropogenic CO<sub>2</sub> between the ocean and the terrestrial biosphere.

One of these is the combination of atmospheric measurements with inverse modeling techniques: The atmosphere acts as an integrator of carbon fluxes and is therefore an unbribable witness of the entire flux history. To derive information on surface sources and sinks from atmospheric measurements of CO<sub>2</sub> and other tracers, spatial and temporal variations in the atmospheric tracer concentration at the measurement locations are simulated using a transport model. By minimizing the differences between observed and modeled concentrations, the contributing surface fluxes are estimated using inverse techniques. This method is called ‘atmospheric transport inversion’ and has become a well-established tool during the past two decades (Tans et al. 1990; Rayner et al. 1999; Gurney et al. 2002; Gerbig et al. 2003; Rödenbeck et al. 2003; Zeng et al. 2005).

However, information on carbon sources and sinks can not be derived from measurement of CO<sub>2</sub> alone. One way to obtain additional information consists in measuring atmospheric oxygen (O<sub>2</sub>) in addition to CO<sub>2</sub> (see e.g. Keeling and Shertz 1992; Keeling et al. 1996; Battle et al. 2000).

The biogeochemical cycle of oxygen is closely coupled to the carbon cycle through photosynthesis, respiration, fossil fuel combustion and biomass burning. Changes in the atmospheric concentration of  $O_2$  and  $CO_2$  are usually anti-correlated: For example, photosynthesis produces oxygen and consumes  $CO_2$  whereas fossil fuel combustion consumes  $O_2$  and produces  $CO_2$ .

Ocean-related processes, however, lead to dissimilar patterns in the atmospheric  $O_2$  and  $CO_2$  signals. One reason for this is the difference in air-sea exchange on subannual time scales:  $O_2$ , like most other gases, equilibrates within a few weeks; therefore changes in oceanic  $O_2$  (caused by marine photosynthesis and respiration) are quickly transferred into the atmosphere.  $CO_2$  exchanges are much slower (on the order of one year) because most oceanic  $CO_2$  exists in the form of bicarbonate and carbonate ions, and only 1% is in the gaseous form that can be exchanged across the air-sea interface. A consequence of this is a difference in the seasonal cycles of  $O_2$  and  $CO_2$ . Another difference results from the dissimilar solubility of  $O_2$  and  $CO_2$  in seawater: Since oxygen is relatively insoluble in seawater, 99% of the oxygen in the ocean-atmosphere system is located in the atmosphere, whereas only 2% of the total carbon is airborne (Bender and Battle 1999).

Therefore rising levels of atmospheric  $CO_2$  easily disturb the atmosphere-ocean system and induce a  $CO_2$  flux from the atmosphere into the oceans that is not mirrored by an  $O_2$  flux from the oceans to the atmosphere. These differences allow us to use measurements of the atmospheric oxygen concentration to separate the  $CO_2$  uptake into land and ocean processes. Additional information can be gained from the fact that the different land processes have different 'oxidative ratios', i.e. molar  $O_2/CO_2$  exchange ratios.

Table 1.1 gives a simplified summary of the relevant biosphere and ocean processes and the expected  $O_2/CO_2$  ratios (following Keeling et al. (1995), numbers updated).

Process	Description	O <sub>2</sub> /CO <sub>2</sub>	Comment
terrestrial photosynthesis and respiration	$6\text{CO}_2 + 6\text{H}_2\text{O} \leftrightarrow$ $\text{C}_6\text{H}_{12}\text{O}_6 + 6\text{O}_2$	- 1.1	The deviation from 1.0 is caused by the influence of other elements than carbon (e.g. nitrogen). The ratio given here is a global average, determined by elemental abundance analyses and soil chamber measurements (Severinghaus 1995)
fossil fuel combustion	$\text{CH}_y + (1 + y/4) \text{O}_2$ $\leftrightarrow y/2 \text{H}_2\text{O} + \text{CO}_2$	- 1.4	Global average for 1990-2000 (Manning and Keeling 2006), determined from fossil fuel production data (Marland et al. 2002) and O <sub>2</sub> /CO <sub>2</sub> ratio for different fuel types (Keeling et al. 1998b)
Oceanic uptake of excess CO <sub>2</sub>	$\text{H}_2\text{O} + \text{CO}_2 + \text{CO}_3^-$ $\leftrightarrow 2\text{HCO}_3^-$	0	
Ocean photosynthesis and respiration	$106\text{CO}_2 + 16 \text{NO}_3^-$ $+ \text{H}_2\text{PO}_4^- + 17 \text{H}^+ \leftrightarrow$ $\text{C}_{106}\text{H}_{263}\text{O}_{110}\text{N}_{16}\text{P}$ $+ 138 \text{O}_2$	- 2 to -8	The ratio for oceanic photosynthesis and respiration as determined by the composition of marine plant matter is ~1.3 (Redfield et al. 1963), the actual air-sea fluxes however vary depending on the different efficiencies of gas exchange for O <sub>2</sub> and CO <sub>2</sub> and vary for different timescales (Keeling and Severinghaus 2000)

*Table 1.1 Summary of processes influencing the atmospheric O<sub>2</sub> and CO<sub>2</sub> concentrations and the stoichiometric values for O<sub>2</sub>/CO<sub>2</sub> exchange*

### 1.3.1 The global budgets of atmospheric CO<sub>2</sub> and O<sub>2</sub>

The global budgets of atmospheric CO<sub>2</sub> and O<sub>2</sub> can therefore be expressed as

$$\Delta\text{CO}_2 = F - B - O \quad (1.1)$$

$$\Delta\text{O}_2 = -\alpha_F F + \alpha_B B + Z \quad (1.2)$$

$\Delta\text{CO}_2$  and  $\Delta\text{O}_2$  represent the changes in the atmospheric CO<sub>2</sub> and O<sub>2</sub> concentration, respectively.  $F$  denotes the fossil fuel source of atmospheric CO<sub>2</sub>,  $B$  the sink due to biospheric processes and  $O$  the ocean uptake of CO<sub>2</sub>.

The greater part of the oxygen budget can be conveyed in terms of CO<sub>2</sub> sources and sinks, since biospheric and fossil fuel exchanges of O<sub>2</sub> and CO<sub>2</sub> occur at relatively fixed stoichiometric ratios. Therefore the biospheric oxygen source is  $B_{\text{O}_2} = -\alpha_B B$ , with  $\alpha_B = 1.1$  the average O<sub>2</sub>/CO<sub>2</sub> ratio for terrestrial photosynthesis and respiration (Severinghaus 1995), whereas the oxygen sink due to fossil fuel combustion is given as  $F_{\text{O}_2} = -\alpha_F F$ , with an oxidative ratio  $\alpha_F = 1.4$  (Keeling 1988). These ratios are global averages and may vary on smaller spatial and temporal scales (see Chapter 2). Not coupled to CO<sub>2</sub> sources and sinks is  $Z$ , the net exchange of atmospheric oxygen with the oceans, which is considered to be small compared to the other contributions.

The separation of the CO<sub>2</sub> uptake into ocean and biosphere can be performed using the equations above (see e.g. Keeling et al. 1996; Bender et al. 1998; Rayner et al. 1999; Battle et al. 2000; Bender et al. 2005; Manning and Keeling 2006). A graphical solution for the separation is shown in figure 1.3 on the following page.

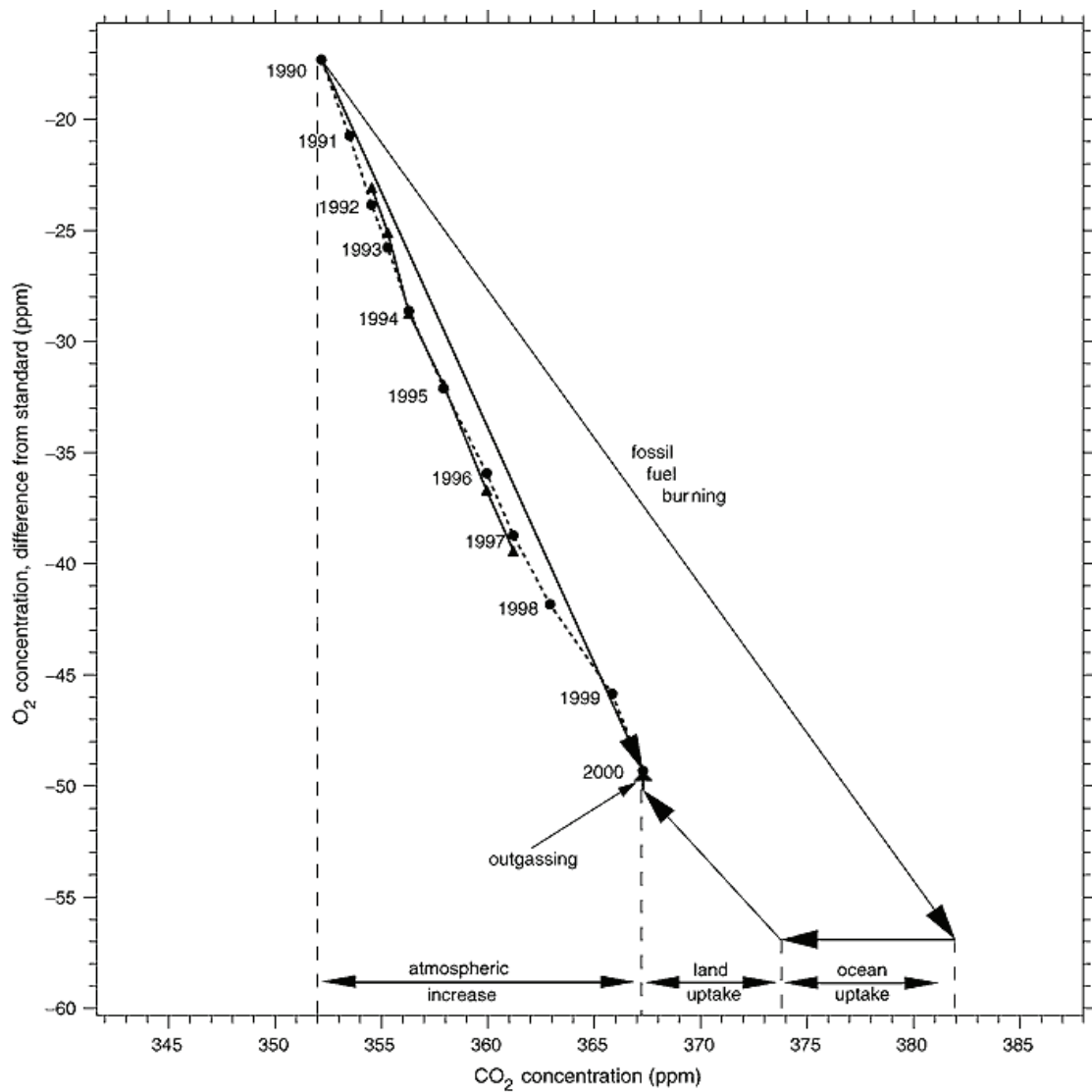


Figure 1.3: Partitioning of fossil fuel CO<sub>2</sub> uptake using O<sub>2</sub> measurements, taken from Prentice et al (2001). The graph shows the relationship between changes in CO<sub>2</sub> (horizontal axis) and O<sub>2</sub> (vertical axis). Data points are annual averages of observed O<sub>2</sub> and CO<sub>2</sub>, with different symbols indicating different sources of data. O<sub>2</sub> data are from (Keeling et al. 1996; Battle et al. 2000; Manning 2001), CO<sub>2</sub> data from (Conway et al. 1994). The slopes of the arrows for fossil fuel burning, land and ocean uptake are defined by the above mentioned O<sub>2</sub>/CO<sub>2</sub> stoichiometric ratios of these processes. The arrow labeled 'outgassing' denotes O<sub>2</sub> changes from oceanic outgassing (Levitus et al. 2001)

### 1.3.2 Atmospheric Potential Oxygen

Starting from this decoupling, it is possible to combine O<sub>2</sub> and CO<sub>2</sub> to a new (artificial) tracer, called atmospheric potential oxygen (APO) which is used to study ocean processes (Stephens et al. 1998). APO is defined as a weighted sum of CO<sub>2</sub> and O<sub>2</sub>:

$$\Delta \text{APO} = \Delta \text{O}_2 + \alpha_B \Delta \text{CO}_2 = (-\alpha_F + \alpha_B)F + (Z - \alpha_B O) \quad (1.3)$$

Here the weighting factor is chosen so that APO is conservative with respect to land biosphere processes. It consists only of an ocean part and a reduced contribution from fossil fuel that is usually negligible at the remote stations used to measure atmospheric CO<sub>2</sub> and O<sub>2</sub> concentration.

## 1.4 Oxygen measurements

Measuring variations in atmospheric O<sub>2</sub> concentration is very challenging because of the high atmospheric oxygen concentration of about 21%. Relevant changes in the O<sub>2</sub> concentration have about the same amplitude as changes in CO<sub>2</sub> (on the order of parts per million = ppm) and therefore require the same absolute measurement precision, but need to be detected against a much higher background signal.

For example, a plant that removes one CO<sub>2</sub> molecule per million air molecules by photosynthesis and releases an equivalent number of O<sub>2</sub> molecules to the atmosphere will leave a 1/380 or 0.26% signal in the background CO<sub>2</sub> mixing ratio, but only a 1/210000 or 0.00048% signal in the oxygen concentration. Therefore the relative precision required for O<sub>2</sub> measurements exceeds the requirements for CO<sub>2</sub> and other trace gas measurements by a factor of more than 500. At this precision level technical aspects such as gas handling and measurement artifacts also become much more critical.



### 1.4.1 Measurement techniques

The first successful method for measuring oxygen with the required precision was developed by Keeling (1988). Based on interferometry, this method detects changes in the O<sub>2</sub> mole fraction by measuring changes in the relative refractivity of air. Later, Bender et al. (1994) succeeded in measuring the O<sub>2</sub>/N<sub>2</sub> ratio of air with similar precision on an isotope ratio mass spectrometer. In the last 20 years, more high-precision techniques have been developed using paramagnetic (Manning et al. 1999; Manning 2001), vacuum ultraviolet adsorption (Stephens 1999; Stephens et al. 2003), gas chromatographic (Tohjima et al. 2003), and electrochemical methods (Stephens et al. 2001; Stephens 2007).

Presently, it is not possible to determine the absolute mole fraction of O<sub>2</sub> to the ppm level with any of these methods; only the detection of relative changes in O<sub>2</sub> at this level is feasible. The precision for relative measurements achievable with the different methods is not only determined by the precision of the O<sub>2</sub> sensor itself, but also by the whole surrounding setup, including the gas handling of the sample on the way to the sensor as well as the ability to relate the measurements to international reference scales.

### 1.4.2 The O<sub>2</sub>/N<sub>2</sub> ratio

The oxygen mole fraction in an air parcel,  $X_{O_2}$ , is defined as the number of oxygen molecules,  $M_{O_2}$ , divided by the total number of molecules in that air parcel:

$$X_{O_2} [\text{mole/mole}] = M_{O_2}/M_{\text{air}} \quad \text{with } M_{\text{air}} = M_{O_2} + M_{N_2} + M_{CO_2} + M_{Ar} + M_{\text{other trace gases}}$$

It can be seen that the O<sub>2</sub> mole fraction is also sensitive to variations in other air components. These dilution effects are not negligible: For example, a change of 1ppm in the number of CO<sub>2</sub> molecules already causes a change of 0.21ppm in the O<sub>2</sub> mole fraction. Hence O<sub>2</sub> variations are usually expressed as changes in the O<sub>2</sub>/N<sub>2</sub> ratio ( $=M_{O_2}/M_{N_2}$ ) that can only vary due to changes in the number of oxygen or nitrogen molecules. In most cases changes in the O<sub>2</sub>/N<sub>2</sub> ratio can be considered as being caused

only by changes in the oxygen mole number. This is because the atmospheric nitrogen variations are much smaller than oxygen variations (Keeling and Shertz 1992). In addition, the effect of nitrogen changes on the  $O_2/N_2$  ratio is four times smaller than the effect of oxygen changes of the same magnitude, since nitrogen is four times more abundant in the atmosphere.

The  $O_2/N_2$  ratio is commonly reported in units of ‘per meg’, i.e. as relative deviations from an arbitrary standard and multiplied by  $10^6$  (Keeling and Shertz 1992):

$$\delta(O_2 / N_2) = \left( \frac{(O_2 / N_2)_{sample} - (O_2 / N_2)_{reference}}{(O_2 / N_2)_{reference}} \right) \times 10^6 \quad (1.4)$$

Adding or removing 1  $\mu$ mole of  $O_2$  to a mole of dry air therefore causes a change of 4.8 per meg in the  $O_2/N_2$  ratio.

Of the different instruments mentioned above, mass spectrometers measure the  $O_2/N_2$  ratio directly, while the other methods measure changes related to the oxygen mole fraction. When converting to  $O_2/N_2$ , dilution effects need to be taken into account. Most of these effects are caused by changes in  $CO_2$  or water vapor. Therefore, it is necessary to simultaneously measure – and correct for – variations in  $CO_2$  (Keeling et al. 1998b) and to dry the sample air to avoid water dilution effects. Changes in measured oxygen mole fractions can be converted to  $O_2/N_2$  ratios using the following formula (Keeling et al. 1998a; Stephens et al. 2003):

$$\delta(O_2 / N_2) = \frac{\delta X_{O_2} + X_{O_2} \delta X_{CO_2}}{(1 - X_{O_2}) X_{O_2}} \quad (1.5)$$

Here  $\delta X_{O_2}$ ,  $\delta X_{CO_2}$  and  $\delta(O_2/N_2)$  denote the changes in the  $O_2$  and  $CO_2$  concentrations (in ppm) and in the  $O_2/N_2$  ratio (in per meg) and  $X_{O_2} = 0.20946$  (Machta and Hughes 1970) the standard mole fraction of oxygen in the air. Changes in  $X_{CO_2}$  are hereby expressed as deviations from 363.29 ppm, which is the average  $CO_2$  concentration of the reference cylinders defining zero on the international  $O_2/N_2$  per meg scale, defined

by the Scripps Institution of Oceanography (SIO). This equation is valid under the condition that the relative abundances of other air constituents (e.g.  $N_2$ , Ar,  $H_2O$ ) are constant.

### 1.4.3 Gas handling issues and fractionation effects

The development of oxygen sensors of adequate precision is only one part of the experimental challenge of measuring the small oxygen changes in the atmosphere. Also important are methods for gas handling, i.e for collecting and drying air samples, for the gas flow inside the measurement system or for storing reference gases that do not significantly alter the oxygen content of the air. Various effects can influence the oxygen concentration inside the measurement instrument or even at the sample intake: pressure and temperature-induced changes, chemical reactions, adsorption and desorption on internal surfaces of tubing and diffusion through some materials. Several authors already studied these effects, proposed strategies to minimize them and gave advice on gas handling procedures and the storage of reference cylinders (Keeling et al. 1998a; Manning 2001; Langenfelds et al. 2005; Sturm et al. 2005c).

Most measurement artifacts are caused by fractionation effects. The term fractionation originates from isotope measurements and denotes the separation of different components of an initially homogenous mixture. In the case of  $O_2/N_2$  measurements the term fractionation refers to the separation of oxygen with respect to nitrogen. One type of fractionation is the diffusive separation of oxygen and nitrogen by gradients in temperature, pressure and humidity. Oxygen, being the heavier molecule, tends to accumulate in regions with lower temperature, higher pressure and higher absolute humidity (Grew and Ibbs 1952; Chapman and Cowling 1970; Severinghaus et al. 1996).

For small temperature, pressure and humidity gradients, the magnitude of the fractionation effects can be calculated linearized equations (Keeling et al. 1998a), described in the following.

$$\textbf{Thermal fractionation: } \delta(O_2 / N_2) [\text{per meg}] = -\alpha \frac{\Delta T}{T} \cdot 10^6 \quad (1.6)$$

with  $\Delta T$  being the temperature difference,  $T$  the absolute gas temperature and  $\alpha = 0.018$  the thermal diffusion coefficient for  $O_2$  and  $N_2$  (Grew and Ibbs 1952). The effect of a  $1^\circ\text{C}$  difference in temperature is thus already on the order of -60 per meg. Thermal fractionation is also attributed to be the cause for fractionation at T-junctions where an incoming air stream divides into two outlet air streams (Manning 2001). The reason for this is that, unless the temperature is somehow controlled, the gas transported to the outlets never has exactly the same temperature on both sides. Manning (2001) reported that these fractionation effects occurred in the range of  $\pm 30$  per meg and seemed to increase with increasing flow difference of the two outlet streams. The same effect has also been observed at air inlets (which can also be considered as a special kind of T-junction) (Sturm et al. 2005c).

Besides this, temperature gradients can occur between the top and bottom of pressurized cylinders used for storing reference gases. If for example the outlet part of the tank is always slightly colder than the bottom,  $O_2$  is more likely to enter the outlet than  $N_2$ . Since the remaining air is then enriched in  $N_2$ , the resulting thermal fractionation leads to a drift in the  $O_2/N_2$  signal from this tank. To minimize these effects, long-term tests performed by Keeling et al. (2007) suggest the horizontal storage of reference cylinders as well as the use of ‘dip-tubes’ to take the air from the (presumably more well mixed) center of the tank instead of taking it from the upper part directly.

$$\textbf{Pressure induced fractionation: } \delta(O_2 / N_2) [\text{per meg}] = \frac{m_{O_2} - m_{N_2}}{m_{air}} \cdot \frac{\Delta p}{p} \cdot 10^6 \quad (1.7)$$

Here  $\Delta p$  is the pressure gradient,  $p$  the absolute gas pressure and  $m_{O_2}=32$ ,  $m_{N_2}=28$  and  $m_{air}\sim 29$  are the molecular masses of oxygen, nitrogen and air, respectively. This type of fractionation occurs for both hydrostatic pressure differences induced by gravity and flow-related pressure gradients. The fractionation effect for a 1‰ gradient in pressure, e.g. 1 mbar difference for 1 bar, is thus 138 per meg. Whereas flow-related pressure gradients are usually more important within a measurement system,

gravimetric fractionation is observed in air captured in snow or ice (Craig et al. 1988), but also plays a role in the storage of high-pressure cylinders. As estimated by Keeling et al. (1998a), at barometric equilibrium the  $O_2/N_2$  ratio at the top of a gas cylinder with a height of 1 m, positioned vertically, would be lower than the ratio at the bottom. As mentioned above, cylinders containing reference gas should therefore be stored horizontally to minimize any fractionation effects.

$$\textbf{Humidity induced fractionation: } \delta(O_2 / N_2) \text{ [per meg]} = \left( \frac{D_{N_2:H_2O}}{D_{O_2:H_2O}} - 1 \right) \cdot \Delta X_{H_2O} \cdot 10^6 \quad (1.8)$$

$\Delta X_{H_2O}$  denotes the gradient in water vapor mole fraction.  $D_{N_2:H_2O}$  is the diffusivity of nitrogen to water vapor and  $D_{O_2:H_2O}$  the diffusivity of oxygen to water vapor, with  $D_{N_2:H_2O} / D_{O_2:H_2O} = 0.965$  (Severinghaus et al. 1996). Considering air at 20°C and 1 bar pressure and a difference between 100% and 50% relative humidity, the gradient in the absolute water content is 11.5 mmol/mol, what leads to a fractionation effect of about 400 per meg.

The estimates above show that the potential fractionations are large compared to atmospheric variations in the  $O_2/N_2$  ratio. However, these equations describe the effect for flow conditions under which molecular diffusion is the only gas transport. If macroscopic flow also contributes to gas transport, as is normally the case, the actual degree of fractionation will be smaller by a factor that equals the ratio of the timescale for diffusive transport divided by the timescale for turbulent mixing or replacement of the sample air by a macroscopic flow (Keeling et al. 1998a). Considering for example a flow velocity of 1m/s on a length scale of 1cm and a diffusivity of 0.2 cm<sup>2</sup>/s, the reduction factor is already  $(100\text{cm/s} \cdot 1\text{cm}) / (0.2\text{cm}^2/\text{s}) = 500$ .

This suggests that appropriate gas handling strategies can reduce the fractionation to levels below 1 per meg or even less. However, care must be taken to work in the right flow regime and avoid larger gradients, since the potential for huge artifacts is always present.

Another potential fractionation mechanism is caused by gas **effusion through small orifices**, for example leaks. When the dimension of the orifice is smaller than the mean free path of the gas molecules, the dominant transport mechanism is Knudsen diffusion. In this flow regime, the molecular flow is proportional to the difference in partial pressure and to the molecular velocity, which varies inversely with the square root of the molecular weight (Dushman 1962). The O<sub>2</sub>/N<sub>2</sub> ratio of the gas escaping from the leak is therefore smaller by a factor of  $(28/32)^{1/2} = 0.946$  than upstream of the leak. For example, a small leak, leading to a loss of only 0.1% of the sample, can potentially enrich the O<sub>2</sub>/N<sub>2</sub> ratio of the remaining sample by 54 per meg.

Finally, fractionation can occur by **adsorption or desorption** of oxygen and nitrogen onto solid surfaces or by **dissolution into permeable solids**, e.g. elastomer seals. Normally, physical adsorption is reversible and depends on the gas pressure. That means that gases are adsorbed when the pressure increases and desorbed when it decreases, usually with different coefficients for different gases. Therefore changes in the O<sub>2</sub>/N<sub>2</sub> ratio with pressure are often observed when air is e.g. extracted from a high pressure cylinder. Adsorption can also be irreversible when chemical reactions of the gas (here oxygen) with the surface take place (chemisorption). For example, Keeling et al. (1998a) observed a long-term decrease in the O<sub>2</sub>/N<sub>2</sub> ratios of glass flasks contaminated with grease. Sturm et al. (2004) studied the permeation of different gases through various polymeric O-ring seals used to close glass flasks filled with sample air. They found that the gas inside the flask can be significantly affected during storage, depending on the materials and geometry of the seal and the stopcock as well as on partial pressure differences between the sample and surrounding air. The permeation coefficient is specific for gas-solid combinations, with the permeability of O<sub>2</sub> being higher than that of N<sub>2</sub> for most elastomers. Similar permeation phenomena can also affect the air inside a measurement system, for example if tubing or valve seats made of polymeric materials are used. In order to avoid these effects, care must be taken in choice of materials and equipment used within the whole measurement system, including high-pressure cylinders for reference gases and pressure regulators used to extract the air from them.

## 1.5 Platforms for CO<sub>2</sub> and O<sub>2</sub> measurements

A dense observational network monitoring atmospheric greenhouse gases and related tracers is fundamental for improving our understanding of the climate system. Measurements of atmospheric constituents are mostly made from ground-based stations, but also from moving platforms such as ships and aircraft. Independent of the platform, one can distinguish between two types of measurements: in-situ and flask measurements. As the name implies, in-situ measurements are made directly at the chosen station, ship or aircraft. In the case of flask measurements, air samples are taken at the location of interest and sent to a laboratory for analysis. Usually, glass flasks with a volume of 0.5 to 2ℓ are filled with a pressure of a few bar with sample air. The advantage of this method is that fewer expensive instruments or complex setups are required at each station, and the flasks can be measured for various species at different locations. Besides this, it allows intercomparison between laboratories or different methods since samples can be analyzed for the same species by different groups. On the other hand, in-situ measurements can be made continuously and therefore provide a higher temporal resolution. This is useful for capturing synoptic events and is especially important when the measurement platform is moving, i.e. an aircraft or a ship.

### 1.5.1 Ground-based measurements

A large number of globally distributed monitoring stations are measuring the atmospheric CO<sub>2</sub> concentration, with the longest systematic record running since 1958 (at Mauna Loa, Hawai (Keeling et al. 1995; Keeling and Whorf 2005)). By now more than 100 stations are measuring CO<sub>2</sub> and other greenhouse gases, providing long term observational records from all over the world (see e.g. (Conway et al. 1994; Keeling and Whorf 2005)). Measurements of atmospheric oxygen are still sparse compared to greenhouse gas measurements. Worldwide, O<sub>2</sub> is measured regularly at around 25 stations by several groups (Bender et al. 1996; Langenfelds et al. 1999; Battle et al. 2000; Tohjima et al. 2003; Sturm et al. 2005b; Manning and Keeling 2006), with 15 stations having an observational record of more than 15 years. These

observations are usually flask measurements, however in recent years continuous measurements have also been started at several stations (Manning 2001; Stephens 2007; Popa et al. 2009; Thompson et al. 2009; Lujikx et al. 2010) Figure 1.4 shows the location of all in-situ and flask measurement stations.

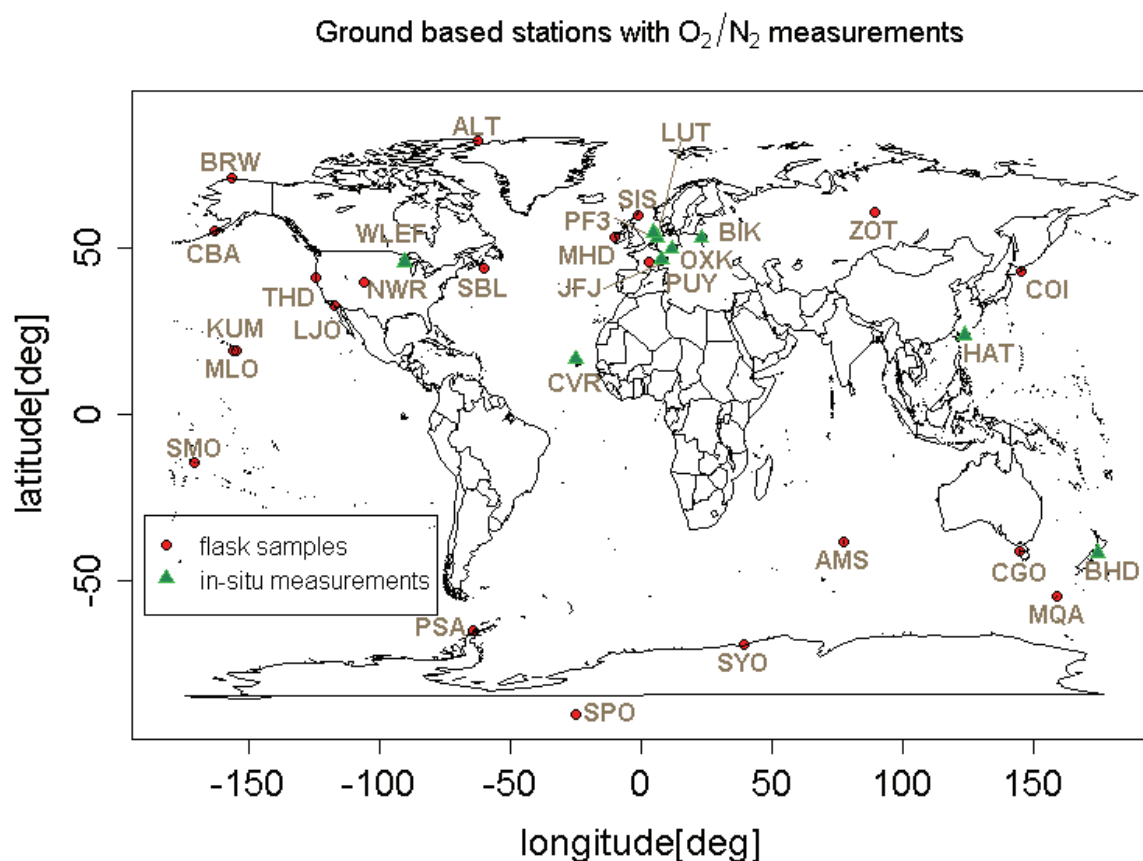


*Figure 1.4: Locations of ground-based stations measuring  $O_2/N_2$ . Station names are given as the official 3-letter codes.*

Traditionally, most of the measurement stations are located remotely. Signals measured in remote environments are more representative for the hemispheric or global scale since they are not dominated by strong local sources. Continental stations were avoided in the beginning because of the higher risk of local disturbances by terrestrial and industrial sources and sinks. In recent years however, inverse modeling studies have identified the lack of continental stations as strong limitation in resolving the longitudinal distribution of sources and sinks (Fan et al. 1998; Gloor et al. 2000). To solve this problem, Tans (1991) proposed measurements of trace gases at different heights on tall towers. Close to the surface, the measured signals are highly variable



since they are dominated by local sources and sinks – they can be useful for inferring fluxes at local or regional level with high temporal resolution. However, at a sufficient height above the ground – ideally a few hundred meters – the signal is representative for a larger influence area (with a radius on the order of 500 to 1000km). Continuous sampling from different heights therefore allows to separate local from regional signals (Gloor et al. 2000). Following this strategy, several tall towers have been set up in the US (NOAA/ESRL-GMD Tall Tower and Aircraft Network, see e.g.(Bakwin et al. 1998)), Japan (Inoue and Matsueda 2001), Siberia (Kozlova 2009) and Europe (CHIOTTO project, see (Vermeulen et al. 2007)). The Max Planck Institute for Biogeochemistry in Jena (MPI-BGC) is operating three of these tall towers, the one in Siberia and two in Europe – Ochsenkopf in Germany (Thompson et al. 2009), and Bialystok in Eastern Poland (Popa et al. 2009). The latter two also perform continuous measurements of atmospheric oxygen from different levels from near-ground to the top of the tower.

### **1.5.2 Airborne measurements**

Airborne measurements of greenhouse gases and related tracers are an important complement to the global network of surface sampling stations since they provide access to different spatial and temporal scales. Data from aircraft campaigns can be used for getting detailed information on regional budgets as well as for testing or evaluating atmospheric transport models (Gerbig et al. 2003; Dolman et al. 2006). Aircraft are uniquely suited to measure distributions of atmospheric tracers both in the vertical and the horizontal direction. Depending on aircraft type, they allow high-density observations from ground level up to around 12 km in the upper troposphere and lower stratosphere and horizontal scales from a few kilometers to hundreds or thousands of kilometers. Apart from that, aircrafts can conduct ‘Lagrangian experiments’, i.e. follow a certain airmass. Comparing the tracer concentrations measured upstream and downstream of a location provides constraints on regional fluxes that can not be achieved easily with other methods. Airborne measurements of O<sub>2</sub>/N<sub>2</sub> in the troposphere give information on the regional distribution of the different flux components that are associated with differing O<sub>2</sub>/CO<sub>2</sub> ratios. In addition, profile

measurements of  $O_2/N_2$  and  $CO_2$  in the stratosphere can provide information on transport processes, but have also been used to get information on past tropospheric  $O_2/N_2$  ratios when transport times are known from e.g. profiles of  $CO_2$  (Ishidoya et al. 2006).

During the last 30 years, an increasing number of different airborne measurements using various types of airplanes has been carried out – aircraft campaigns (e.g. Stephens et al. 2000; Lin et al. 2006), regular profiling in the vicinity of surface stations or measurements on board commercial airliners (Marenco et al. 1998; Machida et al. 2008). In-situ measurements on board aircraft are challenging since instruments need to perform under extreme conditions of changing pressure and temperature and resist mechanical stress due to shock and vibrations. Besides, due to space and weight limitations, especially on board small research aircraft, instruments are required to be rather small and lightweight. High-accuracy analyzers for in-situ measurements of  $CO_2$  already exist for quite some time (Anderson et al. 1996; Daube Jr. et al. 2002), but for many other species flask sampling is still the standard method. Although very reliable, flask samples can only provide a limited temporal and spatial resolution. Continuous measurements are preferable to improve the understanding of atmospheric transport and mixing processes.

The first airborne measurements of  $O_2/N_2$  were made during the COBRA experiment (Stephens et al. 2000) using flask sampling, an approach that was also used by (Sturm et al. 2005a) for profile measurements. First continuous in-situ airborne measurements of  $O_2/N_2$  were performed by Stephens during the IDEAS (<http://www.eol.ucar.edu/raf/Projects/IDEAS/>) and HIPPO campaign (Stephens 2009).

## 1.6 Thesis objectives

Over the past decade, the global network of stations monitoring the atmospheric  $CO_2$  and  $O_2$  content has been growing continuously and has also become more representative due to the addition of continental stations. Data from these stations

allow fluxes from regional to continental scales to be better constrained, but due to the proximity of highly variable local (e.g. anthropogenic) sources and sinks additional effort is needed to interpret the measurements.

This thesis deals with two aspects that are important for improving the utility of these data: First, the characterization of anthropogenic sources, their spatial and temporal variability and their influence on the atmospheric composition, and second, the use of airborne measurements to characterize the spatial variability of fluxes in between the ground-based monitoring stations.

The first aspect is addressed in Chapter 2 of this thesis by investigating the global oxygen uptake caused by fossil fuel burning. The  $O_2/CO_2$  exchange ratio for combustion processes depends on the type of fuel and varies from 1 to 2. However, for separating different processes, both on global and local scales, the global average of 1.4 is usually used. Here a high-resolution dataset for the global distribution of oxidative ratios related to fossil fuel burning is compiled using  $CO_2$  emission inventories together with fuel consumption data. Based on that dataset, it is investigated whether the influence of the local fuel mix can be detected in measured signals of atmospheric oxygen, and whether this information can be used to better interpret measured signals of atmospheric  $O_2$  and  $CO_2$ .

The subsequent chapters deal with airborne measurements of atmospheric oxygen, investigating oxidative ratios derived from flask data taken during an aircraft campaign in Chapter 3 and presenting the development of a new instrument for airborne in-situ measurements in Chapter 4.

Chapter 3 presents results of  $O_2/N_2$  and  $CO_2$  measurements from flasks taken during the BARCA (Balanço Atmosférico Regional de Carbono na Amazônia) aircraft campaign in the Amazon Basin (Brazil). The Amazon Basin is climatically a very interesting region, since it contains half of the world's undisturbed tropical forest and accounts for about 10% of global terrestrial net primary productivity (NPP). However, deforestation and agricultural development have led to huge  $CO_2$  sources in recent

decades. Therefore, estimates of CO<sub>2</sub> fluxes over Amazonia are subject to large uncertainties that propagate into the global carbon budget. The BARCA aircraft campaign was addressing the ‘missing scale’ for measurements of atmospheric CO<sub>2</sub>, intermediate between local point measurements and global modeling efforts. In the thesis chapter it is examined how simultaneous measurements of atmospheric oxygen and the resulting O<sub>2</sub>/CO<sub>2</sub> ratios can help to better interpret measured CO<sub>2</sub> signals.

As information from flask samples is limited due to their lower spatial and temporal resolution, Chapter 4 addresses the need for in-situ airborne measurements of O<sub>2</sub>/N<sub>2</sub>. The development of a new instrument, based on vacuum ultraviolet (VUV) absorption technique, is presented. The design of the instrument targets the use aboard small research aircrafts, therefore being small, lightweight, robust, insensitive to vibrations and able to perform measurements fully automated. This was achieved by a 2-cell design that allows simultaneous measurement of the sample and a reference gas and is based on creating equal pressure and temperature conditions in the two cells rather than controlling them. A prototype version of this instrument has been built and tested in the laboratory in the course of this thesis.

## 1.7 References

- Anderson, B. E., G. L. Gregory, J. E. Collins Jr., G. W. Sachse, T. J. Conway and G. P. Whiting (1996). "Airborne observations of spatial and temporal variability of tropospheric carbon dioxide." Journal of Geophysical Research-Atmospheres **101**(D1): 1985-1997.
- Andreae, M. O. and P. Merlet (2001). "Emission of trace gases and aerosols from biomass burning." Global Biogeochemical Cycles **15**(4 ): 955–966.
- Arrhenius, S. (1896). "On the influence of carbonic acid in the air upon the temperature of the ground (deutsch: "Über den Einfluß von Kohlensäure in der Luft auf die Bodentemperatur") " The London, Edinburgh and Dublin Philosophical Magazine and Journal of Science **5**: 237-276.
- Baker, D. F., R. M. Law, K. R. Gurney, P. Rayner, P. Peylin, A. S. Denning, P. Bousquet, L. Bruhwiler, Y.-H. Chen, P. Ciais, I. Y. Fung, M. Heimann, J. John, T. Maki, S. Maksyutov, K. Masarie, M. Prather, B. Pak, S. Taguchi and Z. Zhu (2006). "TransCom 3 inversion intercomparison: Impact of transport model errors on the interannual variability of regional CO<sub>2</sub> fluxes, 1988-2003." Global Biogeochemical Cycles **20**(1): doi:10.1029/2004GB002439.

- Bakwin, P. S., P. P. Tans, D. F. Hurst and C. L. Zhao (1998). "Measurements of carbon dioxide on very tall towers: results of the NOAA/CMDL program." Tellus Series B-Chemical and Physical Meteorology **50**(5): 401-415.
- Barnett, T. P., D. W. Pierce and R. Schnur (2001). "Detection of anthropogenic climate change in the world's oceans." Science **292**(5515): 270-274.
- Battle, M., M. L. Bender, P. P. Tans, J. W. C. White, J. T. Ellis, T. Conway and R. J. Francey (2000). "Global carbon sinks and their variability inferred from atmospheric O<sub>2</sub> and  $\delta^{13}\text{C}$ ." Science **287**(5462): 2467-2470.
- Bender, M., M. Battle and R. F. Keeling (1998). "The O<sub>2</sub> Balance of the Atmosphere: A Tool for Studying the Fate of Fossil-Fuel CO<sub>2</sub>." Annu. Rev. Energy Environ. **23**: 207 -223.
- Bender, M., T. Ellis, P. Tans, R. Francey and D. Lowe (1996). "Variability in the O<sub>2</sub>/N<sub>2</sub> ratio of southern hemisphere air, 1991-1994: Implications for the carbon cycle." Global Biogeochemical Cycles **10**(1): 9-21.
- Bender, M. L. and M. O. Battle (1999). "Carbon cycle studies based on the distribution of O<sub>2</sub> in air." Tellus Series B-Chemical and Physical Meteorology **51**(2): 165-169.
- Bender, M. L., D. T. Ho, M. B. Hendricks, R. Mika, M. O. Battle, P. P. Tans, T. J. Conway, B. Sturtevant and N. Cassar (2005). "Atmospheric O<sub>2</sub>/N<sub>2</sub> changes, 1993-2002: Implications for the partitioning of fossil fuel CO<sub>2</sub> sequestration." Global Biogeochemical Cycles **19**: GB4017, doi:10.1029/2004GB002410.
- Bender, M. L., T. Sowers, J.-M. Barnola and J. Chappellaz (1994). "Changes in the O<sub>2</sub>/N<sub>2</sub> ratio of the atmosphere during recent decades reflected in the composition of air in the firn at Vostok Station, Antarctica." Geophysical Research Letters **21**(3): 189-192.
- Bousquet, P., P. Peylin, P. Ciais, C. Le Quéré, P. Friedlingstein and P. P. Tans (2000). "Regional changes in carbon dioxide fluxes of land and oceans since 1980." Science **290**(5495): 1342-1346.
- Brenninkmeijer, C. A. M., P. Crutzen, F. Boumard, T. Dauer, B. Dix, R. Ebinghaus, D. Filippi, H. Fischer, H. Franke, U. Frieß, J. Heintzenberg, F. Helleis, M. Hermann, H. H. Kock, C. Koeppel, J. Lelieveld, M. Leuenberger, B. G. Martinsson, S. Miemczyk, H. P. Moret, H. N. Nguyen, P. Nyfeler, D. Oram, D. O'Sullivan, S. Penkett, U. Platt, M. Pupek, M. Ramonet, B. Randa, M. Reichelt, T. S. Rhee, J. Rohwer, K. Rosenfeld, D. Scharffe, H. Schlager, U. Schumann, F. Slemr, D. Sprung, P. Stock, R. Thaler, F. Valentino, P. v. Velthoven, A. Waibel, A. Wandel, K. Waschitschek, A. Wiedensohler, I. Xueref-Remy, A. Zahn, U. Zech and H. Ziereis (2007). "Civil Aircraft for the regular investigation of the atmosphere based on an instrumented container: The new CARIBIC system." Atmos. Chem. Phys. **7**: 4953-4976.
- Brohan, P., J. J. Kennedy, I. Harris, S. F. B. Tett and P. D. Jones (2006). "Uncertainty estimates in regional and global observed temperature changes: a new data set from 1850." Journal of Geophysical Research-Part D-Atmospheres **111**(D12): 21 pp.-21 pp.
- Canadell, J. G., C. Le Quere, M. R. Raupach, C. B. Field, E. T. Buitenhuis, P. Ciais, T. J. Conway, N. P. Gillett, R. A. Houghton and G. Marland (2007). "Contributions to accelerating atmospheric CO<sub>2</sub> growth from economic activity, carbon intensity, and efficiency of natural sinks." Proceedings of the

- National Academy of Sciences of the United States of America **104**(47): 18866-18870.
- Chapman, S. and T. G. Cowling (1970). The Mathematical Theory of Non-Uniform Gases, Cambridge Math. Libr.
- Conway, T. J., P. P. Tans, L. S. Waterman and K. W. Thoning (1994). "Evidence for Interannual Variability of the Carbon-Cycle from the National-Oceanic-and-Atmospheric-Administration Climate-Monitoring-and-Diagnostics-Laboratory Global-Air-Sampling-Network." Journal of Geophysical Research-Atmospheres **99**(D11): 22831-22855.
- Craig, H., Y. Horibe and T. Sowers (1988). "Gravitational separation of gases and isotopes in polar ice caps." Science **242**(4886 ): 1675-1678.
- Daube Jr., B. C., K. A. Boering, A. E. Andrews and S. C. Wofsy (2002). "A high-precision fast-response airborne CO<sub>2</sub> analyzer for in situ sampling from the surface to the middle stratosphere." Journal of Atmospheric and Oceanic Technology **19**(10): 1532-1543.
- Dolman, A. J., J. Noilhan, P. Durand, C. Sarrat, A. Brut, B. Piguet, A. Butet, N. Jarosz, Y. Brunet, D. Loustau, E. Lamaud, L. Tolck, R. Ronda, F. Miglietta, B. Gioli, V. Magliulo, M. Esposito, C. Gerbig, S. Körner, R. Glademard, M. Ramonet, P. Ciais, B. Neininger, R. W. A. Hutjes, J. A. Elbers, R. Macatangay, O. Schrems, G. Pérez-Landa, M. J. Sanz, Y. Scholz, G. Facon, E. Ceschia and P. Beziat (2006). "The CarboEurope regional experiment strategy." Bulletin of the American Meteorological Society **87**: 1367-1379.
- Dushman, S. (1962). Scientific Foundations of Vacuum Technique, Wiley.
- Fan, S., M. Gloor, J. Mahlman, S. Pacala, J. Sarmiento, T. Takahashi and P. Tans (1998). "A large terrestrial carbon sink in North America implied by atmospheric and oceanic carbon dioxide data and models." Science **282**(5388): 442-446.
- Fourier, J. (1824). "Remarques Générales Sur Les Températures Du Globe Terrestre Et Des Espaces Planétaires." Annales de Chimie et de Physique **27**: 136-67.
- Friedlingstein, P., P. Cox, R. Betts, L. Bopp, W. von Bloh, V. Brovkin, P. Cadule, S. Doney, M. Eby, I. Fung, G. Bala, J. John, C. Jones, F. Joos, T. Kato, M. Kawamiya, W. Knorr, K. Lindsay, H. D. Matthews, T. Raddatz, P. Rayner, C. Reick, E. Roeckner, K.-G. Schnitzler, R. Schnur, K. Strassmann, A. J. Weaver, C. Yoshikawa and N. Zeng (2006). "Climate-carbon cycle feedback analysis: Results from the C<sup>4</sup>MIP model intercomparison." Journal of Climate **19**(14): 3337-3353.
- Gerbig, C., J. C. Lin, S. C. Wofsy, B. C. Daube, A. E. Andrews, B. B. Stephens, P. S. Bakwin and C. A. Grainger (2003). "Toward constraining regional-scale fluxes of CO<sub>2</sub> with atmospheric observations over a continent: 1. Observed spatial variability from airborne platforms." Journal of Geophysical Research-Atmospheres **108**(4756): doi:4710.1029/2002JD00301.
- Gloor, M., S.-M. Fan, S. Pacala and J. Sarmiento (2000). "Optimal sampling of the atmosphere for purpose of inverse modeling: A model study." Global Biogeochemical Cycles **14**(1): 407-428.
- Grew, K. E. and L. T. Ibbs (1952). Thermal Diffusion in Gases, Cambridge Univ. Press, New York.

- Gurney, K. R., R. M. Law, A. S. Denning, P. J. Rayner, D. Baker, P. Bousquet, L. Bruhwiler, Y.-H. Chen, P. Ciais, S. Fan, I. Y. Fung, M. Gloor, M. Heimann, K. Higuchi, J. John, T. Maki, S. Maksyutov, K. Masarie, P. Peylin, M. Prather, B. C. Pak, J. Randerson, J. Sarmiento, S. Taguchi, T. Takahashi and C.-W. Yuen (2002). "Towards robust regional estimates of CO<sub>2</sub> sources and sinks using atmospheric transport models." Nature **415**(6872): 626-630.
- Hegerl, G. C., F. W. Zwiers, P. Braconnot, N.P. Gillett, Y. Luo, J.A. Marengo Orsini, N. Nicholls, J.E. Penner and P.A. Stott, 2007: (2007). Understanding and Attributing Climate Change. In: Climate Change The Physical Science Basis. Contribution of Working Group I to the Fourth Assessment Report of the Intergovernmental Panel on Climate Change S. [Solomon, D. Qin, M. Manning, Z. Chen, M. Marquis, K.B. Averyt, M. Tignor and H.L. Miller (eds.)]. Cambridge University Press, Cambridge, United Kingdom and New York, NY, USA.
- Hofmann, D. J., J. H. Butler, E. J. Dlugokencky, J. W. Elkins, K. Masarie, S. Montzka, A. and P. Tans (2006). "The role of carbon dioxide in climate forcing from 1979 to 2004: introduction of the Annual Greenhouse Gas Index." Tellus Series B-Chemical and Physical Meteorology **58**: 614–619.
- Houghton, R. A. (2003). "Revised estimates of the annual net flux of carbon to the atmosphere from changes in land use and land management 1850-2000." Tellus Series B-Chemical and Physical Meteorology **55**(2): 378-390.
- Inoue, H. Y. and H. Matsueda (2001). "Measurements of atmospheric CO<sub>2</sub> from a meteorological tower in Tsukuba, Japan." Tellus Series B - Chemical and Physical Meteorology **53B**: 205-219.
- IPCC (2007). Climate Change 2007: Synthesis Report. Contribution of Working Groups I, II and III to the Fourth Assessment Report of the Intergovernmental Panel on Climate Change [Core Writing Team, Pachauri, R.K and Reisinger, A. (eds.)]. Cambridge, Cambridge University Press.
- Ishidoya, S., S. Sugawara, G. Hashida, S. Morimoto, S. Aoki, T. Nakazawa and T. Yamanouchi (2006). "Vertical profiles of the O<sub>2</sub>/N<sub>2</sub> ratio in the stratosphere over Japan and Antarctica." Geophysical Research Letters **33**.
- Keeling, C. D. and T. P. Whorf (2005). Atmospheric CO<sub>2</sub> records from sites in the SIO air sampling network. Trends: A Compendium of Data on Global Change. O. R. N. L. Carbon Dioxide Information Analysis Center, U.S. Department of Energy, Oak Ridge, Tenn., U.S.
- Keeling, C. D., T. P. Whorf, M. Wahlen and J. van der Plicht (1995). "Interannual extremes in the rate of rise of atmospheric carbon dioxide since 1980." Nature **375**(6533): 666-670.
- Keeling, R. F. (1988). Development of an interferometric analyzer for precise measurements of the atmospheric oxygen mole fraction. Cambridge, Massachusetts, Harvard University. **PhD thesis**: 178p.
- Keeling, R. F., A. C. Manning, E. M. McEvoy and S. R. Shertz (1998a). "Methods for measuring changes in atmospheric O<sub>2</sub> concentration and their application in southern hemisphere air." Journal of Geophysical Research-Atmospheres **103**(D3): 3381-3397.
- Keeling, R. F., A. C. Manning, W. J. Paplawsky and A. C. Cox (2007). "On the long-term stability of reference gases for atmospheric O<sub>2</sub>/N<sub>2</sub> and CO<sub>2</sub>

- measurements." Tellus Series B-Chemical and Physical Meteorology **59**(1): 3-14.
- Keeling, R. F., S. C. Piper and M. Heimann (1996). "Global and hemispheric CO<sub>2</sub> sinks deduced from changes in atmospheric O<sub>2</sub> concentration." Nature **381**(6579): 218-221.
- Keeling, R. F. and J. Severinghaus (2000). Atmospheric oxygen measurements and the carbon cycle. The Carbon Cycle. T. M. L. Wigley and D. S. Schimel. Cambridge, Cambridge University Press: 134-140.
- Keeling, R. F. and S. R. Shertz (1992). "Seasonal and interannual variations in atmospheric oxygen and implications for the global carbon cycle." Nature **358**(6389): 723-727.
- Keeling, R. F., B. B. Stephens, R. G. Najjar, S. C. Doney, D. Archer and M. Heimann (1998b). "Seasonal variations in the atmospheric O<sub>2</sub>/N<sub>2</sub> ratio in relation to the kinetics of air-sea gas exchange." Global Biogeochemical Cycles **12**(1): 141-163.
- Knorr, W. (2009). "Is the airborne fraction of anthropogenic CO<sub>2</sub> emissions increasing?" Geophysical Research Letters **36**.
- Kozlova, E. (2009). "Methodology and calibration for continuous measurements of biogeochemical trace gas and O<sub>2</sub> concentrations from a 300-m tall tower in central Siberia." Atmospheric Measurement Techniques **2**: 205-220.
- Langenfelds, R. L., R. J. Francey and L. P. Steele (1999). "Partitioning the global fossil CO<sub>2</sub> sink using a 19-year trend in atmospheric O<sub>2</sub>." Geophysical Research Letters **26**(13): 1897-1900.
- Langenfelds, R. L., M. V. van der Schoot, R. J. Francey, L. P. Steele, M. Schmidt and H. Mukai (2005). "Modification of air standard composition by diffusive and surface processes." Journal of Geophysical Research - Atmospheres **110**: D13307, doi:10.1029/2004JD005482.
- Le Quere, C., M. R. Raupach, J. G. Canadell, G. Marland, L. Bopp, P. Ciais, T. J. Conway, S. C. Doney, R. A. Feely, P. Foster, P. Friedlingstein, K. Gurney, R. A. Houghton, J. I. House, C. Huntingford, P. E. Levy, M. R. Lomas, J. Majkut, N. Metzl, J. P. Ometto, G. P. Peters, I. C. Prentice, J. T. Randerson, S. W. Running, J. L. Sarmiento, U. Schuster, S. Sitch, T. Takahashi, N. Viovy, G. R. van der Werf and F. I. Woodward (2009). "Trends in the sources and sinks of carbon dioxide." Nature Geoscience **2**(12): 831-836.
- Le Quéré, C., C. Rödenbeck, E. T. Buitenhuis, T. J. Conway, R. Langenfelds, A. Gomez, C. Labuschagne, M. Ramonet, T. Nakazawa, N. Metzl, N. Gillett and M. Heimann (2007). "Saturation of the Southern Ocean CO<sub>2</sub> sink due to recent climate change." Science **316**: 1735-1738.
- Levitus, S., J. I. Antonov, J. L. Wang, T. L. Delworth, K. W. Dixon and A. J. Broccoli (2001). "Anthropogenic warming of Earth's climate system." Science **292**(5515): 267-270.
- Lin, J. C., C. Gerbig, S. C. Wofsy, B. C. Daube, D. M. Matross, V. Y. Chow, E. Gottlieb, A. E. Andrews, M. Pathmathevan and J. W. Munger (2006). "What have we learned from intensive atmospheric sampling field programmes of CO<sub>2</sub>?" Tellus Series B-Chemical and Physical Meteorology **58**(5): 331-343.



- Luijkx, I. T., R. E. M. Neubert, S. v. d. Laan and H. A. J. Meijer (2010). "Continuous measurements of atmospheric oxygen and carbon dioxide on a North Sea gas platform." Atmospheric Measurement Techniques **3**: 113-125.
- Machida, T., H. Matsueda, Y. Sawa, Y. Nakagawa, K. Hirotani, N. Kondo, K. Goto, T. Nakazawa, K. Ishikawa and T. Ogawa (2008). "Worldwide Measurements of Atmospheric CO<sub>2</sub> and Other Trace Gas Species Using Commercial Airlines." Journal of Atmospheric and Oceanic Technology **25**(10): 1744-1754.
- Machta, L. and E. Hughes (1970). "Atmospheric oxygen in 1967 to 1970." Science **168**(3939): 1582-1584.
- Manning, A. C. (2001). Temporal variability of atmospheric oxygen from both continuous measurements and flask sampling network: Tools for studying the global carbon cycle. Oceanography. San Diego, University of California.
- Manning, A. C. and R. F. Keeling (2006). "Global oceanic and land biotic carbon sinks from the Scripps atmospheric oxygen flask sampling network." Tellus Series B-Chemical and Physical Meteorology **58**(2): 95-116.
- Manning, A. C., R. F. Keeling and J. P. Severinghaus (1999). "Precise atmospheric oxygen measurements with a paramagnetic oxygen analyzer." Global Biogeochemical Cycles **13**(4): 1107-1115.
- Marengo, A., V. Thouret, P. Nédélec, H. Smit, M. Helten, D. Kley, F. Karcher, P. Simon, K. Law, J. Pyle, G. Poschmann, R. Von Wrede, C. Hume and T. Cook (1998). "Measurement of ozone and water vapor by Airbus in-service aircraft: The MOZAIC airborne program, An overview." Journal of Geophysical Research - Atmospheres **103**(D19): 25631-25642.
- Marland, G., T. A. Boden and R. J. Andres (2002). Global, regional, and national fossil fuel CO<sub>2</sub> emissions from Fossil-Fuel Burning, Cement Production, and Gas Flaring: 1751-1999, Carbon Dioxide Information Analysis Center, Oak Ridge National Laboratory, U.S. Department of Energy, Oak Ridge, Tenn., U.S.A.
- Marland, G., T. A. Boden and R. J. Andres (2007). Global, regional, and national fossil fuel CO<sub>2</sub> emissions from Fossil-Fuel Burning, Cement Production, and Gas Flaring. Oak Ridge, Tenn., U.S.A., Carbon Dioxide Information Analysis Center, Oak Ridge National Laboratory, U.S. Department of Energy.
- Popa, M. E., M. Gloor, A. C. Manning, A. Jordan, U. Schultz, F. Haensel, T. Seifert and M. Heimann (2009). "Measurements of greenhouse gases and related tracers at Bialystok tall tower station in Poland." Atmospheric measurement Techniques Discussions **2**: 2587-2637.
- Prentice, I. C., G. D. Farquhar, M. J. R. Fasham, M. L. Goulden, M. Heimann, V. J. Jaramillo, H. S. Kheshgi, C. L. Quéré, R. J. Scholes and D. W. R. Wallace (2001). The carbon cycle and atmospheric carbon dioxide In: Climate Change 2001: The Scientific Basis: Contribution of Working Group I to the Third Assessment Report of the Intergovernmental Panel on Climate Change. J. T. Houghton, Cambridge Univ. Press, New York: 881 pp.
- Rayner, P. J., I. G. Enting, R. J. Francey and R. Langenfelds (1999). "Reconstructing the recent carbon cycle from atmospheric CO<sub>2</sub>, delta C-13 and O-2/N-2 observations." Tellus Series B-Chemical and Physical Meteorology **51**(2): 213-232.

- Redfield, A. B., B. H. Ketchum and F. A. Richards (1963). The influence of organisms on the composition of seawater In: The Sea. M. N. Hill. New York, Wiley Intersciences. **vol 2:** p 26-77.
- Rödenbeck, C., S. Houweling, M. Gloor and M. Heimann (2003). "CO<sub>2</sub> flux history 1982-2001 inferred from atmospheric data using a global inversion of atmospheric transport." Atmospheric Chemistry and Physics **3**: 1919-1964.
- Severinghaus, J. P. (1995). Studies of terrestrial O<sub>2</sub> and Carbon Cycles in Sand Dune Gases and in Biosphere 2. New York, Columbia University. **PhD thesis:** 148p.
- Severinghaus, J. P., M. L. Bender, R. F. Keeling and W. S. Broecker (1996). "Fractionation of soil gases by diffusion of water vapor, gravitational settling, and thermal diffusion." Geochimica Et Cosmochimica Acta **60**(6): 1005-1018.
- Stephens, B. B. (1999). Field-based Atmospheric Oxygen Measurements and the Ocean Carbon Cycle. San Diego, California, U.S.A., University of California
- Stephens, B. B. (2007). "Application of a Differential Fuel-Cell Analyzer for Measuring Atmospheric Oxygen Variations." Journal of Atmospheric and Oceanic Technology **24**: 82-93.
- Stephens, B. B. (2009). Airborne Observations of O<sub>2</sub> and CO<sub>2</sub> on Regional to Global Scales 8<sup>th</sup> International CarbonDioxide Conference Jena, Germany.
- Stephens, B. B., P. Bakwin, P. Tans and R. Teclaw (2001). Measurements of atmospheric O<sub>2</sub> variations at the WLEF tall-tower site. In: Sixth International Carbon Dioxide Conference. Tohoku Univ., Sendai, Japan. **Extended Abstracts, vol. I:** 78-80.
- Stephens, B. B., R. F. Keeling, M. Heimann, K. D. Six, R. Murnane and K. Caldeira (1998). "Testing global ocean carbon cycle models using measurements of atmospheric O<sub>2</sub> and CO<sub>2</sub> concentration." Global Biogeochemical Cycles **12**(2): 213-230.
- Stephens, B. B., R. F. Keeling and W. J. Paplawsky (2003). "Shipboard measurements of atmospheric oxygen using a vacuum-ultraviolet absorption technique." Tellus Series B-Chemical and Physical Meteorology **55**(4): 857-878.
- Stephens, B. B., S. C. Wofsy, R. F. Keeling, P. P. Tans and M. J. Potosnak (2000). The CO<sub>2</sub> budget and rectification airborne study: strategies for measuring rectifiers and regional fluxes. Inverse Methods in Global Biogeochemical Cycles, Geophys. Monogr. Series, vol 114. P. Kasibhatla. Washington, D.C., AGU: 311 - 324.
- Stone, D. A., M. R. Allen and P. A. Stott (2007). "A multimodel update on the detection and attribution of global surface warming." Journal of Climate **20**(3): 517-530.
- Stott, P. A., S. F. B. Tett, G. S. Jones, M. R. Allen, W. J. Ingram and J. F. B. Mitchell (2001). "Attribution of twentieth century temperature change to natural and anthropogenic causes." Climate Dynamics **17**(1): 1-21.
- Sturm, P., M. Leuenberger, J. Moncrieff and M. Ramonet (2005a). "Atmospheric O<sub>2</sub>, CO<sub>2</sub>, and d13C measurements from aircraft sampling over Griffin Forest, Perthshire, UK." Rapid Communications in Mass Spectrometry **19**: 2399-2406.
- Sturm, P., M. Leuenberger and M. Schmidt (2005b). "Atmospheric O<sub>2</sub>, CO<sub>2</sub> and δ<sub>13</sub>C observations from the remote sites Jungfraujoch, Switzerland, and Puy de Dome, France." Geophysical Research Letters **32**(17): 4 pp.-4 pp.

- Sturm, P., M. Leuenberger, C. Sirignano, R. E. M. Neubert, H. A. J. Meijer, R. Langenfelds, W. A. Brand and Y. Tohjima (2004). "Permeation of atmospheric gases through polymer O-rings used in flasks for air sampling." Journal of Geophysical Research-Atmospheres **109**(D4): D04309, doi:10.1029/2003JD004073.
- Sturm, P., M. Leuenberger and F. L. Valentino (2005c). On thermal fractionation effects at air intakes. 13th WMO/IAEA Meeting of Experts on Carbene Dioxide Concentration and Related Tracers Measurement Techniques, Boulder, Colorado, USA, WMO-GAW Report 168.
- Tans, P. (1991). "Uncertainties in the global carbon-cycle." Pure and Applied Chemistry **63**(5): 766-768.
- Tans, P. P., I. Y. Fung and T. Takahashi (1990). "Observational constraints on the global atmospheric CO<sub>2</sub> budget." Science **247**(4949): 1431-1438.
- Thompson, R. L., A. C. Manning, M. Gloor, U. Schultz, T. Seifert, F. Haensel, A. Jordan and M. Heimann (2009). "In-situ measurements of oxygen, carbon monoxide and greenhouse gases from Ochsenkopf tall tower in Germany." Atmospheric Measurement Techniques **2**: 573–591.
- Tohjima, Y., H. Mukai, T. Machida and Y. Nojiri (2003). "Gas-chromatographic measurements of the atmospheric oxygen/nitrogen ratio at Hateruma Island and Cape Ochi-ishi, Japan." Geophysical Research Letters **30**(12): 1653, doi:10.1029/2003GL017282.
- Trenberth, K. E., P. D. Jones, P. Ambenje, R. Bojariu, D. Easterling, A. Klein Tank, D. Parker, F. Rahimzadeh, J. A. Renwick, M. Rusticucci, B. Soden and P. Zhai (2007). Observations: Surface and Atmospheric Climate Change. Climate Change 2007: The Physical Science Basis. Contribution of Working Group I to the Fourth Assessment Report of the Intergovernmental Panel on Climate Change. D. Q. [S. Solomon, M. Manning, Z. Chen, M. Marquis, K.B. Averyt, M. Tignor and H.L. Miller (eds)], Cambridge University Press, Cambridge, United Kingdom and New York, NY, USA.
- Vermeulen, A. T., G. Pieterse, A. Hensen, M. Schmidt, M. Ramonet, C. Messager, L. Jourdain, A. C. Manning, M. Gloor, A. Jordan, M. E. Popa, R. L. Thompson, E. Kozlova, E. Moors, J. Elbers, W. Jans, H. t. Maat, J. Moncrieff, F. Conen, L. Haszpra, Z. Barca, I. Szilagyi, P. Stefani, F. Miglietta and A. Lindroth. (2007). "CHIOTTO – Continuous High-Precision Tall Tower Observations of Greenhouse Gases. Final report." from <http://www.ecn.nl/docs/library/report/2007/e07052.pdf>.
- Zeng, N., H. F. Qian, C. Roedenbeck and M. Heimann (2005). "Impact of 1998-2002 midlatitude drought and warming on terrestrial ecosystem and the global carbon cycle." Geophysical Research Letters **32**(22): L22709, doi:10.1029/2005GL024607.



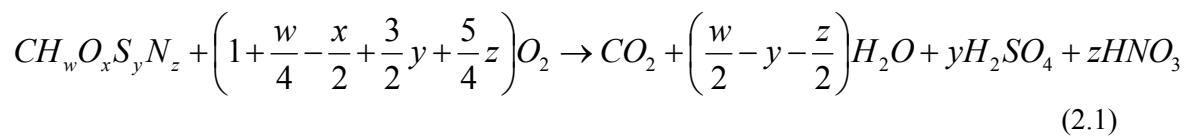
# Chapter 2

## O<sub>2</sub>/CO<sub>2</sub> ratios from fossil fuel combustion

Simultaneous measurements of atmospheric O<sub>2</sub> and CO<sub>2</sub> mole fractions allow the identification of local source/sink patterns since different processes have different oxidative ratios (OR = - ΔO<sub>2</sub> [mole]/ΔCO<sub>2</sub> [mole]). Therefore, atmospheric O<sub>2</sub> measurements can help to differentiate between industrial and terrestrial influences on observed CO<sub>2</sub> variations. This chapter investigates whether measured oxidative ratios, together with information on spatial patterns of O<sub>2</sub>/CO<sub>2</sub> emission ratios from combustion of different fuel types, can also be used for separating different anthropogenic emission sources and thus for better interpretation of regional CO<sub>2</sub> budgets. For this purpose, a global dataset of CO<sub>2</sub> emissions and O<sub>2</sub> uptake related to fossil fuel burning has been created using emission inventories and fuel consumption data. The potential influence of spatial patterns and temporal trends in the resulting O<sub>2</sub>/CO<sub>2</sub> emission ratios on the atmospheric oxygen signal is investigated for different stations in the global measurement network, using model simulations. The simulated results are compared in detail to observations from two selected stations. Finally, the influence of varying oxidative ratios on partitioning of the land and ocean sinks of anthropogenic carbon is investigated.

### 2.1 Oxidative ratios for fossil fuel combustion

As described in Chapter 1, fossil fuel combustion of CO<sub>2</sub> causes a decrease in atmospheric oxygen as for each mole of CO<sub>2</sub> on average 1.4 moles of O<sub>2</sub> are consumed (Keeling 1988). The exact oxidative ratio, i.e. the ratio of moles O<sub>2</sub> consumed per mole CO<sub>2</sub>, depends on the amount of carbon and other elements contained in a particular fuel. Following Keeling (1988), the oxidation process for fossil fuel burning can be described as



Here CH<sub>w</sub>O<sub>x</sub>S<sub>y</sub>N<sub>z</sub> represents the composition of the fuel. However, in most cases the sulfur and nitrogen content of fuels is negligible compared to the carbon and hydrogen content, therefore often the following simplified formula is used.



The oxidative ratio of the process is therefore  $OR_{ff} = 1 + y/(4x)$ . It can range from 1 to 2, with the ratio being 1 for pure carbon and 2 for methane. Usually, the following oxidative ratios are used for the three main types of fossil fuel: 1.17 for coal (or solid fuels in general), 1.44 for oil and other liquid fuels, and 1.95 for gaseous fuels (Keeling 1988). Cement production, accounting for 7% of total anthropogenic CO<sub>2</sub> emissions, does not consume oxygen and thus has an oxidative ratio of 0.

For the partitioning of global carbon sinks, a weighted average oxidative ratio is used. This ratio has been determined as 1.4 (Keeling 1988) and updated by (Manning and Keeling 2006) to  $1.39 \pm 0.04$  for the 1990s. This average is also usually used for distinguishing ecosystem and industrial processes when interpreting atmospheric O<sub>2</sub> and CO<sub>2</sub> signals measured at monitoring stations. However, in some cases deviations from this average caused by the local fuel mix have been observed: In the Netherlands, a region with high usage of natural gas, oxidative ratios as high as 1.5 have been measured (Sirignano et al. 2008; van der Laan-Luijkx et al. 2010). At Hateruma Island close to Japan, pollution events have shown oxidative ratios ranging from 1.05 to 1.4, correlated with the origin of the air (from China ( $OR_{ff} \sim 1.11$ ), Korea ( $OR_{ff} \sim 1.31$ ) or Japan ( $OR_{ff} \sim 1.37$ )) (C. Minejima, personal communication).

## 2.2 The COFFEE dataset

### 2.2.1 Data and Methodology

To estimate spatial and temporal patterns in O<sub>2</sub>/CO<sub>2</sub> emission ratios, high-resolution CO<sub>2</sub> emissions were combined with oxidative ratios at country level, calculated using fuel consumption statistics.

CO<sub>2</sub> emissions are taken from the *Emission Database for Global Atmospheric Research* (EDGAR,(Olivier and Berdowski 2001)). A version of EDGAR 3.2 with CO<sub>2</sub> emissions split into different categories is used (provided by S. Houweling, SRON, Utrecht). This version provides annual emissions on a 1° x 1° grid for the years 1991 to 2001 and 16 categories (e.g. power generation, transport). For comparison with recent atmospheric observations (see Chapter 2.4 and 4.3.2), the dataset was extended until the year 2008 by keeping the spatial distribution and relative contributions of the different categories of the year 2001 and extrapolating the amount of emissions using fuel consumption data at national level (assembled by BP, available at <http://www.bp.com/statisticalreview>).

Fuel-mix specific oxidative ratios for each country, year and category were determined using worldwide energy statistics compiled by the United Nations Statistics Division (available at <http://data.un.org/>). Data in these statistics, currently available for the years 1990 to 2006, are derived primarily from annual questionnaires distributed by the UN Statistical Office and supplemented by official national statistical publications. The dataset contains data on fuel production, import, export, consumption and conversion for 44 fuel types and over 200 countries. Fuel types include different sorts of coal, liquid and gaseous fuels as well as biofuels (e.g. fuelwood, biodiesel and various waste types). The reason for choosing this dataset was that the information on fuel consumption and conversion is not only given as national totals, but also split into different categories. These categories were merged to match the EDGAR categories; therefore the combination of the two datasets provides a resolution higher than country level.

To calculate the fuel-mix specific oxidative ratios from this consumption data, CO<sub>2</sub> emissions and oxygen uptake are at first derived for each fuel, country, category and year separately. CO<sub>2</sub> emissions are estimated from the carbon content of the consumed fuels, following the procedure and using the fuel-specific conversion factors from the 2007 statistics report by the International Energy agency (IEA 2007): Fuel consumption is first converted to a common energy unit (terajoules) and then multiplied with carbon emission factors (CEF, given in tons of carbon per terajoule).

Full combustion of fuels is assumed, therefore the resulting carbon emissions are not corrected for unoxidized carbon, which is also consistent with the EDGAR methodology. Instead of applying a general correction (in terms of a percentage) for carbon stored in non-energy products, only the categories that actually produce CO<sub>2</sub> emissions were chosen. To express the results in terms of CO<sub>2</sub> emissions rather than carbon emissions, they were multiplied with the molar weight ratio of CO<sub>2</sub> to C (44/12).

For calculating the corresponding O<sub>2</sub> uptake, CO<sub>2</sub> emissions for each entry in the dataset were multiplied with their specific oxidative ratio. Different oxidative ratios were given for the four main fuel types: coal, oil, gas and biofuels. For coal, oil and gas the ratios from Section 2.1 are used, for biofuels a weighted average of 1.07 was taken. That average was derived by calculating the oxidative ratios of the biofuels present in the dataset from Equation 2.1 and taking into account their relative contribution. It would be possible to further distinguish oxidative ratios e.g. for different types of coal, but the variations within the fuel types are rather small compared to the differences between the four fuel groups – for example the ratio for coal ranges from 1.09 for anthracite to 1.18 for bitumen (Keeling 1988).

CO<sub>2</sub> emissions and O<sub>2</sub> uptake for the different fuel types were added up for each country, category and year. The total O<sub>2</sub> uptake divided by the total CO<sub>2</sub> emissions gives the specific oxidative ratio for this set. Unlike EDGAR, the UN dataset has no information on CO<sub>2</sub> emissions from cement production. However, this is not problematic since cement production does not consume oxygen, therefore OR<sub>ff</sub> for the category cement production is always 0.0. After the calculation of the oxidative ratios, the dataset was checked for missing values that were then replaced by ‘best estimate’ oxidative ratios: If the information on the fuel mix was just missing for one year in a certain category and country, the mean oxidative ratio for the surrounding years was used. If there was no information for the whole category in a certain country, either the mean oxidative ratio for the category or for the country was used, depending on the category. Since the fuel consumption data for the early 1990s seemed not very reliable (showing unrealistically large variations and many missing values), only data



from 1995 onward was used. In order to extend the dataset for the two years after 2006, the fuel mix per category and country was kept the same as in 2006.

To derive the  $O_2$  uptake on gridcell level, the EDGAR  $CO_2$  emissions for each category and year were multiplied with the obtained oxidative ratios for the country to which the respective gridcell belongs. Temporal factors for seasonal, weekly and daily cycles for the different categories were applied to the resulting annual values of  $CO_2$  emission and  $O_2$  uptake. These temporal factors are based on a set of factors provided in the EDGAR database, but were slightly modified to provide a better global representation: Seasonal cycles in fuel use were reversed for Northern and Southern Hemisphere and suppressed in the lower latitudes for those categories where it seemed reasonable. In addition, the original step functions for monthly cycles were smoothed to avoid discontinuities in the final timeseries. Finally, the sum of emissions and uptake over all categories was taken for each gridcell. The resulting dataset consists of hourly fluxes of  $CO_2$  emissions and  $O_2$  uptake for the years 1995 to 2008. In the following, it will be referred to as the COFFEE dataset, with COFFEE standing for ‘ $CO_2$  release and  $O_2$  uptake from Fossil Fuel Emissions Estimate’.

### 2.2.2 Spatial distribution of fossil fuel related oxidative ratios

Figure 2.1 shows global maps of the annual fossil fuel related  $CO_2$  emissions and the corresponding oxygen uptake for the year 2006. It can be seen that the patterns in oxygen uptake mostly follow the patterns of the  $CO_2$  emissions. As expected, high  $CO_2$  emissions occur mainly in the US, Europe and some parts of Asia while they are rather low in South America and Africa. The lines in between the continents represent ship tracks. Figure 2.2 shows the oxidative ratios, i.e. the  $O_2$  uptake divided by  $CO_2$  emissions, determined from the COFFEE dataset, also annual averages for the year 2006. The ratios cover the whole range from  $\sim 1$  to 1.95 (a few gridcells with  $OR_{ff} < 1$  from significant cement production have been omitted from the plot for better visibility), with the colors being representative for the different fuel types: green for biofuels, black for coal, brown for oil and blue for gas.

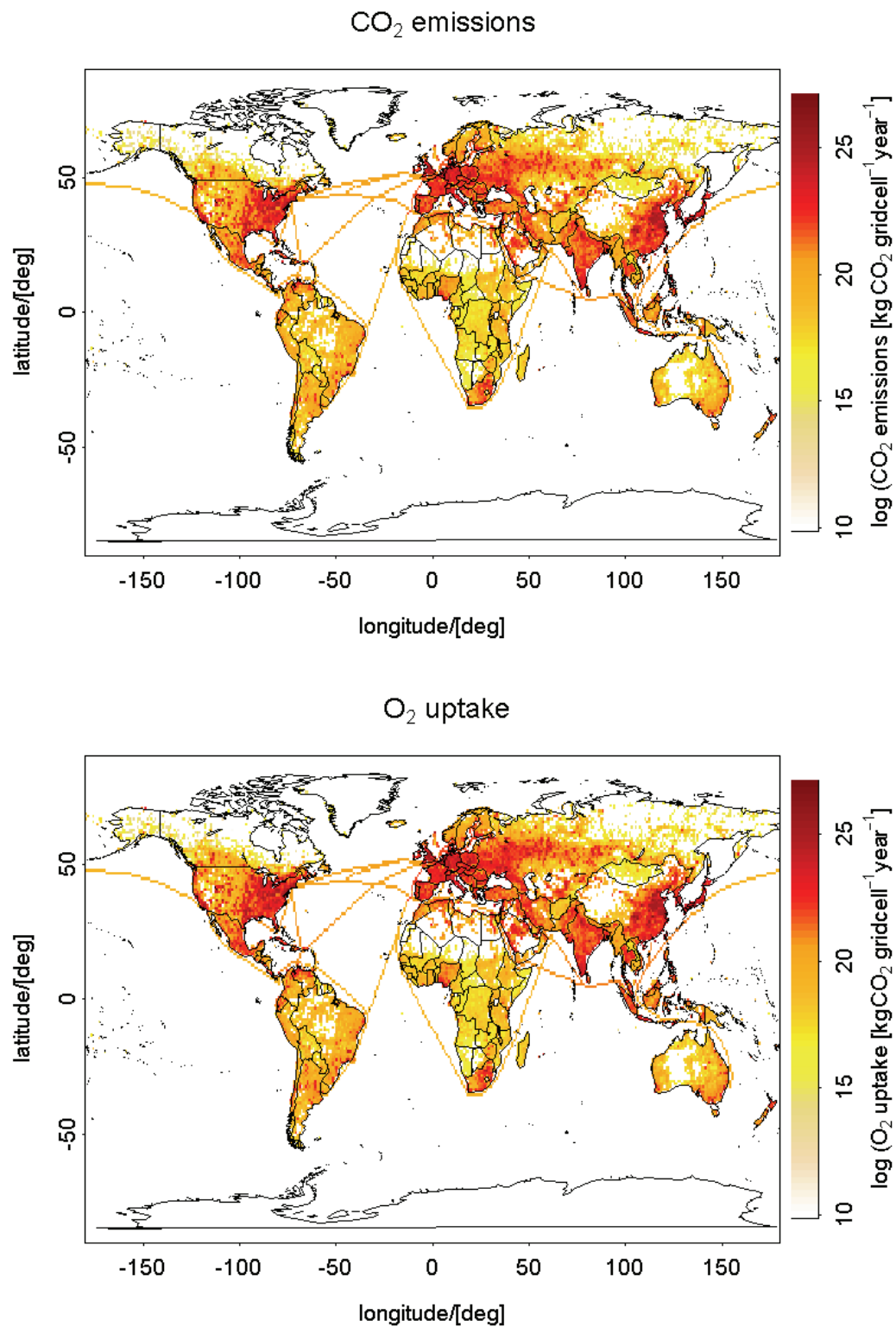


Figure 2.1 Global maps of fossil fuel related CO<sub>2</sub> emissions and oxygen uptake for the year 2006 as calculated from the COFFEE dataset.

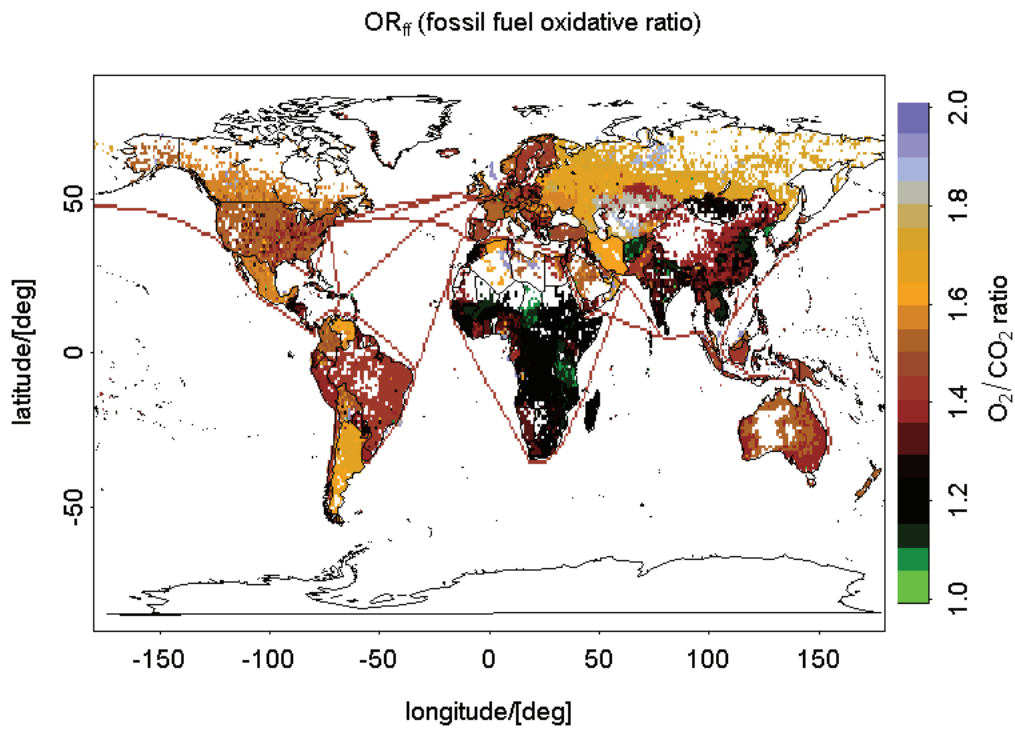


Figure 2.2: Global map of fuel related oxidative ratio for the year 2006, calculated from the COFFEE dataset. See text in Section 2.2.2 for explanation of the color scheme.

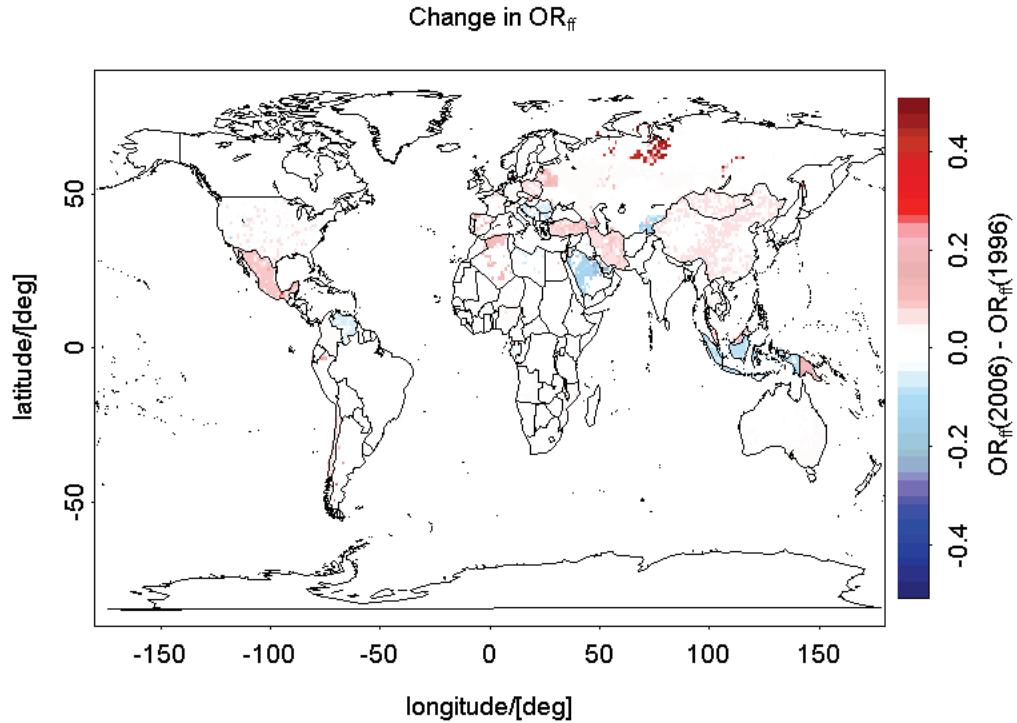


Figure 2.3: Change in the fossil fuel related oxidative ratio over the decade 1996 to 2006. The map shows  $OR_{ff}(2006) - OR_{ff}(1996)$ , therefore red colors indicate an increase and blue colors a decrease in  $OR_{ff}$ .

In the US and most of Europe, the OR is close to the global average, representing an oil-coal mix. Emissions caused by international shipping are expectedly dominated by oil. On the other hand, fossil fuel combustion in Africa, China and India are dominated by coal and biofuels (e.g. fuelwood and animal manure), leading to a low oxidative ratio in these countries. Cement production also plays an important role in China and contributes to a further decrease in the ratio. A high contribution of gas can be seen in the oxidative ratios from e.g. Russia, Argentina and Canada. The blue and grey colors show oxidative ratios above 1.8, where gas is the main source of fossil fuel burning, while the orange colors (representing ratios higher than 1.6) are a sign of significant contribution of gas to the fuel mix.

### 2.2.3 Temporal variations in fossil fuel related oxidative ratios

Apart from spatial variations, it is also interesting to check whether and where temporal changes in the O<sub>2</sub>/CO<sub>2</sub> emission ratios have occurred. Figure 2.3 shows changes during the decade from 1996 to 2006, with red colors indicating an increase and blue colors a decrease. It can be seen that there seems to be no general positive or negative trend, but rather tendencies occurring in both directions for different regions.

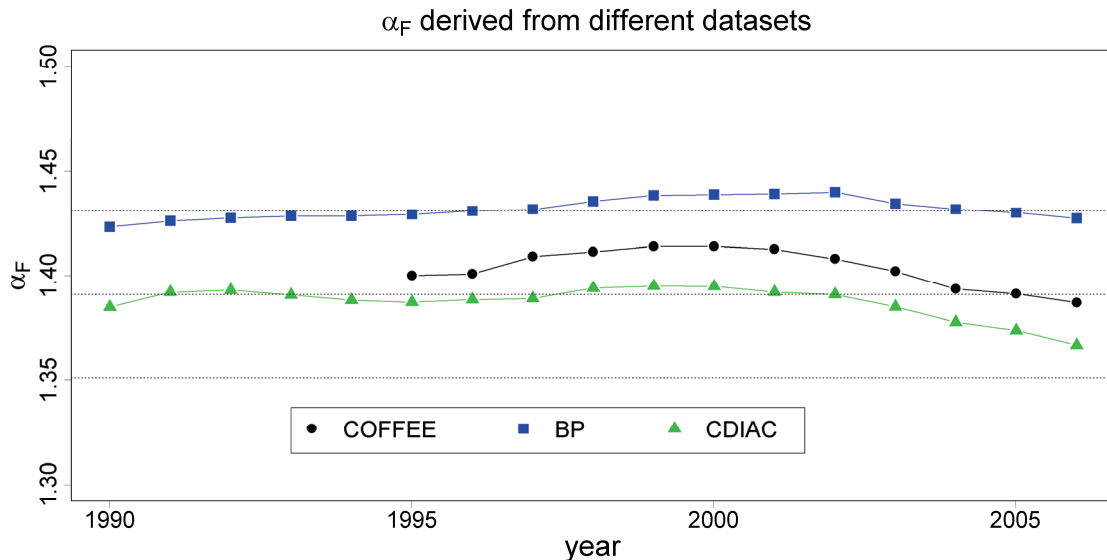


Figure 2.4: Global average oxidative ratio from fossil fuel burning, derived from different fossil fuel inventories. The grey lines show the mean value and uncertainty for  $\alpha_F$  used by Manning and Keeling for the most recent calculation of global carbon sinks (see text for details).

This is confirmed in the timeseries of the global average  $OR_{ff}$  (in the following referred to as  $\alpha_F$  for consistency with the terminology in Chapter 1), shown in Figure 2.4 above. The global average obtained from the COFFEE dataset, represented by the black line, is close to the value of 1.4 that is normally used for  $\alpha_F$ . The mean  $\alpha_F$  over the whole timeseries shown here is  $1.402 \pm 0.003$  with maximal deviations of  $\pm 1\%$  from 1.4. Again, no general trend in one direction is visible.

In this diagram, the results from COFFEE are also compared with the results derived from two other datasets. The blue line shows  $\alpha_F$  obtained from fuel consumption data from BP (that was also used for deriving  $CO_2$  emission trends in COFFEE after 2001). The BP dataset contains continental and national level consumption data of coal, oil and natural gas, but no information on biofuels and cement production. The third dataset (represented by the green line) is the CDIAC dataset (Boden et al. 2009) that – like the oxidative ratios in COFFEE – is primarily based on the UN energy statistics, but also uses additional sources to complete the information. This inventory provides country level  $CO_2$  emissions from the consumption of coal, oil and gas as well from gas flaring and production of cement. The global oxidative ratios from those two datasets are calculated by dividing the total oxygen uptake by the total  $CO_2$  emissions. The oxygen uptake  $O_{2\ total}$  was determined by  $O_{2\ total} = \Sigma (1.17 \cdot CO_2(\text{coal}) + 1.44 \cdot CO_2(\text{oil}) + 1.95 \cdot CO_2(\text{gas}) + 1.98 \cdot CO_2(\text{gas flaring}))$ , with  $CO_2(\text{fuel})$  being the  $CO_2$  emissions of that fuel type.

It can be seen in Figure 2.4 that  $\alpha_F$  shows similar patterns in all three datasets; however the temporal variations are small against the offset between the different inventories (up to 4%). This is mainly due to the fact that the different datasets include different fuel types: CDIAC does not have any biofuels, BP only has biodiesel and fuel ethanol (there being counted as oil), no cement production and gas flaring, and gas consumption is limited to natural gas. When calculating  $\alpha_F$  from the common part of all dataset (coal, oil and natural gas), the maximal offset in the results decreases below 1%.

The question now arises whether these variations in the global average are significant for the partitioning of global carbon sinks. The most recent sink estimate for the period 1990 to 2006 has given a result of  $1.9 \pm 0.6$  and  $1.2 \pm 0.8$  Pg C/year (uncertainties given here as  $1\sigma$  standard deviations) for the total oceanic and land biotic sink, respectively (Manning and Keeling 2006). The uncertainty in  $\alpha_F$ , assumed by Manning and Keeling as  $\pm 0.04$ , results in a significant contribution of  $\pm 0.2$  PgC/year to the uncertainty of both sinks. However, Figure 2.4 shows that the temporal variations of  $\alpha_F$  in any of the datasets are about a factor 6 smaller the uncertainty value of  $\pm 0.04$ , thus resulting in maximum uncertainties of  $\pm 0.035$  PgC/yr. Nevertheless, Manning and Keeling (2006) already stated that temporal variations, in their case derived from CDIAC data for the 1990s, are not the major source of uncertainty in  $\alpha_F$ . Their uncertainty is rather determined by the uncertainty in the absolute value, since interannual changes in fuel production or consumption are resolvable to a finer degree than the total production in any given year. This uncertainty can not be quantified in the COFFEE dataset; only the offset between the different inventories could be used as an estimate for this uncertainty. However, this only works if they are based on independent sources. This is unfortunately not the case, since both the COFFEE and the CDIAC dataset are based on the UN statistics, and BP uses ‘governmental sources’ for its inventory that might also overlap with the UN statistics.

## 2.3 Influence of fuel mix on atmospheric O<sub>2</sub> concentration

The spatial and temporal variations in  $OR_{ff}$  shown above leave a signature in atmospheric oxygen that can potentially be seen in the network of oxygen measurements. For investigating this influence, CO<sub>2</sub> and O<sub>2</sub> signals from the COFFEE dataset were used as input for atmospheric transport models to simulate the fossil-fuel related changes in the atmospheric CO<sub>2</sub> and O<sub>2</sub> mixing ratios (hereinafter called CO<sub>2ff</sub> and O<sub>2ff</sub>) for a number of monitoring stations. Two different transport models were used: the global model TM3 (Heimann and Körner 2003) and the regional model REMO (Langmann 2000; Chevillard et al. 2002). The regional model has the advantage of a higher temporal and spatial resolution: It gives hourly output compared

to 6-hourly output in the global model; the resolution is  $0.5^\circ \times 0.5^\circ$  (approximately  $55 \times 55$  km), whereas the highest resolution in the global model is  $1.8^\circ \times 1.8^\circ$ . Thus synoptic variations in fossil fuel use are better captured in the regional model. The global model, on the other hand, provides worldwide coverage and therefore can give a global overview of fossil fuel related effects. Figure 2.5 shows the locations of the stations for which the atmospheric signals were calculated, with red circles indicating the stations with output from the global model, and blue diamonds those where regional model output was available.

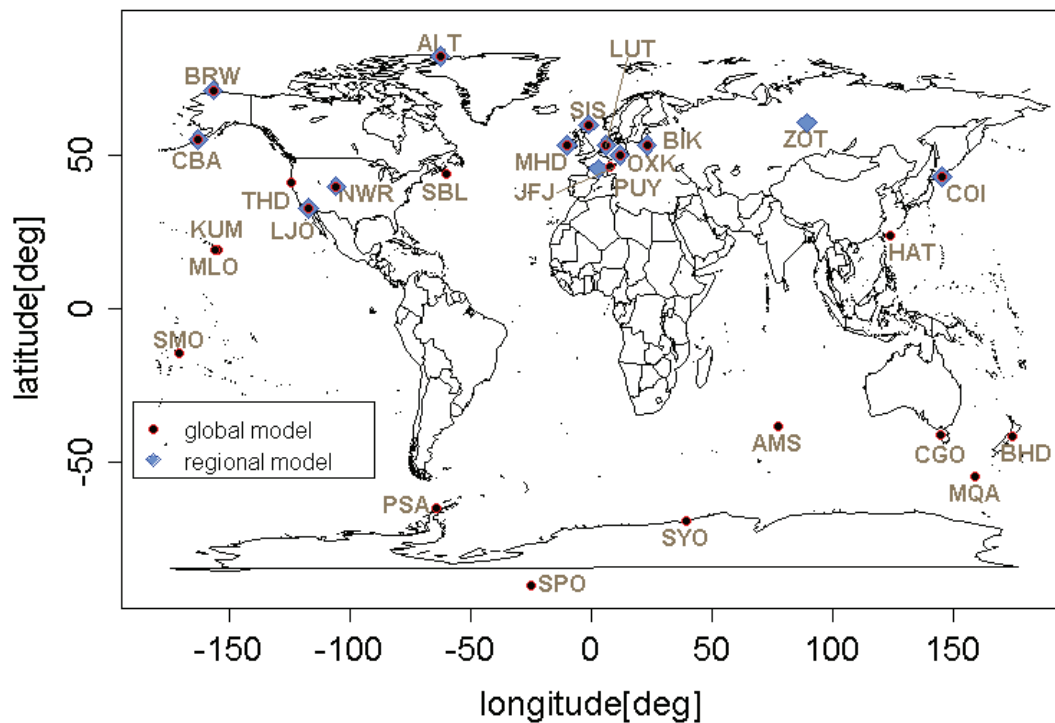


Figure 2.5: Location of oxygen monitoring stations for which fossil fuel related signals were simulated. Red circles show stations for which atmospheric mixing ratios were simulated using the global transport model TM3, blue diamonds show output locations of the regional model.

Comparison of the results for CO<sub>2ff</sub> and O<sub>2ff</sub> from the global and the regional model for stations that are within both domains shows similar patterns in both models. An example is given in Figure 2.6 which contains simulations of the station Ochsenkopf in Germany for the year 2006, showing in black the results from the global model and in blue those from the regional model. Simulated CO<sub>2ff</sub> and O<sub>2ff</sub> signals are shown in

the plot on the left side, given in ppm and expressed as deviations from the value of January 1, 2006, 0h.

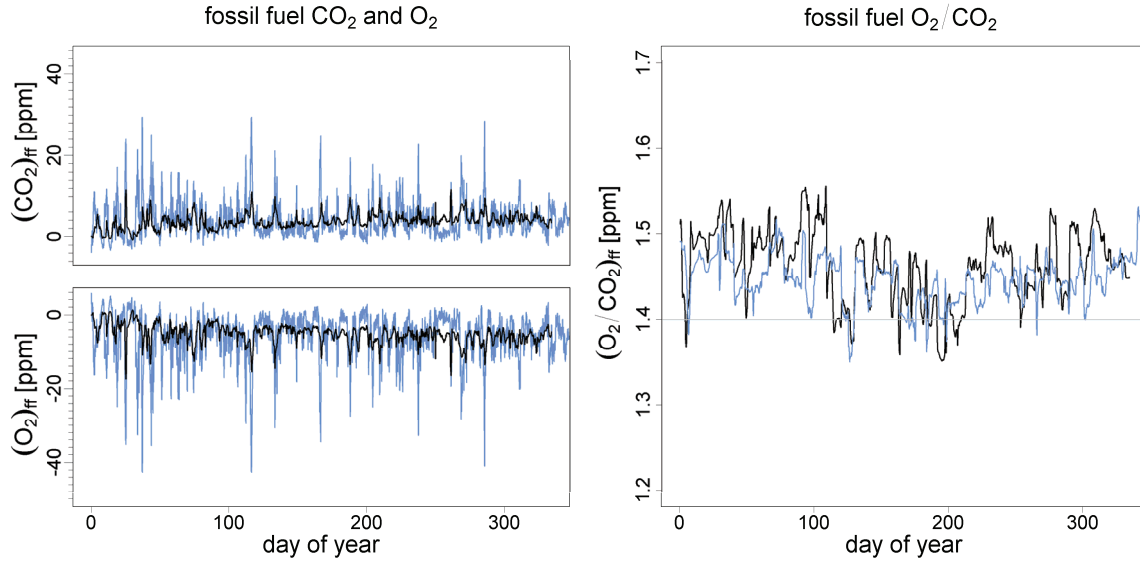


Figure 2.6: Comparison of results from the global model TM3 (black) and the regional model REMO (blue) for the station Ochsenkopf (Germany). Left: fossil fuel related changes in the atmospheric mixing ratios of CO<sub>2</sub> (upper plot) and O<sub>2</sub> (lower plot). Right: fossil fuel related oxidative ratio  $OR_{ff}$ , determined from a running regression of  $O_{2ff}$  vs  $CO_{2ff}$ .

As expected, the signals from the regional model show higher variability, resulting in sharper peaks with higher increases in CO<sub>2</sub> and higher decrease in O<sub>2</sub>. Although the input from the COFFEE dataset has a seasonal cycle (for example, more fuel is used for heating in the winter), seasonal and other periodic variations appear negligible in the model result that is rather dominated by synoptic scale pollution events. The plot on the right presents the effective oxidative ratio  $OR_{ff} = -\Delta O_{2ff}/\Delta CO_{2ff}$  at the station location. The ratio shown here was derived from a running regression of  $O_{2ff}$  versus  $CO_{2ff}$ . A timeframe of 5 days was used for the regression, to get a signal representative of synoptic scale variations, while suppressing seasonal variations. The resulting values for  $OR_{ff}$  from the two models do not show significant systematic differences. Since the results for the other stations look similar, the results from the regional model are used where available, since they presumably capture the fossil fuel related variations better. Since both models show similar results for oxidative ratios on the synoptic timescale, both models can be used for the respective set of stations, depending on their availability.



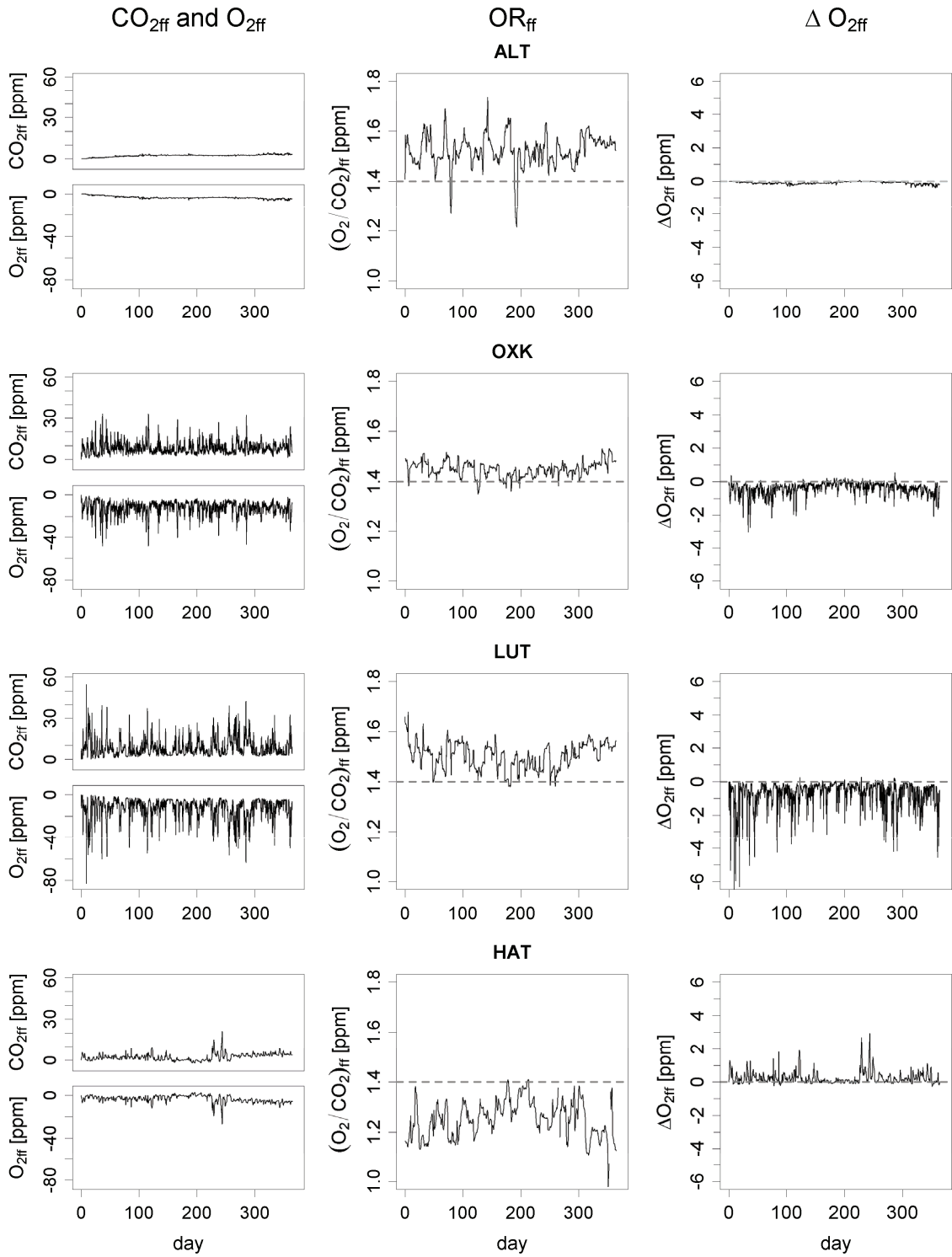


Figure 2.7: Model output for selected stations. Stations from top to bottom are Alert (Canada), Ochsenkopf (Germany), Lutjewad (Netherlands) and Hateruma Island (Japan). The three columns show results for fossil fuel related  $\text{CO}_2$  and  $\text{O}_2$  mixing ratios ( $\text{CO}_2$  and  $\text{O}_{2\text{ff}}$ ), oxidative ratios ( $\text{OR}_{\text{ff}}$ ) and the effect of the variable OR on the atmospheric oxygen concentration ( $\Delta \text{O}_{2\text{ff}}$ ).

Figure 2.7 shows the model output for four selected stations: Alert (ALT) in Greenland, Ochsenkopf (OXK) in Germany, Lutjewad (LUT) in the Netherlands and Hateruma Island (HAT) close to Japan. The exact locations of the stations can be seen in Figure 2.5. Only Hateruma is outside the domain of the regional model. Thus results for this station are from TM3 simulations, while the results for the other three stations are from REMO. The three plots for each station show the following: The left and middle column show the CO<sub>2ff</sub> and O<sub>2ff</sub> signals and the synoptic-scale oxidative ratio OR<sub>ff</sub> as in Figure 2.6. In the right column, the difference  $\Delta O_{2ff} = O_{2ff}(OR_{COFFEE}) - O_{2ff}(OR=const)$  is shown, i.e. the difference in the fossil fuel related O<sub>2</sub> signal caused by the use of the variable oxidative ratios from COFFEE in comparison to the use of a constant ratio of 1.4. As expected,  $\Delta O_{2ff}$  increases with both higher fossil fuel signals and higher deviations of the local fuel mix from the global average. Compared to the measurement precision of ~1ppm for measurements of atmospheric oxygen, these deviations are, however, rather small.

Comparison of the results for the different stations shows that the influence of fuel mix depends to a large degree on their location:

- For Alert, a remote coastal station, fossil fuel contributions to the atmospheric signals are small in general. No significant  $\Delta O_{2ff}$  signal is caused although OR<sub>ff</sub> has a mean of about 1.5 (thus somewhat higher than the global average) and exhibits variations up to  $\pm 0.2$
- The Ochsenkopf tower, a continental station located in the middle of Europe (see also Chapter 2.4.1), experiences more fossil fuel events, causing increases in CO<sub>2</sub> and decreases in O<sub>2</sub> up to 40 ppm. With OR<sub>ff</sub> being slightly higher than 1.4, differences up to -3 ppm in the fossil fuel related O<sub>2</sub> signal can be observed.
- At Lutjewad, located on the Northern Coast of the Netherlands, the pollution events are larger (up to 60 ppm) and more frequent; combined with an oxidative ratio up to 1.65, they cause  $\Delta O_{2ff}$  to be as big as -7 ppm.

- Hateruma Island (see also Chapter 2.4.2) is a small island next to Japan, and is exposed to airmass influence from the adjacent Asian countries. As it can be seen from Figure 2.2, OR<sub>ff</sub> in these countries is in general lower than the global average, leading to a mean OR<sub>ff</sub> of 1.3 for the station. ΔO<sub>2ff</sub> peaks at + 4 ppm. In comparison to the results from the other stations, it needs to be taken into account that the results for Hateruma are calculated using the global model, thus the peaks in ΔO<sub>2ff</sub> are significantly underestimated compared to simulations from a regional model (see also Figure 2.6).

Following the detailed results of these representative stations, Figure 2.8 gives an overview of the fossil fuel related oxidative ratios for all monitoring stations. Again, only data from the year 2006 is used and OR<sub>ff</sub> is determined in the same way as for figures 2.6 and 2.7 (i.e. using a 5-day running regression of O<sub>2ff</sub> versus CO<sub>2ff</sub>). In Figure 2.8, blue lines showing results from REMO and black lines results from TM3. Represented in this diagram are minimum, maximum, and quartile scores of OR<sub>ff</sub> for the different stations in the form of a box-and-whisker plot. Here the box covers the 50% of the data values between the 25<sup>th</sup> (bottom line of the box) and the 75<sup>th</sup> percentile (top line of the box). The bold line close to the middle of the box represents the median (i.e. the 50th percentile), while the ‘whiskers’ (dashed lines) extend to the minimum and maximum of the distribution.

Figure 2.8 shows that the median of OR<sub>ff</sub> for most of the classical remote stations (marked by green labels) is close to the global average and the range of the distribution is rather small, whereas the OR<sub>ff</sub> of continental stations or stations with dominant continental influence (marked with black labels), show large variations and a median significantly different from 1.4. Nevertheless this is not always the case, for example the OR<sub>ff</sub> of the remote station Alert exhibit large variations. However, the results from Figure 2.7 have shown that large variations in the oxidative ratios do not necessarily lead to detectable changes in the atmospheric signal at the station. This can also be seen from the example of Alert: despite the variable OR<sub>ff</sub>, no significant difference in O<sub>2ff</sub> is caused by using these variable oxidative ratios compared to the use of a constant OR<sub>ff</sub>, since the fossil fuel related CO<sub>2</sub> and O<sub>2</sub> fluxes are very small.

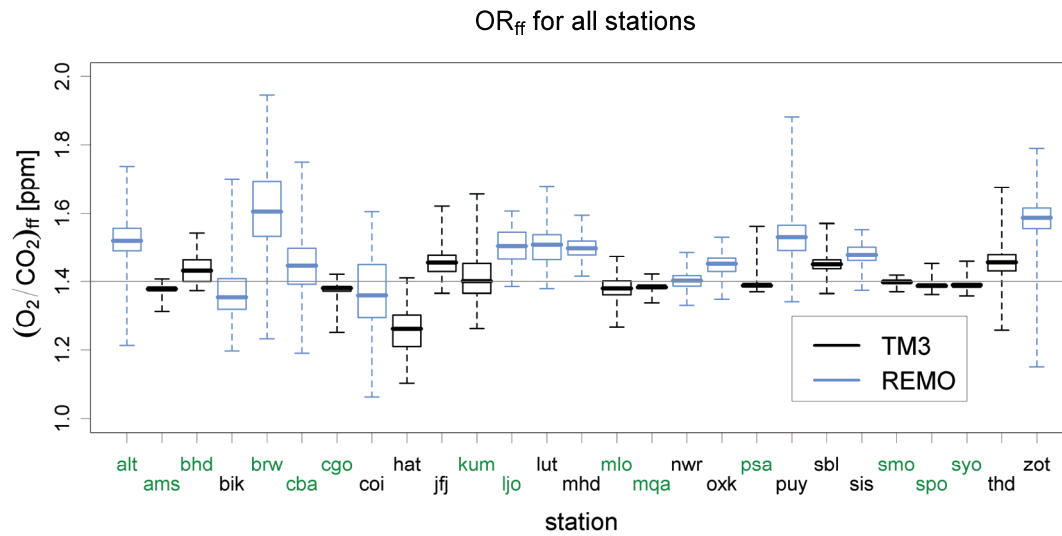


Figure 2.8: Fossil fuel related oxidative ratios from TM3 and REMO model simulations for all available monitoring stations. Labels denote the official station code, as given in Figure 2.5 where the station locations are shown. To facilitate the recognition of continental and remote stations in this plot, labels of remote stations are green, whereas labels of stations on the continent or on islands mainly influenced by continental air masses are black

## 2.4 Comparison with observations

When interpreting fossil fuel related oxidative ratios, as shown in Figure 2.8, one needs to keep in mind that the total oxidative ratio observable at a monitoring station is not only determined by fossil fuel related signals, but also contributions from biospheric and oceanic processes. Whether a specific fuel signature can be seen in measured oxidative ratios at a given station depends on the size of fossil fuel related signals compared to the atmospheric signals caused by other processes. This section examines oxidative ratios derived from CO<sub>2</sub> and O<sub>2</sub> observations at the two stations Ochsenkopf and Hateruma and investigates whether it is possible to detect specific fuel signatures in these observations.

### 2.4.1 Ochsenkopf

The Ochsenkopf monitoring station is a tall tower (163m height), located on the summit of the Ochsenkopf mountain (1020m above sea level) in the Fichtelgebirge in Northern Bavaria, Germany. The area around the tower is mainly covered with

conifer forest and has a relatively low population density. Air measured at this station originates primarily from Western and Central Europe. The synoptic scale variability of atmospheric CO<sub>2</sub> and O<sub>2</sub> signals experiences contributions from both biospheric and anthropogenic fluxes. Due to the elevation of station, signals from the well-mixed planetary boundary layer (PBL) can be captured. Air is sampled alternately at three heights on the tower (163, 90 and 23m above ground level) and is analyzed in-situ in a temperature-controlled container laboratory at the foot of the tower. A detailed description of the tower site and the instrumentation can be found in Thompson et al (2009).

Figure 2.9a shows hourly averages of O<sub>2</sub> and CO<sub>2</sub> measurements for the year 2006 with the different colors representing data from the three different measurement levels as explained in the legend. Gaps in the data are due to instrumental problems. In Figure 2.9b the simulated CO<sub>2ff</sub> and O<sub>2ff</sub> values for the 163m level from the REMO model are presented for the same time frame. For better comparison, the y-scales have been adjusted to have the same range for model and observations. Figure 2.9c comprises oxidative ratios derived from both observations and model, with the colors corresponding to those in Figure 2.9a and 2.9b. Oxidative ratios have been derived from running regression as described before. Shaded areas indicate the error of the calculated slopes (only the error of the linear fit itself, not taking into account additional errors due to measurement uncertainty for the observations). Poorly defined slopes, classified as those with an error > 0.05, have been omitted from the plot. To simplify the comparison between model and observations, model results are not shown for times in which no oxidative ratios derived from the observations exist (either due to missing observational data or bad fit results).

For better interpretation of the resulting oxidative ratios, the dashed horizontal lines in Figure 2.9c show the values of the global average oxidative ratios for fossil fuel combustion ( $\alpha_F$ , grey line) and biospheric exchange ( $\alpha_B$ , green line). The (purely fossil fuel related) oxidative ratio from the REMO model, as already shown in Figure 2.6 and 2.7, does not show any seasonal variations and is on average slightly higher than  $\alpha_F$ .

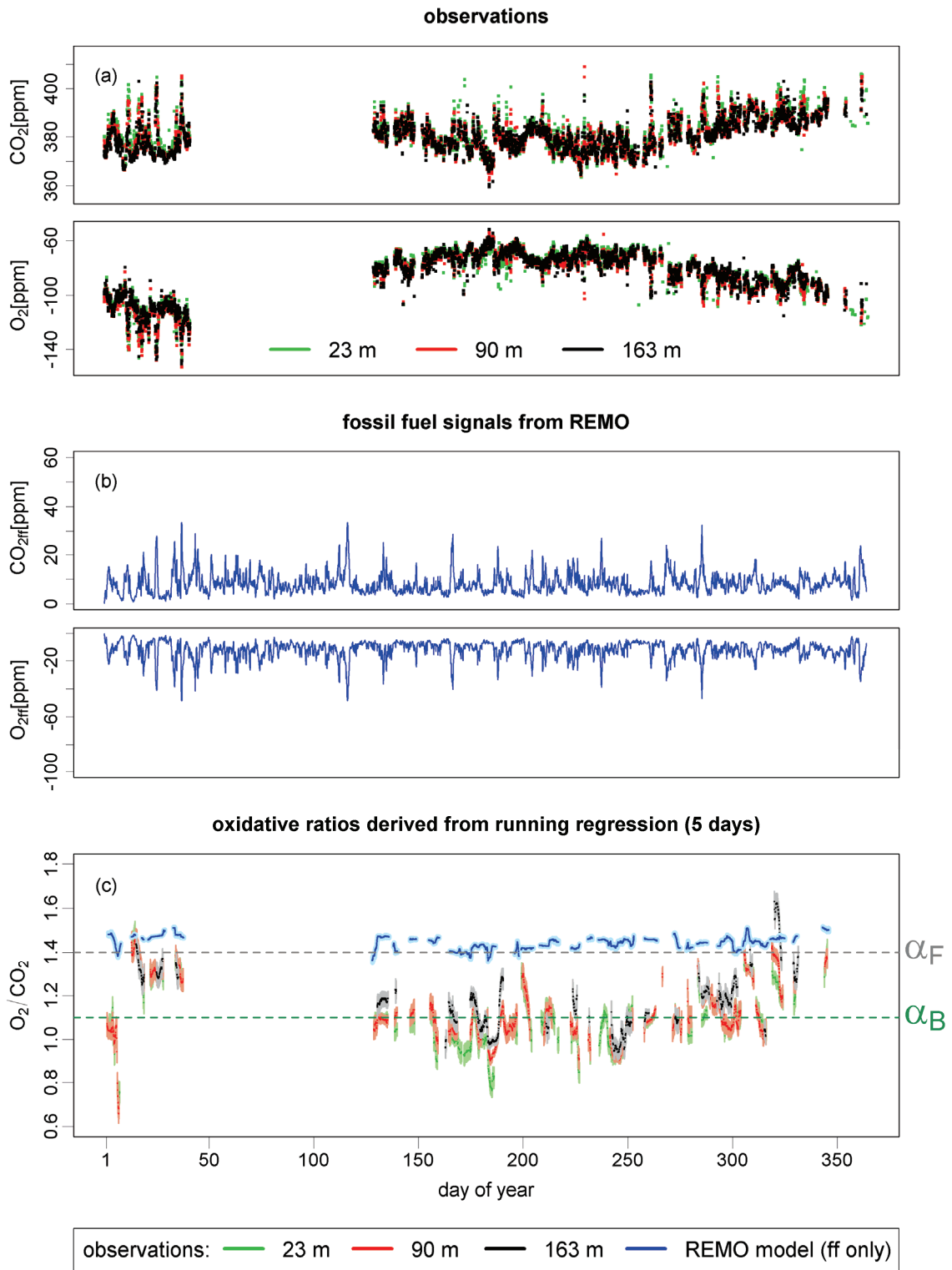


Figure 2.9: CO<sub>2</sub> and O<sub>2</sub> observations from the Ochsenkopf station (a), compared to CO<sub>2ff</sub> and O<sub>2ff</sub> simulations from the REMO model (b) and oxidative ratios derived from observation and model results (c). For comparison, the dashed grey and green lines indicate values of  $\alpha_F$  and  $\alpha_B$ , the global average oxidative ratios for fossil fuel combustion and biospheric exchange, respectively.

Oxidative ratios derived from the observations are expected to vary between 1.1 and 1.4 depending on the relative contributions of biospheric and anthropogenic sources and sinks. The influence of ocean processes can be neglected at this location and the timescales regarded here. Biospheric contributions are expected to be strongest in summer and rather negligible in winter, therefore the influence of the non-constant  $OR_{ff}$  is most likely to be seen in winter. The data show indeed a clear seasonal cycle with higher OR values in winter and lower values in summer. The reason for some OR values being even lower than 1.1, is due to the fact that  $\alpha_B$  is not a fixed value as well, but also depends on the local plant types and different processes. For a thorough discussion of this issue, see (Popa 2008). However, even in the winter months the observed OR are smaller than 1.4, suggesting that there is still some non-negligible contribution of the biosphere.

To get an estimate of the biospheric influence, simulations of atmospheric  $CO_2$  variations caused by interactions with the biosphere were performed with the STILT-VPRM model (Matross et al. 2006). This model combines the particle dispersion model STILT (Gerbig et al. 2003; Lin et al. 2003) with the diagnostic biosphere model VPRM (Mahadevan et al. 2008) as well as a fossil fuel emission inventory at high spatial resolution ( $10 \times 10 \text{ km}^2$ ), provided by IER Stuttgart (<http://www.ier.uni-stuttgart.de/>).

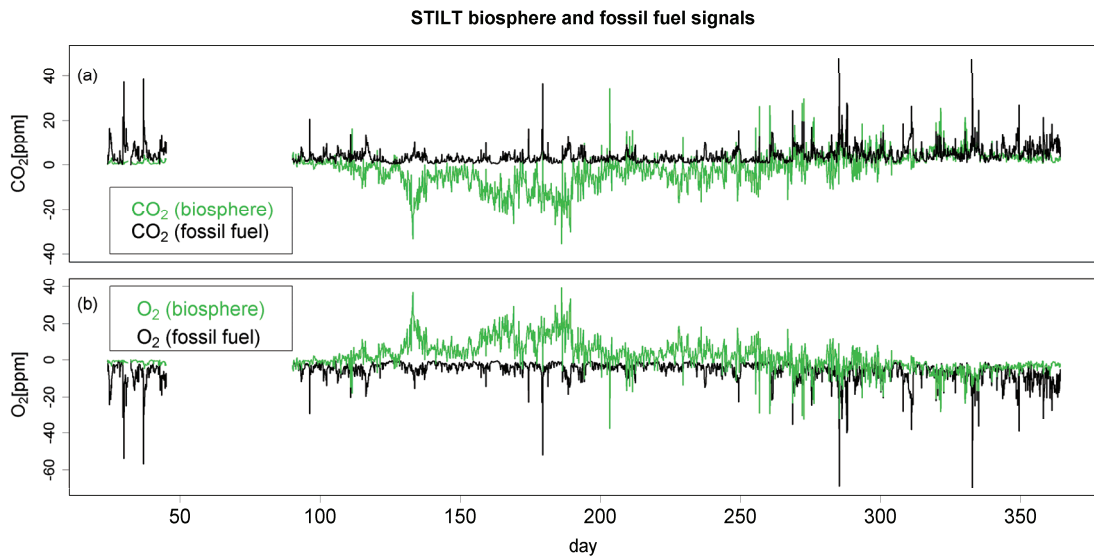


Figure 2.10: Biospheric and fossil fuel related contributions to the atmospheric  $CO_2$  concentration at the Ochsenkopf station (a) and the corresponding  $O_2$  concentrations (b), calculated as  $O_2(bio) = -1.1 \cdot CO_2(bio)$  and  $O_2(ff) = OR_{ff}(REMO) \cdot O_2(ff)$ .

Figure 2.10a above shows the biosphere and fossil fuel related CO<sub>2</sub> signals, demonstrating that the biospheric signal is not completely negligible during winter. In order to interpret this information in terms of oxidative ratios, the corresponding oxygen signals are calculated by multiplying the biospheric CO<sub>2</sub> signals with  $\alpha_B$  and the fossil fuel signals with  $OR_{ff}$  derived from REMO. The resulting O<sub>2</sub> concentrations are shown in Figure 2.10b.

In Figure 2.11, the oxidative ratios calculated from that combined fossil fuel and biosphere signal are compared to the oxidative ratios derived from the observations. It can be seen that the model captures the seasonal patterns in the observations quite well. However, the question remains whether the contribution of variable oxidative ratios from fossil fuel combustion has a significant impact on this agreement.

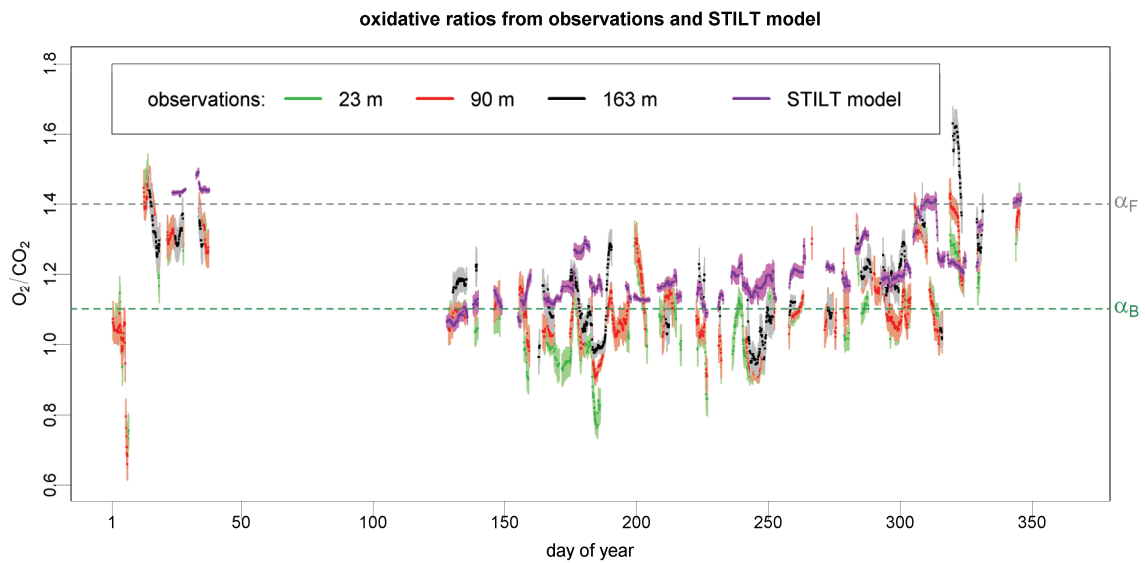


Figure 2.11: Oxidative ratios from observations at different levels of the Ochsenkopf station (equivalent to those in Figure 2.9), compared to oxidative ratios derived from the STILT model results (Figure 2.10). Shaded areas indicate error bars. Calculated oxidative ratios are not shown if the error of the linear fit (either that of the model or of the observations) is higher than 0.05.

This question is answered in Figure 2.12 which depicts two kinds of oxidative ratios of the calculation with the STILT model. The violet line represents the model results with a variable  $OR_{ff}$  as described above whereas the brown line represents the fossil



fuel signal which is calculated using a constant  $OR_{ff}$  of 1.4. For better visibility, results from the observations are kept in grey for all levels in this plot.

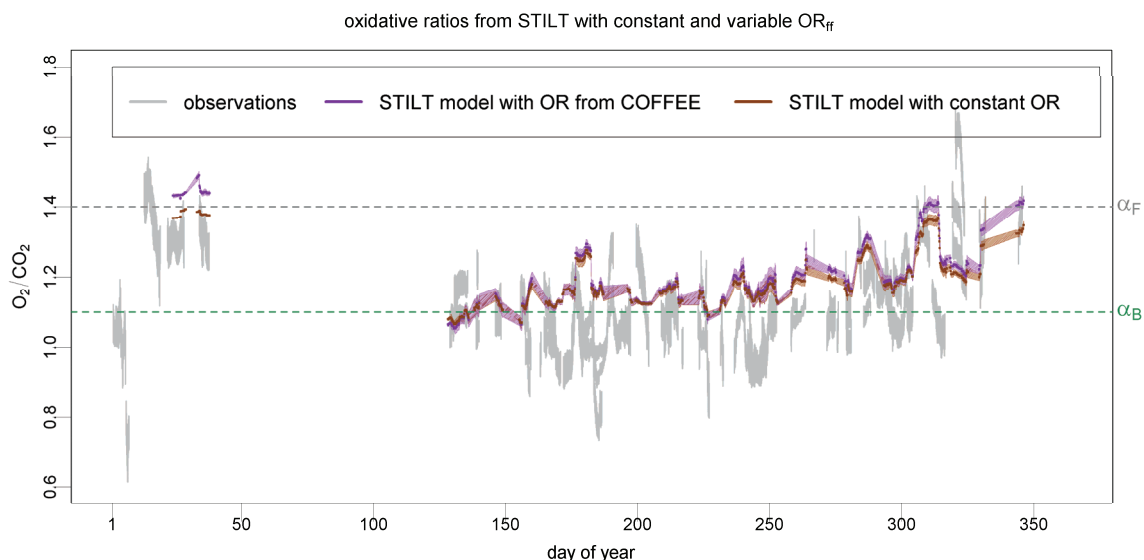


Figure 2.12: Oxidative ratios derived from the STILT model, using constant (brown) and variable (violet)  $OR_{ff}$ . Observational results from all measurement levels are shown in grey in this plot.

Figure 2.12 shows that the influence of variable  $OR_{ff}$  seems not to have a significant effect at this station. The differences compared to the signal calculated using a constant  $OR_{ff}$  are rather small and do not significantly improve the agreement between model and observations. This can be explained by two facts: With a mean value of 1.44,  $OR_{ff}$  for the Ochsenkopf station is not that different from the global average. Besides, the fossil fuel influence is not the predominant contribution to the total  $O_2/CO_2$  ratio seen at this location because of the strong signals caused by biospheric processes.

## 2.4.2 Hateruma Island

The Hateruma monitoring station is situated on the eastern edge of Hateruma Island, the southernmost inhabited island of Japan with an area of 13 km<sup>2</sup>. Air masses arriving at Hateruma are mostly influenced by the Asian continent during winter time and from the Pacific Ocean in summer (Tohjima 2000). The elevation of the station is

only 10m above sea level; the air is sampled from the top of a small observation tower at a height of 36 m above ground and analyzed in a laboratory below. In-situ measurements of O<sub>2</sub>/N<sub>2</sub> have started at Hateruma in October 2006, before only flask data existed. Here observations from the period October to December 2006 are used, provided by the National Institute of Environmental Studies (NIES), Japan. Hateruma is a rather polluted station: Model simulations show that the mean fossil fuel contribution to the atmospheric CO<sub>2</sub> signal on synoptic scales is about 76 % for the period investigated here (C. Minejima, personal communication).

Figure 2.13 is the analogue of Figure 2.9 for the Hateruma station, with the CO<sub>2</sub> and O<sub>2</sub> observations for October to December 2006 in Figure 2.13a, the corresponding fossil fuel signals from TM3 in Figure 2.13b and the oxidative ratios from the observations and the model in Figure 2.13c. Unfortunately, the measurement period here is quite short and several calculated oxidative ratios need to be removed from the plot because of large uncertainties in the slope of the measured O<sub>2</sub> versus CO<sub>2</sub> (the same filter as for the results in Figure 2.9 was used here).

Nevertheless, the results indicate even with only the fossil fuel component of the coarse global model a significant part of the observed variations in the oxidative ratios can be captured. This shows that the influence of variable OR<sub>ff</sub> is definitely not negligible at this station. Regional modeling efforts with high spatial resolution using the STILT and FLEXPART model (Stohl et al. 1998; Stohl et al. 2005) in combination with the COFFEE dataset as input are currently ongoing at NIES and MPI-BGC to see whether it is possible to fully capture the variability in the observations and to investigate the possibility of using variations in the oxidative ratios for detecting the origin of air masses arriving at Hateruma (Minejima et al. in preparation)

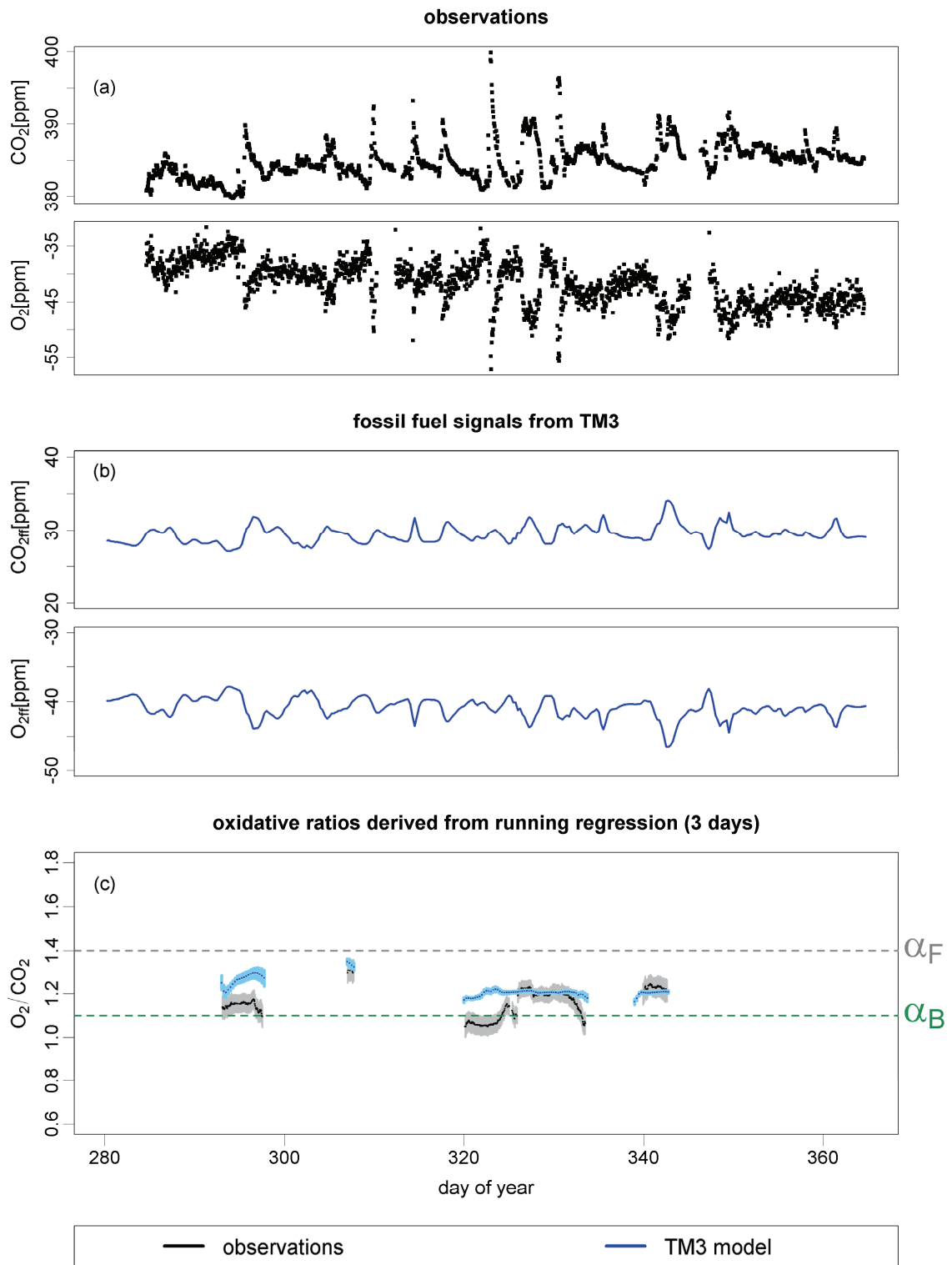


Figure 2.13:  $\text{CO}_2$  and  $\text{O}_2$  observations from Hateruma Island (a), compared to  $\text{CO}_{2\text{ff}}$  and  $\text{O}_{2\text{ff}}$  simulations from the TM3 model (b) and oxidative ratios derived from observation and model results (c). For further explanations see text and caption of Figure 2.9.

## 2.5 Impact on separation of ocean and land carbon sinks

Spatial and temporal variations in  $OR_{ff}$  are likely to influence the partitioning of land and ocean carbon sinks derived from atmospheric measurements. In Section 2.2.3 the effect of variations and uncertainties in the global average  $OR_{ff}$  on long-term global carbon budgets was already discussed. This section takes now a closer look at the spatial distribution of fossil-fuel related fluxes and investigates where the assumption of a constant  $OR_{ff}$  leads to misinterpretations of these fluxes and thus affects the land-ocean-partitioning. As introduced in Chapter 1.3.2, usually the tracer  $APO = O_2 + 1.1 CO_2$  is used to isolate the oceanic component from measured oxygen signals. Whereas APO is by definition not changed by biospheric processes with an  $OR_b$  of 1.1, the influence from fossil fuel burning is reduced, but still present in the signal. This is usually accounted for by using fossil fuel statistics to calculate a fuel-corrected APO signal (assuming a constant value for  $OR_{ff}$ ). One method to interpret measured APO signals in terms of surface fluxes is the atmospheric transport inversion. As described in Chapter 1.3, this method uses inverse techniques to derive surface fluxes that minimize the mismatch between measured and model-derived atmospheric concentrations.

In the following it is investigated whether it is necessary to include variable  $OR_{ff}$  in these APO inversions to avoid mistaking fossil fuel related variations for signals caused by ocean processes. As a setup for the APO inversion, the standard configuration from (Rödenbeck et al. 2008) was used with the TM3 transport model. Atmospheric CO<sub>2</sub> and O<sub>2</sub> data from 16 monitoring stations (in the following referred to as ‘inversion stations’, for their locations see Figure 2.15b) are used as observational input. APO fluxes are calculated for the period 1995 to 2006, with the first year considered as spin-up time of the model and hence removed from the results. For testing the effects of variable oxidative ratios, a synthetic dataset was created, containing the simulated difference  $\Delta APO_{ff} = APO_{ff}(OR_{COFFEE}) - APO_{ff}(OR=const)$  at the monitoring stations level. These differences were inverted, resulting in a set of fluxes  $\Delta F_{APOff}$ . Since the inversion can only adjust the ocean fluxes, the differences caused by non-constant oxidative ratios are interpreted as oceanic signals.

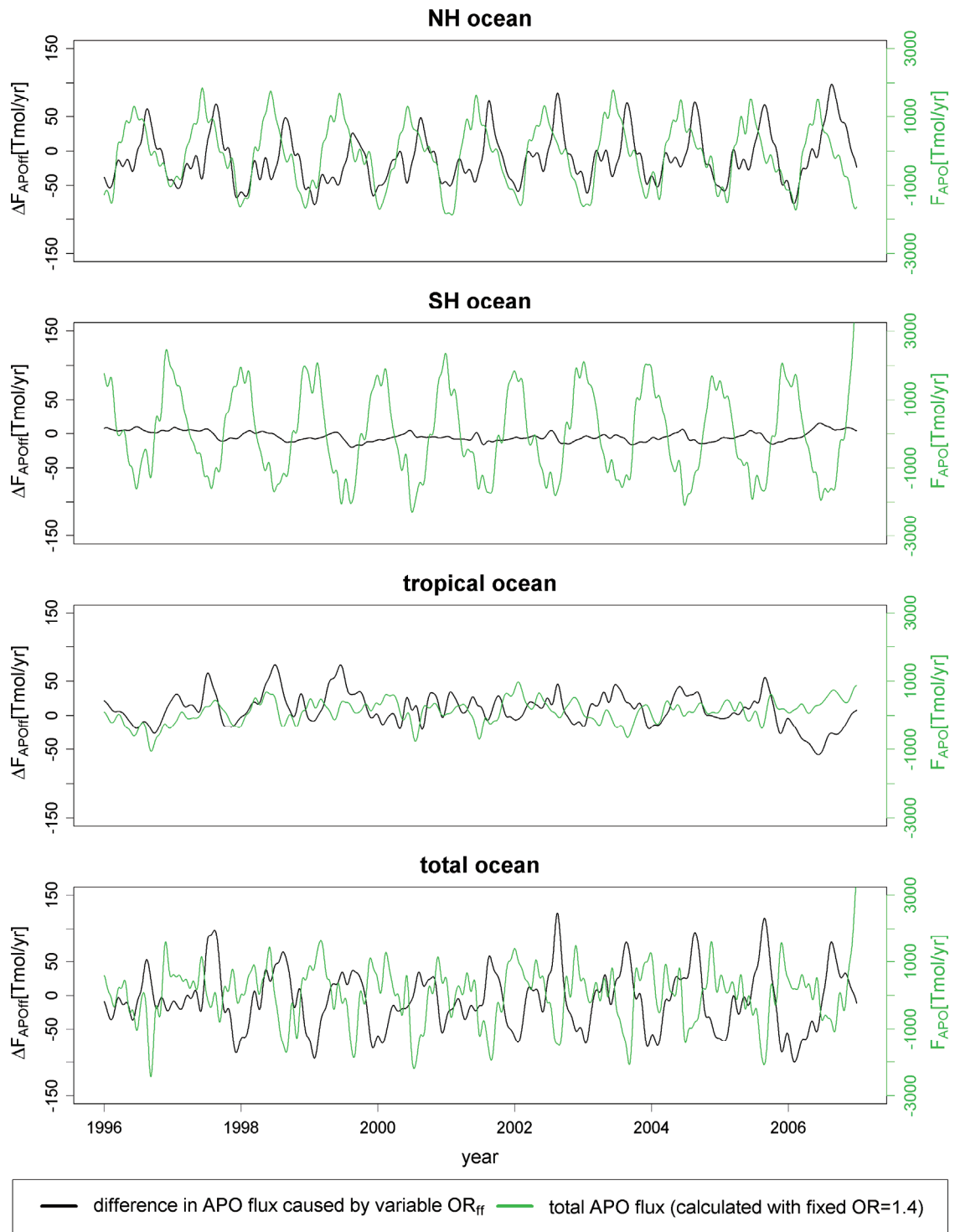


Figure 2.14 Timeseries of APO fluxes for different latitudinal bands (NH - Northern Hemisphere, ranging from  $+20^\circ$  to  $+90^\circ$ , SH - Southern Hemisphere, ranging from  $-20^\circ$  to  $-90^\circ$ , and Tropical Ocean, ranging from  $-20^\circ$  to  $+20^\circ$ ). Green fluxes (right y-axis) show the total APO fluxes, as derived from the normal atmospheric inversion with real observational input, black fluxes (left y-axis with smaller range) show the part of fossil fuel related fluxes that is misinterpreted as ocean fluxes.

Figure 2.14 shows timeseries of the resulting  $\Delta F_{\text{APOff}}$ , integrated over three latitudinal bands and over the total ocean. Together with these fluxes, represented by black lines with the scale on the left y-axis, the APO ocean fluxes  $F_{\text{APO}}$  – as derived from actual observations – are shown in green and refer to the right y-axis.

In terms of the seasonal amplitudes, the fossil fuel fluxes misinterpreted as ocean fluxes account for about 4% of the total fluxes, with slightly a higher contribution in the tropical ocean (6.5%) and the Northern Hemisphere Ocean (4.7%) and a low contribution in the Southern Hemisphere Ocean (0.5%). The low  $\Delta F_{\text{APOff}}$  in the Southern Hemisphere is most likely due to the lower fossil fuel emissions in the SH and the oxidative ratios of the remote stations that do not differ much from the global average (see Figure 2.8). Significant contribution to the variations in the Northern Hemispheric and Tropical Ocean might come from the Hateruma station that has been shown to be a rather polluted station with a lower  $\text{OR}_{\text{ff}}$  (see Chapter 2.3 and 2.4.2). However, these differences are small against the uncertainties in the seasonal cycles of the inversion that are in the range of 25 – 35 % for the different regions (uncertainties determined by the range of the plausible inversion parameters in (Rödenbeck et al. 2008)).

Apart from the seasonal variations, a small systematic offset in the long-term mean of the ocean fluxes is caused, amounting to values of –10.8, – 4.1 and +9 Tmoles for Northern Hemisphere, Southern Hemisphere and Tropical Oceans and – 5.6 Tmoles for the total ocean. However, with the respective uncertainty ranges for the long-term mean ranging from 18 – 27 Tmoles, this small shift is not significant.

Nevertheless, possible significant effects on local or regional levels might be hidden in these hemispherically integrated results. To check whether such effects exist, to identify critical regions and to resolve the influence of different stations, gridded output of  $\Delta F_{\text{APOff}}$  is shown in the following figures.

To first get an idea about the temporal variability on the gridcell level, Figure 2.15a shows the standard deviation of for  $\Delta F_{\text{APOff}}$  over the time period 1996-2006. As

already seen in the regional results in Figure 2.14, effects of variable oxidative ratios occur mainly in the Northern Hemisphere and the tropics. Highest variations occur in the Pacific area close to the Asian Coast (and close to the Hateruma Island station) and in the Northern Atlantic. However, in general these variations are rather small compared to the temporal variations in  $F_{\text{APO}}$ , shown in Figure 2.15b. With a factor of 14 difference in the maximum standard deviation of  $\Delta F_{\text{APOff}}$  and  $F_{\text{APO}}$ , the influence of temporal variations in  $\Delta F_{\text{APOff}}$  seems negligible, even on local scales.

This is, however, not the case for the offset caused by neglecting the variable  $\text{OR}_{\text{ff}}$ . Figure 2.16a shows the long-term mean of  $\Delta F_{\text{APOff}}$  over the whole time period. The range of the long-term mean of  $\Delta F_{\text{APOff}}$  due to spatial variability (-0.1 to +0.3 Tmol/yr/gridcell) is only a four times smaller than the corresponding range of the long-term mean fluxes  $F_{\text{APO}}$ , shown in Figure 2.16b. Significant bias occurs mainly in the same regions that already showed higher temporal variations. A dominant feature is the large positive  $\Delta F_{\text{APOff}}$  signal around the Hateruma station, locally causing a bias on the order of 50 -100 % of the  $F_{\text{APO}}$  signal.

To better quantify the effect of the other stations, Hateruma was removed from the inversion setup. The results for the long-term mean and standard deviation of  $\Delta F_{\text{APOff}}$  derived from the inversion without Hateruma are shown in Figure 2.17. It can be seen that the patterns in the long-term mean change significantly and the range decreases by a factor of 6. The patterns in the standard deviation change mainly locally around Hateruma, but the maximum range of temporal variations decreases by a factor of 2. Although it is surprising that the removal of just one station has such a large influence, however, it seems reasonable considering that Hateruma differs significantly from the other inversion stations in terms of its low oxidative ratio and proximity to pollution sources (see results of Chapters 2.3 and 2.4.2).

At the moment no continental – and therefore possibly polluted – monitoring stations are included in the stationset for the inversion. It has already been mentioned that the lack of those stations is a strong limitation for resolving sources and sinks.

Since atmospheric measurements at several continental stations have become available in the recent decade, future inversions will probably include data from these stations. The question is therefore whether the effects of these stations are as significant as the effects caused by the Hateruma station.

This issue is tested in a further synthetic experiment; here a new set of synthetic data is created for all monitoring stations that currently measure O<sub>2</sub>/N<sub>2</sub> and CO<sub>2</sub>. For those stations where no data existed in the MPI-BGC database, weekly sampling was assumed over the whole time period.

Figure 2.18a and b show the long-term mean and standard deviation of  $\Delta F_{\text{APOff}}$  for this setup together with the locations of the stations included in the calculation. The addition of those stations does not change the global picture completely, but mainly causes more negative  $\Delta F_{\text{APOff}}$  signals in the Northern Atlantic and the Mediterranean and North Sea that account for ~50% of the  $F_{\text{APO}}$  signals in this region. This is in accordance with expectations as most of the additional stations are located in Europe or North America, and have an  $\text{OR}_{\text{ff}}$  slightly higher than 1.4. In addition, temporal variations in the North Atlantic are slightly lower compared to the inversion with the classical inversion stations, while they are slightly higher around Hateruma. This is due to the fact that contrary to the inversion with the classical stationset, fluxes in the North Atlantic are now better constrained and the inversion algorithm has less degrees of freedom to distribute the excess fluxes globally.

Summarizing the results of this chapter, it can be stated that neglecting the influence of variable oxidative ratios when running an atmospheric APO inversion is not problematic if only the observational input from remote stations is used. When more polluted stations are included, the effects on the global level and integrated over larger oceanic regions are still small compared to other uncertainties. However, on local and regional scales, these influences are not negligible. Depending on the application, it is thus recommended to use spatially variable oxidative ratios such as those provided by the COFFEE dataset for the calculation.



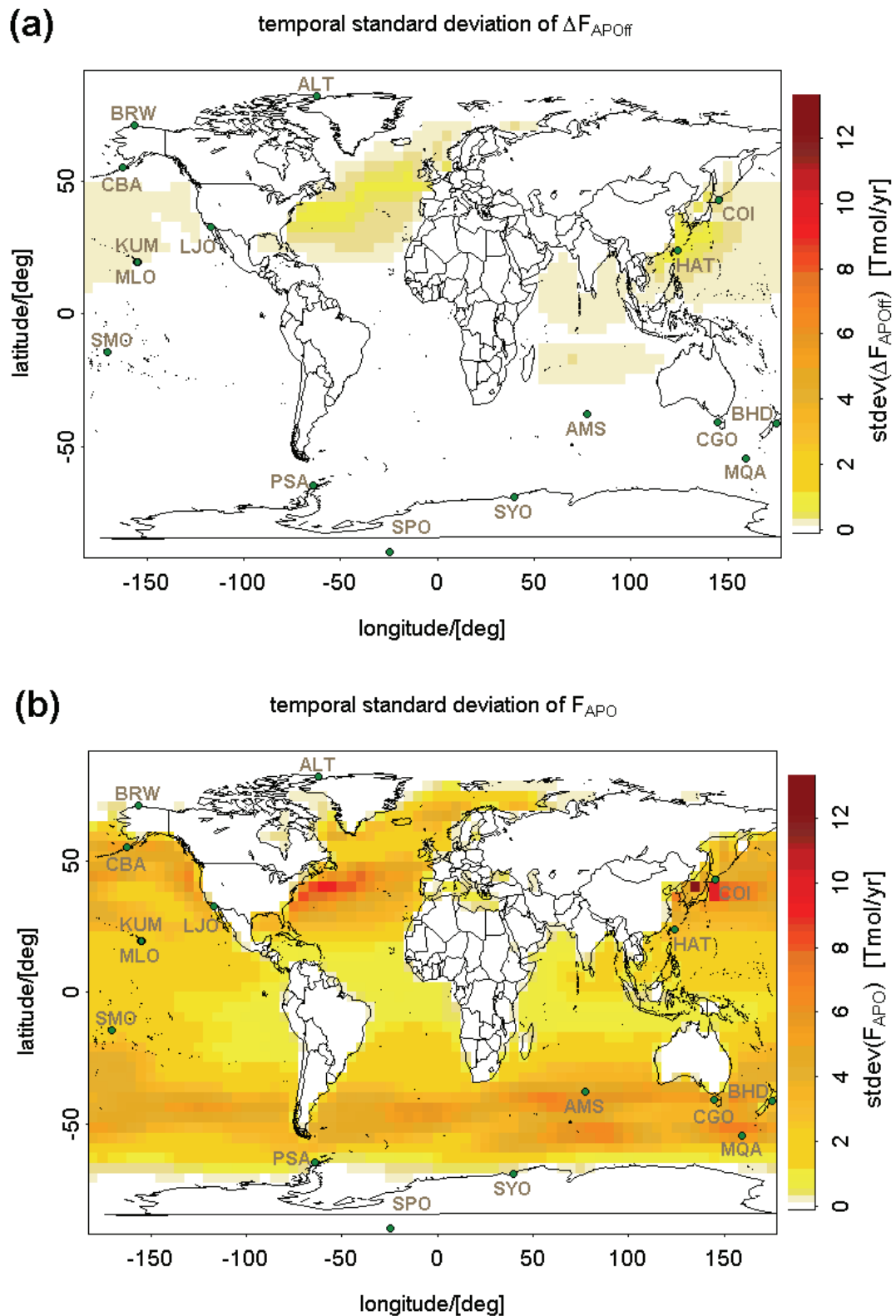


Figure 2.15: Global maps of (temporal) standard deviation of  $\Delta F_{APOff}$  (a) and  $F_{APO}$  (b) for the period 1996 to 2006. The size of the gridcells here and in the following figures is  $5 \times 3.82$  degrees (longitude x latitude).

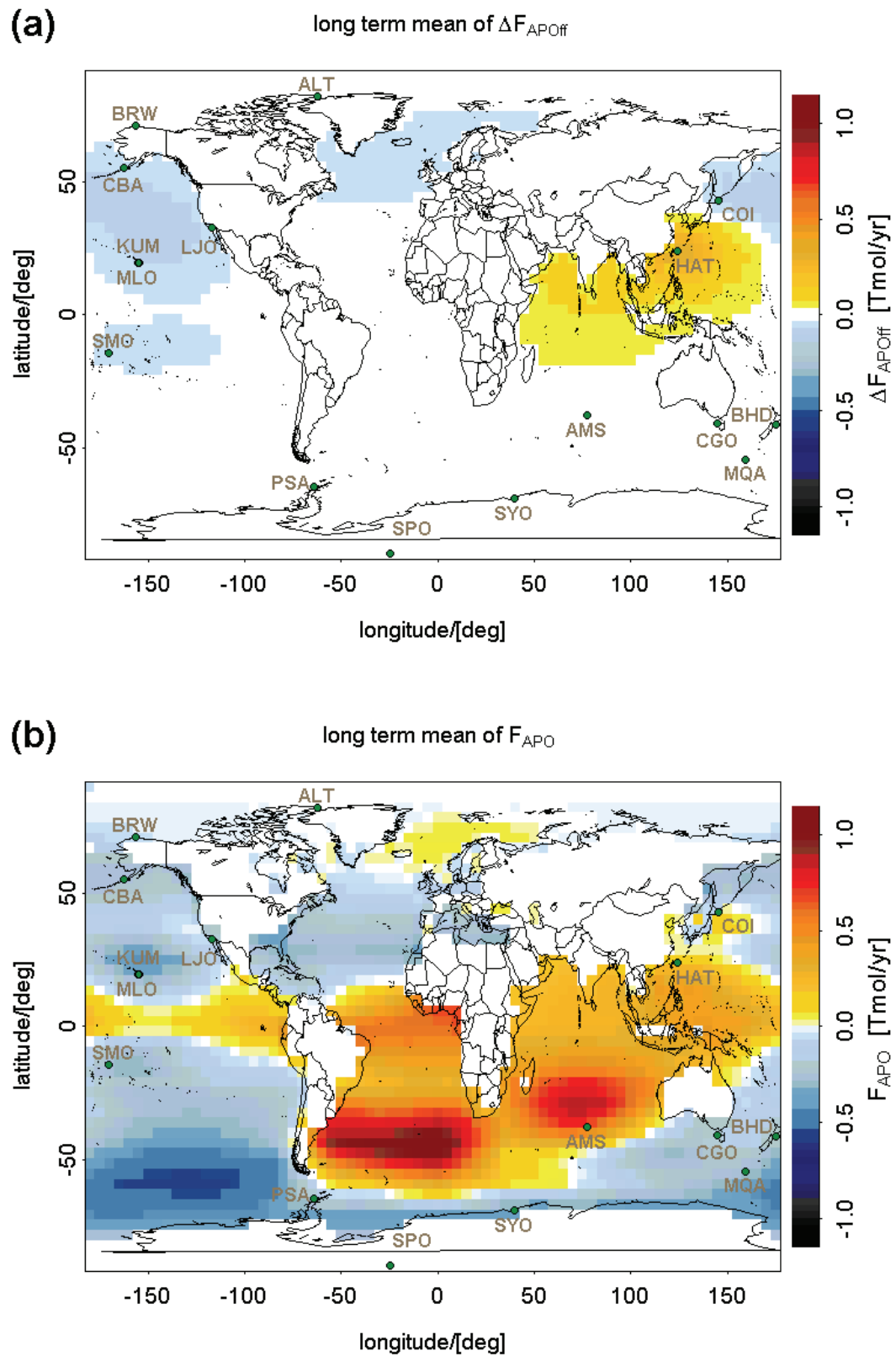


Figure 2.16: Global maps of long-term mean of  $\Delta F_{\text{APOff}}$  (a) and  $F_{\text{APO}}$  (b) for the period 1996 – 2006.

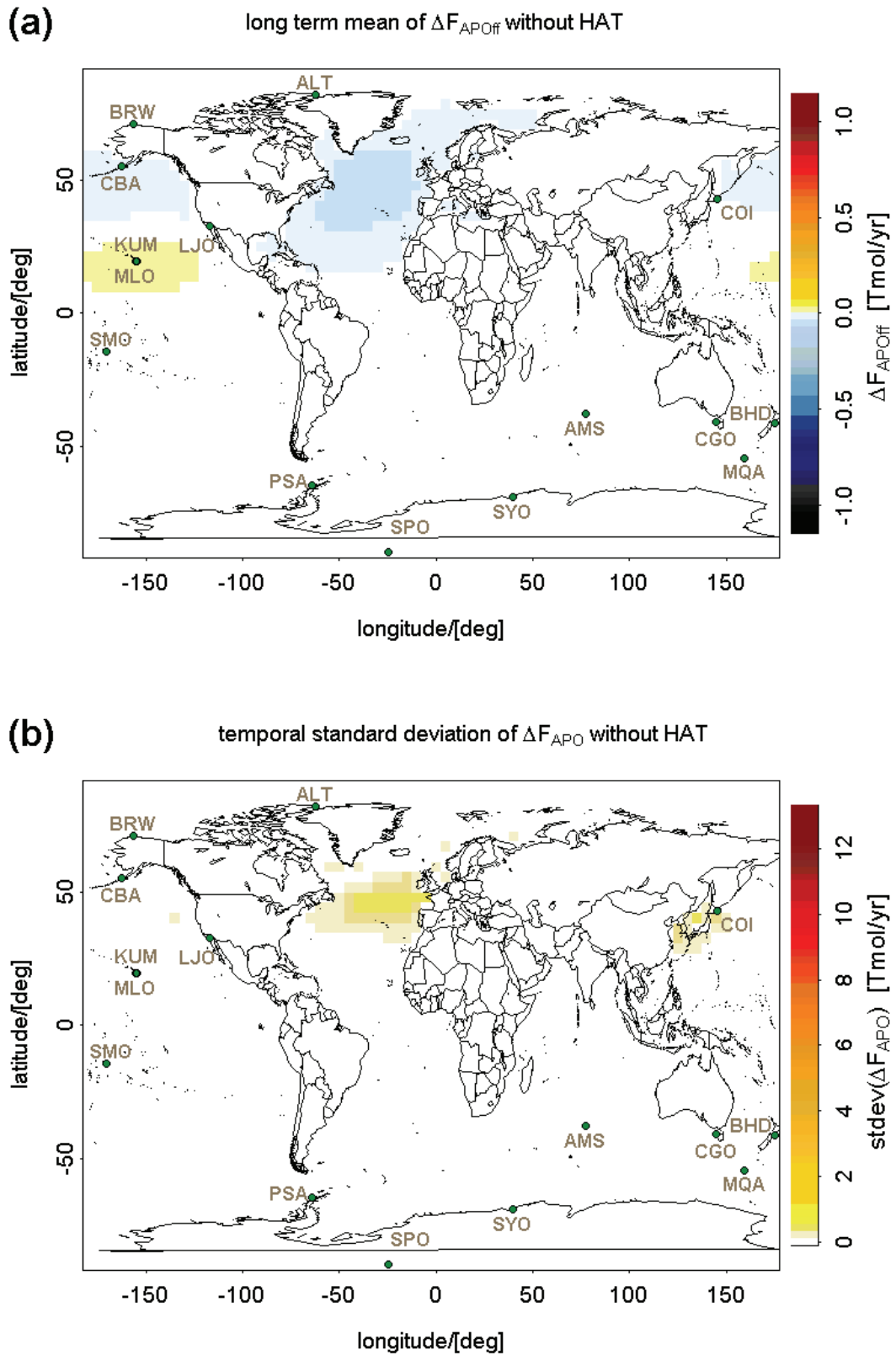


Figure 2.17: Global maps of long-term mean (a) and standard deviation (b) of  $\Delta F_{\text{APOff}}$  for inversion without Hateruma. The color scales correspond to those in Figure 2.15.

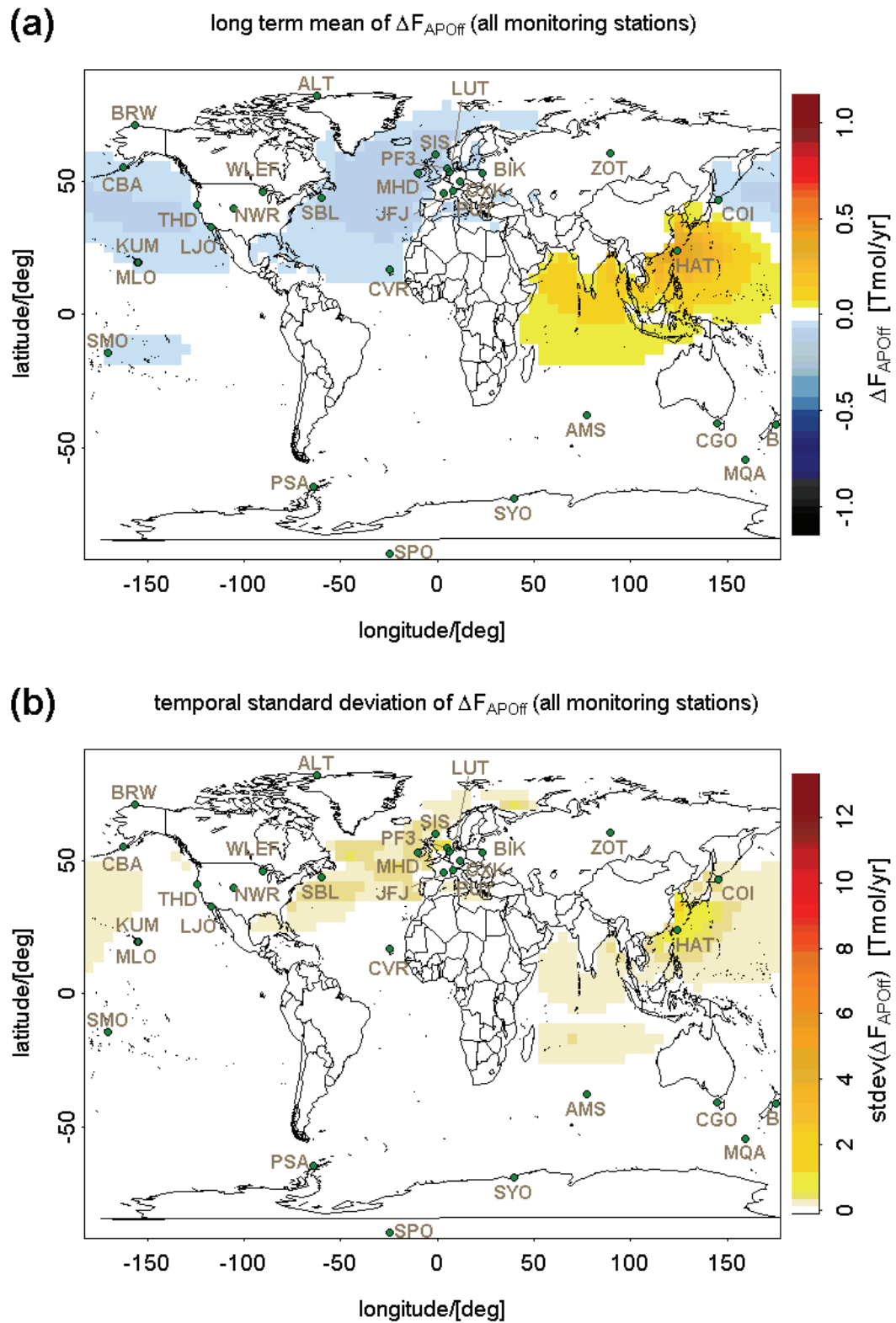


Figure 2.18: Global maps of long-term mean (a) and standard deviation (b) of  $\Delta F_{\text{APOff}}$  for inversion with synthetic data input from all atmospheric monitoring stations currently measuring atmospheric oxygen. The color scales correspond to those in Figure 2.15

## 2.6 Conclusion

In this chapter, the influence of variable oxidative ratios from fossil fuel combustion has been investigated. For this purpose, the COFFEE dataset, containing hourly resolved anthropogenic CO<sub>2</sub> emissions and the corresponding O<sub>2</sub> uptake for the years 1995 to 2008 on a 1° x 1° grid, has been created from emission inventories and fuel consumption data. Global maps derived from this dataset show that spatial variations of oxidative ratios cover the whole range from around 1 to 1.95. Temporal changes during the decade from 1996 to 2006, show a spatial range of -0.24 to 0.45 and no predominant positive or negative trend.

The value for the global average oxidative ratio for fossil fuel burning, usually assumed to be  $\alpha_F = 1.4$ , is  $1.402 \pm 0.003$  when calculated from the COFFEE dataset. Comparison with the global average derived from two other fossil fuel inventories shows similar patterns for the temporal variations and an offset of up to 4% between the datasets that could mainly be attributed to differences in the fuels included in the different inventories. The deviations from  $\alpha_F$  due to temporal variations in the COFFEE fuel mix relate to a maximum change of  $\pm 0.035$  PgC/y in the global oceanic and land carbon sink, which corresponds to around 10% of the total uncertainty in the sink calculation. However, the uncertainty in the absolute value of the global average due to uncertainties in fuel production numbers is probably a factor of 6 higher than the range of temporal variations.

The potential influence of variable oxidative ratios on the atmospheric oxygen signal measured at ground-based monitoring stations has been investigated using simulations from regional and global transport models. Although for many of the stations, especially the ones located on the continent, the specific oxidative ratios show large variations and deviations from  $\alpha_F$ , this does not always lead to detectable signals. Also depending on the magnitude of fossil fuel related CO<sub>2</sub> fluxes at the measurement location, the influence of the local fuel mix usually changes the atmospheric O<sub>2</sub> concentration by a few ppm, with maximum deviations ranging from -7 ppm to +4ppm.

Whether these effects can be detected in atmospheric CO<sub>2</sub> and O<sub>2</sub> observations has been examined for two cases. For the Ochsenkopf tall tower, a continental station in Germany, the influence of variable fossil fuel related oxidative ratios has been shown negligible, since the atmospheric signal at this station is mainly dominated by biospheric processes and the fuel mix does not differ significantly enough from the global average. However, for the Hateruma station in Japan, which is more influenced by fossil fuel emissions with a relatively low and variable oxidative ratio, it is crucial to take into account the local fuel mix when interpreting observations.

Finally, the influence of varying oxidative ratios on the partitioning of the land and ocean carbons sinks was examined using APO inversions. It was calculated which part of the fossil fuel signal is misinterpreted as oceanic signal when employing a constant oxidative ratio for fossil fuel burning. The difference in the seasonal variations caused by this simplifying assumption accounts for only 5-10% of the real oceanic APO fluxes and is therefore rather small compared to other uncertainties in the inversion, that are in the range of 25 – 35 %. However, depending on the set of stations used for the inversion, systematic offsets in the fluxes are caused in certain areas. Whereas this offset is negligible when using only remote stations, it becomes more significant as soon as observations from more polluted stations are included. An extreme example is the Hateruma station that causes a regional bias on the order of 50–100% of the oceanic APO fluxes. Adding observations from more of the existing continental stations, mainly in Europe and North America, leads to a significant additional negative bias in the Northern Atlantic region.

To summarize, the COFFEE dataset has proven to be a useful tool for quantifying the effects of variable oxidative ratios from fuel combustion. This chapter has shown that while for observations from the classical remote stations and many global implementations the use of a constant global average is sufficient, there are applications where more precise information on fossil-fuel related oxidative ratios is needed. In two cases, the COFFEE dataset has already been used successfully for interpreting atmospheric oxygen measurements at monitoring stations: in the first case for the separation of the fossil fuel part from APO signals measured at the Lütjehad

station in the Netherlands (van der Laan-Luijkx et al. 2010), and in the second case for using oxidative ratios of pollution events to determine the origin of air masses arriving at the Hateruma station in Japan (Minejima et al. in preparation)

## 2.7 References

- Boden, T. A., G. Marland and R. J. Andres (2009). Global, Regional, and National Fossil-Fuel CO<sub>2</sub> Emissions from Fossil-Fuel Burning, Cement Manufacture, and Gas Flaring: 1751-2006 Carbon Dioxide Information Analysis Center, Oak Ridge National Laboratory, U.S. Department of Energy, Oak Ridge, Tenn., U.S.A. .
- Chevillard, A., U. Karstens, P. Ciais, S. Lafont and M. Heimann (2002). "Simulation of atmospheric CO<sub>2</sub> over Europe and western Siberia using the regional scale model REMO." Tellus Series B-Chemical and Physical Meteorology **54**(5): 872-894.
- Gerbig, C., J. C. Lin, S. C. Wofsy, B. C. Daube, A. E. Andrews, B. B. Stephens, P. S. Bakwin and C. A. Grainger (2003). "Toward constraining regional-scale fluxes of CO<sub>2</sub> with atmospheric observations over a continent: 1. Observed spatial variability from airborne platforms." Journal of Geophysical Research-Atmospheres **108**(4756): doi:4710.1029/2002JD00301.
- Heimann, M. and S. Körner (2003). The global atmospheric tracer model TM3. Technical Report 5, Max Planck Institute for Biogeochemistry, Jena, Germany
- IEA (2007). CO<sub>2</sub> emissions from fossil fuel combustion: 1971-2005 (2007 edition), International Energy Agency
- Keeling, R. F. (1988). Development of an interferometric analyzer for precise measurements of the atmospheric oxygen mole fraction. Cambridge, Massachusetts, Harvard University. **PhD thesis**: 178p.
- Langmann, B. (2000). "Numerical modelling of regional scale transport and photochemistry directly together with meteorological processes." Atmospheric Environment **34**(21): 3585-3598.
- Lin, J. C., C. Gerbig, S. C. Wofsy, A. E. Andrews, B. C. Daube, K. J. Davis and C. A. Grainger (2003). "A near-field tool for simulating the upstream influence of atmospheric observations: The Stochastic Time-Inverted Lagrangian Transport (STILT) model." Journal of Geophysical Research-Atmospheres **108**(D16): 4493, doi:10.1029/2002JD003161.
- Mahadevan, P., S. C. Wofsy, D. M. Matross, X. Xiao, A. L. Dunn, J. C. Lin, C. Gerbig, J. W. Munger, V. Y. Chow and E. W. Gottlieb (2008). "A satellite-based biosphere parameterization for net ecosystem CO<sub>2</sub> exchange: Vegetation Photosynthesis and Respiration Model (VPRM)." Global Biogeochemical Cycles **22**: GB2005, doi:10.1029/2006GB002735.
- Manning, A. C. and R. F. Keeling (2006). "Global oceanic and land biotic carbon sinks from the Scripps atmospheric oxygen flask sampling network." Tellus Series B-Chemical and Physical Meteorology **58**(2): 95-116.

- Matross, D. M., A. Andrews, M. Pathmathevan, C. Gerbig, J. C. Lin, S. C. Wofsy, B. C. Daube, E. W. Gottlieb, V. Y. Chow, J. T. Lee, C. L. Zhao, P. S. Bakwin, J. W. Munger and D. Y. Hollinger (2006). "Estimating regional carbon exchange in New England and Quebec by combining atmospheric, ground-based and satellite data." Tellus Series B-Chemical and Physical Meteorology **58**(5): 344-358.
- Olivier, J. G. and J. J. M. Berdowski (2001). Global emission sources and sinks. The Climate System: 33-77. J. Berdowski, R. Guicherit and B. J. Heij, Lisse: Swets & Zeitlinger Publishers.
- Popa, M. E. (2008). Continuous tall tower multispecies measurements in Europe for quantifying and understanding land-atmosphere carbon exchange. Jena, Friedrich-Schiller-Universitaet. **PhD thesis: 237p**.
- Rödenbeck, C., C. Le Quere, M. Heimann and R. F. Keeling (2008). "Interannual variability in oceanic biogeochemical processes inferred by inversion of atmospheric O-2/N-2 and CO2 data." Tellus Series B Chemical and Physical Meteorology **60**(5): 685-705.
- Sirignano, C., R. E. M. Neubert, H. A. J. Meijer and C. Rödenbeck (2008). "Atmospheric oxygen and carbon dioxide observations from two European coastal stations 2000-2005: continental influence, trend changes and APO climatology." Atmos. Chem. Phys. Discuss **8**: 20113-20154.
- Stohl, A., C. Forster, A. Frank, P. Seibert and G. Wotawa (2005). "Technical note: The Lagrangian particle dispersion model FLEXPART version 6.2." Atmospheric Chemistry and Physics **5**: 2461-2474.
- Stohl, A., M. Hittenberger and G. Wotawa (1998). "Validation of the Lagrangian particle dispersion model FLEXPART against large-scale tracer experiment data." Atmospheric Environment **32**(24): 4245-4264.
- Thompson, R. L., A. C. Manning, M. Gloor, U. Schultz, T. Seifert, F. Haensel, A. Jordan and M. Heimann (2009). "In-situ measurements of oxygen, carbon monoxide and greenhouse gases from Ochsenkopf tall tower in Germany." Atmospheric Measurement Techniques **2**: 573–591.
- Tohjima, Y. (2000). "Method for measuring changes in the atmospheric O-2/N-2 ratio by a gas chromatograph equipped with a thermal conductivity detector." Journal of Geophysical Research-Atmospheres **105**(D11): 14575-14584.
- van der Laan-Luijkx, I. T., U. Karstens, J. Steinbach, C. Gerbig, C. Sirignano, R. E. M. Neubert, S. van der Laan and H. A. J. Meijer (2010). "CO<sub>2</sub>, δO<sub>2</sub>/N<sub>2</sub> and APO: observations from the Lütjehad, Mace Head and F3 platform flask sampling network." Atmos. Chem. Phys. Disc.



# Chapter 3

## O<sub>2</sub>/CO<sub>2</sub> ratios derived from airborne flask sampling in Amazonia

In this chapter, results of O<sub>2</sub>/N<sub>2</sub> and CO<sub>2</sub> measurements from flasks taken during the BARCA (Balanço Atmosférico Regional de Carbono na Amazônia) aircraft campaign in the Brazilian Amazon Basin are presented. This campaign was aiming to quantify the carbon budget of the Amazon Region by addressing the ‘missing scale’ between local measurements and modeling studies on global scales. In the following, it is investigated how far simultaneous measurements of atmospheric oxygen and the resulting O<sub>2</sub>/CO<sub>2</sub> ratios can contribute to the interpretation of measured CO<sub>2</sub> signals.

### 3.1 The BARCA mission

#### 3.1.1 Motivation

The Amazon Basin plays a key role in the carbon cycle, since it accounts for ~10% of global terrestrial net primary productivity (Melillo et al. 1993) and contains one half of the world's undisturbed tropical forest (FAO 1993). With around 120 Pg, the amount of carbon stored in Amazonian trees is equivalent to 1.5 decades of current worldwide anthropogenic carbon emissions to the atmosphere (Soares et al. 2006). However, deforestation and agricultural development have reduced the forested areas with rates of up to 25000km<sup>2</sup>/year in the 1990s (Achard et al. 2002), representing a large source of CO<sub>2</sub> to the atmosphere. By 2007, the deforestation rates have decreased by a factor of 2 (Malhi et al. 2008), due to a combination of economic factors and active intervention by the Brazilian government (Nepstad et al. 2006).

The overall magnitude and even the sign of the net carbon balance of the Amazon Basin is thus subject to large uncertainties that propagate into the global carbon budget (Prentice et al. 2001). Over the last decades, a number of studies have been conducted in the Amazon region, mainly based on eddy flux measurements. Several studies indicate that Amazônia is a large net CO<sub>2</sub> sink (Grace et al. 1995; Malhi and

Grace 2000), while analysis based on remote sensing data rather suggests that carbon sinks and sources balance to a net effect close to zero (Houghton et al. 2000).

Since scaling up from local measurements to the whole Amazon basin is difficult, the idea of the BARCA project was to address the ‘missing scale’ – in between the local point measurements and global models. This was done by aircraft measurements of CO<sub>2</sub> and several other tracers in combination with an integrative modeling framework. Aircraft measurements are uniquely suited to quantify Basin-scale fluxes of CO<sub>2</sub> (and other tracers), since they allow observing three-dimensional tracer distributions in the atmosphere at high-resolution and can thus be used to determine spatially resolved sources and sinks of trace gases.

The BARCA mission was conducted as a cooperation of the MPI-BGC, the MPI for Chemistry (Mainz, Germany), Harvard University (Boston, USA), the INPE (Instituto Nacional de Pesquisas Espaciais, São Paulo, Brazil), the University of São Paulo, NOAA/ESRL (Earth System Research Laboratory of the National Oceanic and Atmospheric Administration, Boulder, USA), and the University of Utrecht (the Netherlands).

### **3.1.2 Aircraft campaigns**

Within the BARCA mission, two aircraft campaigns (hereinafter called BARCA-A and BARCA-B) were conducted at the transition from dry to wet seasons in November/December 2008 and at the end of the wet season in May 2009. Since this chapter deals with the results of the O<sub>2</sub>/N<sub>2</sub> measurements, it will focus on BARCA-A for which O<sub>2</sub>/N<sub>2</sub> data are already available.

The aircraft, an EMB 110 Bandeirante belonging to INPE, was based in Manaus (60°1'34"W, 3°6'26"S), the capital of the Brazilian state Amazonas, from which most of the research flights started. Figure 3.1 shows the flight pattern of the 15 flights conducted during BARCA-A, with the colors representing the different flights. Limited by the fuel supply of the aircraft, the duration of the single flights was usually

3-4 hours, covering a spatial scale of up to 800 km. Profile measurements, as shown in Figure 3.2 were conducted to acquire optimal vertical coverage.



Figure 3.1: Flighttracks of BARCA-A campaign. Colors represent different flight days.

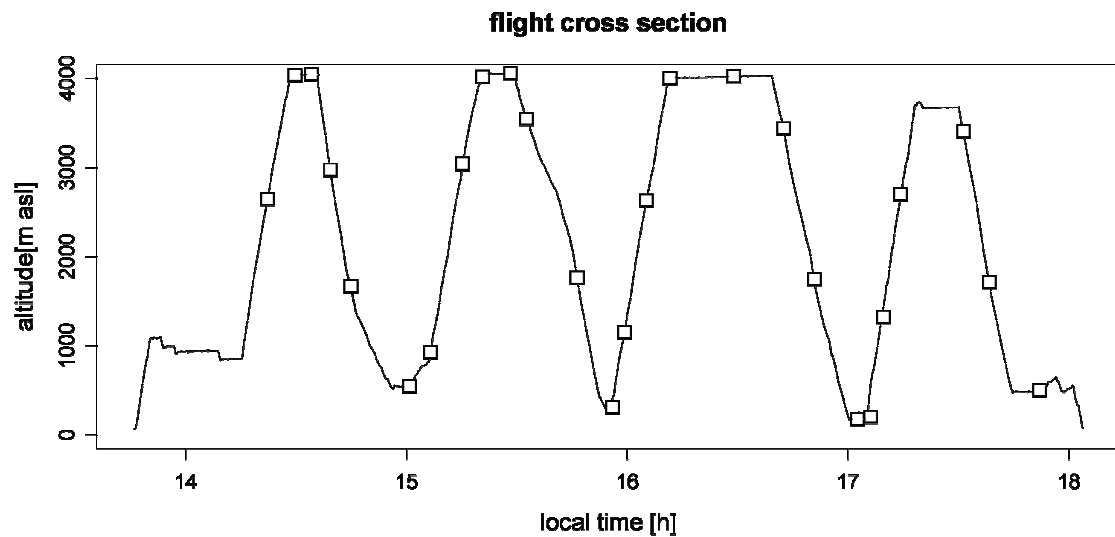


Figure 3.2: Typical cross section of a flight during BARCA-A, here a local-area flight around Manaus. The squares indicate times when flask samples were taken.

### 3.1.3 Measurements during BARCA

Onboard the aircraft in-situ measurements of CO<sub>2</sub>, CO, O<sub>3</sub>, CH<sub>4</sub> (only phase B), aerosols and meteorological parameters (pressure, temperature, water vapor) were performed. In addition, flask samples were taken that were analyzed at MPI-BGC for O<sub>2</sub>/N<sub>2</sub>, Ar/N<sub>2</sub>, CH<sub>4</sub>, CO<sub>2</sub>, N<sub>2</sub>O, H<sub>2</sub>, CO and SF<sub>6</sub> as well as for carbon and for a small subset of the collected flask samples, methane isotopes. This chapter deals with the analysis and interpretation of the O<sub>2</sub>/N<sub>2</sub> results.

## 3.2 O<sub>2</sub>/N<sub>2</sub> ratios from flask samples

### 3.2.1 Flask sampling and analysis

Flask samples were taken manually during the flight using a custom built flask sampler. As shown in the simplified flow diagram in Figure 3.3, the air is drawn into the sampler by a small vacuum pump upstream of the flask, using no pressure control at the intake (therefore the flask filling time varies with height due to changes in the outside pressure). Prior to entering the flasks, the air is dried with a chemical dryer (magnesium perchlorate). Each flask is flushed with a flow of ~5 ℓ/min for at least 5 minutes first, then filled to a pressure of ~1bar above ambient.

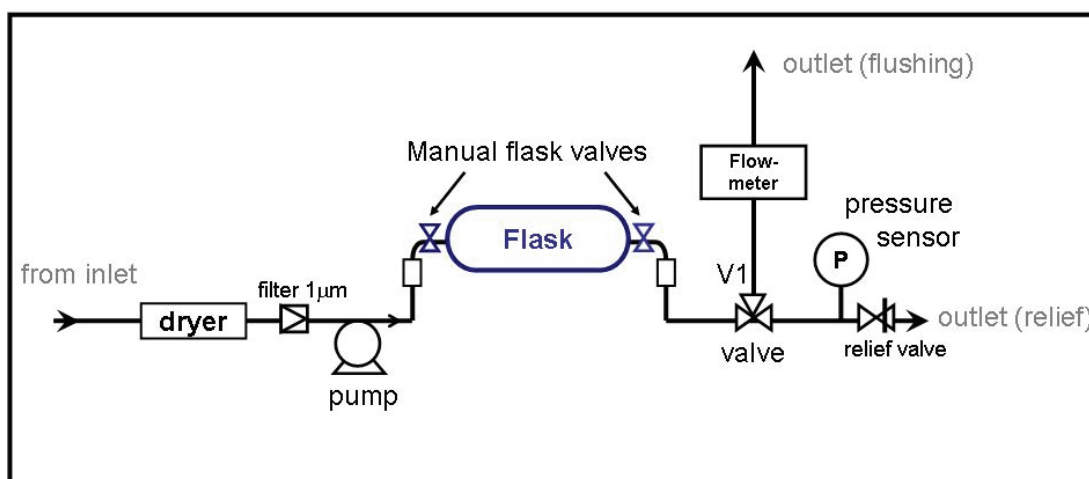


Figure 3.3: Simplified flow diagram of the flask sampler used during the BARCA campaign.

The transition from flushing to filling is performed manually by switching the downstream valve V1. The operator writes down the flask code, the sampling time (start of flushing and start of filling = time of switching the downstream valve) as well as the current height of the aircraft on a flask sheet that is kept with the samples. Since these values might be not always accurate, additionally the pressure in the flask is recorded at a frequency of 0.5Hz with the pressure sensor P to allow exact synchronization with the in-situ measurements.

After the campaign flask samples were analyzed at MPI-BGC for the above mentioned species, using mass spectrometric analysis (Brand 2003) for O<sub>2</sub>/N<sub>2</sub> and Ar/N<sub>2</sub> and a gas chromatograph (Jordan and Brand 2003) for measurement of CO<sub>2</sub> and the other species.

### 3.2.2 Merging flask and in-situ data

To obtain information on the location, height and meteorological parameters for flask sampling times, but also to correlate the flask results with gas species measured in-situ, the flask data was merged to the in-situ data. For this, a weighted average of the in-situ data was calculated, using a weighting function based on the recorded flask pressure  $p$ .

The relative contribution  $W$  of air entering the flask at a certain time  $t$  within the flushing or filling process of the flask is derived in Appendix 1 as

$$W(t) = \begin{cases} \exp\left\{(t - t_1) \cdot p(t_1) / \frac{dp}{dt}(t_1)\right\} & \text{for } t_0 < t < t_1 \quad (\text{flushing period}) \\ \frac{1}{dp_{\max}} \frac{dp}{dt} & \text{for } t_1 < t < t_2 \quad (\text{filling period}) \end{cases} \quad (3.1)$$

Figure 3.4 illustrates the temporal distribution of the weighting function, together with the corresponding time series of the flask pressure.

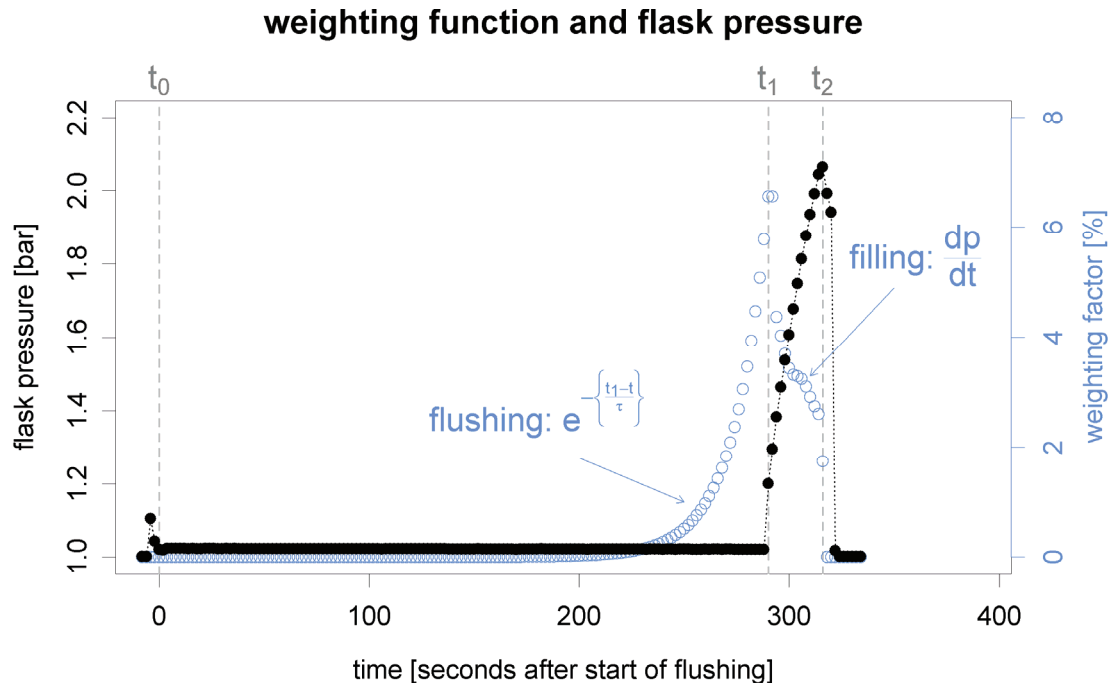


Figure 3.4: Weighting function (blue) to calculate averaged in-situ data corresponding to the times of flask measurements, together with timeseries of flask pressure during flushing and filling of a flask (black)

Before applying the weighting function to the measured data, the exact sampling times were derived from the recorded flask pressure by detecting an increase in pressure (start of filling =  $t_1$ ), followed by a sudden decrease (removal of the flask at the end of filling =  $t_2$ ). These times are compared to the sampling times written down by the operator to assign a flask code to each sampling time. A constant flushing time of 5 minutes was assumed for all flasks. Although the actual flushing times are sometimes much longer, this does not effect the averaging significantly due to the exponential decrease in the flushing part of the weighting function.

To finally merge the flask data to the weighted in-situ data, the time lag between the aircraft's inlet on the flask sampler (or the respective in-situ instrument) needs to be taken into account. Thus the time  $t$  in Equation 3.1 needs to be replaced by the time  $t'$  of the air entering the inlet. Since the intake flow of the sampler is not controlled, the time lag varies with the outside pressure:

$$t' = t - (p_a(t)/p_s) \cdot t_l \quad (3.2)$$

Here,  $t_l$  is the time lag at surface level,  $p_a$  the ambient pressure at the time  $t$  and  $p_s \sim 1013 \text{ mbar}$  the ambient pressure at the surface. The time lag at the surface level is calculated relative to that of the in-situ measurement, using the best correlation between in-situ and flask measurements for those species measured both in-situ and in the flask samples (CO<sub>2</sub> and CO).

### 3.2.3 Fractionation correction for O<sub>2</sub>/N<sub>2</sub>

Fractionation artifacts in the O<sub>2</sub>/N<sub>2</sub> ratio of the sampled air are likely to be caused both at the aircraft's intake and during the filling process of the flasks. Fractionation effects during flask filling could either be caused by pressure or temperature gradients or by adsorption on surfaces such as o-rings. However, adsorption effects are largely avoided by the flushing of the flasks. In addition, any pressure or temperature gradient inside the flask system is unlikely to cause significant fractionation as molecules would need to diffuse backward against the intake flow that runs with  $\sim 3 \text{ l/min}$ . Thus fractionation occurring at the aircraft's intake is more likely the dominant effect.

To check and correct for fractionation artifacts, the measured Ar/N<sub>2</sub> results were used. This is possible since most fractionation mechanisms affecting the O<sub>2</sub>/N<sub>2</sub> ratio also have an effect on Ar/N<sub>2</sub>. For diffusive fractionation effects (see Chapter 1.4.3), the effect on Ar/N<sub>2</sub> is a factor 2-4 larger than for O<sub>2</sub>/N<sub>2</sub> (Keeling et al. 2004; Langenfelds et al. 2005) and therefore easier to detect. In addition, atmospheric variations in the Ar/N<sub>2</sub> ratio are rather small, as they are only caused by air-sea gas exchange due to changes in the ocean temperature (Battle et al. 2003; Keeling et al. 2004; Cassar et al. 2008). Taking into account the spatial and temporal scales covered by the BARCA flask samples, measured variations in the Ar/N<sub>2</sub> ratio can be considered to be mostly due to fractionation artifacts. This is confirmed by looking at Figures 3.5 and 3.6: Although the range of variations in the measured Ar/N<sub>2</sub> is quite large, varying from around 40 to 170 per meg, no dominant spatial patterns are seen (Figure 3.5)

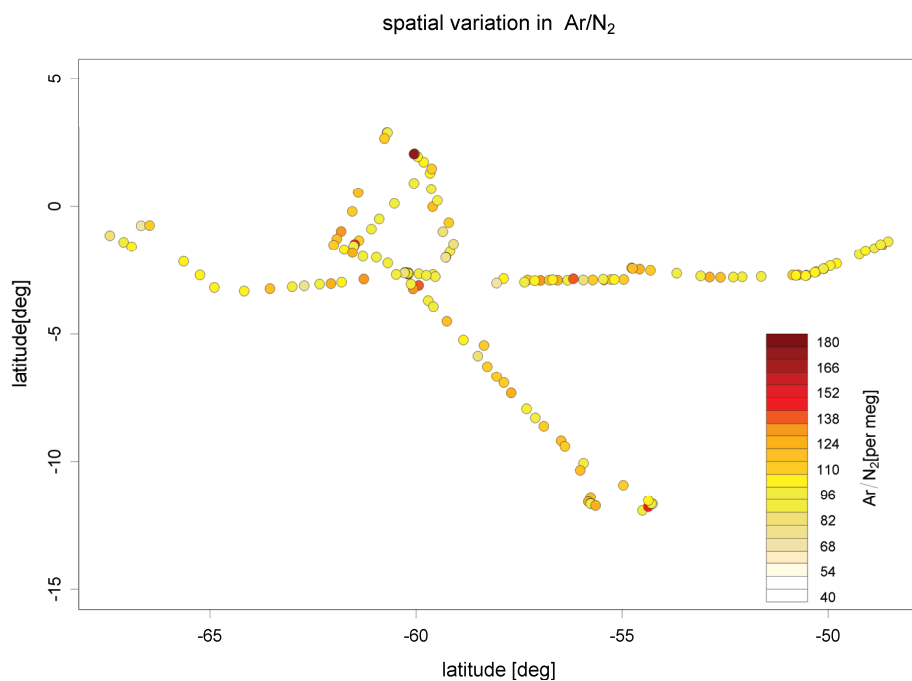


Figure 3.5: Spatial variations in measured Ar/N<sub>2</sub> ratios of flask samples.

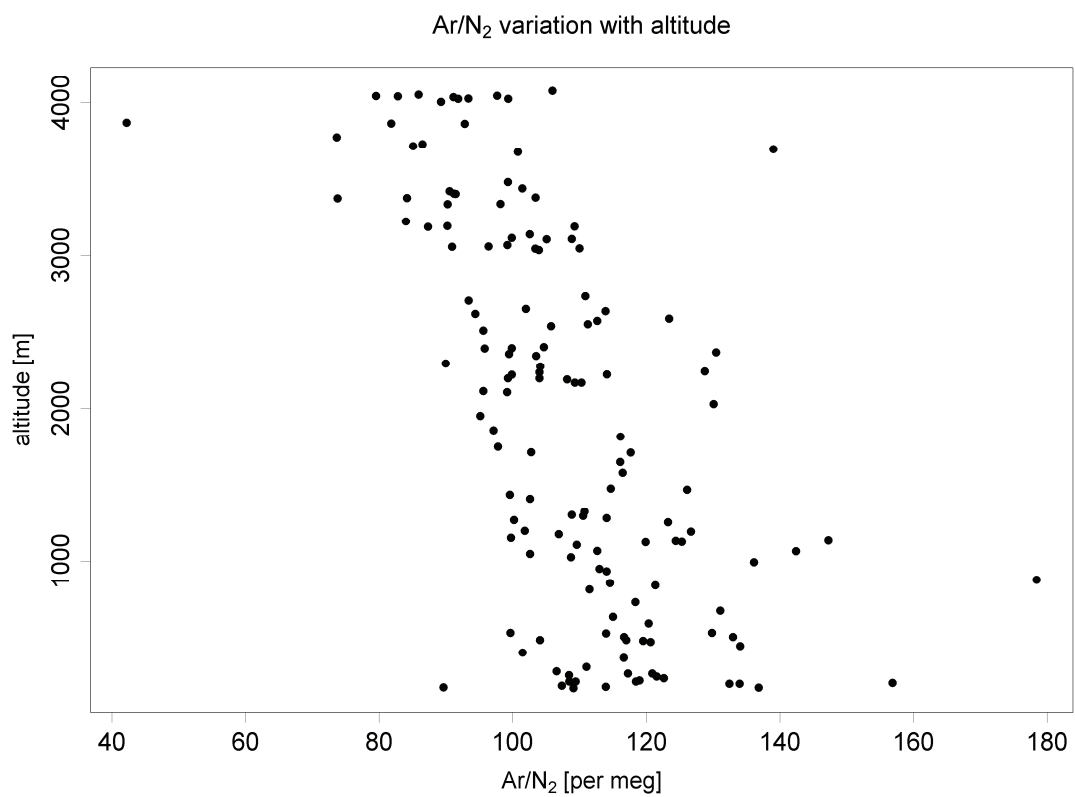


Figure 3.6: Ar/N<sub>2</sub> variation with altitude.



On the other hand, Ar/N<sub>2</sub> decreases significantly with increasing altitude (Figure 3.6), with a difference of ~30 per meg between ground level and 4000m. The rate of decrease is constant up to high altitudes, indicating that it is caused by pressure or temperature related fractionation artifacts related to sample intake or flask filling rather than ‘natural’ (thermal or gravimetric) fractionation of the ambient air. (The ‘natural’ fractionation effect is sometimes observed within stable surface layers, capped by a strong inversion, but does not extend into the free troposphere, since there it is overwhelmed by turbulent mixing (Keeling et al. 2004))

To translate the fractionation artifacts in Ar/N<sub>2</sub> to effects in the O<sub>2</sub>/N<sub>2</sub> signal, one needs to make an assumption about their dominant nature, as the ratio of O<sub>2</sub>/N<sub>2</sub> fractionation to Ar/N<sub>2</sub> fractionation depends on this mechanism. The scaling factor  $f = \delta(\text{Ar}/\text{N}_2) / \delta(\text{O}_2/\text{N}_2)$  is  $f_E = 2.5$  for effusion through leaks or other small orifices,  $f_T = 3.9$  for thermal fractionation and  $f_p = 2.9$  for pressure-related fractionation (Langenfelds et al. 2005).

Since ambient pressure and temperature both vary with height, both parameters could influence the measured Ar/N<sub>2</sub> signals. Their correlation with Ar/N<sub>2</sub> is shown in Figure 3.7.

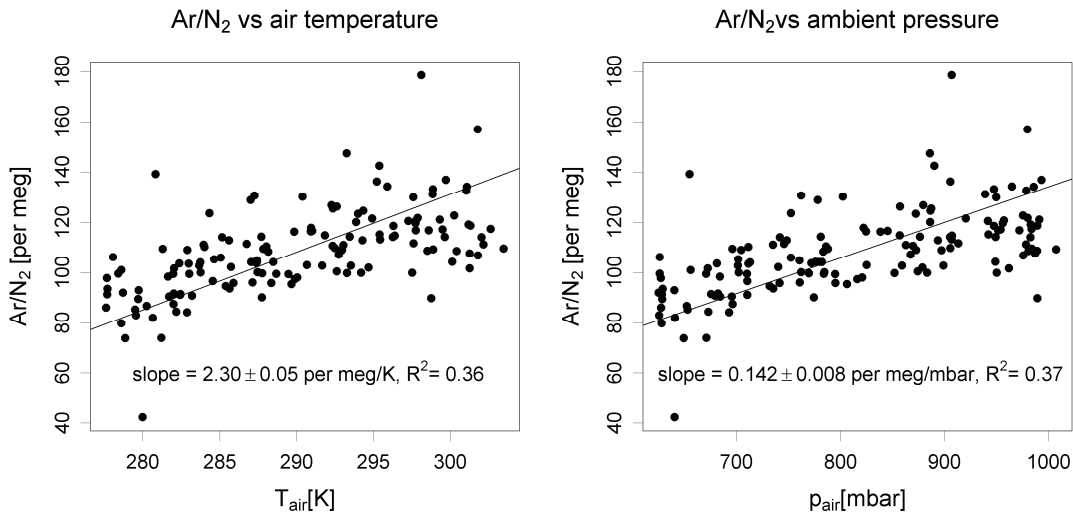


Figure 3.7: Variation of measured Ar/N<sub>2</sub> signals with ambient pressure and temperature (slopes determined by orthogonal distance regression)

It can be seen that Ar/N<sub>2</sub> increases with both increasing pressure and temperature. With values of 0.36 and 0.37, the coefficients of determination ( $R^2$ ) of the two regressions are comparable, related to the fact that temperature and pressure are strongly correlated.

The dominant fractionation mechanism observed in laboratory experiments on inlet fractionation (detailed presentation in Chapter 4) has shown to be related to pressure-induced fractionation. Thus the observed fractionation for Ar/N<sub>2</sub> can be scaled to O<sub>2</sub>/N<sub>2</sub> fractionation using the factor  $f_p$  for pressure-related fractionation. Measured O<sub>2</sub>/N<sub>2</sub> ratios are therefore corrected using the following formula:

$$(O_2 / N_2)_{corr} = (O_2 / N_2)_{meas} - 2.9 \cdot [(Ar / N_2)_{meas} - \text{mean}(Ar / N_2)_{meas}] \quad (3.3)$$

Figure 3.8 shows the raw data and corrected values (left plot) and the values of the correction term (right plot), ranging mainly from -15 to +10 per meg. Comparing that to the measurement precision of 2 per meg for flask measurements (Brand 2003) shows that fractionation artifacts can significantly alter the sample composition.

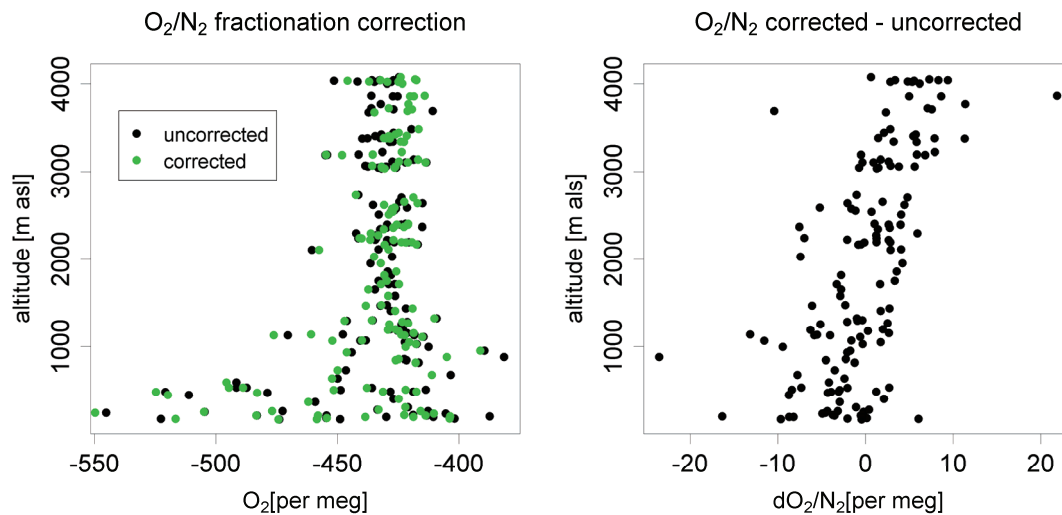


Figure 3.8: Measured O<sub>2</sub>/N<sub>2</sub> profiles, corrected for fractionation artifacts using the measured Ar/N<sub>2</sub> variations. The left plot shows both raw data (black) and corrected results (green), the plot on the right the differences between corrected and uncorrected signals.

### 3.3 O<sub>2</sub>/CO<sub>2</sub> results

The scope of this chapter is to investigate whether O<sub>2</sub>/N<sub>2</sub> results can be used together with the CO<sub>2</sub> measurements to separate the processes that influence the atmospheric CO<sub>2</sub> concentration. For this purpose, oxidative ratios (OR =  $-\Delta\text{O}_2[\text{mol}]/\Delta\text{CO}_2[\text{mol}]$ ) are examined, as they are characteristic of different processes (see Chapters 1.3 and 2).

Processes expected to influence O<sub>2</sub>/CO<sub>2</sub> ratios of the BARCA flask samples are

- Biospheric processes → OR ~ 1.1 (Severinghaus 1995)
- Biomass burning → OR ~ 1.11 (Lueker and Keeling 2001)
- Fossil fuel combustion → OR ~ 1.4 ((Keeling 1988), see Chapter 2)
- Ocean-atmosphere exchanges → OR = 2 – 8 (Keeling and Severinghaus 2000)

In a first step, a total oxidative ratio for all flasks measured was derived to get an idea about the dominant processes. Figure 3.9 shows a plot of O<sub>2</sub> versus CO<sub>2</sub> mole fraction (O<sub>2</sub>/N<sub>2</sub> results are converted to O<sub>2</sub> mole fractions by dividing them by 4.8).

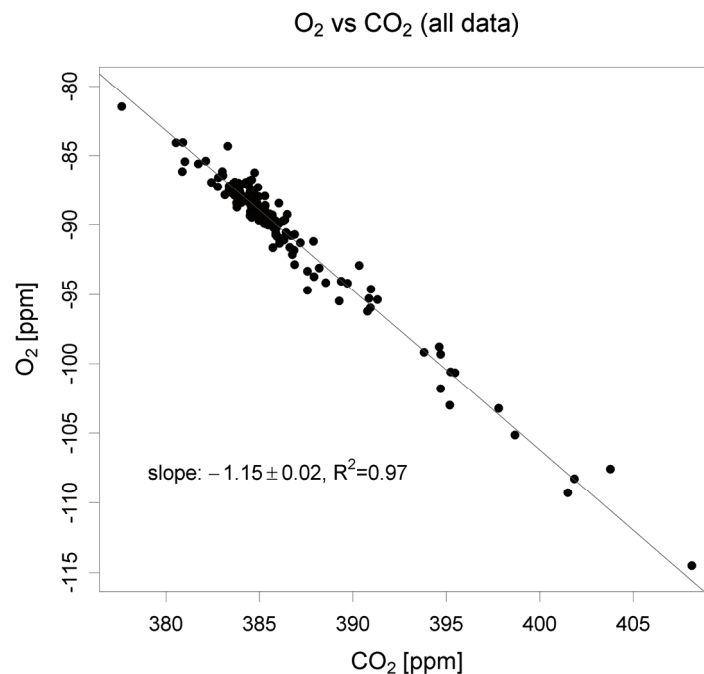


Figure 3.9: Orthogonal distance regression of O<sub>2</sub> versus CO<sub>2</sub> for all flasks. The absolute value of the slope corresponds to the oxidative ratio.

O<sub>2</sub> and CO<sub>2</sub> show a clear linear correlation, with the absolute value of the slope, determined by orthogonal distance regression, corresponding to the oxidative ratio. As expected, the resulting oxidative ratio of  $1.15 \pm 0.02$  shows that the corresponding atmospheric signals are dominated by biospheric influence, but there are also smaller contributions from other processes with a higher oxidative ratio (fossil fuel combustion or oceanic processes).

### 3.3.1 Background signals versus local influences

Figure 3.10 shows the variation of measured CO<sub>2</sub> and O<sub>2</sub> mole fractions with altitude. A similar structure can be seen for both species: The variability is higher close to the ground and decreases with altitude, with most of the variation occurring below 2000m. This can be explained by the fact that the signal at low altitudes is dominated by influences from sources and sinks at the surface, i.e. biospheric or anthropogenic activity.

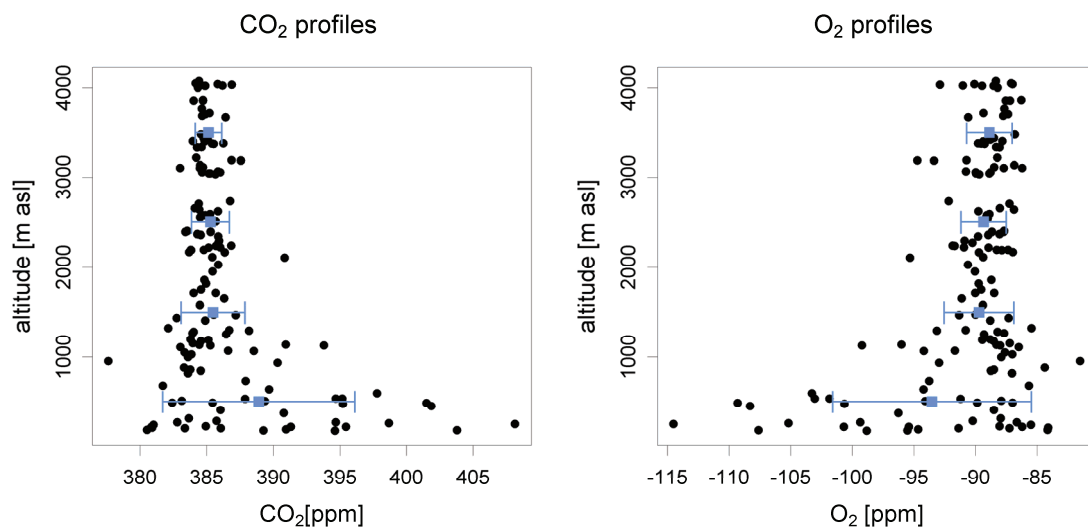


Figure 3.10: Altitude distribution of measured CO<sub>2</sub> and O<sub>2</sub> mole fractions (black dots). The blue lines indicate the mean and standard deviation for different altitude bins (each 1000m)

In addition to spatial variability in the source/sink patterns, CO<sub>2</sub> and O<sub>2</sub> also exhibit a diurnal cycle that is driven by the varying activity of the biosphere and by dynamics of the planetary boundary layer (PBL).

The PBL is defined as the lower part of the troposphere that is directly influenced by its contact with the earth's surface, responding to changes in surface forcings with a timescale of one hour or less.

As illustrated in Figure 3.11, the PBL height is changing in the course of the day: Whereas it is stable and shallow at night (stable boundary layer, SBL), it starts growing shortly after sunrise due to solar heating of the surface and the corresponding convective mixing. PBL growth continues until late afternoon, attaining a maximum height of typically 1-2km. In the evening, radiative cooling from the surface causes the mixing to decrease and the PBL to shrink again. Biospheric activity also exhibits a diurnal cycle with photosynthetic uptake of CO<sub>2</sub> and corresponding release of O<sub>2</sub> dominating during daytime and opposite effects caused by respiration during the night.

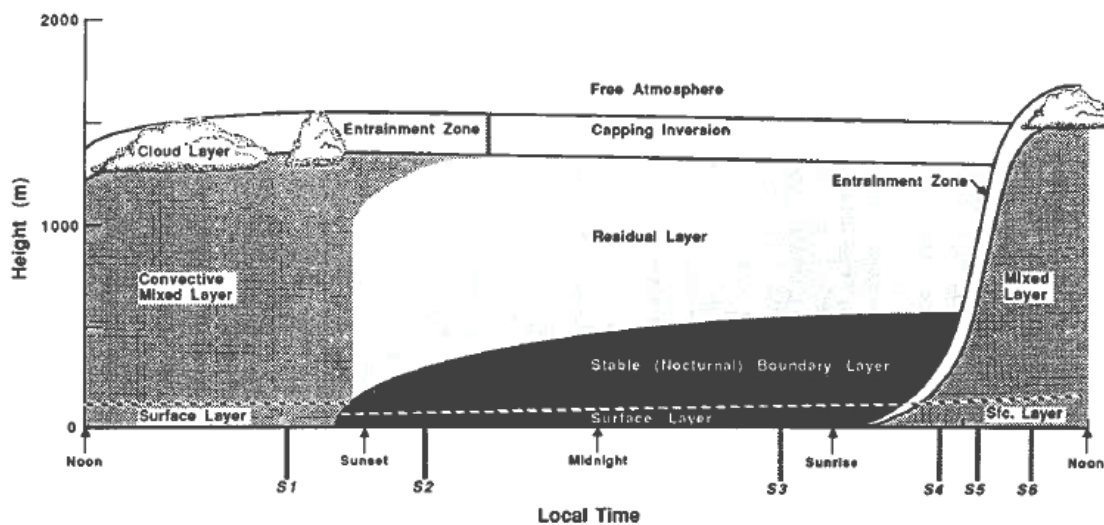


Figure 3.11: Diurnal variation in PBL height (figure from Stull (1988))

The combination of biospheric and PBL dynamics causes the observed variability. For example, when respiration causes CO<sub>2</sub> to build up during nighttime, the CO<sub>2</sub> is trapped within the SBL close to ground, but when the PBL starts rising in the morning, high CO<sub>2</sub> values are also observed at higher altitudes.

In contrast to those variations close to the ground, mixing ratios at higher altitudes, especially in the free atmosphere (see Figure 3.11), are expected to be more

representative for ‘background signals’ that include well-mixed air from a larger influence area.

This also has consequences for the oxidative ratio: Figure 3.12 shows O<sub>2</sub> versus CO<sub>2</sub> for different altitude ranges and the corresponding oxidative ratios. The oxidative ratio increases with increasing altitude and becomes significantly different from the biospheric value for altitudes above 2000m. This is in agreement with expectations: whereas the local signals are most likely dominated by biospheric processes, the background signal measured at higher altitudes contains also oceanic influence and is thus likely to have a higher oxidative ratio.

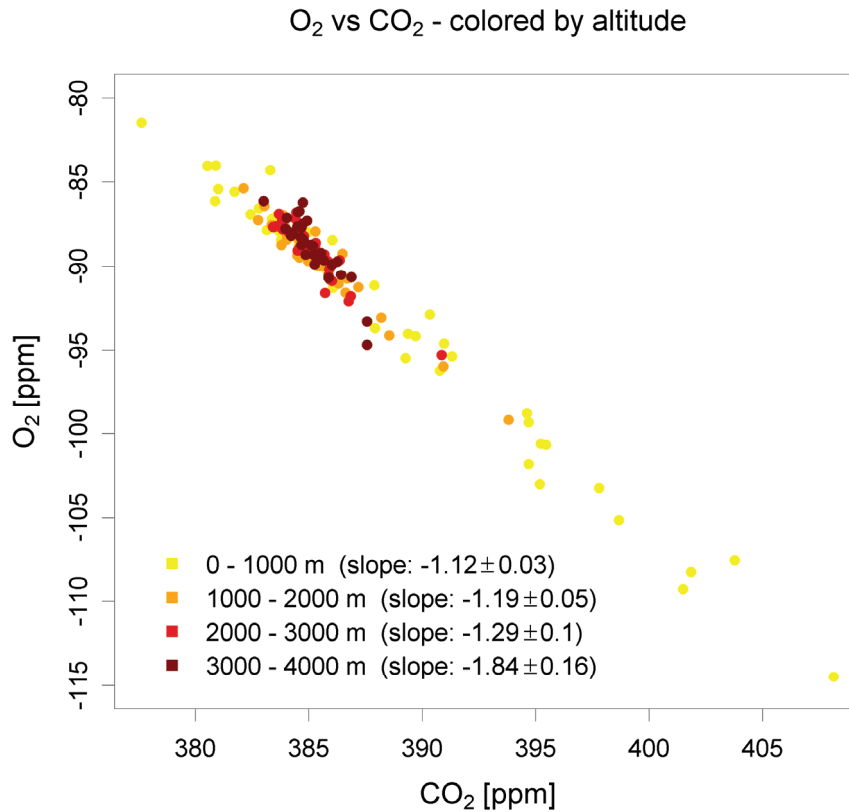


Figure 3.12: Altitude dependence of O<sub>2</sub>/CO<sub>2</sub> ratio. Slopes are determined for the different altitude bins shown in Figure 3.10.

To see whether differences in oxidative ratios can also be detected for samples taken within the PBL and above it, the PBL height was derived from the in-situ profiles of potential temperature, using the parcel method (Seibert et al. 2000).

The potential temperature  $\Theta$  was calculated from measured temperature  $T$  as

$$\Theta = T \left( \frac{p_0}{p} \right)^{\frac{R}{c_p}} \quad (3.4)$$

with  $p$  the ambient and  $p_0$  the surface pressure,  $R = 8.31 \text{ Jmol}^{-1}\text{K}^{-1}$  the gas constant and  $c_p = 29.07 \text{ mol}^{-1}\text{K}^{-1}$  the specific heat capacity at constant pressure.

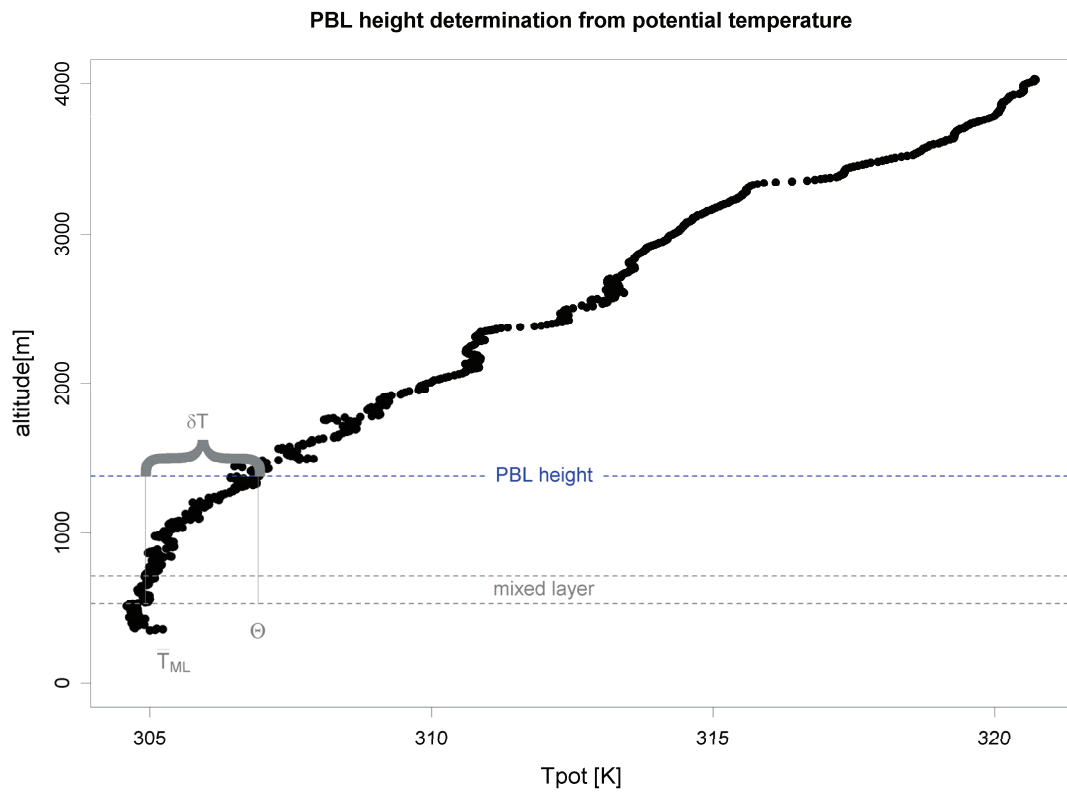


Figure 3.13: Determination of PBL height from profiles of measured potential temperature.

As illustrated in Figure 3.13 above, the boundary layer height is determined as the height where the potential temperature  $\Theta$  equals the mean potential temperature of the mixed layer  $T_{ML}$  plus an excess temperature  $\delta T$ :

$$\Theta = \text{mean}(T_{ML}) + \delta T \quad (3.5)$$

Here, the mixed layer is defined the altitude range with an ambient pressure between 930 and 950 mbar, and  $\delta T$  is chosen as 2K. The resulting boundary layer heights for profiles with flask sampling range from 720 to 1760 m, with a mean value of 1200m.

Figure 3.14 shows the distribution of CO<sub>2</sub> and O<sub>2</sub> values within and above the boundary layer. As expected, the variability is much higher within the PBL than in the free troposphere.

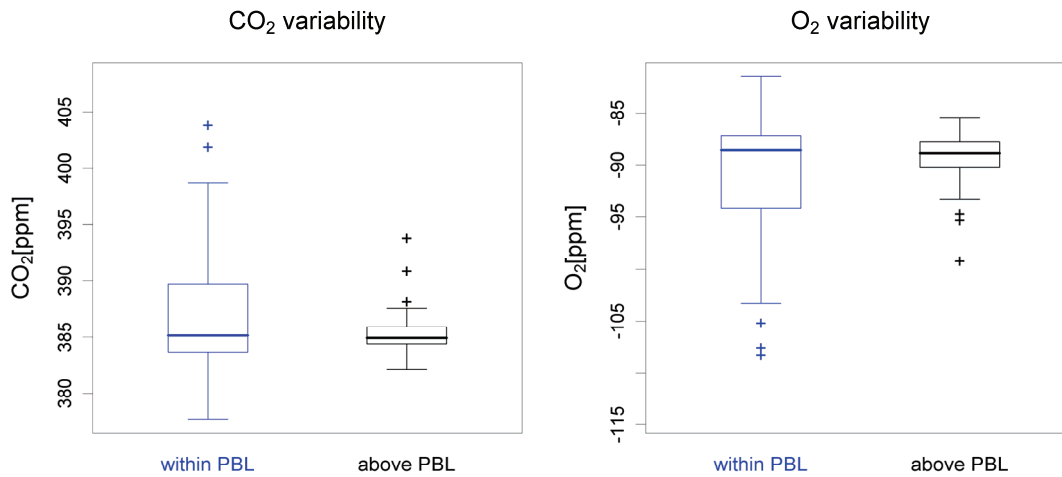


Figure 3.14: Variability of CO<sub>2</sub> and O<sub>2</sub> within and above PBL. In the box-and-whisker plots, the box covers the middle 50% of the data values, with the bottom and top representing the 25th and 75th percentile and the bold line the median. The whiskers extend to 1.5 times the interquartile range; the remaining extreme values are marked by crosses.

Comparison of the oxidative ratios derived from flasks taken within and above the boundary layer (Figure 3.15) shows they also differ: With  $1.31 \pm 0.06$ , the oxidative ratio in the free troposphere is significantly higher than that within the boundary layer ( $1.10 \pm 0.03$ ). The latter matches exactly the oxidative ratio for biospheric processes, showing that this is indeed the dominant influence in the Amazon Basin. However, in the following it is investigated whether other, more localized processes can also be detected in the data.



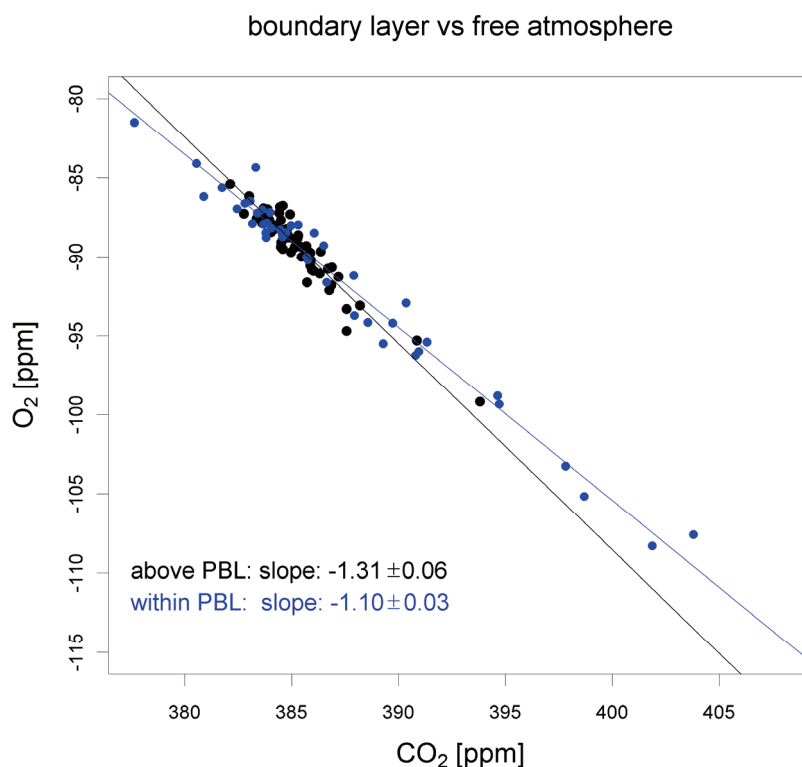


Figure 3.15 Oxidative ratios derived for samples taken within and above the boundary layer

### 3.3.2 Fossil fuel

Fossil fuel emissions in Brazil are for the most part caused by transportation (primarily using ethanol as fuel) and industry. As it can be seen in Figure 3.16a, high CO<sub>2</sub> emissions in the region covered by the BARCA flights occur mostly in the area around Manaus.

Figure 3.16b shows the spatial distribution of the oxidative ratio OR<sub>ff</sub> from fossil fuel burning, derived from the COFFEE dataset (see Chapter 2). Within the BARCA region, OR<sub>ff</sub> does not show much variation and has a value of 1.35 – 1.4. The fossil fuel signature in the atmospheric O<sub>2</sub>/CO<sub>2</sub> is thus significantly different from that of the biosphere. To investigate whether this can be detected in the measured signals, it was checked if the O<sub>2</sub>/CO<sub>2</sub> ratio derived from flasks taken in the Manaus area – which is expected to be influenced by fossil fuel combustion – differs from the other flasks.

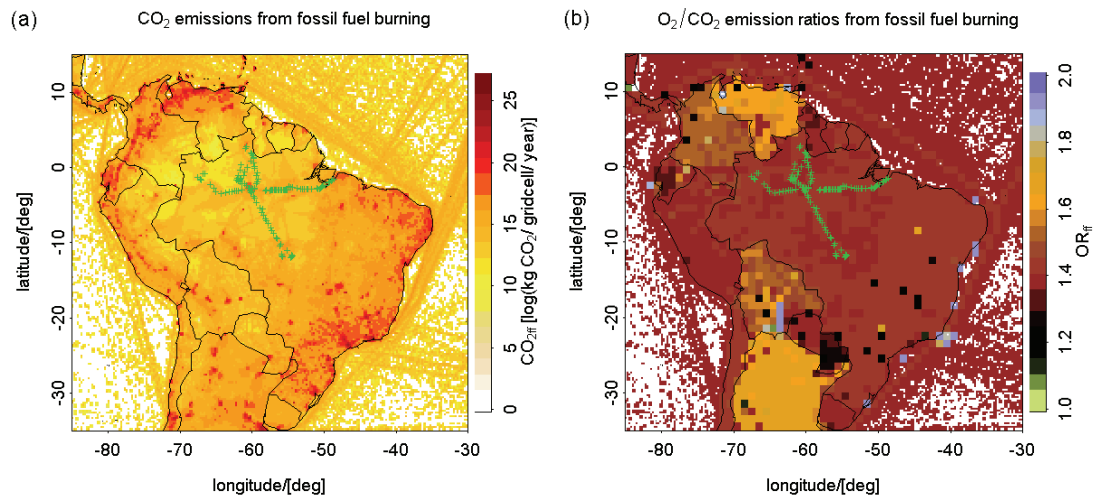


Figure 3.16 CO<sub>2</sub> emissions (a) and oxidative ratios (b) from fossil burning, with CO<sub>2</sub> emissions ( $0.1^\circ \times 0.1^\circ$  resolution) from EDGAR 4 (EC-JRC/PBL 2009) and oxidative ratios ( $1^\circ \times 1^\circ$  resolution) from the COFFEE dataset (see Chapter 2). Green crosses indicate locations of flask sampling.

As the aircraft was based in Manaus, almost all flights started and ended there, allowing for a larger number of samples. For the following analysis, only samples taken within the PBL are used, as a local fossil fuel influence is not likely to extend into the free troposphere. This limits the sample size to 9 flasks, most of them taken either in the early morning (start of the flight) or in the evening (end of the flight)..

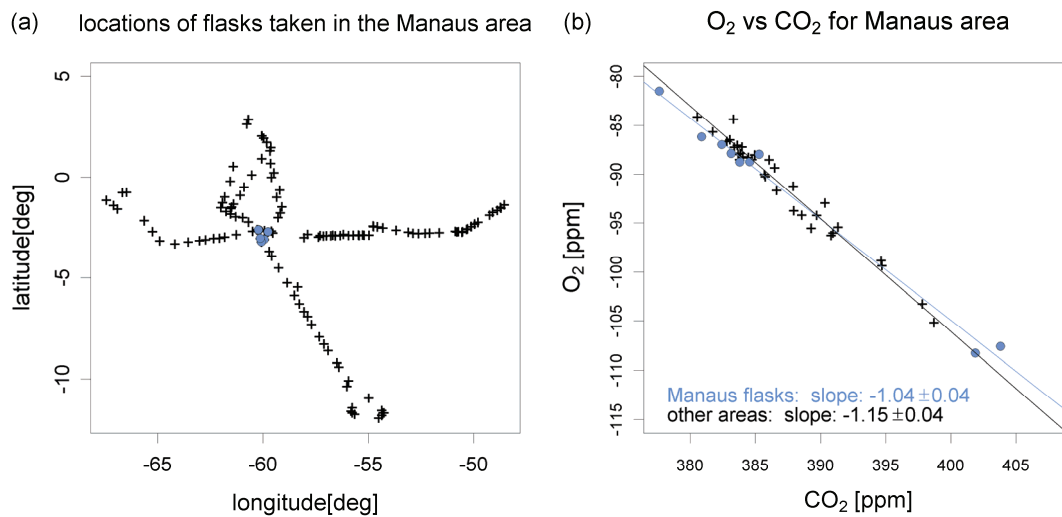


Figure 3.17: Locations of flasks taken in the Manaus area (a) and O<sub>2</sub> vs CO<sub>2</sub> regressions for selected flasks (b).

Figure 3.17a shows their sampling locations and Figure 3.17b the regression of O<sub>2</sub> versus CO<sub>2</sub>. The slope of the fit gives an oxidative ratio of  $OR_M = 1.04 \pm 0.04$  for the flasks in the Manaus area, while the OR for all other flasks sampled within in the PBL is  $1.15 \pm 0.04$ . Contrary to expectation,  $OR_M$  is closer to 1 than the rest of the samples

However, not all flasks taken in the Manaus area are necessary polluted. The high CO<sub>2</sub> values of samples taken in morning hours in particular might as well be caused by nighttime respiration (see Section 3.3.1). A useful tracer for detecting fossil fuel influence in the samples is CO, since any combustion process also causes CO emissions. For fossil fuel burning in the Manaus region, EDGAR 3.2 emission data (Olivier and Berdowski 2001) gives a ratio of  $CO/CO_2 = 5.2\%$ , thus a CO enhancement of 52ppb corresponds to a 1ppm enhancement of CO<sub>2</sub>.

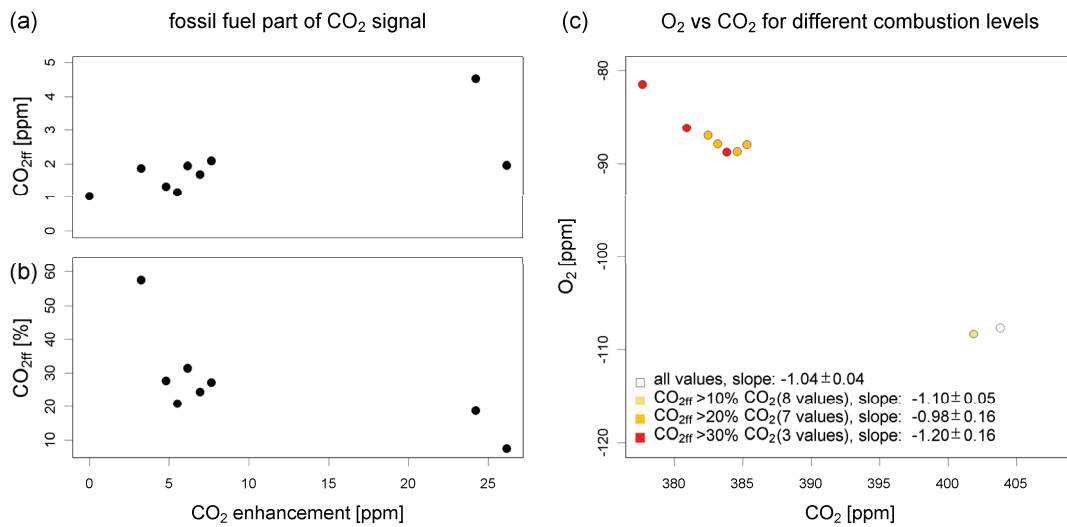


Figure 3.18: fossil fuel part of CO<sub>2</sub> concentrations in the Manaus flasks and its influence on oxidative ratio: Plot (a) shows the CO<sub>2</sub> fossil fuel signal, derived from the CO concentration of the flasks, with  $CO_{2ff} [ppm] = (CO [ppb] - CO_{bg} [ppb]) / 52 ppb$ , while plot (b) shows CO<sub>2ff</sub> as a percentage of the total CO<sub>2</sub> enhancement  $CO_2 - CO_{2bg}$ . Background values  $CO_{bg}$  and  $CO_{2bg}$  were defined as the minimum of the Manaus flasks, being 81 ppb for CO and 377.6 ppm for CO<sub>2</sub>.

This fact is used in Figure 3.18 to calculate the fossil fuel part of the CO<sub>2</sub> signal: Figure 3.18a shows the CO<sub>2</sub> fossil fuel signal derived from the CO enhancement in the Manaus flasks, ranging from 1 to 4.5 ppm. As seen Figure 3.18b, this corresponds

to 7 – 58 % of the total CO<sub>2</sub> enhancement, thus maximal oxidative ratios of  $1.4 \cdot 0.58 + 1.1 \cdot (1 - 0.58) = 1.28$  can be expected from these samples. Figure 3.18 a and b also illustrate that the highest CO<sub>2</sub> values do not necessarily correspond to the highest fossil fuel signals. In Figure 3.18c, O<sub>2</sub> is fitted against CO<sub>2</sub> for different levels of fossil fuel content in the signal of the Manaus samples. The resulting oxidative ratios show indeed a tendency to get closer to 1.4 for higher levels of fossil fuel influence. However these differences are not significant as with the decreasing number of flasks used for the fit the error of the slope increases also. A definite detection of fossil fuel influence is thus not possible under these conditions.

### 3.3.3 Biomass burning

CO is not only a tracer for fossil fuel combustion, but also for biomass burning. To identify samples whose composition might be affected by biomass burning, the CO in-situ data (shown in Figure 3.19) was used. Due to the higher spatial resolution, it gives a better indication of areas affected by biomass burning than the flask samples alone. Figure 3.19 shows the flight tracks for BARCA-A, colored by the in-situ CO concentration. The grey patterns indicate CO emissions from biomass burning integrated for the BARCA-A period. These are based on fire locations from satellite based inventories (MODIS (<http://modis-fire.umd.edu>), GOES WF ABBA (<http://cimss.ssec.wisc.edu/goes/burn/wfabba.html>), and CO emission size calculated based the amount of biomass burnt as well as vegetation-specific emission and combustion factors (Freitas et al. 2005; Longo et al. 2007). Red arrows indicate locations of flask sampling in biomass burning areas (identified by the CO emission map or by the log file of the operator onboard the aircraft).

A subset of 17 flask samples was selected for further analysis. A sample was chosen as presumably influenced by biomass burning if it was taken in the biomass burning areas specified above and the corresponding in-situ CO concentrations was higher than 200ppb. These selected flasks are marked as blue dots in Figure 3.20, whereas black crosses indicate the remaining flasks for comparison. Figure 3.20a shows sampling locations of the flasks and Figure 3.20b the altitude distribution of their CO concentrations.

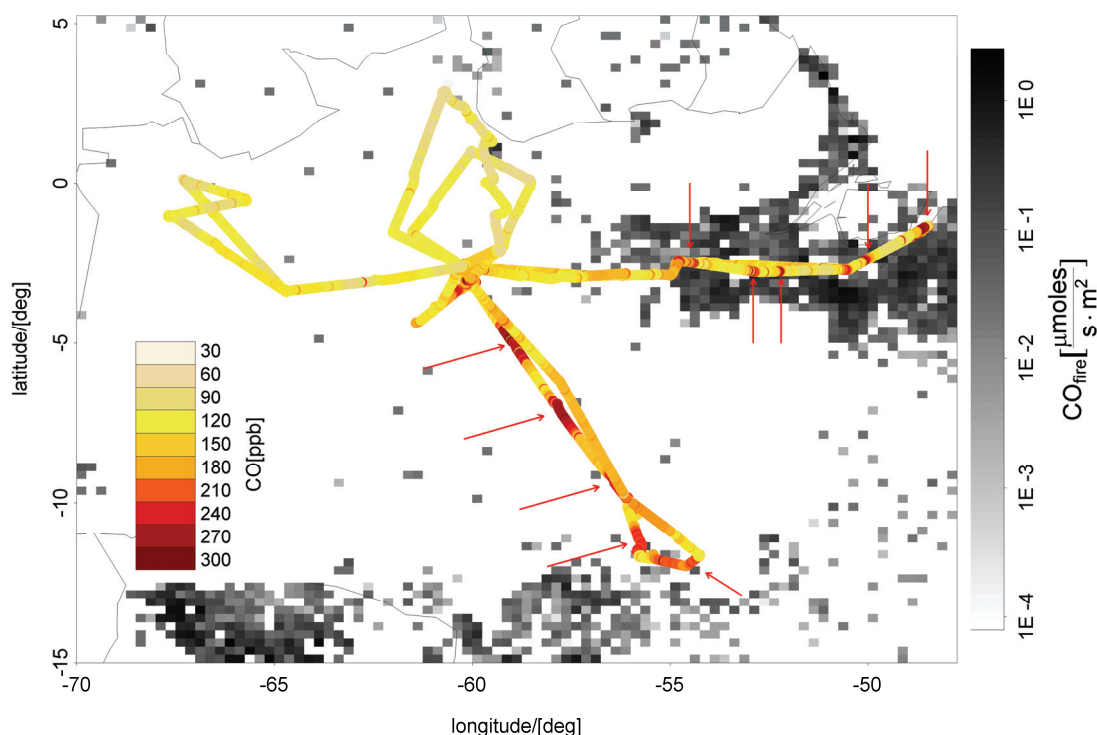


Figure 3.19: Spatial distribution of measured CO concentrations. The colored points show the in-situ data, black crosses indicate locations where flask samples are taken. The red errors mark areas presumably influenced by biomass burning.

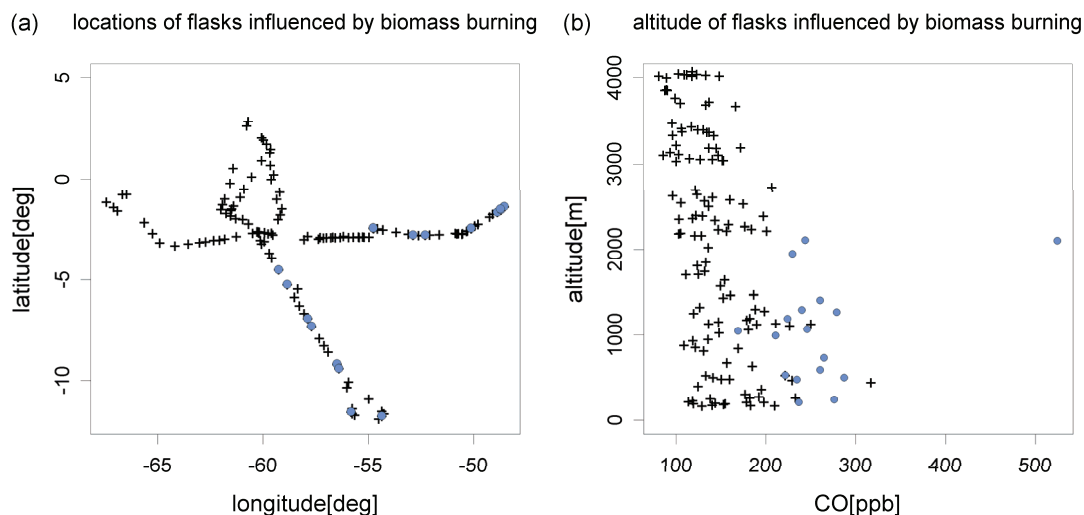


Figure 3.20: Locations (a), altitude and CO distribution (b) for flasks presumably influenced by biomass burning (blue dots). For comparison, black crosses indicate values for the remaining flasks.

It can be seen that most of the higher CO values in the samples are caused from biomass burning. The remaining high CO values at lower altitudes result from fossil fuel burning in the Manaus area (see Figure 3.19). Figure 3.20b shows a higher CO variability at lower altitudes, but the difference between low and high altitudes is not as strong as for CO<sub>2</sub> and O<sub>2</sub> (see Figure 3.10 or comparison). One reason for this is that signals from biomass burning are not limited to the PBL; instead plumes can rise up to ~3km in altitude (Crutzen and Andreae 1990). The other reason is related to atmospheric transport: During the dry season, convection in Central Amazonia is more likely to occur in the afternoon (Angelis and McGregor 2004). Therefore, nocturnal signals do not get lifted into the upper atmosphere. As described in Section 3.3.1, nighttime respiration causes high CO<sub>2</sub> and low O<sub>2</sub> signals inside the boundary layer that are thus not transported to the free troposphere. As such nighttime accumulation does not exist for CO, the altitude gradients are significantly smaller.

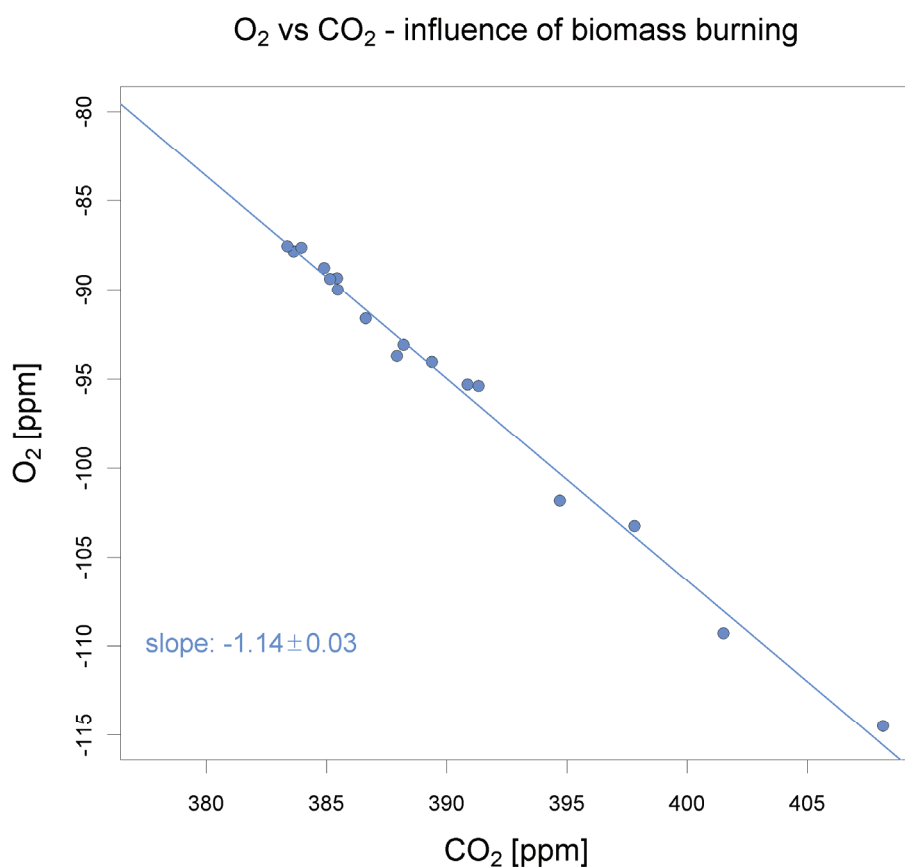


Figure 3.21: O<sub>2</sub> versus CO<sub>2</sub> regression of flasks influenced by biomass burning.

The oxidative ratio for the selected flasks is derived in Figure 3.21 above. With  $1.14 \pm 0.03$ , the result is consistent with the commonly used ratio for biomass burning (1.11) and thus not distinguishable from that for biospheric processes.

The ratio of 1.11 corresponds to the typical biomass burning process where CO emissions account for  $\sim 10\%$  of CO<sub>2</sub> emissions (Crutzen and Andreae 1990). However, depending on the type of fire, the combustion process might be less complete and the CO/CO<sub>2</sub> emission ratio might go up to  $\sim 30\%$ . For these cases, oxidative ratios up to 1.41 have been observed (Lueker and Keeling 2001). Figure 3.22a shows the distribution of CO/CO<sub>2</sub> enhancement. Again, enhancement is defined as the difference to a background value for CO or CO<sub>2</sub>. Since the sampling locations of the flasks show a larger spatial variation, no constant background value as in Section 3.3.2 was used. Instead, separate background values were derived for each profile from the CO and CO<sub>2</sub> in-situ data at an altitude level of around 4000m.

Finding correlations of changes in the oxidative ratio with CO/CO<sub>2</sub> ratios is difficult for the small number of samples; hence only two separate regressions were performed (Figure 3.22b).

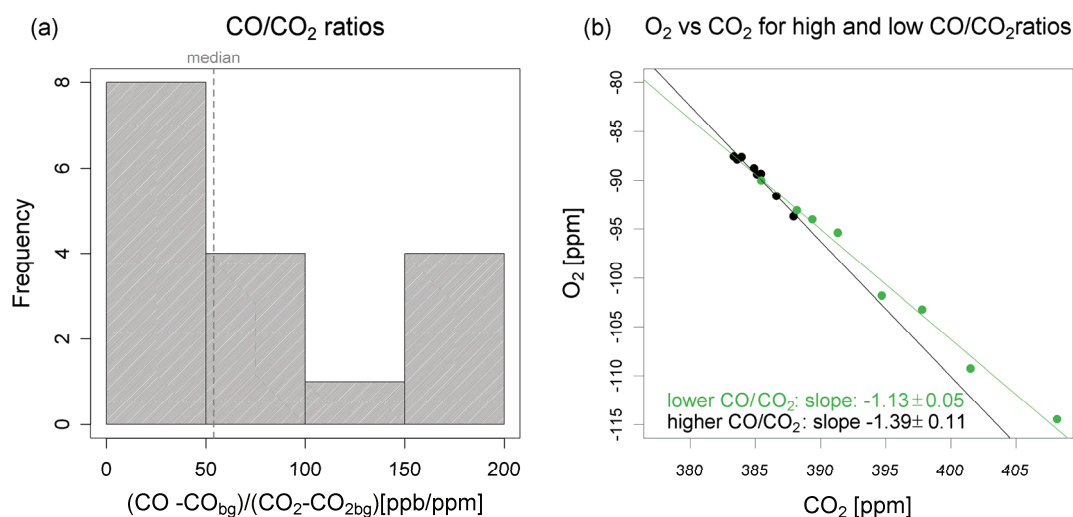


Figure 3.22: Histogram of CO/CO<sub>2</sub> ratios of flasks influenced by biomass burning (a) and O<sub>2</sub> vs CO<sub>2</sub> regressions for the upper and lower half of the distribution (b). The grey line in plot (a) indicates the median of the distribution.

For the lower half of the distribution (i.e. the samples whose CO/CO<sub>2</sub> ratios are smaller than the median CO/CO<sub>2</sub> ratio, see dotted vertical line in Figure 3.22a) an OR of  $1.13 \pm 0.05$  was derived, thus being close to the typical biomass burning OR. For the upper half of the distribution (i.e. CO/CO<sub>2</sub> ratios higher than their median), the OR is expected to be higher. Indeed, the regression results in an OR of  $1.39 \pm 0.11$ .

Although the oxidative ratios for high and low CO/CO<sub>2</sub> ratios are significantly different, one needs to take care in interpreting this result because the CO<sub>2</sub> enhancement is usually not only caused by biomass burning, but also strongly influenced by biospheric activity. Section 3.3.2 already showed that high CO<sub>2</sub> signals are not necessarily related to combustion processes. Another issue is related to the details of vertical transport: the CO/CO<sub>2</sub> correlation in CO and CO<sub>2</sub> enhancements near the emission are not necessarily preserved when convectively lifted to higher altitudes, so the detection as differences between the measured (fire-influenced) signals and a background might be problematic. For a more robust analysis of the impact from the type of burning process on the oxidative ratio, it would be best to look at in-situ data for each fire event separately and to compare the CO/CO<sub>2</sub> ratios with oxidative ratios for this event. However, this would imply separate regressions (both for CO/CO<sub>2</sub> and O<sub>2</sub>/CO<sub>2</sub>) for each event. This is only possible with a higher sampling density, thus requiring continuous measurements of all tracers.

### 3.4 Conclusion

In this chapter, oxidative ratios from flask samples taken during the BARCA aircraft campaign in the Brazilian Amazon basin were studied and the feasibility of using such ratios to separate different processes was investigated.

Oxidative ratios were determined from orthogonal distance regression of the O<sub>2</sub> versus CO<sub>2</sub> mole fraction of the flask samples. With a value of  $1.15 \pm 0.02$ , the oxidative ratio derived from all samples is dominated by biospheric signals, but indicates also influence from other processes with higher oxidative ratios. These contributions have been identified as being mainly related to atmosphere-ocean-exchange, influencing the composition of samples taken in higher altitudes.



Determination of oxidative ratios for different altitude levels showed significantly higher values at higher altitude, as well as significant difference of OR derived from samples taken within the planetary boundary layer (PBL) and above. Apart from the lower oxidative ratio, CO<sub>2</sub> and O<sub>2</sub> mole fractions of flasks sampled within the PBL also show a larger variability, corresponding to the strong influence of surface sources and sinks. With an oxidative ratio of  $1.10 \pm 0.03$  for the samples within the PBL, these influences are mainly biospheric. However, it was further investigated whether other types of local influence, i.e. fossil fuel combustion or biomass burning could be identified locally.

Emission maps for the flight area show that significant fossil fuel emissions are mostly likely to be observed in the Manaus region. The Brazilian oxidative ratio for fossil fuel combustion is  $\sim 1.4$  and thus significantly different from the biospheric ratio of 1.1. However, samples in the Manaus area do not show enhanced oxidative ratios. This can be explained by the fact that the fossil fuel part of the measured CO<sub>2</sub> signals, as derived from the corresponding CO concentrations, is only in the range of 7 to 58% of the total CO<sub>2</sub> enhancement. Oxidative ratios of these samples are thus expected to increase to maximum values of 1.28. Comparing the oxidative ratios of samples with lower and higher fossil fuel contribution shows increases in the mean oxidative ratio for higher fossil fuel contribution, up to a maximum value of  $1.20 \pm 0.16$  for a fossil fuel contribution  $>30\%$ . However, differences between the oxidative ratios of these subsamples are not significant due to larger uncertainties in the slope of the regression associated with the small number of samples.

Flask samples influenced by biomass burning are identified by their locations close to fire locations from biomass burning inventories, together with high CO concentration of the corresponding in-situ data. With a value of  $1.14 \pm 0.03$ , their oxidative ratio corresponds to typical ratios for biomass burning, but can not be distinguished from that of biospheric processes. However, oxidative ratios for biomass burning events vary depending on the type of combustion process; thus events with higher CO/CO<sub>2</sub> ratios are expected to also show higher oxidative ratios. This relation was investigated by comparing the oxidative ratios of samples with low and high CO/CO<sub>2</sub>. Indeed, the

samples with high CO/CO<sub>2</sub> ratios show a significantly higher OR ( $1.39 \pm 0.11$ ) than those with lower CO/CO<sub>2</sub> ratios ( $1.13 \pm 0.05$ ). However, it is not completely evident whether this difference is really caused by the dissimilar combustion processes, since the measured CO<sub>2</sub> signatures can also be influenced by other effects (biospheric activity, atmospheric transport). A definite correlation between fire types and oxidative ratios could only be derived on an event-based analysis with continuous measurements of all tracers.

To summarize, O<sub>2</sub>/CO<sub>2</sub> ratios from the BARCA flask samples could indeed be used to some extent for the separation of different processes. However, whereas it worked quite well to separate background signals from local influences, the significant detection of contributions from different surface processes was limited by the low sampling density. To identify these signatures robustly, continuous measurements of both O<sub>2</sub> and CO<sub>2</sub> are inevitably required. The example of biomass burning detection clearly showed that CO<sub>2</sub> and CO in-situ data provide much better constraints than the flask data alone due to their higher spatial and temporal resolution.

### 3.5 References

- Achard, F., H. D. Eva, H. J. Stibig, P. Mayaux, J. Gallego, T. Richards and J. P. Malingreau (2002). "Determination of deforestation rates of the world's humid tropical forests." *Science* **297**(5583): 999-1002.
- Angelis, C. F. and G. R. McGregor (2004). "Diurnal cycle of rainfall over the Brazilian Amazon." *Climate Research* **26**(2): 139-149.
- Battle, M., M. Bender, M. B. Hendricks, D. T. Ho, R. Mika, G. McKinley, S.-M. Fan, T. Blaine and R. F. Keeling (2003). "Measurements and models of the atmospheric Ar/N<sub>2</sub> ratio." *Geophysical Research Letters* **30**(15): 1786, doi:10.1029/2003GL017411.
- Brand, W. A. (2003). O<sub>2</sub>/N<sub>2</sub> Storage Aspects and Open Split Mass Spectrometric Determination. Report of the 12th WMO/IAEA Meeting of Experts on Carbon Dioxide Concentration and Related Tracer Measurement Techniques (GAW Report 161, WMO TD No.1275). D. Worthy and L. Huang. Toronto, Canada (15-18. September 2003), WORLD METEOROLOGICAL ORGANIZATION/ GLOBAL ATMOSPHERE WATCH: 274p.
- Cassar, N., G. A. McKinley, M. L. Bender, R. Mika and M. Battle (2008). "An improved comparison of atmospheric Ar/N-2 time series and paired ocean-atmosphere model predictions." *Journal of Geophysical Research-Atmospheres* **113**(D21).

- Crutzen, P. and M. O. Andreae (1990). "Biomass burning in the tropics - Impact on atmospheric chemistry and biogeochemical cycles." Science **250**(4988): 1669-1678.
- EC-JRC/PBL. (2009). "Emission Database for Global Atmospheric Research (EDGAR), release version 4.0. ." European Commission, Joint Research Centre (JRC)/Netherlands Environmental Assessment Agency (PBL). . from <http://edgar.jrc.ec.europa.eu>.
- FAO (1993). Third interim report on the state of tropical forests, Food and Agriculture Organization, Rome.
- Freitas, S. R., K. M. Longo, M. Diasb, P. L. S. Diasb, R. Chatfield, E. Prins, P. Artaxo, G. A. Grell and F. S. Recuero (2005). "Monitoring the transport of biomass burning emissions in South America." Environmental Fluid Mechanics **5**(1-2): 135-167.
- Grace, J., J. Lloyd, J. McIntyre, A. C. Miranda, P. Meir, H. S. Miranda, C. Nobre, J. Moncrieff, J. Massheder, Y. Malhi, I. Wright and J. Gash (1995). "Carbon-Dioxide Uptake by an Undisturbed Tropical Rain-Forest in Southwest Amazonia, 1992 to 1993." Science **270**(5237): 778-780.
- Houghton, R. A., D. L. Skole, C. A. Nobre, J. L. Hackler, K. T. Lawrence and W. H. Chomentowski (2000). "Annual fluxes of carbon from deforestation and regrowth in the Brazilian Amazon." Nature **403**(6767): 301-304.
- Jordan, A. and W. A. Brand (2003). Trace gas measurement and quality assurance at the MPI for Biogeochemistry. Report of the 11th WMO/IAEA Meeting of Experts on Carbon Dioxide Concentration and Related Tracer Measurement Techniques (GAW Report 148, WMO TD No 1138). S. Toru and S. Kazuto. (Tokyo, Japan, 25 – 28 September 2001), WORLD METEOROLOGICAL ORGANIZATION/ GLOBAL ATMOSPHERE WATCH: 170p.
- Keeling, R. F. (1988). Development of an interferometric analyzer for precise measurements of the atmospheric oxygen mole fraction. Cambridge, Massachusetts, Harvard University. **PhD thesis**: 178p.
- Keeling, R. F., T. Blaine, B. Paplawsky, L. Katz, C. Atwood and T. Brockwell (2004). "Measurement of changes in atmospheric Ar/N<sub>2</sub> ratio using a rapid-switching, single-capillary mass spectrometer system." Tellus Series B-Chemical and Physical Meteorology **56**(4): 322-338.
- Keeling, R. F. and J. Severinghaus (2000). Atmospheric oxygen measurements and the carbon cycle. The Carbon Cycle. T. M. L. Wigley and D. S. Schimel. Cambridge, Cambridge University Press: 134-140.
- Langenfelds, R. L., M. V. van der Schoot, R. J. Francey, L. P. Steele, M. Schmidt and H. Mukai (2005). "Modification of air standard composition by diffusive and surface processes." Journal of Geophysical Research - Atmospheres **110**: D13307, doi:10.1029/2004JD005482.
- Longo, K. M., S. R. Freitas, A. Setzer, E. Prins, P. Artaxo and M. O. Andreae (2007). "The Coupled Aerosol and Tracer Transport model to the Brazilian developments on the Regional Atmospheric Modeling System (CATT-BRAMS) – Part 2: Model sensitivity to the biomass burning inventories." Atmospheric Chemistry and Physics Discussions **7**: 8571-8595.

- Lueker, T. and R. F. Keeling (2001). "The Oxygen to Carbon Dioxide Ratios observed in Emissions from a Wildfire in Northern California." Geophysical Research Letters **28**(12): 2413-2416.
- Malhi, Y. and J. Grace (2000). "Tropical forests and atmospheric carbon dioxide." Trends in Ecology & Evolution **15**(8): 332-337.
- Malhi, Y., J. T. Roberts, R. A. Betts, T. J. Killeen, W. H. Li and C. A. Nobre (2008). "Climate change, deforestation, and the fate of the Amazon." Science **319**(5860): 169-172.
- Melillo, J. M., A. D. McGuire, D. W. Kicklighter, B. I. Moore, C. J. Vorosmarty and A. L. Schloss (1993). "Global climate change and terrestrial net primary production." Nature **363**: 234-240.
- Nepstad, D. C., C. M. Stickler and O. T. Almeida (2006). "Globalization of the Amazon soy and beef industries: Opportunities for conservation." Conservation Biology **20**(6): 1595-1603.
- Prentice, I. C., G. D. Farquhar, M. J. R. Fasham, M. L. Goulden, M. Heimann, V. J. Jaramillo, H. S. Keshgi, C. L. Quéré, R. J. Scholes and D. W. R. Wallace (2001). The carbon cycle and atmospheric carbon dioxide In: Climate Change 2001: The Scientific Basis: Contribution of Working Group I to the Third Assessment Report of the Intergovernmental Panel on Climate Change. J. T. Houghton, Cambridge Univ. Press, New York: 881 pp.
- Seibert, P., F. Beyrich, S. E. Gryning, S. Joffre, A. Rasmussen and P. Tercier (2000). "Review and intercomparison of operational methods for the determination of the mixing height." Atmospheric Environment **34**(7): 1001-1027.
- Severinghaus, J. P. (1995). Studies of terrestrial O<sub>2</sub> and Carbon Cycles in Sand Dune Gases and in Biosphere 2. New York, Columbia University. **PhD thesis**: 148p.
- Soares, B. S., D. C. Nepstad, L. M. Curran, G. C. Cerqueira, R. A. Garcia, C. A. Ramos, E. Voll, A. McDonald, P. Lefebvre and P. Schlesinger (2006). "Modelling conservation in the Amazon basin." Nature **440**(7083): 520-523.
- Stull, R. B. (1988). An Introduction to Boundary Layer Meteorology, Kluwer Academic, Dordrecht

# Chapter 4

## Development of an instrument for airborne in-situ measurements of atmospheric O<sub>2</sub>/N<sub>2</sub>

Chapter 3 has stated the need for in-situ measurements onboard aircraft that are currently limited by the availability of suitable instruments. In this chapter, the development of an in-situ instrument for airborne measurements of atmospheric oxygen is described. The ICON (In-situ Capability for O<sub>2</sub>/N<sub>2</sub> measurements) is intended for use onboard small research aircraft, with small dimensions, low weight, robustness in operation, and full automation of the measurement.

### 4.1 Motivation

Airborne measurements have been introduced in the previous chapters as an important complement to the network of surface stations. Despite the advances in measurement techniques during the last decades, airborne O<sub>2</sub>/N<sub>2</sub> measurements are still mostly limited to flask sampling. As shown in Chapter 3 for the case of the BARCA campaign, the low temporal and spatial resolution of flask data makes it difficult to use it for separating different processes. Continuous measurements of O<sub>2</sub>/N<sub>2</sub> in combination with other trace gases have the potential to provide much better constraints on atmospheric transport and mixing processes that act on the different source and sink components.

The possibility for in-situ measurements of oxygen onboard aircraft is mainly restricted by the availability of suitable instruments: Unlike for CO<sub>2</sub> measurements, no commercially available instruments exist that can be used ‘off the shelf’ to measure atmospheric O<sub>2</sub> with the required precision. As described in Section 1.4.1, over the last two decades several techniques for O<sub>2</sub> measurements have been developed, most of them based on modifications of commercial instruments. However, the majority of these instruments is not suitable for airborne measurements, especially onboard small research aircraft: Mass spectrometers, gas chromatographs and interferometers are too large and heavy for use in the field, the electrochemical

method suffers from a slow response (see Section 4.5.1) and paramagnetic analyzers are highly motion sensitive. The VUV (vacuum ultraviolet) absorption technique, on the other hand, has already been used onboard aircraft (Stephens 2009), showing measurement precision of  $\pm 2$  per meg for 5s intervals.

Thus the obvious choice was to use VUV absorption for the development of a new airborne instrument. For this technique no commercial instruments exist, so all components have to be designed and custom built. Although the basic idea and the choice of several key components are based on the instrument of B. Stephens (Stephens 1999; Stephens et al. 2003), the instrument developed here has a completely different design, especially adapted for the requirements onboard small research aircraft.

## 4.2 Measurement principle

Vacuum ultraviolet (VUV) radiation denotes the range of the ultraviolet spectra that is absorbed by the oxygen in the air and thus can only be observed in a vacuum, ranging from roughly 5 to 190 nm. For the ICON instrument, the absorption of VUV radiation passing through a flowing air stream is measured and used to calculate the oxygen content of the sample air. As a light source, a commercially available xenon lamp (Opthos) is used, powered by a 15W/180MHz radio frequency (RF) oscillator (LCF Enterprises). This light source has its main emission line at 147 nm and a weaker line at 129.5nm. The emission spectrum is shown in Figure 4.1, together with the absorption cross-section for O<sub>2</sub> for the Schumann-Runge continuum.

For the 147nm line, O<sub>2</sub> is the primary atmospheric absorber. Thus variations in absorption of this line are related to the O<sub>2</sub> mole fraction  $X_{O_2}$  via the Beer-Lambert law

$$I = I_0 \exp\{-OD\} \quad (4.1)$$

with  $I$  being the transmitted (=measured) light intensity,  $I_0$  the intensity emitted by the lamp and  $OD$  the optical density, determined as

$$OD = k \cdot l \cdot p \cdot T_0 / T \cdot X_{O_2} \quad (4.2)$$

with  $k$  the absorption coefficient of  $O_2$  at a pressure of 1013mbar,  $l$  the path length,  $p$  the air pressure,  $T$  the air temperature and  $T_0 = 273.15$  K. Equation 4.1 can also be expressed in differential form as

$$\frac{\Delta I}{I} = -OD \frac{\Delta X_{O_2}}{X_{O_2}} \quad (4.3)$$

To achieve the desired instrument sensitivity, it is necessary to work with optically thick conditions. Nevertheless one needs to optimize between high sensitivity (resulting in lower detector currents) and the size of the signal. Measured currents for this application are in the range of  $\sim 100$  nA, requiring detection of levels  $\sim 100$  fA for ppm precision. Shot noise, due to statistical uncertainty associated with counting a limited number of electrons, and Johnson noise, resulting from random thermal motion in the resistor used for signal amplification (see 4.3.2), can both be significant at these levels (Jenkins 1987).

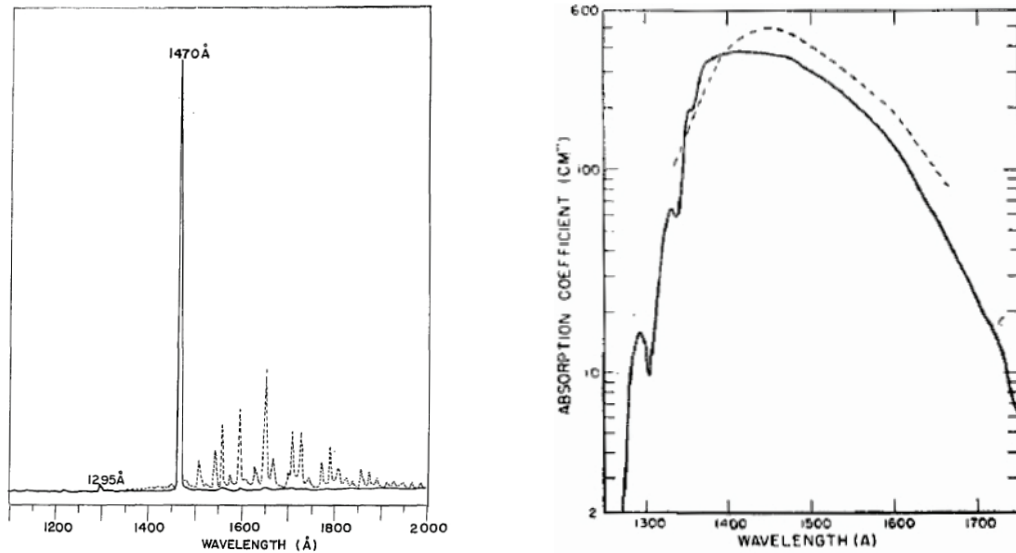


Figure 4.1: Xenon emission lines (left, from (Okabe 1964)) and absorption cross section for  $O_2$  (right, from (Watanabe et al. 1953)). In the emission spectrum, only the solid lines represent Xe lines, the dashed lines represent water impurities in the lamp. In the right plot, the solid curve indicate measurements from (Watanabe et al. 1953), while the dashed lines represent earlier results from (Ladenburg and Van Voorhis 1933).

The optimum of optical density is determined by the optimal signal to noise ratio  $SN$ . As derived in Appendix 2,

$$SN \propto -OD \cdot \exp\{-OD/2\} \quad (4.4)$$

has a maximum for  $OD=2$ , corresponding to absorption of 86% of the emitted light intensity. Following Equation 4.3, a change of 1 ppm in the O<sub>2</sub> mole fraction thus causes a 2ppm change in the measured light intensity. Equation 4.3 also indicates that the response of the instrument to small changes in  $X_{O_2}$  will be linear. For O<sub>2</sub> absorption at 147 nm, deviations from linearity over the natural range of variability are expected to be less than 0.1 per meg and thus negligible. However, there might be influence from the second emission line at 129.5nm.

As it can be seen in Figure 4.1, the intensity of the 129.5nm line is much smaller than that of the 147nm line. Okabe (1964) gives its intensity as ~2% of the 147nm line. However, since the absorption coefficient at 129.5nm is much lower than at 147nm ( $k_{129.5} \sim 20 \text{ atm}^{-1} \text{ cm}^{-1}$ ,  $k_{147} = 320 \text{ atm}^{-1} \text{ cm}^{-1}$ ), the use of both emission lines leads to a lower signal to noise ratio and lower sensitivity. This is illustrated in Figure 4.2, using the formulas derived in Appendix 2 for the signal to noise ratio and the effective optical density.

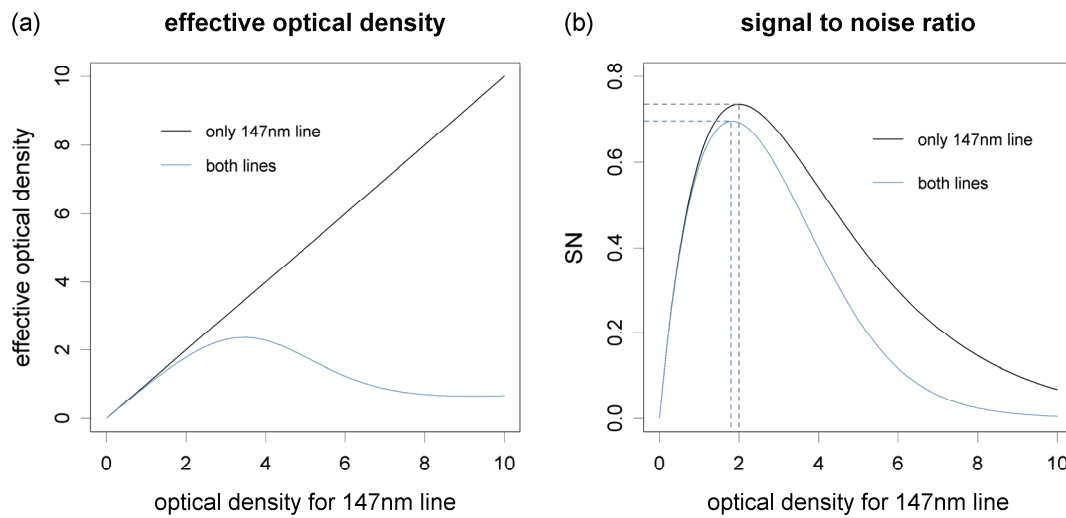


Figure 4.2: Effective optical density (a) and signal to noise ratio (b) for both emission lines (blue) and 147nm line only (black)



The maximum signal to noise ratio for both lines is ~6% lower than that for the 147nm line alone. Another problem that due to the low absorption of the 129.5nm line, more light arrives at the detector. Since the phototubes used here have critical currents around 1μA, the intensity needs to be limited anyway when using both lines. Hence it seems reasonable to remove the second line using suitable filters or windows.

Another problem can arise from potential interference effects due to absorption by CO<sub>2</sub> or water vapor in VUV region (see Figure 4.3).

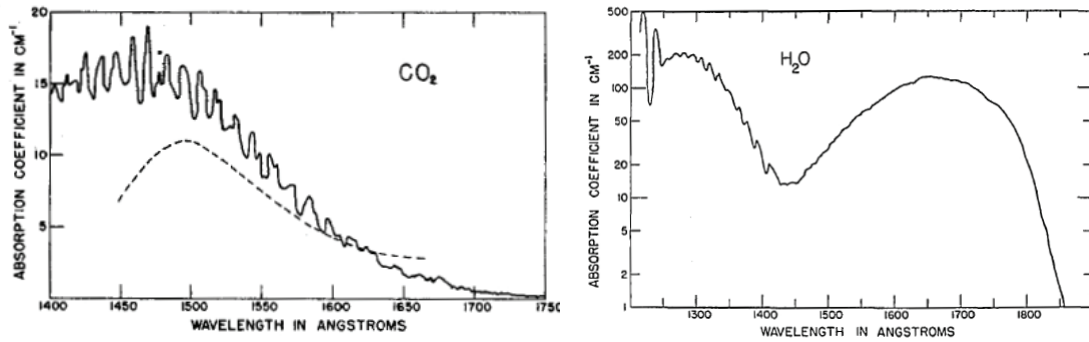


Figure 4.3 Absorption coefficients of CO<sub>2</sub> (left, figure from (Inn et al. 1953) ) and H<sub>2</sub>O (right, figure from (Watanabe and Zelikoff 1953)) in the VUV range

H<sub>2</sub>O interference is avoided by drying the sample air (which needs to be done anyway to avoid dilution and fractionation effects). CO<sub>2</sub> interference needs to be taken into account, since the CO<sub>2</sub> absorption coefficient at 147 nm is ~5% of the O<sub>2</sub> absorption coefficient ((Inn et al. 1953; Watanabe et al. 1953), see Figures 4.1 and 4.3). However, any technique measuring oxygen mole fractions (instead of O<sub>2</sub>/N<sub>2</sub> ratios), requires simultaneous CO<sub>2</sub> measurements to correct for CO<sub>2</sub> dilution effects (see Chapter 1.4.2). Hence the measured CO<sub>2</sub> values can also be used to correct for interference.

Altogether, O<sub>2</sub>/N<sub>2</sub> ratios are derived from the measured O<sub>2</sub> mole fraction as (Chapter 1.4.2, Stephens (1999))

$$\delta(\text{O}_2/\text{N}_2) = \frac{\delta X_{\text{O}_2} + (X_{\text{CO}_2} - 363.29) (X_{\text{O}_2} - 0.05)}{X_{\text{O}_2} (1 - X_{\text{O}_2})} \quad (4.5)$$

## 4.3 Instrument design

As seen from Equations 4.1 to 4.3, the measured VUV signal strongly depends on the pressure of the measured gas stream. In order to detect ppm-level variations in the atmospheric oxygen concentration, the gas pressure needs to be recorded or controlled to ppm-level. Especially with changing intake pressures onboard aircraft, stabilizing the pressure in the sample cell to that level is quite challenging. Usually, this requires several steps of pressure controls. In order to avoid complicated gas handling that could easily exceed space and weight limitations for small research aircraft, the ICON is designed with two measurement cells, allowing for simultaneous measurement of sample and reference gas. Directly connected cell outlets and a pressure regulation based on matching the two cell pressures instead of stabilizing the absolute pressure assure that any change occurring in the sample cell also affects the reference cell.

### 4.3.1 Optical system

Figure 4.4 shows the schematics of optical pathways in the ICON instrument: VUV light emitted by the xenon lamp is split up by a beamsplitter (Laseroptik GmbH), located in a nitrogen-flushed housing to avoid absorption on the way to the sample cells. The beamsplitter and cells are aligned in such a way that both detectors see the same part of the lamp, and that the length of the optical path is identical for both cells.

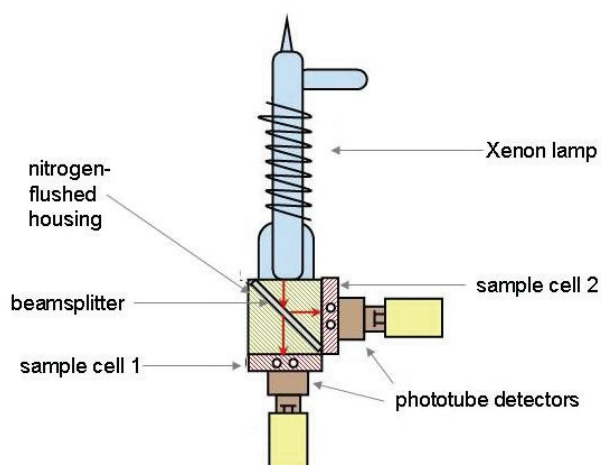


Figure 4.4: Optical design of the ICON

The length of the absorption path in the sample cells is 5mm, thus a pressure of 65mbar is required to achieve the optimal optical density. The cells are separated from the beamsplitter housing by BaF<sub>2</sub> windows. With a cutoff wavelength close to 130nm, these windows block the intensity for the 129.5nm emission line while still letting about 85% of the intensity of the 147nm line pass. Solar-blind phototube detectors (R1187, Hamamatsu Photonics) for measuring the transmitted light intensity are directly attached to the opposite side of the cells, without another window in between.

### **4.3.2 Signal detection and amplification**

The solar-blind phototube detectors are only sensitive to wavelength between 110 and 220nm. At the operating cell pressure, phototube currents are in the range of 100nA. These currents are converted to measurable signals on the order of a few Volts, using a low-noise amplifying circuit as described in (Stephens 1999), that includes a temperature insensitive 125M $\Omega$  resistor (Caddock's) and a low-noise op-amp (AD549, Farnell). As the phototube signal is very sensitive to any external disturbance, e.g. caused by the radio frequency powering the lamp, the diode output is directly connected to the amplifying circuit and both parts are enclosed in a brass housing. Passively regulated voltage from batteries is used as power supply for diodes and op-amps in the amplifying circuit as any other power source has been shown to create significant noise on the measured signals.

### **4.3.3 Data acquisition**

Not only detectors and amplifying circuit, but also the data acquisition system measuring and recording the resulting voltage signals needs to operate at high resolution and low noise levels. Thus a customized 23bit detection system is used, consisting of a CAN-module (Microcontrol), connected to a CR1000 datalogger (Campbell Scientific). This system records signals from both detectors at a frequency of 5Hz and a resolution of 2 $\mu$ V.

In addition, the datalogger is used to record housekeeping data like pressure and temperature at different locations in the instrument. In combination with an external

relay board (SDM-CD16AC, Campbell Scientific), it also controls valves and power switches. After loading a software program in the internal programming language CRBasic prior to a flight, operation of the system is fully automated and data are recorded to the internal storage of the logger. Data can be either retrieved after the flight or visualized onboard with a laptop computer, when required.

#### 4.3.4 Gas handling

The two-cell design of the ICON allows for simplified gas handling, as illustrated in the schematics in Figure 4.5.

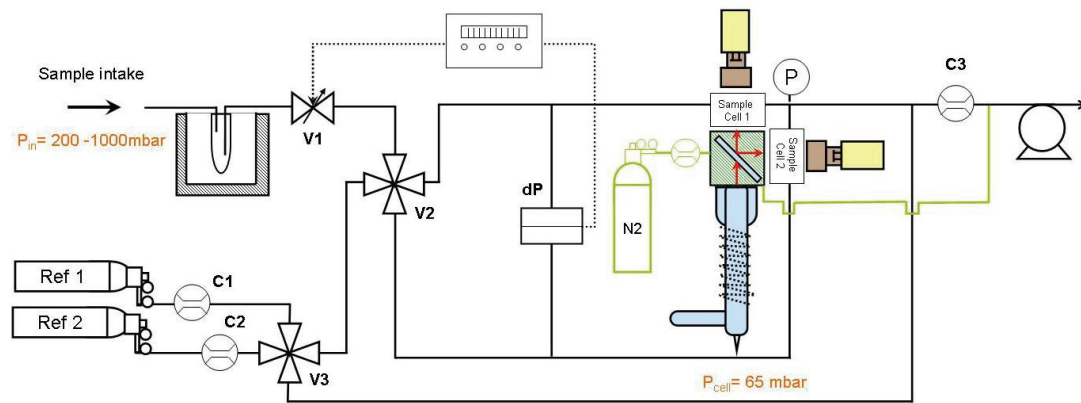


Figure 4.5: Gas handling scheme of the ICON

Instead of several pressure controls to ensure the stability of the pressure at ppm-level, only the pressure difference between the two cells is actively regulated. The absolute cell pressures and flowrates are passively controlled using capillaries. Capillary C1 or C2 sets the flowrate for the reference gas that is supplied from one of two calibration tanks. The intake flow in the sample line is regulated to match this reference flow, using the only active control in the system, the proportional valve V1. This valve is controlled by a customized PID flow control module, driven by the pressure difference between the two cells. To allow for pressure matching on ppm-level, the flow controller is referenced to a 1-mbar full scale differential pressure sensor (MKS Instruments, dP in Figure 4.5). Furthermore, the measured pressure difference dP is larger than the actual pressure difference of the cells by a factor of about 10; this

amplification is achieved using tubing between the differential pressure sensor and cells with a length of about 10 times the length of the tubing downstream of the cells (between the cell outlets and the point where both flows join). Sample and reference gas are periodically switched between the two cells, using the cross-over-valve V2. The absolute pressure in the cells, recorded by a 1-bar absolute pressure gauge at the connected cell outlets, is passively set by the capillary C3 that is located upstream of the vacuum pump. The pressure control was tested for changing intake pressures ranging from 300-1000mbar and proved able to control them without problems.

Due to the small volume of the sample cells ( $0.7 \text{ cm}^3$ ) and compact instrument design that avoids dead volumes or long tubing, the system can run with low flowrates on the order of 10 sccm/min (sccm = standard cubic centimeters, referring to a flow of 10ccm/min at standard pressure ( $p_0=1013\text{mbar}$ ) and temperature ( $T_0=273 \text{ K}$ ) conditions). The low flowrate has the advantage that only small tanks are needed for the reference gases. In addition, not too much gas is lost by continuously purging the non-used reference gas to the vacuum pump with the same flowrate as the one entering the measurement cell. This purging avoids fractionation effects due to pressure changes and adsorption at the pressure regulator surface of the tank that can arise when stopping and restarting the gas flow. Nitrogen flushing of the beamsplitter housing is performed at similarly low flowrates, set by another capillary. To keep the initial flushing time for the beamsplitter housing short, it is kept at low pressure and thus directly connected to the instrument's vacuum pump.

#### 4.3.5 Packaging

The core part of the ICON, containing sample cells, beamsplitter, phototube detectors and amplifying electronics and the xenon lamp and its RF power supply, is shown in Figure 4.6. To reduce both weight and length of optical pathways, the whole package is designed to be as small and compact as possible.

All connections between the separate parts are sealed by Viton o-rings, in addition windows and phototubes are glued with a UV-resistant epoxy to the beamsplitter

housing and their brass housing, respectively. Measurement cells are soldered to the in- and outlet tubing, the connection of the two outlets is soldered as well. As mentioned before, phototubes and their amplifying circuits are enclosed in separate brass housings to protect them from any electronic disturbance. The xenon lamp is mounted in a Teflon collar; inside a small piston provides adequate pressure to compress the o-ring between lamp and beamsplitter housing without damaging the sensitive MgF<sub>2</sub> window of the lamp. In addition, the lamp is enclosed in a brass housing to protect it from damage and to keep disturbance from the RF radiation powering away from the detectors and other sensitive electronics. The RF power supply is directly, i.e. without a cable, connected to the lamp housing since measured signals proved to be sensitive to small movements of the cable.

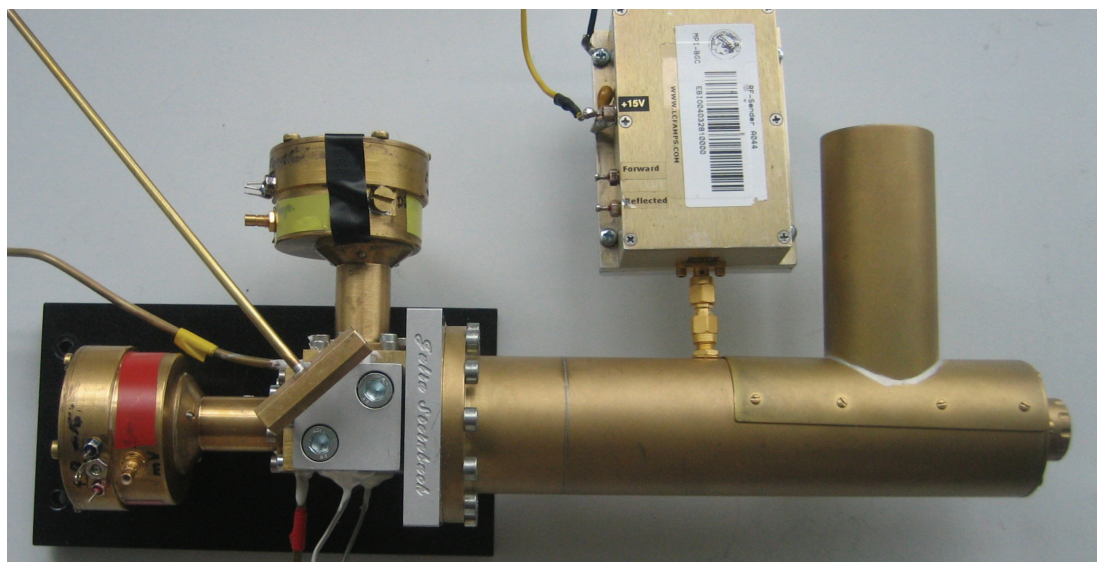


*Figure 4.6: Design of ICON's main part, including sample cells, beamsplitter, phototube detectors, amplifying electronics, xenon lamp and RF power supply*

Together with the components for gas handling and data acquisition, this core part is enclosed in a standard 19" 6HE rack housing (44 cm x 36 cm x 23 cm), with a total weight of 12kg. Figure 4.7 shows the final instrument (1) as well as the additional external parts needed for measurements onboard aircraft: A dry-ice cold trap for drying the sample air (2), a small vacuum pump (3, KNF Neuberger) and a temperature stabilized box containing the two calibration tanks and the nitrogen tank for flushing the housing of the beamsplitter (4).

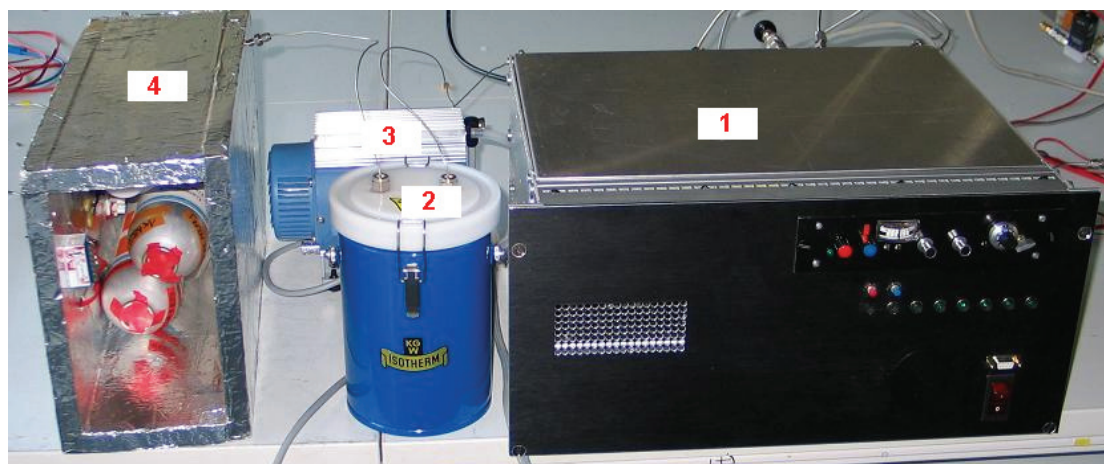


Figure 4.7 The ICON instrument (1) and required external parts (2 – water trap, 3 – vacuum pump, 4 – temperature controlled box containing reference cylinders and nitrogen)

The water trap is placed at the sample intake as shown in Figure 4.5. It consists of a commercial dewar, containing dry ice and a U-shaped  $\frac{1}{4}$ " tubing filled with glass beads. As wet sample air passes the tubing, the water vapor contained in the air freezes out at the surface of the glass beads. As mentioned before, the low flowrates of the ICON allow for the use of small reference cylinders. Here lightweight 1ℓ cartouches (AirLiquide) filled to a pressure of 12 bar are combined with miniaturized regulators (Gloor) with an output pressure of 2bar. As these pressure regulators usually set the output pressure relative to the ambient pressure, the reference side of the regulator is connected to the vacuum pump to guarantee constant output pressure at all heights. The same type of cylinder and regulator is used for the nitrogen flushing.

## 4.4 Instrument performance

### 4.4.1 Signal resolution and short-term noise

Measuring  $O_2/N_2$  with the targeted precision of a few per meg requires not only shielding and low-noise amplification of the phototube currents, but also high resolution and low noise levels of the voltage measurement and data acquisition system. For 2 per meg resolution in the oxygen signal, a corresponding voltage resolution of  $\sim 25\mu V$  in a 10V signal is required. These levels are already close to the theoretical detection limits due to shot and Johnson noise.

Shot noise is given by

$$U_{RS} = R\sqrt{2 \cdot q \cdot I \cdot \Delta f} \quad (4.6)$$

with  $R=125\text{M}\Omega$  the size of the resistor in the amplifying circuit,  $I$  the signal current,  $q=1.6 \cdot 10^{-19}$  C the elementary charge and  $\Delta f$  the measurement frequency.

Johnson noise can be described as

$$U_{RJ} = \sqrt{4 \cdot k \cdot T \cdot \Delta f \cdot R} \quad (4.7)$$

with  $\Delta f$  and  $R$  as above,  $T$  the ambient temperature and  $k = 1.38 \cdot 10^{-23}$  J/K Boltzmann's constant. For the 5Hz measurements performed here, Johnson noise gives a constant noise level of  $3.2\mu\text{V}$ , while shot noise increase with the signal size, resulting in e.g.  $17\mu\text{V}$  for 1V of signal.

The customized data acquisition system used for ICON already provided a resolution of  $2\mu\text{V}$ , but initially showed noise levels with amplitudes around  $100\mu\text{V}$ , even for the dark current of the detector. Modifications in the internal power supply and Teflon housing of the sensitive amplification circuit reduced this noise to levels near the theoretical limits.

Figure 4.8 shows the resulting noise for the final configuration: Red and blue dots show the noise for the two detectors for different voltage levels, generated using of different sample pressures. Noise values are determined as the standard deviation of 50 successive 5Hz-measurements. The dashed line shows the corresponding theoretical values for the sum of Johnson and shot noise.



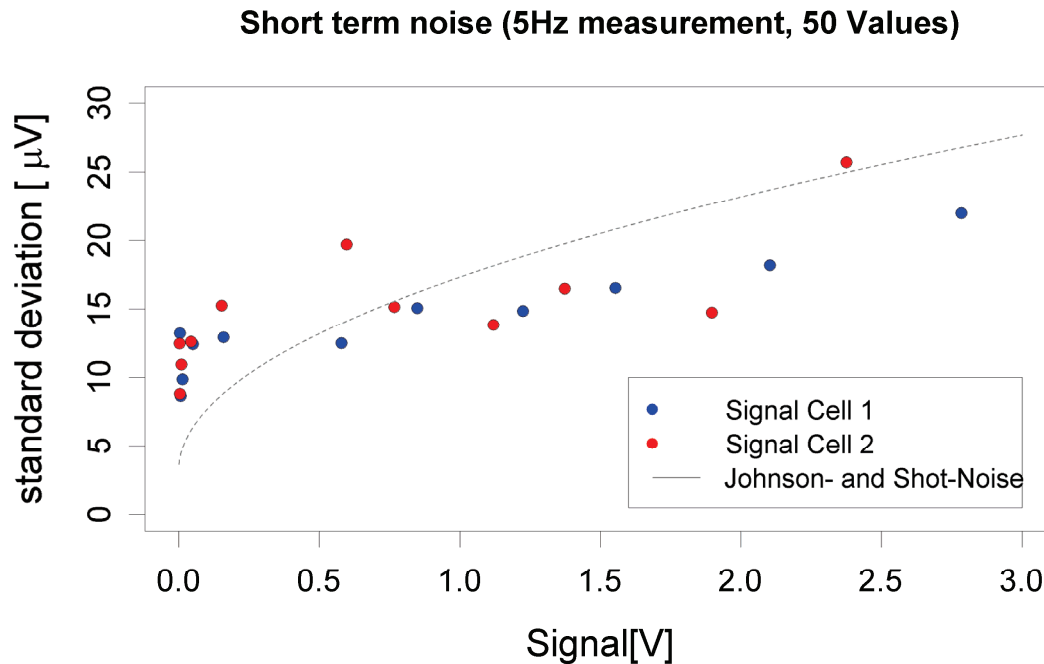


Figure 4.8: Short-term noise levels of the measured voltage signals, compared to theoretical noise levels due to Johnson and shot noise.

#### 4.4.2 In-flight calibration

Reference tanks delivering reproducible  $\text{O}_2/\text{N}_2$  ratios traceable to international scales are an essential component of a measurement system. Thus care must be taken in the choice of tanks and pressure regulators, especially in the choice of materials used. Mainly two effects can influence the  $\text{O}_2/\text{N}_2$  ratio of air supplied by high-pressure cylinders: Adsorption and desorption at cylinders' walls or regulator surfaces and selective permeation through membranes and o-rings contained in regulators (Langenfelds et al. 2005; Keeling et al. 2007). However, especially for pressure regulators information on exact materials and details on the interior are not always available. Tanks and regulators that haven proven to be suitable for oxygen measurements are usually large and heavy which conflicts with the size and weight requirements on board small research aircrafts. Due to low sample flows of  $\sim 10 \text{ sccm/min}$ , the ICON only requires about 2-3  $\ell$  of reference gas for a 3-4h flight.

Therefore the possibility to use lightweight air cartouches with miniaturized regulators was investigated. To assess the stability of the reference tanks independent from any effects caused by the ICON instrument, their O<sub>2</sub>/N<sub>2</sub> ratio was determined by mass spectrometric analysis, using the MPI-BGC mass spectrometer (Brand 2003). For these tests, the tanks were filled with dried ambient air from a high-pressure ‘mother tank’. The pressure regulator were connected to the cylinders and flushed for 5 minutes. For the analysis, cylinders and regulators were placed in the thermostatic box (see Figure 4.7) whose temperature was controlled at 45°C. After the temperature in the box had stabilized, the outlet valve was opened and the O<sub>2</sub>/N<sub>2</sub> ratio of the tank measured as it is drained empty. As the mass spectrometer takes only flow rates of ~1sccm/min, an open split design as shown in Figure 4.9 was used to realize the typical flow rates for the ICON instrument. As later in the flight setup, the reference side of the pressure regulator was evacuated. To avoid any effects by air remaining in the tubing to the spectrometer, the line between the spectrometer and the regulator was also evacuated prior to the measurement.

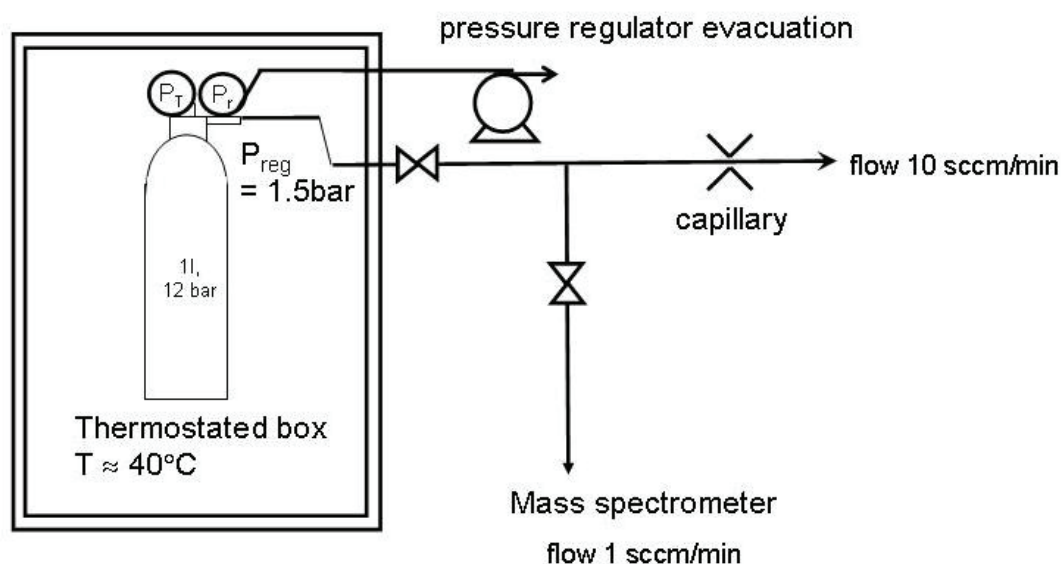


Figure 4.9: Setup for stability tests for small reference tanks.

After some preliminary tests, 12 measurement series were conducted. The resulting timeseries of the measured  $O_2/N_2$  ratio always follow the same pattern, as shown in the example in Figure 4.10: For the first hour, a ‘run-in effect’ is observed, showing exponentially increasing  $O_2/N_2$  ratios. Afterwards,  $O_2/N_2$  exhibits a linear drift of a few per meg/h, until the tank pressures drops below 3 bar and  $O_2/N_2$  starts to drop rapidly.

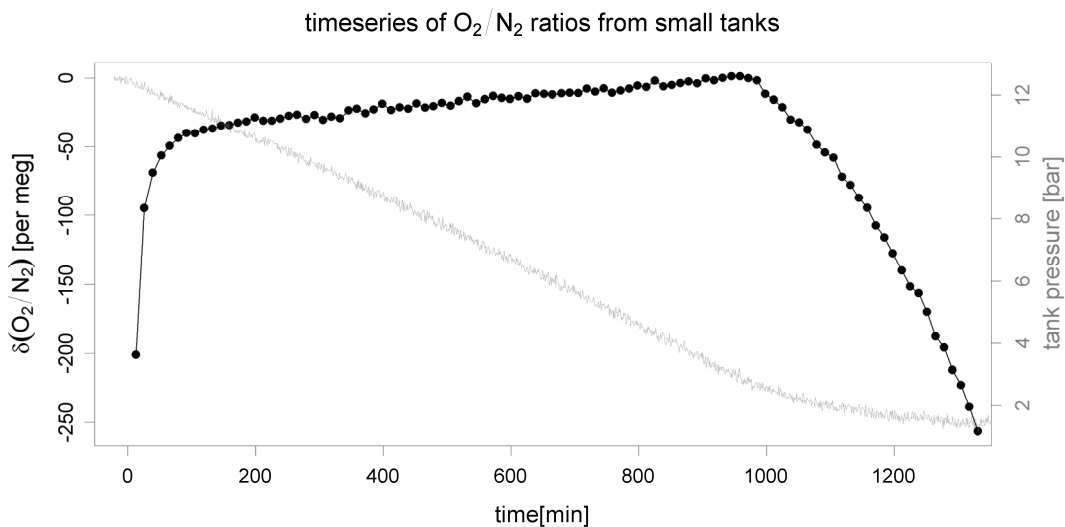


Figure 4.10: Timeseries of  $O_2/N_2$  ratio from small cylinders. The grey line referring to the axis at the right shows the corresponding cylinder pressure at the time of the measurement.

Both exponential run-in effects and different behavior below a certain critical pressure have been already observed, for  $O_2/N_2$  as well as for  $CO_2$  (Keeling et al. 1998a; Daube Jr. et al. 2002; Langenfelds et al. 2005; Keeling et al. 2007; Winderlich 2007). Whereas run-in effects are mostly regulator-related (e.g. selective permeation into o-rings or membranes causing an initial  $O_2$  depletion), the changing behavior below the critical pressure is explained by adsorption of molecules to the cylinders walls that are suddenly released below a certain pressure. However, usually cylinders are filled to  $\sim 200$  bar and reported critical pressures are in the range of 20 – 35 bar, thus it is not clear whether the same mechanism is valid here.

In any case, as only the period of linear drift is suitable for the use as reference gas, the question is whether the drift is reproducible. Figure 4.11a shows time periods with linear drift for the different experiments and Figure 4.11b the respective slopes. For

unknown reasons, half of the experiments show a higher drift (4 – 5.5 per meg/h) than the others (1.5 – 3 per meg/h). Comparing the targeted measurement precision with the range of observed drift rates, the drift can not be considered reproducible, thus independent (e.g. mass spectrometric) analysis of the tanks both before and after each measurement flight is required.

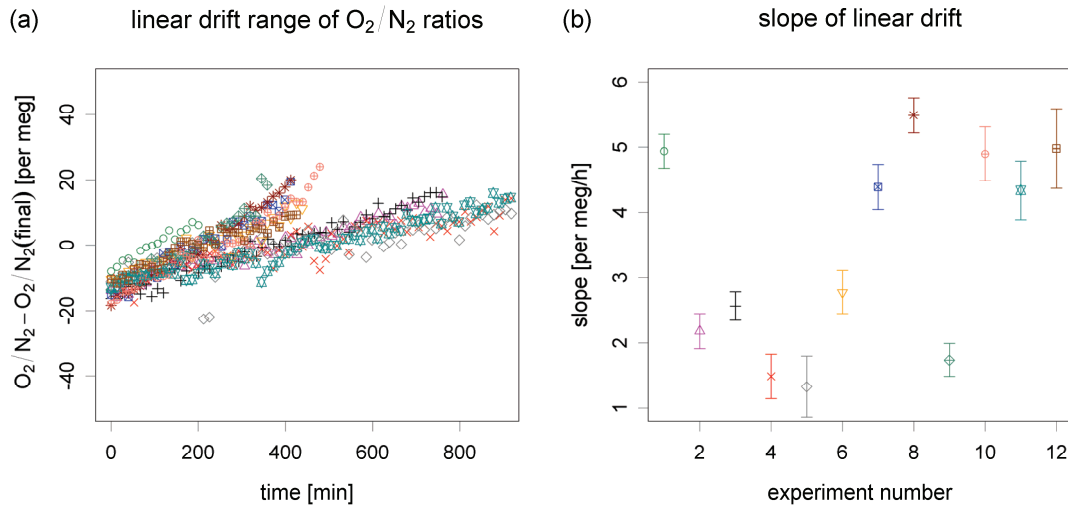


Figure 4.11: Linear drift of O<sub>2</sub>/N<sub>2</sub> ratios from small tanks. Different colors and symbols represent the different experiments.

Although this is not highly convenient in terms of logistics (requiring tanks to be filled in the laboratory prior to a campaign instead of directly at the airport, or do calibrate them in the field against a larger (more stable) tank), it is not critical in terms of gas usage, even if tanks need to be flushed for at least 1h before the start of the actual measurement: 4 hours of flight and 1h flushing time only require 3ℓ of gas, leaving still 6ℓ before the tank pressure drops below the critical 3 bar. With mass spectrometric analysis only requiring flows ~1scm/min, this is sufficient for an analysis before and after the flight. Nevertheless, the long flushing time is also not very convenient. Efforts to reduce the duration of the run-in effect have not been successful so far: The duration showed to be independent of the flowrates during the measurement for a range of 1 to 40 sccm/min. One experiment where the pressure regulator was flushed at a higher flowrate (1ℓ/min) directly before measurement

showed only minor effects, but probably further tests with different flowrates and flushing times can help to solve this problem.

Nevertheless, the results of the analysis show that although the small tanks are probably not the best solution, they can at least be used for short-term calibration during a measurement flight.

#### 4.4.3 Current instrument status

After the individual components of the ICON (gas handling, signal detection system) have been tested and shown to suitable for high-precision oxygen measurements, they have been assembled to the airborne design presented in Section 4.3.4. However, since packaging the components into the 19" rack system, peaks on the order of a few hundred per meg are frequently occurring in the signals of both channels (see Figure 4.12).

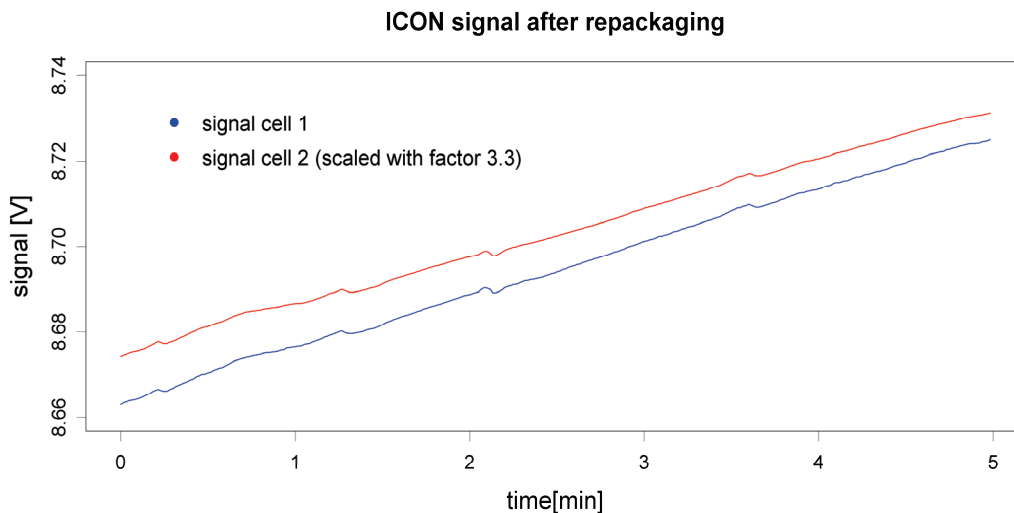


Figure 4.12: Typical signal of the ICON instrument after repackaging.

These disturbances occur about every 1-2 minutes, but also periods with more or less events have been observed. Although they seem to be correlated in the two channels, this fact could not be used for correction as the two signals are not perfectly correlated: Differences arise due to non-equal division of the light by the beamsplitter and due to the fact that the data acquisition system does not sample both signals at exactly the same time.

The reasons for the disturbances are still under investigation. Several possible sources have been considered: Electronic noise due to imperfect shielding of the RF power supply of the lamp or other power supplies inside the instrument or disturbance by other electronic sources in the laboratory environment, artifacts caused by the amplification circuit or the data acquisition system, variations in the lamp intensity or pressure changes caused by leaks or fluctuations in the pressure regulation. All these factors have been thoroughly tested and most of them could be excluded as the origin of the disturbances. The remaining favorite candidate is a very small leak somewhere in the core part, probably in one of the connections (e.g. between cells and the beamsplitter or at the connection of the cells). This would also explain why problems started after repackaging, as the separate parts had been taken apart several times at this time. Replacement of o-rings and polishing the surfaces of the cells and all other sealing surfaces already reduced the magnitude and frequency of the peak events. Further tests and probably a redesign of critical connections are required to identify and remove any remaining leaks and ensure that they were the only reasons for the observed disturbances.

## 4.5 Investigation of possible inlet fractionation effects

Airborne measurements are particularly susceptible to fractionation artifacts due to varying ambient pressure and temperature conditions. In the case of flask sampling, a potential workaround is to use measurements of Ar/N<sub>2</sub> ratios in the same samples as an indicator for this effect (as done in Chapter 3). However, in the case of continuous measurements this information is usually not available. A critical point in each airborne system is the aircraft's intake due to changes in the air velocity and flow patterns. The low sample flows used for ICON lead to large velocity differences between outside and inside of the sample intake (from  $v_{\text{aircraft}} \sim 100 \text{ m/s}$  to  $v_{\text{sample}} < 1 \text{ cm/s}$ ); therefore these effects could be critical. Hence possible fractionation effects at the inlet are investigated here, using laboratory experiments with a miniaturized inlet inside of down-scaled wind tunnel, an idea developed by Mennecke (2006).

#### 4.5.1 Experimental setup

For characterizing the inlet fractionation effect, a series of down-scaled wind tunnel experiments was conducted. A fused silica capillary with an inner diameter of 0.5 mm served as aircraft inlet; a 1.5 mm inner diameter glass tube acted as the down-scaled wind tunnel. To guarantee undisturbed flow conditions at the intake, the inlet tip was sticking only 1-2 mm inside the wind tunnel (see Figure 4.13).

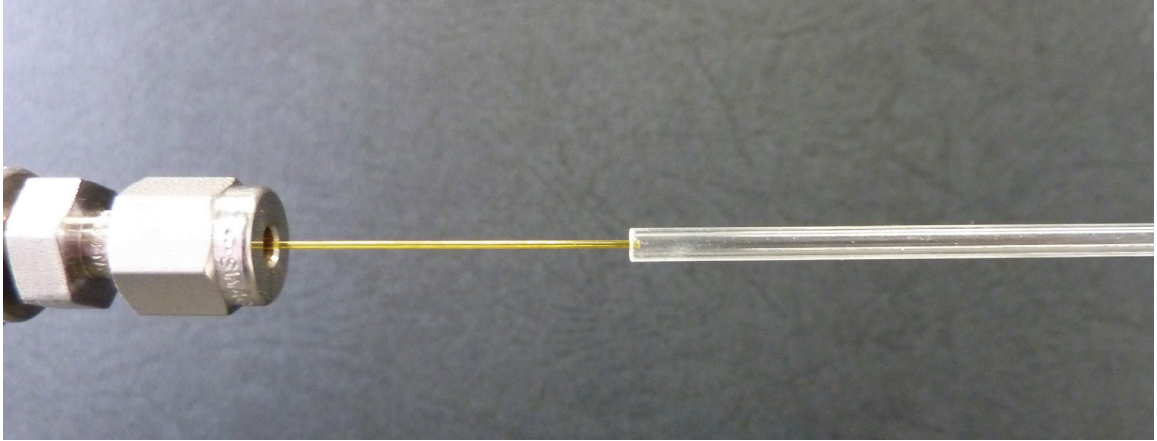


*Figure 4.13: Down-scaled inlet and wind tunnel for laboratory experiments.*

For an airborne sample intake, the inlet tube is usually mounted well outside the turbulent boundary layer of the aircraft, so the flow in the wind tunnel has to be laminar, too. This implies working at Reynolds numbers below 2300. The Reynolds number  $Re$  is defined as

$$Re = \frac{\rho \cdot v \cdot d}{\eta} \quad (4.8)$$

with  $d$  the diameter of the wind tunnel and  $\rho$ ,  $v$  and  $\eta$  the density, velocity and dynamic viscosity of air, respectively. Hence the laminar flow range determined by the wind tunnel parameters implies flow rates below 2500 sccm/min.

Figure 4.14 shows the setup for the down-scaled wind tunnel experiments: Air flow in the wind-tunnel was created by gas effusing from a high-pressure cylinder; the flow rate was regulated using a set of needle valves which allowed for differential measurement at two different ‘aircraft velocities’. As any possible fractionation

effects arise from the changes in air velocity and flow regime, the effects are expected to be negligible for isokinetic intake of the sample air, i.e.  $V_{\text{aircraft}} = V_{\text{intake}}$ .

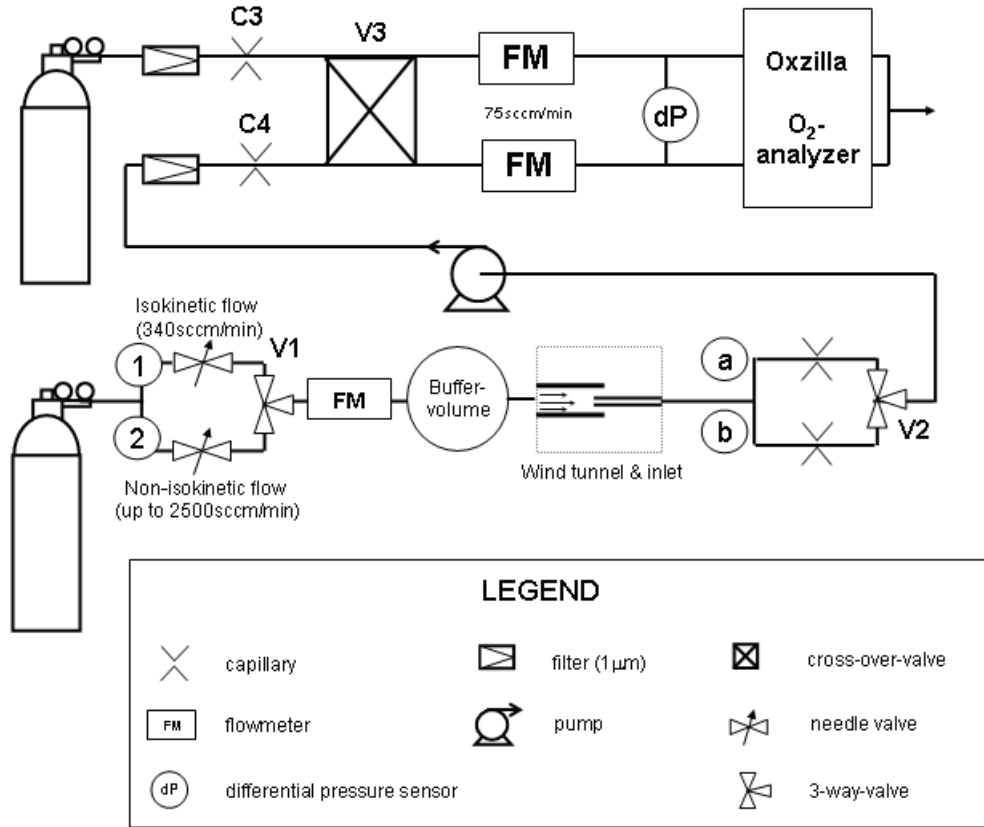


Figure 4.14: Experimental setup for laboratory experiments on inlet fractionation.

Thus the flow in the first line was always adjusted for isokinetic intake, whereas the flow in the second line was varied between consecutive experiments in order to study the flow dependence of the O<sub>2</sub>/N<sub>2</sub> fractionation. The 3-way valve V1 was used to switch between the two lines. Downstream of the inlet, another 3-way valve (V2) was used to switch between two capillaries (C1 and C2) which were adjusted for compensation of the small pressure change at the tip of the inlet when changing the velocity in the wind tunnel. Additionally, a 9L-buffer volume was inserted upstream of the wind tunnel to decouple the inlet effect from possible fractionation related to pressure changes at the tank regulator when switching between the two velocities. After entering the inlet tube the sample air was compressed by a pump before passing another capillary (C4) to reduce the flow rate to a level suitable for the O<sub>2</sub> measurement (here 75 sccm/min).



As the ICON was not ready to perform oxygen measurements at the time of the experiments and mass-spectrometric analysis was not possible for logistical reasons, the oxygen concentration of the sample air was measured by a commercial Oxzilla Differential Oxygen Analyzer (Thompson 2005; Stephens 2007). Based on a comparison of electrical potential from two lead-oxygen fuel cells, this device differentially measures the partial pressure of O<sub>2</sub> of two air flows. Therefore, the measured oxygen concentration difference is highly sensitive to changes in pressure and flow. The flow schematic described above largely avoids any changes in flow and pressure during the measurement. Additionally, the outlets of the two cells were connected directly downstream of the cells to prevent variations in ambient pressure to influence the signal of the two cells differently. No active pressure control was used; instead the pressure difference was monitored by a 1-Torr full-scale differential pressure sensor (MKS) directly upstream of the Oxzilla to make sure no relevant differences occur during the measurement. The flow rates in sample and reference lines were matched by the upstream capillaries (C3 and C4) as depicted in Figure 4.14.

To compensate for dissimilar drifts of the two channels on different timescales, sample and reference gas were switched between the cells every 40s, using an upstream crossover valve (V3 in Figure 4.14). Since the diffusivity of the fuel-cell membranes leads to a slow response of the system, the first 30s of data after each switch were rejected. An example of a measured Oxzilla signal is displayed in Figure 4.15a, with open circles indicating rejected values and filled circles data used for further analysis. Since the differential signal represents alternately *reference - sample* and *sample - reference*, the amplitude of the signal represents twice the difference in the O<sub>2</sub> concentration of sample and reference gas. An additional correction was applied to the resulting 10s-mean-values by linearly interpolating between adjacent reference intervals as seen in Figure 4.15.

With  $r_i$  and  $s_i$  being respective time segments with reference and sample gas in one particular cell, the drift-compensated difference is given by

$$dOx_i = \frac{1}{2} \left( \frac{r_i + r_{i+1}}{2} - s_i \right) \quad (4.9)$$

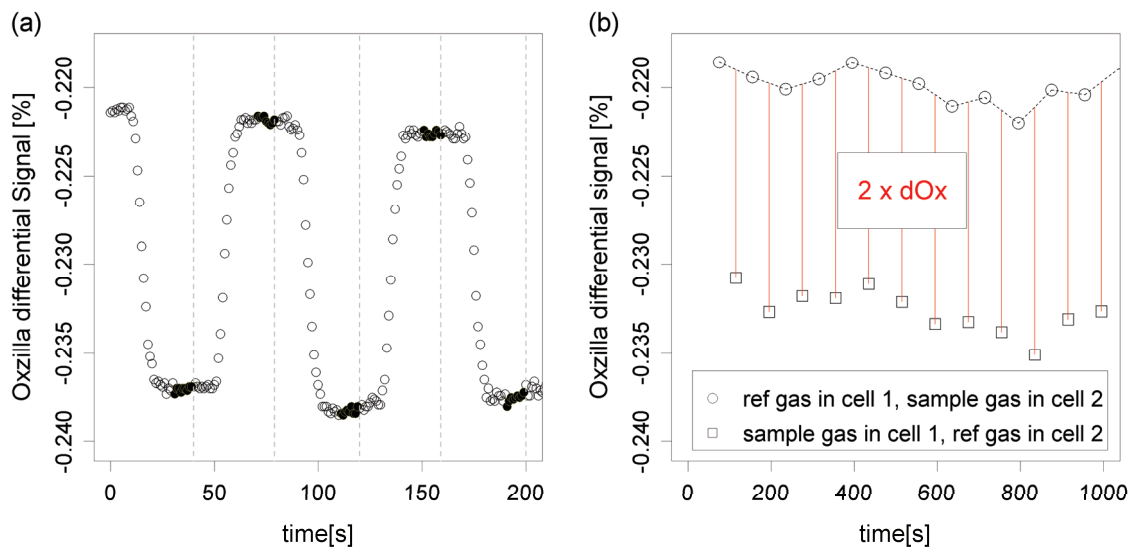


Figure 4.15: Example of the differential Oxzilla signal: (a) Oxzilla differential output ( $O_2[\text{cell } 1] - O_2[\text{cell } 2]$ ). Vertical lines indicate switching times of the crossover valve, open circles show data ignored after switching. (b) 10s-mean values. Circles and squares indicate times with reference and sample gas is in cell 1, respectively. As shown in Equation 4.9, the red lines represent twice the drift-corrected differential O<sub>2</sub> signal  $dO_x$ .

To determine the inlet fractionation effect independent from the long-term drift of the instrument as well, it was also switched periodically (every 12min, rejecting the first 2min after switching) between the isokinetic and the non-isokinetic intake (using a fixed ‘aircraft velocity’). As discussed before, the simultaneous switching of valves V1 and V2 maintained a constant flow rate within the inlet.

The same drift compensation used for the short-term drift was applied to the mean values of each cycle. Five subsequent experiments were performed with different flow rates between 1000 and 2300 sccm/min for the non-isokinetic intake line, which corresponds to a range of ‘aircraft velocities’ from 19 – 43 m/s. The isokinetic intake flow of 340 sccm/min equals a velocity of 6.4 m/s which also corresponds to the intake velocity for the inlet for all experiments.

#### 4.5.2 Experimental results

Figure 4.16 shows the measured O<sub>2</sub>/N<sub>2</sub> differences between the non-isokinetic and isokinetic intake for the five different ‘aircraft velocities’, each averaged over several

hours.  $O_2/N_2$  ratios were calculated from the measured  $O_2$  concentration using Equation 1.5 with constant  $CO_2$  concentration (as air from a cylinder was used,  $CO_2$  is expected to be stable, and fractionation effects are unlikely to have a significant influence on  $CO_2$ ). The results show a significant fractionation effect that increases proportional to aircraft velocity, with  $O_2/N_2$  for the non-isokinetic case being higher than for the isokinetic case.

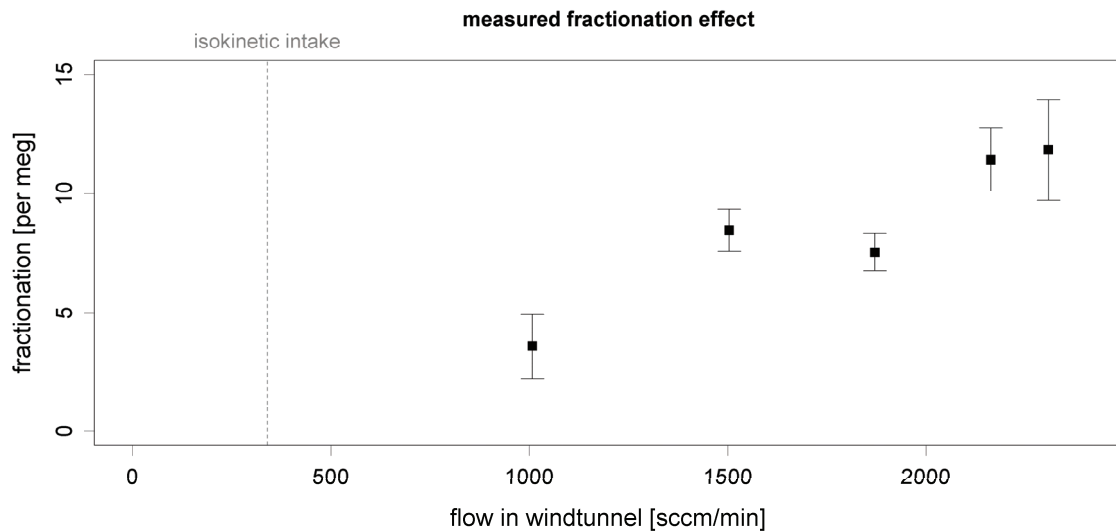


Figure 4.16: Measured fractionation effect. Error bars show the error of the mean determined from averaging over the total measurement time.

As already mentioned in Section 4.5.1, a buffer volume was inserted upstream of the inlet to avoid possible fractionation effects induced by the tank regulators being mistaken for inlet fractionation. The 9ℓ-buffer allows separating these two effects temporally: While an inlet fractionation effect is expected to be seen immediately in the measured signal, an effect caused at the regulator would show up delayed and smoothed in time since the fractionated air needs some time to mix into and cross the buffer volume. To test this hypothesis, an experiment with longer switching cycles was performed. As the observed effect increases with the flow rate in the wind tunnel, in this experiment the highest laminar flowrate was used. The exchange time of the 9ℓ-buffer for this flow rate is 4 min at ambient pressure and 26 min for isokinetic intake. Thus 12 and 40 min were chosen as the length of the individual cycles at the respective flow rates. If any fractionation was occurring at the regulator, the values at the beginning and the end of the cycle would be expected to be different. However,

the results of this experiment show no significant trend in the data, hence the observed fractionation is in fact due to an effect occurring at the inlet.

### 4.5.3 Theoretical considerations

The question is now which mechanism is responsible for the observed fractionation. When the air is slowed down at the intake, adiabatic heating (ram-heating) causes the air inside the inlet to be higher than outside. However, thermal fractionation due to this temperature gradient would result in a negative fractionation effect (lower O<sub>2</sub>/N<sub>2</sub> ratios) instead of the enhancement observed here. In addition, reducing the velocity causes the air pressure to be slightly higher inside the inlet.

Pressure-induced fractionation would cause enhanced O<sub>2</sub>/N<sub>2</sub> ratios and an increasing effect with increasing difference between aircraft and intake velocity, as observed in the experiments. Estimating the pressure fractionation using Equation 1.7, however, is not straightforward in this case, as the pressure gradient responsible for fractionation is not the static pressure difference between the inside and outside of the inlet. Decisive here is rather the component of the pressure gradient that is perpendicular to the direction of the flow (i.e. to the stream lines).

A fractionation mechanism related to this component of the pressure gradient is ‘separation nozzle effect’, i.e. the mass separation by centrifugal forces as molecules enter the inlet on curved stream lines. This mechanism is a well-known method to separate heavier and lighter molecules in a gas mixture, that is mainly used for enrichment of uranium (Becker et al. 1967; Becker 1986). The Treaty on the Non-Proliferation of Nuclear Weapons makes it difficult to find detailed characterization of the process in publicly available literature, however, some experimental results and relevant equations are given by Li et al. (2007). Following that paper, the diffusive flux characterizing the separation process can mainly be expressed as

$$\vec{J} \sim \rho \cdot \frac{\nabla p}{p} \quad (4.10)$$

Here,  $\rho$  is the gas density,  $p$  the gas pressure and  $\nabla p$  the pressure gradient. The separation process is driven by the component of the pressure gradient that is normal to the streamlines and can be expressed in terms of the centrifugal force:

$$\nabla p = \frac{dp}{dr} = \frac{v^2}{r} \quad (4.11)$$

with  $v$  being the velocity of the fluid and  $r$  the radius of curvature of the streamline.

The overall separation effect  $S$  can then be described as the integrated flux along the streamline:

$$S \sim \int \frac{\rho \cdot v^2}{p \cdot r} dt \quad (4.12)$$

To see whether this mechanism can explain the observed fractionation effect, Computational Fluid Dynamics (CFD) simulations of particle trajectories in the wind tunnel were used. These simulations (provided by M. Hermann, Leibniz Institute for Tropospheric Research, Leipzig) were performed with the commercial CFD code FLUENT (Fluent Inc., Lebanon, [www.fluent.com](http://www.fluent.com)) for the highest and lowest ‘aircraft velocity’ used in the laboratory experiment.

Figure 4.17 shows these trajectories for the two aircraft velocities, with the upper plot representing the lowest aircraft velocity (19 m/s) and the lower plot the highest aircraft velocity (43 m/s). In these plots, air is entering the inlet from the left side; the grey bars indicate the cross section of the tube walls. Only half of the inlet is shown, the dashed line at  $y = 0$  designates the middle of the inlet. For each case, 50 trajectories were calculated, mainly covering the range close to the borderline between trajectories that still enter the inlet and those that get diverted. Trajectories are colored by air velocity, corresponding to the color scale at the bottom of Figure 4.17.

The calculation of  $S$  was done by performing the integration from Equation 4.12 for each trajectory, until the point where the trajectories do not have the chance to be influenced by each other (indicated by the dashed lines in Figure 4.17).

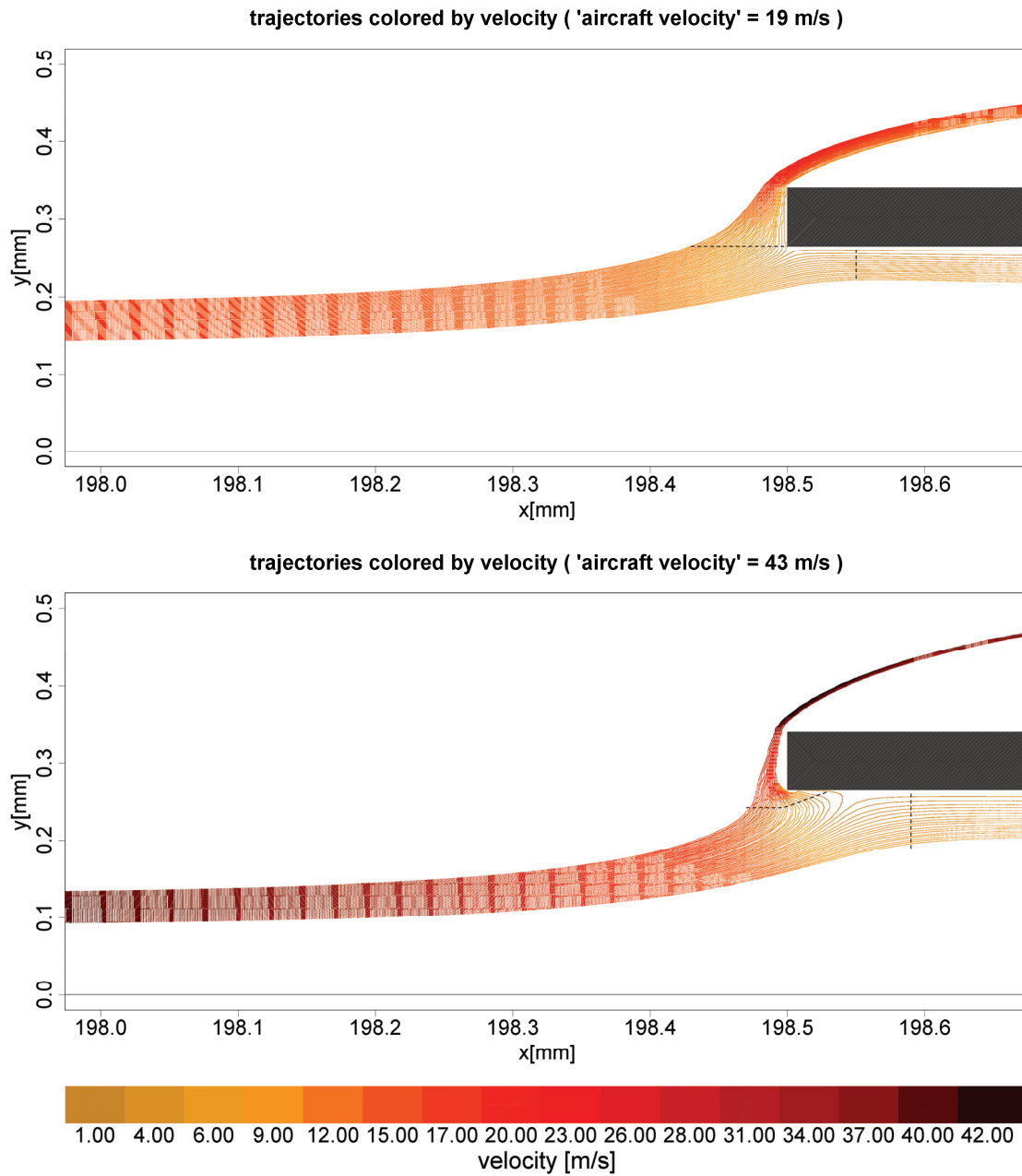


Figure 4.17: Particle trajectories in air entering the inlet for aircraft velocities of 19m/s (upper plot) and 43m/s (lower plot). Trajectories are colored by air velocity, corresponding to the color below. Only trajectories close to inlet walls are shown. Air is entering the inlet from the left, the grey bar indicates the cross section of the inlet wall at the horizontal line at  $y=0$  the middle of the inlet (only half cross section plotted here). Dashed lines indicate the points where inside and outside trajectories can not communicate with each other (endpoint for the integration from Equation 4.12)

Results of the integration are shown in Figure 4.18; here the resulting separation effect is plotted against the trajectory number. Blue dots indicate the results for the lower aircraft velocity, red dots results for the higher aircraft velocity. The vertical

lines in the respective color show the border between trajectories that enter the inlet (in the following called ‘inside trajectories’) and those that get deflected (in the following called ‘outside trajectories’). Trajectory numbering starts from the middle of the inlet, thus inside trajectories are located left of the separation line whereas outside trajectories are situated on the right side of the respective line.

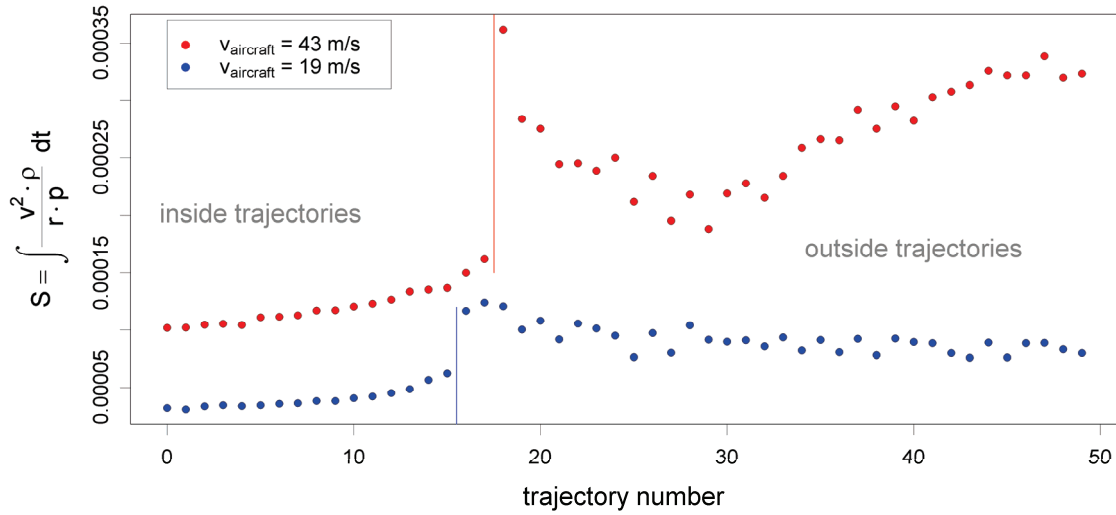


Figure 4.18: Separation effect (integrated centrifugal force) for all trajectories and two different aircraft velocities. Vertical lines indicate separation between trajectories that enter the inlet and those who get deflected.

It can be seen that all values are positive, thus molecules moving on all investigated trajectories are enriched in  $O_2$ . However, the enrichment is significantly higher for the higher aircraft velocity, as it is in the experiment. In addition, a clear difference can be seen between inside and outside trajectories for velocity, with the integrated centrifugal force being higher for the outside trajectories. The effect is highest on the two boundary trajectories at the transition from inside to outside and decreases at both sides of the transition. The best measure for the separating effect for a given velocity is the value  $S_b$  at the outside boundary trajectory; this is to first order expected to be proportional to the measured fractionation effect (in per meg). The ratio  $r_s = S_b(v_a = 43\text{m/s}) / S_b(v_a = 19\text{m/s})$  results in a value of  $r_s = 3.09$ . This ratio is in agreement with the ratio of the measured fractionation effects ( $r_m = \delta(v_a = 43\text{m/s}) / \delta(v_a = 19\text{m/s}) = 3.31 \pm 1.38$ , indicating that the calculated effect (i.e. Equation 4.12) is indeed proportional to the observed fractionation effect.

#### 4.5.4 Scaling to aircraft measurements

The dependence of the observed fractionation effects on the aircraft velocity can thus be explained by the separation nozzle effect. However, the information from measurements and CFD simulations so far is not sufficient to upscale the effect to the real situation at an aircraft's inlet. When working with Reynolds numbers similar to those in the laboratory experiment, the curvature of the streamlines is probably similar, with the fractionation being a function of the ratio of  $V_{\text{aircraft}}/V_{\text{intake}}$ . To derive the magnitude of the effect for other combinations of velocities and inlet diameters, and to see whether it exceeds the measurement precision significantly, further CFD simulations are required.

Critical for airborne measurements is the fact that fractionation effects can also be altitude dependent rather than causing a constant offset. In higher altitudes, the air pressure is lower, which usually also leads to an increase in aircraft velocity. If no active pressure control is used, the intake velocity might also vary with altitude as constant performance of the intake pump corresponds to constant volume flow and hence lower mass flow at higher altitudes. This leads to higher differences between aircraft and intake velocities. Under these conditions, Equation 4.12 suggests higher O<sub>2</sub> values at higher altitudes.

As described in Chapter 3, analysis of flask samples for Ar/N<sub>2</sub> in addition to O<sub>2</sub>/N<sub>2</sub> can be used as a diagnostic for fractionation in O<sub>2</sub>/N<sub>2</sub>. This is possible as most fractionation mechanisms affecting the O<sub>2</sub>/N<sub>2</sub> ratio also have an effect on Ar/N<sub>2</sub> that is usually larger than the effect on O<sub>2</sub>/N<sub>2</sub>.

This is also true for the effect here: As it is a form of pressure fractionation, it scales with the mass difference between the two components (see Equation 1.7), the difference between Ar/N<sub>2</sub> and O<sub>2</sub>/N<sub>2</sub> fractionation is thus:  $(m_{\text{Ar}} - m_{\text{N}_2}) / (m_{\text{O}_2} - m_{\text{N}_2}) = 3$ , with  $m_i$  between the molecular weight of the species  $i$  ( $m_{\text{O}_2}=32$ ;  $m_{\text{N}_2}=28$ ;  $m_{\text{Ar}}=40$ ).



The separation nozzle effect would thus also cause higher Ar/N<sub>2</sub> ratios in higher altitudes. This is in agreement with observations by Graven et al (personal communication) who observed a small increase in Ar/N<sub>2</sub> with altitude during the COBRA experiment (CO<sub>2</sub> Budget and Rectification Airborne study, see (Stephens et al. 2000), resulting in a difference of 9 per meg over 8 km. However, the results from flask samples taken during the BARCA campaign, presented in Chapter 3, show the opposite effect. In addition, the difference of -30 per meg over 4 km is much larger than the one observed in COBRA. The main reason for that is that for BARCA a rearward-facing inlet was used for the sample intake, while in COBRA the inlet was forward-facing (and thus corresponding to the situation in the laboratory experiment). As streamlines look completely different for a rearward-facing inlet, the separation nozzle effect goes most likely in the opposite direction in this case. Therefore the observed altitude variation in the BARCA results could also be explained by the separation nozzle effect. The higher magnitude of the variation in the BARCA results could be due to the difference between rearward and forward-facing inlet, as streamlines are probably stronger curved for the rearward intake. Other reasons for the higher difference could be the smaller inlet diameter in BARCA (1/4" versus 3/8" in COBRA), the lower intake flow (~3 versus ~10 l/min) and the fact that, contrary to COBRA, no intake pressure or flow control was used in BARCA. Here again, further CFD simulations are required to fully understand and qualify the effect for rearward-facing inlets.

## 4.6 Conclusion and Outlook

In this chapter, the development of an in-situ instrument for airborne measurements of atmospheric O<sub>2</sub> is presented. ICON, the In-situ Capability for O<sub>2</sub>/N<sub>2</sub> measurements, is designed for use onboard small research aircraft, targeting a fast instrument response, the ability for fully automated use as well small size, low weight and robustness.

The instrument uses vacuum-ultraviolet (VUV) absorption to detect changes in the oxygen content of the sample air, as this method is best suited for the use onboard aircraft. As the need for ppm-level stability of the sample pressure calls for a complicated (and thus weight and space intensive) gas handling system, here a two-

cell design is used instead: Simultaneous measurements of the sample air and a reference gas are performed. Directly connected cell outlets allow for a simplified pressure control based on matching the pressure difference between the cells rather than controlling the absolute pressure. The differential pressure control is able to control intake pressures ranging from 300–1000 mbar, covering more than the full range of ambient pressures usually experienced by small research aircraft.

For detecting and recording changes in the VUV radiation, an electronic system consisting of phototube detectors, amplifying electronics and a 23bit data acquisition system was assembled and tested. In its final version, the system is able to perform at noise levels close to the theoretical limits for Johnson and shot noise. The whole setup was assembled into a standard 19" rack with a size of 44 cm x 36 cm x 23 cm and a weight of 12kg.

In addition, the possibility to use lightweight air cartouches with miniaturized regulators as reference cylinders for the ICON was investigated. Mass-spectrometric measurements of O<sub>2</sub>/N<sub>2</sub> ratios delivered from these small tanks showed that they can at least be used for short-term calibration during a measurement flight: After an exponential run-in effect of ~1h, the tanks exhibit a stable linear drift of 1.5 – 5.5 per meg/h. As the drift proved not to be reproducible for subsequent tanks in a measurement series, independent analysis of their content before and after the flight is required.

The targeted precision of the device on the order of a few per meg has been shown achievable with respect to individual components' performance, but the development of the instrument could not be fully completed in the course of this thesis. The main reason for this is a disturbance in the signal that started after repackaging the device to the airborne design, currently making any high-precision measurement impossible. Thorough investigation of possible sources for these disturbances indicates the presence of small leaks in the system, most likely at one of the connections between the core parts (lamp, beamsplitter, measurement cells and detectors). To some extent, leaks were already removed, resulting in a significant enhancement of the signal

quality. However, further tests and probably a redesign of critical connections are required before the instrument can perform with the targeted precision.

In addition, there is still a significant amount of work required to get from the current status to a final prototype. Further laboratory tests are required to determine the timescales for temporal stability and calibration intervals for the system. It needs be investigated whether dissimilar drift of the two channels and the fact that the data acquisition system does not measure both signals at exactly the same time cause any problems for the measurement. Finally, the instrument needs to be thoroughly tested in the field. Although it is designed to be robust and insensitive to vibrations and to deal with a wide range of intake pressures, field experiments have to show how the different components perform under real flight conditions. However, from the results so far, the ICON clearly shows potential to become a valuable instrument. With its fast response, compact design and easy handling it is not only well-suited for in-situ airborne measurements, but could also be used on ground- or ship based platforms.

In the course of the development of ICON, possible influences of fractionation at the aircraft's inlet have also been investigated. Airborne measurements are susceptible for these effects because of the changing ambient conditions. In addition, the effects could be especially critical for ICON as the low sample flows imply higher differences between aircraft and intake velocity. Laboratory experiments with a down-scaled inlet in a miniaturized wind tunnel have shown significant  $O_2/N_2$  fractionation effects up to 12 per meg. Measurements at constant intake flow at different 'aircraft velocities' show  $O_2$  enrichment of the sample air, increasing with increasing difference between aircraft and intake velocities. The separation nozzle effect, i.e. the mass-dependent fractionation caused by centrifugal forces that the molecules experience on their way into the inlet, was identified as a possible reason for the observed fractionation. With the help of Computational Fluid Dynamics (CFD) simulations, it could be shown that this effect can explain the sign and velocity dependence of the observed fractionation. Further CFD simulations are required to quantify the absolute value of the effect and to predict it for other inlet diameters and velocity ranges.

The separation nozzle effect has also been shown to be the likely explanation for variations in Ar/N<sub>2</sub> observed during the airborne campaign COBRA and BARCA. In both campaigns, Ar/N<sub>2</sub> derived from flask samples showed a dependence of the sample altitude. Whereas Ar/N<sub>2</sub> increased with height for COBRA (where a forward-facing inlet was used), it decreased with height for BARCA (where the inlet was facing backward). The sign of the altitude dependence for forward and rearward inlet agrees with the expectations for fractionation due to the separation nozzle effect. Whether this effect can also explain the magnitude of the observed variations remains to be determined.

## 4.7 References

- Becker, E. W. (1986). "Development of the separation nozzle process for enrichment of uranium." German Chemical Engineering **9**: 204-208.
- Becker, E. W., K. Bier, W. Bier, R. Schutte and D. Seidel (1967). "Separation of the isotopes of uranium by the separation nozzle process." Angew. Chem. Int. Edit. Engl. **6**: 507-518.
- Brand, W. A. (2003). O<sub>2</sub>/N<sub>2</sub> Storage Aspects and Open Split Mass Spectrometric Determination. Report of the 12th WMO/IAEA Meeting of Experts on Carbon Dioxide Concentration and Related Tracer Measurement Techniques (GAW Report 161, WMO TD No.1275). D. Worthy and L. Huang. Toronto, Canada (15-18. September 2003), WORLD METEOROLOGICAL ORGANIZATION/ GLOBAL ATMOSPHERE WATCH: 274p.
- Daube Jr., B. C., K. A. Boering, A. E. Andrews and S. C. Wofsy (2002). "A high-precision fast-response airborne CO<sub>2</sub> analyzer for in situ sampling from the surface to the middle stratosphere." Journal of Atmospheric and Oceanic Technology **19**(10): 1532-1543.
- Inn, E. C. Y., K. Watanabe and M. Zelikoff (1953). "Absorption Coefficients of Gases in the Vacuum Ultraviolet. Part III. CO<sub>2</sub>." Journal of Chemical Physics **21**(10): 1648-1650.
- Jenkins, T. E. (1987). Optical Sensing Techniques and Signal Processing, Prentice-Hall, Englewood Cliffs, NJ.
- Keeling, R. F., A. C. Manning, E. M. McEvoy and S. R. Shertz (1998). "Methods for measuring changes in atmospheric O<sub>2</sub> concentration and their application in southern hemisphere air." Journal of Geophysical Research-Atmospheres **103**(D3): 3381-3397.
- Keeling, R. F., A. C. Manning, W. J. Paplawsky and A. C. Cox (2007). "On the long-term stability of reference gases for atmospheric O<sub>2</sub>/N<sub>2</sub> and CO<sub>2</sub> measurements." Tellus Series B-Chemical and Physical Meteorology **59**(1): 3-14.

- Ladenburg, R. and C. C. Van Voorhis (1933). "The continuous absorption of oxygen between 1750 and 1300Å and its bearing upon the dispersion." Physical Review **43**(5): 315-321.
- Langenfelds, R. L., M. V. van der Schoot, R. J. Francey, L. P. Steele, M. Schmidt and H. Mukai (2005). "Modification of air standard composition by diffusive and surface processes." Journal of Geophysical Research - Atmospheres **110**: D13307, doi:10.1029/2004JD005482.
- Li, S., J. C. Dayb, J. J. Park, C. P. Cadoub and R. Ghodssi (2007). "A fast-response microfluidic gas concentrating device for environmental sensing." Sensors and Actuators A **136** 69–79.
- Mennecke, A. (2005). Evaluation und Optimierung eines Luftprobennahmesystems für flugzeuggestützte Messungen des atmosphärischen O<sub>2</sub>/N<sub>2</sub> - Verhältnisses, Friedrich-Schiller-Universitaet, Jena. **Dipoma Thesis**.
- Okabe, H. (1964). "Intense Resonance Line Sources for Photochemical Work in the Vacuum Ultraviolet Region." Journal of the optical society of America **54**(4): 478-481.
- Stephens, B. B. (1999). Field-based Atmospheric Oxygen Measurements and the Ocean Carbon Cycle. San Diego, California, U.S.A., University of California **PhD thesis**.
- Stephens, B. B. (2007). "Application of a Differential Fuel-Cell Analyzer for Measuring Atmospheric Oxygen Variations." Journal of Atmospheric and Oceanic Technology **24**: 82-93.
- Stephens, B. B. (2009). Airborne Observations of O<sub>2</sub> and CO<sub>2</sub> on Regional to Global Scales 8<sup>th</sup> International CarbonDioxide Conference Jena, Germany.
- Stephens, B. B., R. F. Keeling and W. J. Paplawsky (2003). "Shipboard measurements of atmospheric oxygen using a vacuum-ultraviolet absorption technique." Tellus Series B-Chemical and Physical Meteorology **55**(4): 857-878.
- Stephens, B. B., S. C. Wofsy, R. F. Keeling, P. P. Tans and M. J. Potosnak (2000). The CO<sub>2</sub> budget and rectification airborne study: strategies for measuring rectifiers and regional fluxes. Inverse Methods in Global Biogeochemical Cycles, Geophys. Monogr. Series, vol 114. P. Kasibhatla. Washington, D.C., AGU: 311 - 324.
- Thompson, R. L. (2005). Atmospheric Oxygen and Carbondioxide Variability in the Southern Ocean Region from continous ship-based Measurements. Wellington, New Zealand, Victoria University.
- Watanabe, K., E. C. Y. Inn and M. Zelikoff (1953). "Absorption Coefficients of Oxygen in the Vacuum Ultraviolet." Journal of Chemical Physics **21**(10): 1026-1031.
- Watanabe, K. and M. Zelikoff (1953). "Absorption Coefficients of Water Vapor in the Vacuum Ultraviolet." Journal of the optical society of America **43**(9): 753-755.
- Winderlich, J. (2007). Entwicklung und Test eines Probenahme- und Kalibriersystems für einen kontinuierlich messenden Hochpräzisions-CO<sub>2</sub>-Analysator zum Einsatz in kommerziellen Flugzeugen, Friedrich-Schiller-Universitaet Jena. **Diploma Thesis**.

# Chapter 5

## Summary and Conclusions

High-precision measurements of atmospheric oxygen play an increasingly important role in our understanding of the global carbon cycle. As the biogeochemical cycles of  $O_2$  and  $CO_2$  are closely coupled, different processes have characteristic oxidative ratios ( $OR = -\Delta O_2 [\text{mole}]/\Delta CO_2 [\text{mole}]$ ). Hence measurements of atmospheric  $O_2$ , together with  $CO_2$ , help partitioning the global oceanic and terrestrial carbon sinks and to identify different processes influencing the atmospheric  $CO_2$  concentration on local or regional scales. However, measurements of atmospheric  $O_2$  are quite challenging, as relevant variations occur on a parts-per-million (ppm) level against the high background value of  $\sim 21\%$ . Measurement artifacts caused by fractionation, i.e. diffusive separation of molecules due to gradients in pressure, temperature and humidity or adsorption onto surfaces, become critical at these levels.

Over the past two decades, advances in measurement techniques and the growing density of the global network of monitoring stations have increased the scientific knowledge on atmospheric oxygen and its use as a tracer for carbon cycle processes. Especially the increasing number of continental monitoring stations allows better constraining surface-atmosphere exchange fluxes from regional to continental scales. However, the proximity of these stations to highly variable (e.g. anthropogenic) sources and sinks complicates the interpretation of measurements.

This thesis addresses two important aspects to improve the ability to utilize those data: First, the characterization of anthropogenic sources, their spatial and temporal variability and their influence on the atmospheric composition, and second, the use of airborne measurements to characterize the spatial heterogeneity of atmospheric mixing ratios in between the ground-based monitoring stations.

The first aspect is addressed in Chapter 2 by investigating whether simultaneous O<sub>2</sub> and CO<sub>2</sub> measurements can be used to identify different fossil fuel sources as different combustion processes have different oxidative ratios, depending on fuel compositions. For this purpose, a high-resolution dataset of anthropogenic CO<sub>2</sub> emissions and the corresponding O<sub>2</sub> uptake was created from emission inventories and fuel consumption data. The COFFEE (CO<sub>2</sub> release and O<sub>2</sub> uptake from Fossil Fuel Emissions Estimate) dataset contains hourly CO<sub>2</sub> and O<sub>2</sub> data for the years 1995 to 2008 on a 1°x1° grid. Based on this dataset, it was investigated whether spatial and temporal variations in O<sub>2</sub>/CO<sub>2</sub> emissions ratios leave a detectable signature in atmospheric oxygen. Model simulations from the (global) TM3 and (regional) REMO model show that the influence of the local fuel mix changes the atmospheric O<sub>2</sub> concentration at the measurement stations in the atmospheric monitoring network by several ppm.

Whether these effects can actually be detected in atmospheric CO<sub>2</sub> and O<sub>2</sub> observations was examined for two cases: the Ochsenkopf tall tower, a continental station in Germany that is operated by MPI-BGC, and Hateruma Island in Japan, a rather polluted station operated by the Japanese National Institute of Environmental Studies (NIES). For the first case, influences of variable fossil fuel related oxidative ratios could not be detected, as both fossil fuel signals and variations in the local fuel mix are rather small at the Ochsenkopf station, where atmospheric signals are mainly dominated by biospheric processes. However, for Hateruma Island subjected to air masses from different Asian countries with different oxidative ratios, a significant part of the observed variations in oxidative ratios could be captured using modeled fossil fuel variations. In addition, regional modeling results performed at NIES (using the COFFEE dataset as input) indicate the possibility to use measured variations in oxidative ratios for detecting of the origin of the air arriving at Hateruma.

In addition, the global perspective of variable oxidative ratios was investigated, using atmospheric inversions of APO (atmospheric potential oxygen). The artificial tracer  $\text{APO} = \text{O}_2 + 1.1 \text{ CO}_2$  is used to isolate the oceanic component from measured oxygen signals. For the calculation of APO fluxes, assumptions on global oxidative ratios for biospheric activity and fossil fuel combustion need to be made. As the inversion

method derives fluxes by minimizing the mismatch between measured and model-derived atmospheric concentrations, this works as long as the atmospheric concentration at the monitoring stations is not significantly influenced by the local fuel mix. This is the case for the classical remote monitoring stations, but the use of stations closer to anthropogenic sources leads to part of the fossil fuel signal being misinterpreted as oceanic signal. Synthetic data experiments with different sets of monitoring stations showed that the differences caused in the seasonal variations of APO fluxes are in any case negligible compared to other uncertainties in the inversion. However, the influence of the local fuel mix causes systematic offsets in certain areas, as soon as more polluted stations, for example Hateruma Island, are used. Future inversions will most likely also include observational input from existing continental stations, mainly in Europe and North America. Results of the synthetic data experiments indicate that the inclusion of these stations leads to a significant negative bias in the Northern Atlantic region when using the simplified assumption of constant oxidative ratios for fossil fuel combustion. Thus, a dataset as COFFEE that characterizes spatial and temporal variations of anthropogenic CO<sub>2</sub> emissions and the related O<sub>2</sub> uptake is indeed a useful tool for this purpose.

Chapters 3 and 4 address the second important aspect for improving the interpretation of atmospheric measurements from continental stations. As atmospheric variations of tracers over continents are influenced by sources and sinks with strong temporal, but also spatial variability, it is important to characterize the impact on spatial tracer distribution in the atmosphere near monitoring stations. The best characterization can be done with airborne measurements. Aircraft can not only provide access to different temporal and spatial scales, but are also uniquely suited for measuring three-dimensional distributions of atmospheric tracers or to follow air masses.

In spite of the advances in measurement techniques for atmospheric oxygen, airborne measurements are still rare and mostly limited to flask sampling, providing limited information due to the lower temporal and spatial resolution. In Chapter 3 of this thesis, the feasibility of using oxidative ratios from airborne flask samples for the separation of different processes was investigated. This was done for the case of the



BARCA (Balanço Atmosférico Regional de Carbono na Amazônia) aircraft campaign in the Brazilian Amazon Basin.

Oxidative ratios were determined from linear regression of the  $O_2$  versus  $CO_2$  mole fraction of the flask samples after correcting the  $O_2$  mole fraction for possible fractionation effects using measured  $Ar/N_2$  ratios in the flasks. With  $1.15 \pm 0.02$ , the overall oxidative ratio is close to 1.1, the oxidative ratio for biospheric activity. Apart from the dominating biospheric processes, also other contributions could be identified: Oxidative ratios in higher altitudes/above the planetary boundary layer showed significantly higher values, most likely related to atmosphere-ocean-exchange. Closer to the ground, influences from fossil fuel combustion ( $OR=1.4$ ) and biomass burning ( $OR = 1.11-1.4$ ) could be identified, using  $CO$  as an additional tracer for these processes. However, the detection of these signals was complicated by the fact that the atmospheric composition is a mixture of signals from these combustion processes and the strong biospheric signals. Comparison with the  $CO$  data indicates that the contribution from fossil fuel or biomass burning is less than 60 % of the total  $CO_2$  enhancement. When focusing on samples where the contribution from non-biospheric processes is high enough to cause considerable changes in oxidative ratio, the sample size quickly becomes too small to determine oxidative ratios robustly. Significant identification of different processes is thus limited by the low sampling density here. To identify signatures robustly and get a more detailed insight, e.g. identifying different kinds of biospheric activity, types of wildfires or emissions from different fossil fuel sources, continuous measurements of both  $O_2$  and  $CO_2$  are inevitable.

This need for continuous  $O_2$  measurements – that are currently limited by the availability of suitable instruments – is addressed in Chapter 4. Here the development of an in-situ instrument for airborne measurements of atmospheric  $O_2$  is presented. ICON, the In-situ Capability for  $O_2/N_2$  measurements, is designed for the use onboard small research aircraft, targeting a fast instrument response, the ability for fully automated use as well small size, low weight and robustness. This target is achieved by using VUV absorption as measurement principle (allowing fast instrument response and low motion sensitivity), and a two-cell design for simultaneous

measurement of the sample air and a reference gas (allowing a simple differential pressure control instead of a complicated – and thus weight and space intensive – gas handling system. In addition, low sample flows reduce the required amount of reference gas and thus allow using light-weight 1L-cartouches instead. As no commercial VUV based instrument for O<sub>2</sub> measurements exist, all components of the optical, gas handling, detection and data acquisition system had to be designed and custom built. The whole setup was assembled into a standard 19" housing with a size of 44 cm x 36 cm x 23 cm and a weight of 12kg. In the course of thesis, the targeted precision of the device in the order of few per meg was shown achievable with respect to individual components' performance. The final instrument package has to be further tested in the laboratory and in the field, before it can be fully deployed onboard research aircraft. However, overall the ICON instrument development clearly shows the potential to become a valuable instrument, not only for airborne measurements.

In the course of the development of ICON, also possible fractionation effects at the aircraft's inlet have been investigated. These effects are critical in the case of airborne measurements because of the changing pressure and temperature conditions; and especially dangerous for ICON as the low sample flows imply higher differences between aircraft and intake velocity. In the case of airborne flask sampling, O<sub>2</sub>/N<sub>2</sub> fractionation can be corrected for using measured Ar/N<sub>2</sub> ratios, as done in Chapter 3. However, this workaround is not possible for in-situ measurements as performed by the ICON. Laboratory experiments with a down-scaled inlet in a miniaturized wind tunnel show significant fractionation effects. With the help of Computational Fluid Dynamics (CFD) simulations, the observations could be explained by mass-dependent fractionation caused by centrifugal forces that the molecules experience on their way into the inlet. The same fractionation mechanism has also been shown to be the likely explanation of variations in Ar/N<sub>2</sub> observed during the airborne campaign COBRA and BARCA. Further CFD simulations are required to describe the effect as a general function of inlet parameters, aircraft velocity and ambient pressure and temperature conditions.

Overall, the work of this thesis contributes to advancing the knowledge of the small scientific community dealing with measurements of atmospheric O<sub>2</sub> especially over continents and in the vicinity of strong sources. Investigation of observed oxidative ratios in Chapter 2 and 3 has shown two examples how oxidative ratios can be used to separate different processes. It has been discussed under which conditions this separation is possible, and current limitations of this method have been pointed out. In addition, two useful tools have been developed in the course of this thesis – the COFFEE dataset as a modelling tool for improving the interpretation of measured O<sub>2</sub> signals and the ICON instrument as an experimental device for improving the measurements itself.

# Appendix 1

## Derivation of flask weighting function

Air contained in a flask sample is a mixture of the air that entered during the actual filling time and some air that entered during the flushing time before filling. Assuming the flushing starts at the time  $t_0$  and the filling starts at  $t_1$  and ends at  $t_2$ , the weighting function can be derived as follows: For the flushing process, less air from the beginning of the flushing time will be contained in the final sample than from the end of the flushing time. Presuming perfect mixing of the air, the weight  $W$  of air entering the flask at a certain time  $t$  within the flushing period can be described by a decreasing exponential function of the form

$$W(t) = \exp\left\{-\frac{t_1 - t}{\tau}\right\} \quad (\text{A1.1})$$

with  $\tau = V/f$  being the exchange time of the volume  $V$  of the flask at flowrate  $f$ .

For the 1ℓ flasks used here,  $\tau$  can directly be expressed in terms of relative changes in

the flask pressure  $p$ :  $\tau = \frac{dp}{dt}(t_1) / p(t_1)$  (A1.2)

During the filling process, the relative contribution of the air entering the flask at the time  $t$  is directly proportional to the flowrate and therefore to the changes in flask

pressure:  $W(t) = \frac{1}{p(t_1)} \frac{dp}{dt}(t)$  (A1.3)

In summary, the weighting function can thus be written as:

$$W(t) = \begin{cases} \exp\{(t - t_1) \cdot f\} & \text{for } t_0 < t_i < t_1 \\ \frac{1}{dp_{\max}} \frac{dp}{dt} & \text{for } t_1 < t < t_2 \end{cases} \quad (\text{A1.4})$$

## Appendix 2

### Derivation of optimal optical density

The optimal optical density is defined as the optical density with the optimal signal to noise ratio. The relevant signal here is the intensity change that is caused by a certain change in oxygen.

#### Case 1: only 147nm line

Following Equations 4.1, the transmitted light intensity for the 147nm line is given as

$$I = I_0 \exp\{-OD\} \quad (A2.1)$$

Instead of depending on the O<sub>2</sub> concentration, as written in Equation 4.2, OD can also be expressed in terms of the number  $n$  of O<sub>2</sub> molecules:

$$OD = \sigma \cdot n \cdot l \quad (A2.2)$$

with  $l$  the path length as in Equation 4.2 and  $\sigma$  the absorption cross section.

The change in signal when changing the number of O<sub>2</sub> molecules in the sample is thus

$$\frac{dI}{dn} = -\frac{OD}{n} \cdot I_0 \exp\{-OD\} \Rightarrow dI = -OD \cdot I_0 \exp\{-OD\} \frac{dn}{n} \quad (A2.3)$$

With  $dn/n \approx 10^{-6} = \text{const}$  for the ppm-level variations observed here, it follows for relative changes in signal:  $dI \propto -OD \cdot I \Rightarrow dI/I \propto -OD$  (A2.4)

Assuming the noise to vary with  $\sqrt{I}$ , the optimal signal to noise ratio (SN) is given for a maximum in  $dI/\sqrt{I}$

$$\rightarrow SN = \frac{|dI|}{\sqrt{I}} = \frac{\text{const} \cdot OD \cdot \exp\{-OD\}}{\text{const} \cdot \exp\{-OD/2\}} \propto OD \cdot \exp\{-OD/2\} \quad (A2.5)$$

$$\rightarrow OD \cdot \exp\{-OD/2\} \stackrel{!}{=} \max \quad (A2.6)$$

$$\rightarrow d\left(\frac{dI}{\sqrt{I}}\right)/dOD = [1 - OD/2] \exp\{-OD/2\} \rightarrow OD = 2 \quad (A2.7)$$

### Case 2: both emission lines

Taking into account the two emission lines at 147nm (index 1) and 129.5nm (index 2), the transmitted intensity is given as

$$I = I_{01} \exp\{-OD_1\} + I_{02} \exp\{-OD_2\} \quad (\text{A2.8})$$

Equation 4.2 gives

$$OD_x = k_x \cdot l \cdot p \cdot \frac{T_0}{T} \cdot X_{O2} \quad (\text{A2.9})$$

$$\rightarrow OD_1/OD_2 = k_1/k_2 \Rightarrow OD_2 = OD_1 \cdot k_2/k_1 \quad (\text{A2.10})$$

Changes in the signal can be determined in analogy to Case 1:

The individual optical densities can be written as  $OD_x = \sigma_x l n$

$$\rightarrow \frac{dI}{dn} = -\frac{OD_1}{n} I_{01} \exp\{-OD_1\} - \frac{OD_2}{n} I_{02} \exp\{-OD_2\} \quad (\text{A2.11})$$

$$\rightarrow dI = -[OD_1 I_{01} \exp\{-OD_1\} + OD_2 I_{02} \exp\{-OD_2\}] \frac{dn}{n} \quad (\text{A2.12})$$

$$\text{with } \frac{dn}{n} \approx 10^{-6} = \text{const.} \rightarrow dI \propto -(OD_1 I_1 + OD_2 I_2) \quad (\text{A2.13})$$

Relative changes in the signal are thus given by

$$\frac{dI}{I} = -\frac{OD_1 I_1 + OD_2 I_2}{I_1 + I_2} \frac{dX_{O2}}{X_{O2}} \quad (\text{A2.14})$$

By comparing this equation with Equation 4.3, an effective optical density can be defined as

$$OD_{eff} = \frac{OD_1 I_1 + OD_2 I_2}{I_1 + I_2} \quad (\text{A2.15})$$

With  $r = I_{01} / I_{02}$ ,

$$OD_{eff} = \frac{OD_1 [\exp\{-OD_1\} + k_2 / k_1 \cdot r \cdot \exp\{-k_2 / k_1 \cdot OD_1\}]}{\exp\{-OD_1\} + r \cdot \exp\{-k_2 / k_1 \cdot OD_1\}} \quad (A2.16)$$

The signal to noise ratio is again given by  $dI / \sqrt{I}$

$$\text{with } dI \propto OD_1 I_{01} \exp\{-OD_1\} [1 + r \cdot k_2 / k_1 \exp\{k_2 / k_1\}] \quad (A2.17)$$

$$\text{and } \sqrt{I} \propto \sqrt{I_{01} \exp\{-OD_1\} + I_{02} \exp\{-OD_2\}}$$

$$= \sqrt{I_{01} \exp\{-OD_1\} [1 + r \exp\{k_2 / k_1\}]} \quad (A2.18)$$

$$\begin{aligned} dI / \sqrt{I} &\propto \frac{I_{01} OD_1 \exp\{-OD_1\} + I_{01} \cdot r \cdot OD_1 \cdot k_2 / k_1 \exp\{-k_2 / k_1 \cdot OD_1\}}{\sqrt{I_{01} \exp\{-OD_1\} + I_{01} \cdot r \cdot \exp\{-k_2 / k_1 \cdot OD_1\}}} \\ &= \frac{OD_1 \sqrt{I_{01}} \cdot [\exp\{-OD_1\} + r \cdot k_2 / k_1 \exp\{-k_2 / k_1 \cdot OD_1\}]}{\sqrt{\exp\{-OD_1\} + r \cdot \exp\{-k_2 / k_1 \cdot OD_1\}}} \end{aligned} \quad (A2.19)$$

The optimum of this ratio is determined graphically (see Figure 4.2.)

# Selbstständigkeitserklärung

Ich erkläre, dass ich die vorliegende Arbeit selbstständig und nur unter Verwendung der angegebenen Hilfsmittel, persönlichen Mitteilungen und Quellen angefertigt habe.



# Curriculum Vitae

- 1999 School education finished with Abitur  
(Diltheyschule, Wiesbaden)
- 10/1999 – 04/2005 Studies of Physics at Friedrich Schiller University, Jena  
During studies work as student scientific assistant  
Astrophysical Department  
Department of Applied Low Temperature Physics  
Institute for Physical High Technology (IPHT) Jena  
Internship at the company Carl-Zeiss-Jena
- 10/2004 – 02/2005 Diploma thesis on ‘Optical Manipulation of Microparticles in Dilute Gases under Microgravity Conditions’(Astrophysical Institute, FSU Jena)
- 04/2005 – 05/2010 PhDthesis at Max Planck Institute for Biogeochemistry  
/ Friedrich Schiller University, Jena

## Publications

Steinbach, J., Blum, J., Krause, M.: Development of an optical trap for microparticle clouds in dilute gases, Eur. Phys. J. E 15, 287-291, 2004

Chen, H., Winderlich, J., Gerbig, C., Hoefer, A., Rella, C. W., Crosson, E. R., Van Pelt, A. D., Steinbach, J., Kolle, O., Beck, V., Daube, B. C., Gottlieb, E. W., Chow, V. Y., Santoni, G. W. and Wofsy, S. C.: High-accuracy continuous airborne measurements of greenhouse gases (CO<sub>2</sub> and CH<sub>4</sub>)

van der Laan-Luijkx, I.T., Karstens, U., Steinbach, J., Gerbig, C., Sirignano, C., Neubert, R.E.M., van der Laan, S., Meijer, H.A.J.: CO<sub>2</sub>, δO<sub>2</sub>/N<sub>2</sub> and APO: observations from the Lutjewad, Mace Head and F3 platform flask sampling network, submitted to Atmos. Meas. Tech. Discuss.

# Acknowledgements

I am grateful to many people whose contributions made this thesis possible. First of all, I like to thank my two supervisors, Christoph Gerbig from the MPI-BGC and Lothar Viereck-Götte from the Friedrich-Schiller-Universität who have been very helpful in different ways complementing each other. Being my ‘everyday supervisor’, Christoph was always there when I needed him. Although he is always very busy with his own research and his responsibility for altogether 8 PhD and undergraduate students (lately especially for the two of them that were struggling to finish at the same time), he was always taking his time for scientific questions, discussion of problems with experimental results that wouldn’t fit any theory or practical help in the lab when I knocked at his door (or just entered his office). On the other hand, he never tried to micromanage me and my work, but let me work relatively independent instead.

Professor Viereck, my university advisor, I met only once or twice a year, but nevertheless he was a huge help by keeping in mind ‘the bigger picture’ of my thesis, looking at it from the geophysical point of view and giving me new perspectives of problems I have been stuck with for long time. Finally, he was the one motivating me to start writing up my thesis and not trying to solve every little problem before that what has been shown a very good discussion, both causing me to finally finish and also still solving some problems in the course of writing (as fixed deadlines cause enormous raise in productivity)

Annette Freibauer, who was a scientist at MPI-BGC before she moved to Braunschweig, was the third member of my PhD advisory committee. Moving away from Jena didn’t cause her to miss any of my advisory committee meetings but only shifted them to preferably take place on a Monday or Friday. Annette has been very helpful in providing fresh insights and new ideas while politely stating all the time that she was not an expert in the field of  $O_2/N_2$ , and enhancing my motivation by providing a look of positive feedback.

Apart from my supervisors, many other people have contributed to the work of this thesis in one or the other way, and I find it difficult to place them in an order, as it is difficult to quantify the helpfulness they provided in terms of practical help, useful discussions or just motivation for me not to give up. Therefore, I start my further acknowledgements in the order of my different thesis chapters:

For the work on fossil fuel related oxidative ratios in Chapter 2, I like to thank Christian Rödenbeck and Ute Karstens for many useful discussions on oxidative ratios, fuel influences on atmospheric signals as well as for their useful comments on this thesis chapter. In addition, I thank Ute for providing REMO modeling results and Christian for introducing the TM3 model and the atmospheric inversions to me. Besides, I like to thank Valentina Sicardi and Bakr Badawy for answering my (sometime stupid) questions on the subtleties of TM3 handling when Christian was not available or when I was afraid to ask him same question for the third time. Valentina I also thank for discussions on the exact definition and usefulness of APO. For providing observational data for the Ochsenkopf station, I would like to thank Rona Thompson and the MPI-BGC tall tower technicians, for data from Hateruma Island I am grateful to Chika Minejima, Yasunori Tohjima, Hiroaki Yamagishi and Histoshi Mukai. Chika I also like to thank for interesting discussions on oxidative ratios and modeling.

For my work presented in Chapter 3, I would like to thank the whole BARCA team. Apart from being grateful for the various efforts that some of these people had to undertake for the BARCA campaigns to finally take place (which started way before my PhDtime) and the contributions of others in terms of flight planning and measurement onboard the Bandeirante, I am very happy that I had the opportunity to join this campaign. I very much enjoyed working together with the BARCA people, as well with the ‘field crew’ during the campaigns in Brazil as with the science team during the meeting in Jena and the countless telecons (well, the latter were probably the least enjoying part). Although it has been quite stressful, I consider the time I spent in Brazil during BARCA as one of the greatest parts in my thesis time, and I learned a lot during this periods. Here I want to mention especially two people, Olaf

Kolle from MPI-BGC and Steve Wofsy from Harvard University. Being the head of the Field Instrumentation Facility of MPI-BGC, Olaf is genius in everything related to meteorology, data acquisition and in general technical things. Apart from the technical stuff I learned from him, I also enjoyed that he is a person that proves ‘that people can be grown up scientists and still be really cool’ (a really striking comment about Olaf that was stated by a pupil visiting the MPI-BGC’s Girls’ Day). And I will try to consider his advice to be more relaxed and let people finish talking before I start speaking...Discussions with Steve Wofsy, leader of the Atmosphere-Biosphere-Exchange group of the Harvard University, were also highly enjoyable as he has both a lot of experience, both in the field as in science in general as well a great way to explain scientific facts in a clear and understandable way. In addition to scientific discussions, I learned a lot of useful stuff about R-programming from him during BARCA-B. In addition to the BARCA team, I like to thank the members MPI-BGC’s Iso- and Gaslab for analysis of the flask samples and Stephan Baum for organizing the flask logistics.

The instrument development I presented in Chapter 4 of this thesis I would consider the most challenging part of my thesis. Working on instrument development is not an easy task in the scientific community, especially if not everything works out straightforward (which it usually does not). People doing ‘real science’ sometimes tend to find it strange that one is ‘still testing stuff’ and comment presentations on one’s work with questions like ‘well..nice, but where are your data?’. As it was once correctly diagnosed by Britt Stephens in a conference talk about his VUV-instruments: ‘showing the results of your development work to other people is like showing them pictures of your baby – they might find it ugly or just looking like every other baby and not understand that you are so upset about it’. Nevertheless, altogether I enjoyed working on this task as I really learned a lot about electronics, gas handling issues, CAD drawing and many other aspects of instrument design. Besides, the effect of people commenting my work as described above was more than compensated by numerous contributions of people being helpful in terms of practical, discussion related and emotional support. Karl Kübler from the MPI-BGC Field Instrumentation Facility helped me to get started by introducing me to the other technical members of

the institute and telling me who to address to for which issues. This was followed by a many useful discussions during the course of my thesis, and his systematic way of thinking and the fact that he immediately has the right literature at hand for each problem or question, has proved very helpful. The members of the institute's Mechanical and Electronic Workshop were doing a great job in putting my ideas into practice, although it was sometimes a long way from my extremely colorful CAD drawings to the final construction. My special thanks go to Reimo Leppert from the Electronic Workshop who did not only do a great job in the design of low-noise amplification circuit and RF-powering of the xenon lamp for ICON, but was also spending a lot of time helping me with various (not only purely electronic) experimental issues, e.g. the identification of noise sources or assembling of the electronics for the airborne design. Together with spend many weekends and evenings working in lab while everybody else was enjoying the great weather outside. Frank Voigt and Bernd Schlöffel were responsible for the mechanical construction and have also been of great help. My ideas for the tiny and complicated ICON parts were quite far from the stuff the usually build, and at the beginning of the work on ICON I knew very little about what was feasible in terms mechanical design. Therefore, the final version of the instrument's core part was the result of many discussions and iteration steps. Frank and Bernd were also providing additional parts as the reference gas box (which looks much better in its final version as in Figure 4.7) and many small parts, e.g. customized 4-way-valves. Altogether, I enjoyed great atmosphere in the workshop (as a physical meeting place) and working together with the members of the workshop team.

For testing of the lightweight reference cylinders, I thank Willi Brand and Jürgen Richter for helpful discussions and for letting me use their mass spectrometer when they were on vacation. Willi Brand has also been helpful in general for discussion on many oxygen- and measurement technique-related topics as well as in planning the setup for inlet fractionation experiments. These experiments were started by Angelika Mennecke in the course of her Diploma thesis with whom I also had many inlet-related email and ICQ-based discussion after she left. The CFD-Simulations for explaining the observed effects were provided by Markus Hermann from the Institute

of Tropospheric Research in Leipzig. I thank Markus very much for all the different simulations he performed in order to help me finding the right fractionation mechanism that could explain the observations, and many useful discussions.

Finally coming to the people that could not be put in the drawer of any of the chapters, I'd like to thank some other (current and former) members of the MPI-BGC's Department of Biogeochemical Systems:

Angelika Mennecke has been a great help for me when starting my thesis. At the same time conducting her Diploma thesis and being the mother of three kids, she always was (and still is) amazingly full of energy and is a great source of motivation for everybody else. I very much enjoyed our discussions on oxygen measurements, fractionation issues and scientific basics and our evening meetings where we discussed papers until late night.

For many helpful discussions I also like to thank Huilin Chen and Jan Winderlich, my office mates and fellow PhD students. Together, we formed the experimental part of Christoph's group until we all more or less independently started to get involved more and more into modeling.

Another member of my group deserves special acknowledgement: Marc Geibel has been incredibly helpful during my whole thesis time, both as a fellow PhD student and colleague and as my boyfriend. In the course of my thesis, he has often provided me with helpful ideas from the engineering side. Apart from that, he was always there for me, providing me with all kinds of support, both emotional and practical. In the final phase of my thesis writing, the latter included cooking and taking over all household activities, as well as staying up until late at night with me, proof reading my thesis writing and replacing the ae,ue,oe in my German summary by the ä's, ö's and ü's my English keyboard doesn't provide.

In terms of proof-reading, I also thank Julia Marshall for checking my writing from the native speaker's point of view, thereby getting deep into the problem of three-word-hyphenation and other language subtleties, as well as raising many interesting

comments on scientific contents of my thesis and discovering even the smallest errors in my plots.

In addition, I like to thank Stephan Baum for flask analysis logistics, many interesting technical and scientific discussions and for sharing his interesting literature findings with me; Elena Popa and Rona Thompson for interesting oxygen discussion; Iris Möbius for the experimental support she provided during the period where she was working as my student assistant; Falk Hänsel and Michael Hielscher for providing reference gases and gas-handling-related support; Veronika Beck, Dhanya Pillai and Roberto Kretschmer for interesting scientific and PhD-related discussions, and finally Martin Heimann, whose lecture on Biogeochemical Cycles inspired me to start the thesis at the MPI-BGC.

In the end, I would like thank to my family for always supporting me and believing in me. Special thanks go to my parents for making my studies possible, and for being always there for me while on the other hand letting me live my own life. My brother Jan has been a great help with problems concerning Word-formatting in my thesis and also provided useful comments to its content, seeing it from a viewpoint outside the field of atmospheric science.